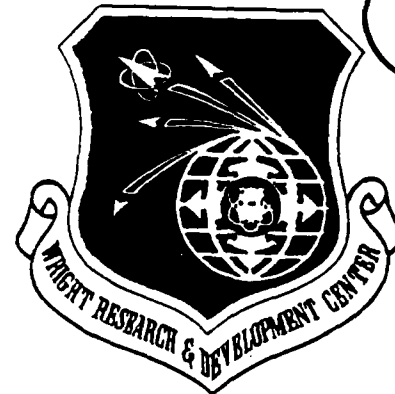WRDC-TR-89-4055

AD-A233 400

COMPENDIUM OF FRACTOGRAPHIC DATA FOR COMPOSITE
MATERIALS

INTERIM REPORT
Covering 9-22-86 through 10-31-88

C. Hua
M. Yamashita
Boeing Advanced Systems
P.O. Box 3707
Seattle, WA 98124

DTIC
ELECTE
MAR 1 5 1991
S
D
D

December 1989

Approved for public release; distribution is unlimited

MATERIALS LABORATORY
WRIGHT RESEARCH AND DEVELOPMENT CENTER
AIR FORCE SYSTEMS COMMAND
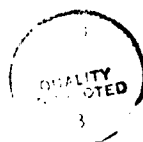WRIGHT-PATTERSON AIR FORCE BASE, OHIO 45433-6533

91 3 14 044

Erratum:

The figures in Section 4.0 do not follow the correct sequence as it relates to the subsections. Figures 4.2-5 through 4.2-12 should be numbered 4.3-1 through 4.3-8; Figures 4.4-13 through 4.4-141 should be 4.4-1 through 4.4-128.

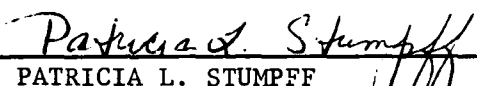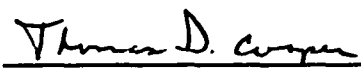Numbers called out in text do correctly correspond to the figures.

NOTICE

When Government drawings, specifications, or other data are used for any purpose other than in connection with a definitely Government-related procurement, the United States Government incurs no responsibility or any obligation whatsoever. The fact that the government may have formulated or in any way supplied the said drawings, specifications, or other data, is not to be regarded by implication, or otherwise in any manner construed, as licensing the holder, or any other person or corporation; or as conveying any rights or permission to manufacture, use, or sell any patented invention that may in any way be related thereto.
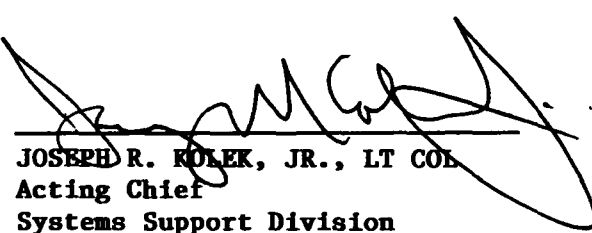
This report is releasable to the National Technical Information Service (NTIS). At NTIS, it will be available to the general public, including foreign nations.

This technical report has been reviewed and is approved for publication.

PATRICIA L. STUMPFF
Air Force Project Engineer

THOMAS D. COOPER, Chief
Materials Integrity Branch
Systems Support Division
Materials Laboratory

FOR THE COMMANDER

JOSEPH R. KOLEK, JR., LT COL
Acting Chief
Systems Support Division

If your address has changed, if you wish to be removed from our mailing list, or if the addressee is no longer employed by your organization please notify WRDC/MLSA, WPFAB, OH 45433-6533 to help us maintain a current mailing list.

Copies of this report should not be returned unless return is required by security considerations, contractual obligations, or notice on a specific document.

REPORT DOCUMENTATION PAGE

1a. REPORT SECURITY CLASSIFICATION	1b. RESTRICTIVE MARKINGS
Unclassified	

2a. SECURITY CLASSIFICATION AUTHORITY	3. DISTRIBUTION/AVAILABILITY OF REPORT
	Approved for public release; distribution is unlimited
2b. DECLASSIFICATION/DOWNGRADING SCHEDULE	

4. PERFORMING ORGANIZATION REPORT NUMBER(S)	5. MONITORING ORGANIZATION REPORT NUMBER(S)
	WRDC-TR-89-4055

6a. NAME OF PERFORMING ORGANIZATION	6b. OFFICE SYMBOL (If applicable)	7a. NAME OF MONITORING ORGANIZATION
Boeing Advanced Systems		Wright Research and Development Center, Materials Laboratory

6c. ADDRESS (City, State and ZIP Code)	7b. ADDRESS (City, State and ZIP Code)
P.O. Box 3707, MS 33-05 Seattle, WA 98124	WRDC/MLSA Wright Patterson AFB, OH 45433-6533

8a. NAME OF FUNDING/SPONSORING ORGANIZATION	9b. OFFICE SYMBOL (If applicable)	9. PROCUREMENT INSTRUMENT IDENTIFICATION NUMBER
	WRDC/MLSA	Contract No. F33615-86-C-5071

9c. ADDRESS (City, State and ZIP Code)	10. SOURCE OF FUNDING NOS			
Wright-Patterson AFB, Ohio 45433-6533	PROGRAM ELEMENT NO	PROJECT NO.	TASK NO	WORK UNIT NO
11. TITLE (Include Security Classification) Compendium of Fractographic Data for Composite Materials (U)	62102F	2418	04	47

12. PERSONAL AUTHOR(S)
Hua, Cam and Mike Yamashita

13a. TYPE OF REPORT	13b. TIME COVERED	14. DATE OF REPORT (Yr, Mo, Day)	15. PAGE COUNT
Interim	FROM 860922 TO 881031	December 1989	358

16. SUPPLEMENTARY NOTATION

17. COSATI CODES			18. SUBJECT TERMS (Continue on reverse if necessary and identify by block number)
FIELD	GROUP	SUB GR	Composites: Composite structure; failure analysis; fractography
11	04		

19. ABSTRACT (Continue on reverse if necessary and identify by block number)

The objective of this program is to enhance the capability of the Air Force in conducting failure analysis investigations on composite structure. This interim report builds upon previous efforts in this area as documented in "Compendium of Post-Failure Analysis Techniques for Composite Materials," AFWAL-TR-86-4137.

This report details the results of the first six tasks which include: 1) identification of techniques for field failure analysts; 2) fractographic techniques other than microscopic examination of the fracture surfaces; 3) a fractographic database of specimens failed under controlled test conditions; 4) a chemical and mechanical property database of constituent and composite materials; 5) data collection format sheets; and, 6) several failure analysis investigations for illustrative purposes. The largest portion of the program was devoted to the fractographic database which includes carbon, fiberglass, kevlar and boron epoxy composites as well as carbon fiber, non-brittle epoxy composites such as carbon/polyetheretherketone (PEEK), carbon/PMR-15, and carbon/multiphase resin (X8551). (mm)

20. DISTRIBUTION/AVAILABILITY OF ABSTRACT	21. ABSTRACT SECURITY CLASSIFICATION
UNCLASSIFIED/UNLIMITED ☒ SAME AS RPT ☐ DTIC USERS ☐	Unclassified

22a. NAME OF RESPONSIBLE INDIVIDUAL	22b. TELEPHONE NUMBER (Include Area Code)	22c. OFFICE SYMBOL
Patricia L. Stumpff	(513) 255-3623	WRDC/MLSA

SS6033 L 356-9

FOREWORD

This final interim report documents work performed under Contract F33615-86-C-5071, "Composite Failure Analysis Handbook", from 22 September 1986 to 30 October 1988.

COMPENDIUM OF FRACTOGRAPHIC DATA FOR COMPOSITE MATERIALS

TABLE OF CONTENTS

TABLE OF CONTENTS (Concluded)

LIST OF FIGURES

LIST OF FIGURES (Continued)

LIST OF FIGURES (Continued)

LIST OF FIGURES (Continued)

LIST OF FIGURES (Continued)

LIST OF FIGURES (Continued)

LIST OF FIGURES (Continued)

LIST OF FIGURES (Continued)

LIST OF FIGURES (Continued)

LIST OF FIGURES (Continued)

LIST OF FIGURES (Concluded)

COMPENDIUM OF FRACTORGRAPHIC DATA FOR COMPOSITE MATERIALS

INTERIM REPORT

1.0 INTRODUCTION

The increasing use of advanced composite materials by the aerospace industry has created a need to reassess failure analysis methods originally developed for metals. New technology necessitates corresponding advances in composite failure analysis. Failures in composites may result from design errors, material and process discrepancies, or anomalous service conditions. New methods of identifying and understanding the causes, mechanisms, and circumstances of composite material failures will lead to corrective actions and design improvements.

1.1 PROGRAM OBJECTIVES

The primary objectives of this program, entitled "Composite Failure Analysis Handbook" (CFAH), USAF Contract F33615-86-C-5071, was to develop a guideline for the analysis of aerospace composite structural component failures. This guide is intended to be a one-of-a-kind failure analysis handbook encompassing methodology and data necessary for composite structure failure investigation. An expansion of the "Compendium of Post-Failure Analysis for Composite Structure" developed under Air Force Contract F33615-84-C-5010, the CFAH program began on 22 September 1986 and the technical effort reported herein was completed on 31 October 1988. Secondary objectives for developing this portion of the handbook were:

a. Development of guidelines for field investigation personnel on handling debris and gathering data at crash sites to supplement laboratory analysis.

b. Expansion of analytical techniques, particularly microscopic and macroscopic fractography.

c. Expansion of the fractographic database for the Hercules AS4/3501-6 system and other materials likely to be encountered in the 1990's.

d. Production of a valuable instruction document in which analytical methods, supporting data, and documented case histories will be presented in a concise and easily used format.

1.2 PROGRAM APPROACH

The overall program approach is shown in Figure 1.2-1. Boeing and General Electric (GE) expertise and supporting scientific literature were used to identify, evaluate, summarize, and demonstrate necessary procedures and techniques for composite failure analysis. Figure 1.2-1 shows six of the eight tasks:

Task 1: Handling and Data Gathering Techniques for Field Representatives.

Task 2: Expansion of Fractographic Techniques in Composite Failure Analysis.

Task 3: Expansion of the Fractographic Database.

Task 4: Development of Data Formats.

Task 5: Documentation of Material Properties.

Task 6: Verification of Composite Failure Analysis System.

Task 7, Administrative Management, and Task 8, Meetings, proceeded smoothly and were reported as appropriate in previous reports.

Tasks 1 through 6 were accomplished by objectively reviewing known information in the technical area, selectively evaluating the speculative information through either proven controlled tests or direct application during the program, gaining an understanding of the scientific fundamentals related to each task, and verifying and demonstrating the information gathered. This report provides the pertinent data and techniques for incorporation into the handbook.

The final handbook will be jointly sponsored by the Air Force and the Federal Aviation Administration (FAA) and compiled by Boeing Advanced Systems, Seattle, Washington, and Northrop Corporation, Hawthorne, California. The tentative outline of the handbook is shown in Figure 1.2-2.

Task 1—develop field rep guidlines

```
Compile field          Develop          Revise
investigation    →     subFALN     →    guidelines
guidelines
```

Task 2—expansion of fractography techniques

```
Identify new          Perform              Evaluate
techniques     →      controlled     →     technique
                      tests Hercules       and revise
                      3501-6/AS4           FALN
```

Task 3A—expansion of fractography   Task 3B—expansion of fractography
database (model system)   database (other systems)

```
Review            Perform            Select other         Perform
C-5010      →     controlled    →    materials for   →    controlled
fractography      tests and          database            tests and
results           fractography                            fractography
```

Task 4—develop data collection formats

```
Identify data          Create data          Apply data
format          →      collection     →     collection
requirements           formats              formats
```

Task 5—compile material properties

```
Identify
sources of             Literature           Compile
material        →      search        →      properties
property data
```

Task 6—verification of system

```
Demonstrate capabilities on
A/F submitted components
```

```
Create Handbook
```

Figure 1.2-1. Program Task Interrelationship

1.0 INTRODUCTION AND PURPOSE

2.0 FUNDAMENTAL SOURCES OF FAILURES

    2.1 Design Errors
    2.2 Materials and Process Discrepancies
    2.3 Anomalous Service Conditions
    2.4 Examples

3.0 FAILURE MODES AND FRACTURE MECHANICS

    3.1 Interlaminar Fractures
        3.1.1 Mode 1 Tension
        3.1.2 Mode 2 Shear
        3.1.3 Mixed Mode
        3.1.4 Fatigue
    3.2 Translaminar Fractures
        3.2.1 Mode 1 Tension
        3.2.2 Mode 1 Compression
        3.2.3 Flexural
        3.2.4 Compression-Buckling
    3.3 Fracture Mechanics
        3.3.1 Fracture Toughness
        3.3.2 Notch Sensitivity
        3.3.3 Rate Sensitivity
        3.3.4 Fatigue

4.0 ANALYTICAL PROCEDURES AND TECHNIQUES

    4.1 Overall Approach to Failure Analysis of Composites
        4.1.1 Overall FALN
    4.2 Field Investigation Guidelines
        4.2.1 Field Investigation FALN-Overview of Approach
        4.2.2 Field Investigation Guidelines-Procedures and Methods
            4.2.2.1 Organization and Planning
              ● *Investigator's equipment*
              ● *Specialist examinations*
            4.2.2.2 Initial On Site Action-Evidence Preservation
              ● General
              ● Protective and corrective measures
              ● Proper handling of failed components
              ● Environmental effects on failure surfaces
              ● Photomacrography
            4.2.2.3 Structures Investigation-Macroscopic
              ● Types and modes of material failure
              ● Recognition of failure types
              ● Determination of failure sequence
              ● Selection of specimens for laboratory analysis
            4.2.2.4 *Specimen Gathering Techniques*
              ● Cutting techniques
              ● Cleaning of fracture surfaces
              ● Packaging for shipment
            4.2.2.5 Safety and Health
              ● Overview
              ● Equipment
    4.3 Nondestructive Evaluation (NDE)
        4.3.1 NDE FALN-Overview of Approach
        4.3.2 NDE Techniques-Overview Methods
        4.3.3 Ultrasonic Methods
        4.3.4 X-Ray Radiography
        4.3.5 Penetrant Inspection
        4.3.6 Specialized NDE Techniques
        4.3.7 Examples of NDE Methods Used in Failure Analysis

    4.4 Materials Characterization
        4.4.1 Materials Characterization FALN-Overview of Approach
        4.4.2 Materials Characterization Techniques-Overview of Methods
        4.4.3 Material Layup Analysis (Ply Count and Orientation)
            ● Optical microscopy
            ● Image analysis
            ● Other techniques
        4.4.4 Material Identification
            4.4.4.1 Uncured Material Identification
              ● High pressure liquid chromatography (HPLC)
              ● Infrared spectroscopy (IR)
              ● Differential scanning calorimetry (DSC)
              ● X-Ray fluorescence (XRF)
              ● Other techniques
            4.4.4.2 Cured Material Identification
              ● Pyrolysis-gas chromatography (PGC)
              ● Pyrolysis gas chromatography mass spectroscopy (PGC/MS)
              ● Infrared spectroscopy (IR)
              ● X-Ray fluorescence (XRF)
              ● Other techniques
        4.4.5 Degree of Cure Analysis
            4.4.5.1 Glass Transition Temperature (TG) Analysis
              ● Thermomechanical analysis (TMA)
              ● Differential scanning calorimetry (DSC)
              ● Dynamic mechanical analysis (DMA)
              ● Other techniques
            4.4.5.2 Extent of Unreacted Material
              ● Differential scanning calorimetry (DSC)
              ● Dynamic mechanical analysis (DMA)
              ● Infrared spectroscopy (IR)
              ● Solvent extraction
        4.4.6 Cured Material Contamination Analysis
            4.4.6.1 Surface Chemical Contamination
              ● Optical microscopy
              ● Scanning electron microscopy and electron microprobe analysis
              ● X-Ray photoelectron spectroscopy (XPS)
              ● Auger electron spectroscopy (AES)
              ● Secondary ion mass spectroscopy (SIMS) and related ion beam method
            4.4.6.2 Foreign Object Inclusion
              ● Visual
              ● Optical microscopy
              ● Scanning electron microscopy and electron microprobe analysis
              ● Radiography
              ● Ultrasonic imaging and defect resolution
        4.4.7 *Environmental Effects on Material Characterization Evaluations*
        4.4.8 Use of Materials Characterization Methods and Examples in Failure Analysis

Figure 1.2-2. Preliminary Outline for Composite Failure Analysis Handbook

(2 of 2)

Figure 1.2-2. Preliminary Outline for Composite Failure Analysis Handbook (Concluded)

2.0 TASK 1: HANDLING AND DATA GATHERING TECHNIQUES FOR FIELD REPRESENTATIVES

2.1 OBJECTIVE

The goal of Task 1 was to develop a sub-failure analysis logic network (sub-FALN). The sub-FALN provides specific guidelines for field investigation of composite component failure.

2.2 APPROACH

The approach to Task 1 was to first compile existing government and industry field investigation guidelines generic to both metal and composite components. The sub-FALN was then developed based on review and comment by field representatives and the guidelines were revised for incorporation into the handbook. This approach ensured compatibility and continuity with current accident field investigation guidelines. This was a low cost approach, since many of the industry field investigation guidelines have already been developed. Figure 2.2-1 illustrates the flow diagram for this task.

2.3 METHODS

In order to develop the sub-FALN, three subtasks were identified: (1) literature search and review, (2) consultation with experts, and (3) test matrix development and performance.

2.3.1 Literature Search and Review

A literature search for handling and data gathering techniques for field representatives was conducted using the following references:

a. Manual of Aircraft Accident Investigation, International Civil Aviation Organization (ICAO), Montreal, Quebec, Canada, Document No. 6920-AN/855/4, 4th edition, 1970.

b. Technical Manual: USAF Material Deficiency Reporting and Investigating System. Document No. TO 00-35D-54(C8), 1 September 1986.

c. AFR 127-4(C2): Investigating and Reporting U.S. Air Force Mishaps, 29 November 1985.

Step 1 — definition of existing procedures and concerns

Initial review
- ICAO manual
- Air Force regulation 127-4
- ASM vol. 10 handbook
- Air Force fractography handbook

Establish list of concerns
- Define common procedures
- Define exceptions
  - Conditions anticipated
  - Sample selection
  - Handling and protection
  - Safety

Review with experts
- AFPE
- Norton AFB
- USC
- Boeing
- GE
- NTSB

Step 2 — composite guidelines compilation and development

Literature search on concerns
- Macroscopic fractography
- Environmental effects
- Handling and protection
- Data gathering
- Safety
- BCAC procedures
- DOD procedures

Define test matrix

Establish tentative guidelines

Review with field reps

Step 3

Perform test matrix
- Environmental effects
- Corrective methods

Step 4

Develop sub FALN for field investigation

Step 5

Presentation to Air force and field reps

Step 6

Final verification on failed components

Air Force approval

Guidelines and procedures into Handbook

Common guidelines

Figure 2.2-1. Task 1 Flow Diagram

2.3.2 Consultation With Experts

After an initial review of existing field procedures and guidelines for both metallic and composite structure, a panel of experts was consulted to confirm and refine concerns to be addressed. The panel consisted of Joseph Tilson, USAF flight safety engineer; Rick Davis, Air Force accident investigation instructor at the University of Southern California; Burton Chesterfield, division manager for the Aircraft Aviation Safety Institute, Department of Transportation; Jim Wildey, National Transportation Safety Board Accident Investigation, Washington, D.C.; and Thurmon Jones, Boeing accident investigator.

2.3.3 Test Matrix Development and Performance

Based on the areas of interest identified, literature regarding specific procedures and analytical methods was surveyed. In areas where no data or literature existed, laboratory tests were performed. The test matrix shown in Figure 2.3-1 was aimed at identifying environmental effects, corrective action techniques, protective methods, and cutting effects (each as related to the preservation of physical evidence). AS4/3501-6 carbon/epoxy was used in the analysis.

Initially, 3/4-inch square specimens were cut from both double cantilever beam (DCB) and end-notched flexure (ENF) specimens. DCB and ENF specimens simulate interlaminar Mode I tension and interlaminar Mode II shear respectively; for full description, see Section 4.3.3. Optical microscopy was performed to confirm that the control fracture features were present prior to the test exposure. Once fractographic features such as rivermarks and hackles were identified, the specimens were exposed to test conditions. Finally, the specimens were analyzed by scanning electron microscopy (SEM) and photomicrographs were taken for documentation.

Environmental Effects. The primary objective of this portion of the test matrix was to evaluate environmental effects on fracture surfaces. Jet fuel, hydraulic fluid, and fire retardant foam can come into contact with fracture surfaces. To test whether such contact could alter fracture surfaces, test specimens were soaked in beakers containing contaminant solutions for 30 minutes. In addition, a specimen was soaked in fire retardant foam for 24 hours, per Air Force request. The jet fuel used was JP-4, the hydraulic fluid was Skydrol, and the fire retardant was Aqueous Film Forming Foam (AFFF). The main chemical ingredients of AFFF are water (76%), diethylene glycol monobutyl ether (15%), urea (4%), fluoroalkyl surfactants and synthetic detergents (<5%).

Condition	Test specimen type		Comments
Environment • Jet fuel (JP-4) • Hydraulic fluid • Fire retardant foam • Water ▷	Mode I DCB	Mode II ENF	• Environment applied after fracture • SEM examination • Examined in Task 3A ▷
Corrective action • Water • Soapy water • MEK • Acetone			• Cleaned after above environment • SEM examination
Packaging • Plastic bags • Paper	Mode I DCB	Mode II ENF	• Hand-pressed onto or wrapped around fracture surfaces • SEM examination
Cutting • Abrasive saw • Toothed saw	Unfractured laminate Unfractured laminate		• Optical microscopy

Figure 2.3 -1.   Task 1 Test Matrix

Corrective Action. The primary objective here was to evaluate the effects of corrective cleaning solution on the fracture surface. Corrective cleaning solutions such as methyl ethyl ketone (MEK), acetone, and soapy water are commonly used to remove foreign particles (such as resin dust) from the fracture surfaces. Tests of the effects of these cleaning solutions on fracture surfaces were conducted in the same manner as those for environmental contaminants. Exposure to MEK for 24 hours was also examined.

Cutting. The primary objective was to evaluate the damage induced by an abrasive saw as compared to a toothed saw. The specimens were cut with toothed and abrasive saws. Subsequently, optical microscopy was used to evaluate the extent of damage due to cutting.

Packaging. The primary objective was to evaluate the effects of packaging with a paper or plastic bag placed directly on a fracture surface. Bags were tightly sealed onto the fracture surface of a test specimen to simulate the packaging of a fractured part. To increase the pressure on the fracture surface, the packaging bags were wrapped with masking tape.

The test results were used to create the preliminary sub-FALN, which was then revised in response to review comments by Air Force field representatives.

2.4 RESULTS

2.4.1 Literature Search and Review

A review of the references produced a generalized outline of composite-specific concerns and guidelines. Emphasis was placed on sample selection, handling, and data gathering. The review of published field investigation guidelines established the following major areas:

a. Safety considerations and initial actions taken at accident investigation site

b. Preservation of evidence and photographic documentation

c. Macroscopic examination procedures

d. Determining need for laboratory analysis and choosing specimens

e. Care and handling of fractured materials

f. Cutting, packaging, and shipping

g. Restoration of fractured specimens after post-failure contamination

2.4.1.1 Safety Considerations and Initial Actions Taken at Accident Investigation Site

Among the initial actions to be taken at the scene of an accident investigation are:

a. Document fleet information.

b. Secure the fractured structure from further damage.

c. Preserve important details for subsequent investigation.

d. Document contaminations such as ice, soot, and organic residue which may degrade with time.

Potential situations which may adversely affect composite fractures may involve exposure to UV radiation, heat, hydraulic fluid, or flame retardant.

Safety considerations in handling fractured composite materials fall into three categories. Typically gloves are needed to handle the fractured components to avoid fiber splinter penetration into the skin. Two practices are suggested when performing high speed cutting of composite parts. Airborne carbon fibers from cutting operations can find their way into electronic components where they present a shorting hazard due to their conductivity. This can be minimized by using a cutting fluid, preferably water. It is also prudent to avoid breathing machining and cutting dust by wearing a dust mask.

2.4.1.2 Preservation of Evidence and Photographic Documentation

Critical fracture information can be obtained by interpretation of the overall appearance of a fractured component. The appearance, orientation, and relative position of fractured component is essential for deducing the sequence of break-up and the significance of a particular fracture in an accident investigation.

Composite components are unique due to their brittle fibrous nature. It is very important to preserve by photographic documentation the patterns of cracks and delaminations which are present in the composite structure. The relative positions and appearance of these fractured segments form the basis for subsequent visual macroscopic fractographic interpretations. A badly damaged composite structure is very fragile and it is imperative that the photographic documentation be made before the component is moved. This step may greatly aid the laboratory fracture analysis with the reconstruction of the sequence of fracture events. Good documentation will also ensure accurate traceability of the fractured component to the overall structure.

2.4.1.3 Macroscopic Examination Procedures

These procedures have been established through the documentation in case histories and the development of some concise visual crack pattern recognition rules.

For composite structures, these rules are just beginning to be realized. There are some important similarities in the crack propagation patterns between metals and composite structures.

Specific composite macroscopic fractographic features which are commonly used are given in Figure 2.4-1.

2.4.1.4 Determining Need for Laboratory Analysis and Choosing Specimens

During the course of a failure analysis it is often necessary to refer to technical experts to determine the ultimate cause of failure. Selection of the appropriate laboratory is based on the level of expertise and the array of laboratory instrumentation required to do the job.

In composite failure analysis, the laboratory selection is critical since the number of established composite failure analysis experts will initially be few in number.

The optimum specimen is the largest, most inclusive portion of the critical failed composite structure. Specimen labeling should be done to allow traceability to the part drawing.

2.4.1.5 Care and Handling of Fractured Materials

In a failed composite component, fragile fibrous fracture features may be damaged in transport. Handling critical fracture surfaces or rubbing together in attempting to put fractured components back together can destroy important fracture features. Protective coatings used for metals fractures in the past should not be used. Avoid introducing cutting an machining debris onto the fracture surface.

2.4.1.6 Cutting, Packaging, and Shipping

Special attention should be given to restraining a fractured component to keep it from being damaged in transit and protect the component from the environment. Some of these issues were examined by completion of the test matrix presented in Figure 2.3-1.

Mode	Environmental condition	Macroscopic fracture features
Interlaminar tension dominated	Low temperature/dry	• Smooth, glassy fracture surface • Major portion of fracture between plies
	Hot or hot/wet	• Smooth but with loose fibers strewn on surface • Major portion of fracture within plies • May be permanent deformation of laminate
Interlaminar shear dominated	Low temperature/dry	• Surface flat, but with "milky" appearance when held at angle to light • Major portion of fracture between plies
	Hot or hot/wet	• Also exhibits "milky" appearance • Tends to fracture within a ply • Loose fibers on surface
Translaminar tension	—	• Rough, jagged fracture surface with individual fibers protruding from surface
Translaminar compression	—	• Extreme surface damage. Large regions of fibers fractured on same plane • Very few, if any, fibers protruding from surface
Translaminar flexure	—	• Two fairly distinct regions, one exhibiting translaminar tension and the other translaminar compression, the regions being separated by a neutral axis line

Figure 2.4-1   Macroscopic Fracture Surface Features

2.4.1.7 Restoration of Fractured Specimens After Post-Failure Contamination

As with fractured metals, cleaning the fracture surface should be undertaken with caution. Often it is possible to perform microscopic examinations in the as-received condition and then initiate a cleaning protocol and repeat the examination.

2.4.2 Consultation With Experts

For the most part, areas of concern voiced by the panel regarded macroscopic inspection methods and the preservation of evidence. It was generally agreed that only time and experience with large test and flight structures would adequately build macroscopic inspection technology for composites to equal that which currently exists for metallic structures. The three major concerns regarding macroscopic fracture analysis were: (1) differentiation between slow crack growth due to fatigue and rapid crack growth due to overload and crash; (2) identification of a primary load types operative during fracture; and (3) determination of crack growth direction.

Macroscopic identification of fatigue damage has been limited to fractures which exhibit closely spaced beach marks on delaminated surfaces. Large components that fail during fatigue loading often do not exhibit these macroscopic features.

Within this program, efforts pertaining to rate sensitivity were restricted to microscopic variations in delamination. Macroscopic identification of load type at fracture has been well understood for several years (see Fig. 2.4-1). However, techniques for determining the direction of crack growth by macroscopic methods have just begun to be developed. Methods which involve crack branching, the T-junction rule, crack alterations at fastener holes, and hand-loading of the cracked (but unfractured) structure have been shown to greatly aid in the determination of crack growth directions.

2.4.3 Test Matrix Development and Performance

Control Specimens. Before exposure to test conditions, specimens showed features typically seen in room temperature/dry fracture specimens. Rivermarks and resin flow exhibited by the interlaminar Mode I tension specimen (Fig. 2.4-2) indicated the crack propagation direction. Hackles and scallops in the interlaminar Mode II shear specimen (Fig. 2.4-3) could not be used to determine crack growth direction.

400X

60 degree tilt

2,000X

60 degree tilt

20X
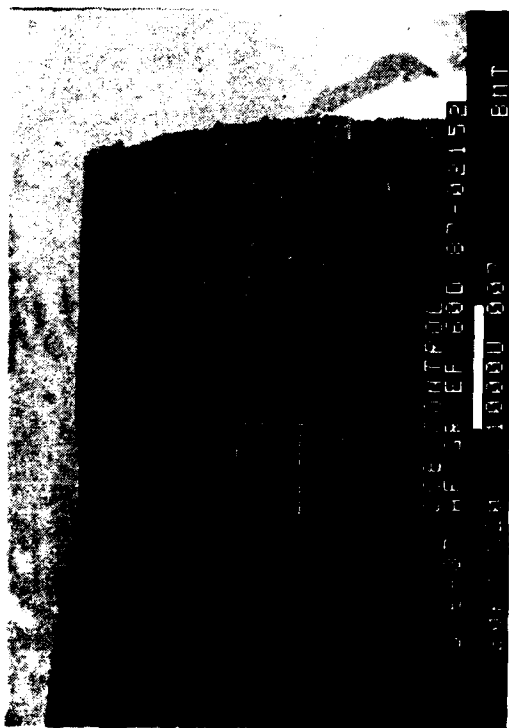
60 degree tilt

Legend:

M resin microflow
R rivermarks

Mechanically induced
crack direction
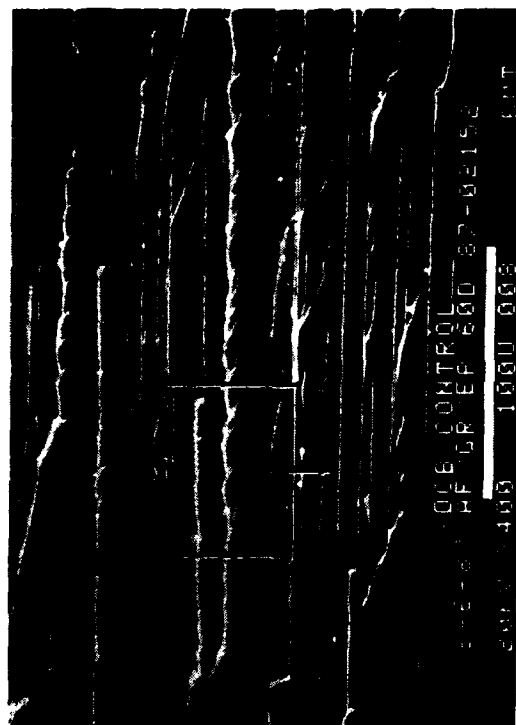
Figure 2.4-2. SEM Fractographs of the Task 1 DCB Control Specimen

400X

60 degree tilt

2,000X

60 degree tilt

20X

60 degree tilt
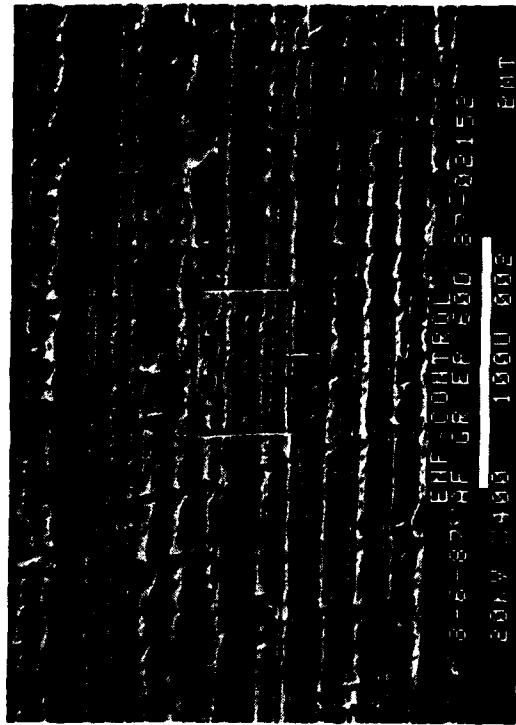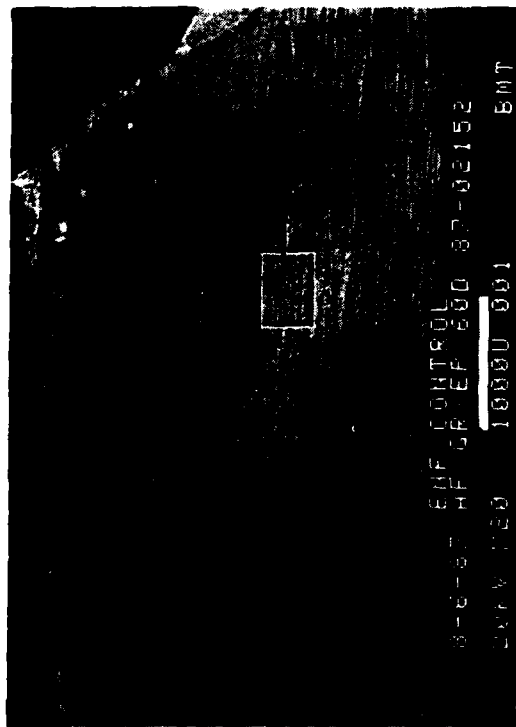
Legend:
R rivermarks
H hackles
S scallops

Mechanically induced
crack direction

Figure 2.4-3. SEM Fractographs of the Task 1 ENF Control Specimen

Environmental Effects. Fracture surfaces exposed to environmental contaminants for 30 minutes showed no sign of degradation in fracture features (Fig. 2.4-4 through 2.4-9). The features observed were consistent with those observed on control specimens. Long-term exposure to AFFF had little effect on fracture features (Fig. 2.4-10 and 2.4-11), although the features were not as defined as in control specimens.

Corrective Action. Fracture surfaces exposed to soapy water, MEK, and acetone for a short time showed no sign of degradation in the fracture features (Fig. 2.4-12 through 2.4-17). In the long-term exposure specimens, the Mode I tension fracture surface exposed to MEK for 24 hours revealed localized pits due to resin swelling, and rivermarks were not as distinct as the control specimen (Fig. 2.4-18). However, the 24-hour Mode II shear fracture surface (Fig. 2.4.-19) was unaffected.

Cutting. The abrasive saw cut produced a smooth, consistent surface (Fig. 2.4-20) highly desirable for handling delicate polymer-based composite structures. On the other hand, the toothed saw created a rough surface from which the fibers were pulled out (Fig. 2.4-21). This was due to the inconsistency in the blade.

Packaging. The fracture features were unaffected by the paper or plastic packaging. Figures 2.4-22 and 2.4-23 are SEM fractographs of the surfaces of fracture specimens that had been packaged with paper bags. Figures 2.4-24 and 2.4-25 are SEM fractographs of the fracture surfaces after packaging with plastic bags. Unlike these test specimens, an actual in-service fractured part may have a very irregular surface and packaging may be extremely difficult. In such cases, it may be impossible to entirely avoid damaging the evidence. Therefore, this test may not be a complete simulation of the packaging effects.
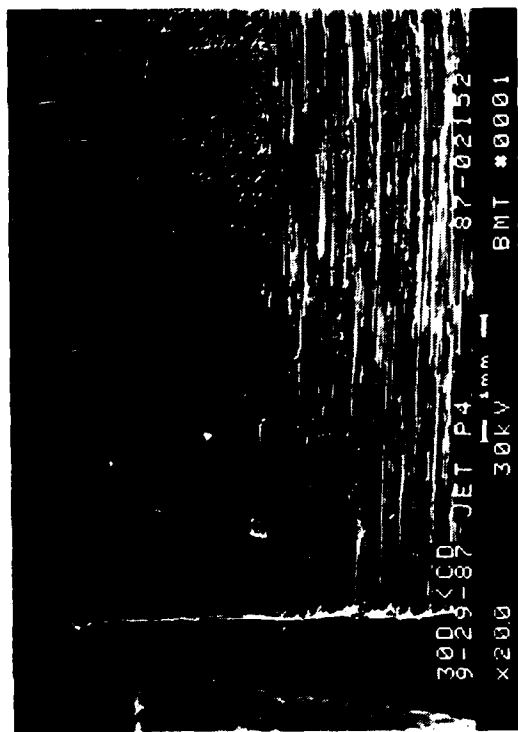
Mechanically induced crack direction

Figure 2.4-4. SEM Fractographs of Interlaminar Mode I Tension, 0/90 Fracture After Exposure to Jet Fuel

Mechanically induced
crack direction

2,000X

60 degree tilt

20X
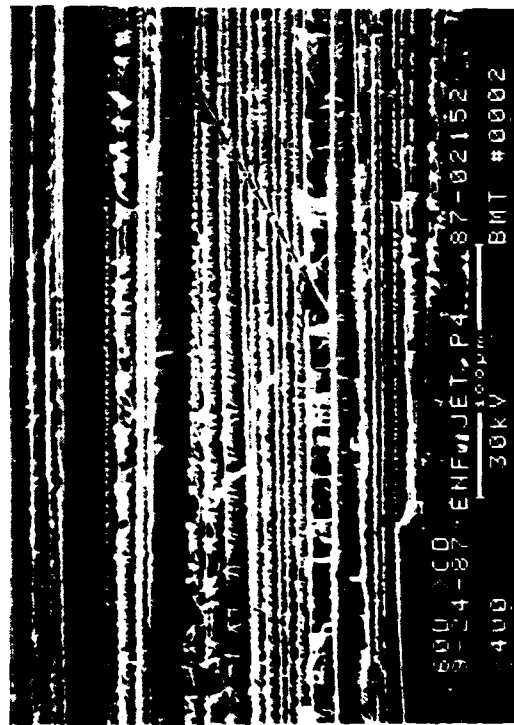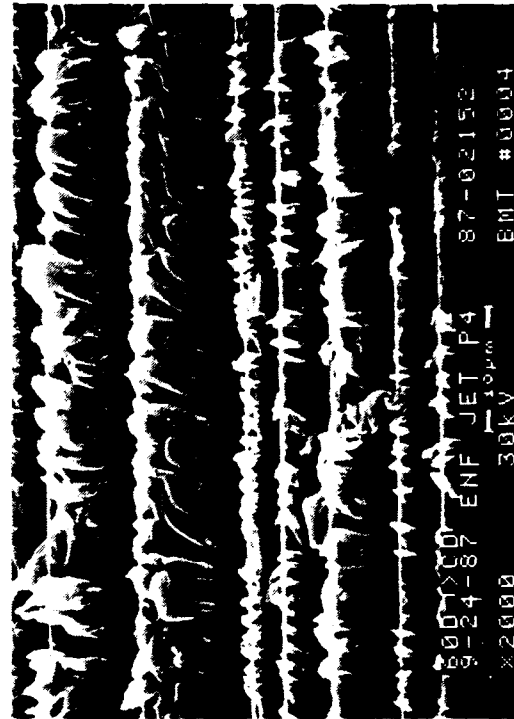
60 degree tilt

400X

60 degree tilt

Figure 2.4-5. SEM Fractographs of Interlaminar Mode II Shear 0/90 Fracture After Exposure to Jet Fuel

Mechanically induced crack direction
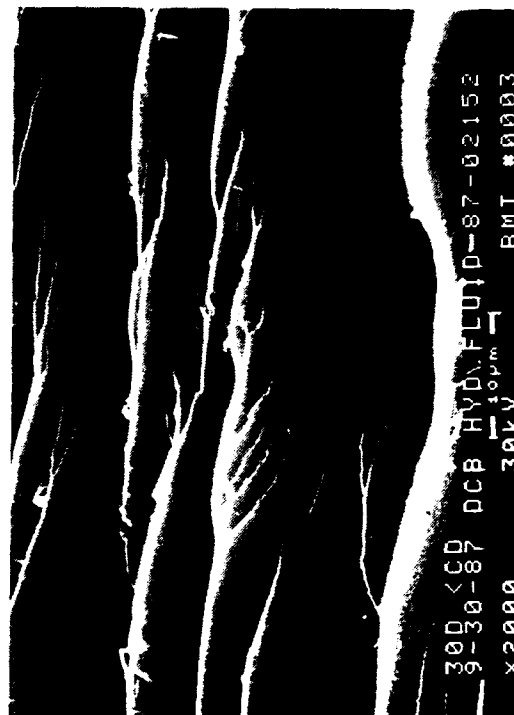
Figure 2.4-6. SEM Fractographs of Interlaminar Mode I Tension, 0/90 Fracture Exposed to Hydraulic Fluid

Mechanically induced crack direction →

2,000X

60 degree tilt

20X

60 degree tilt
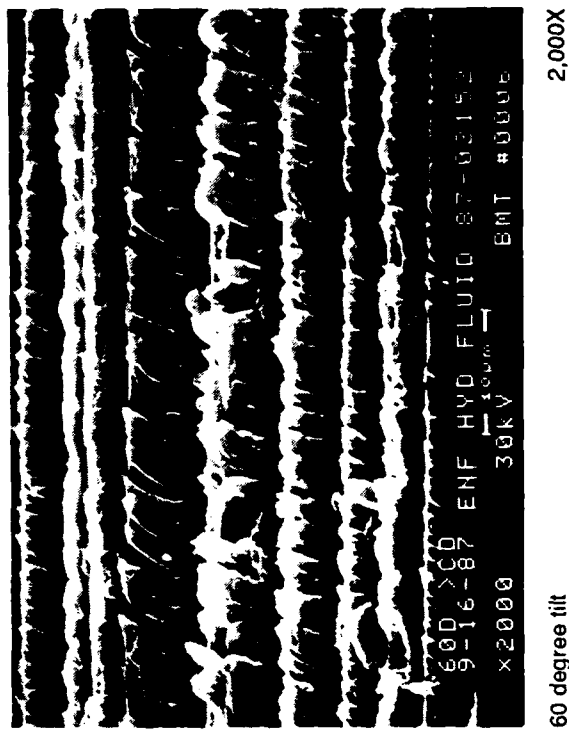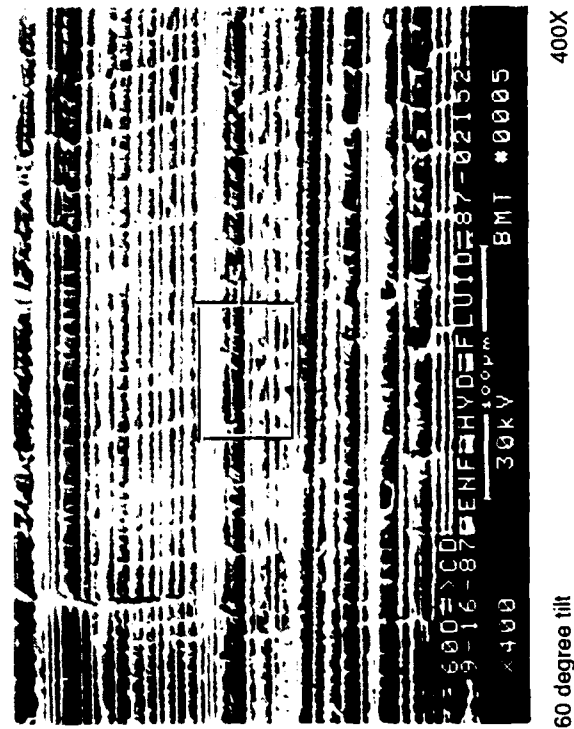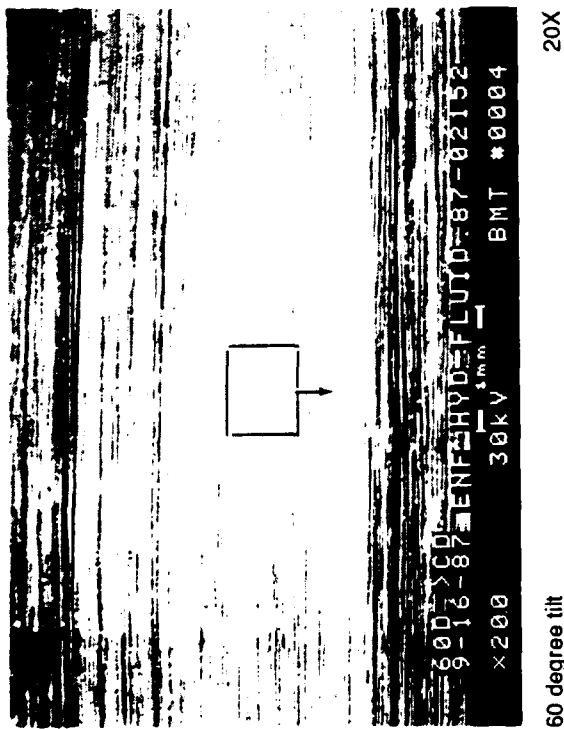
400X

60 degree tilt

Figure 2.4-7. SEM Fractographs of Interlaminar Mode II Shear 0/90 Fracture Exposed to Hydraulic Fluid
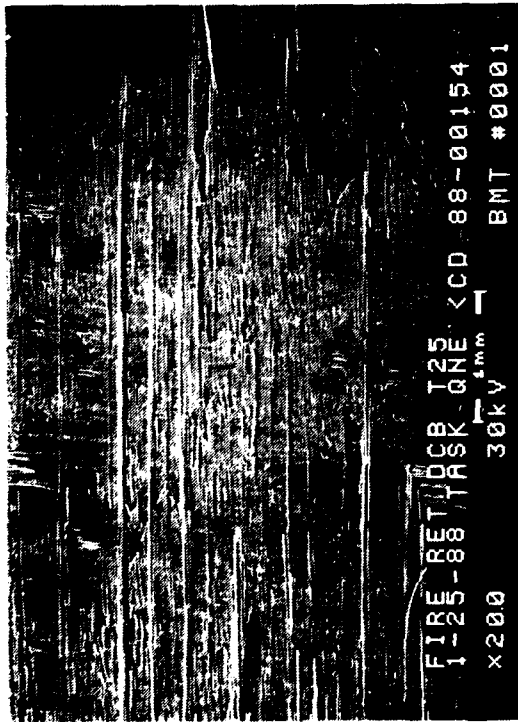
Mechanically induced crack direction

Figure 2.4-8. SEM Fractographs of Interlaminar Mode I Tension, 0/90 Fracture Exposed to Fire Retardant Foam for 30 Minutes
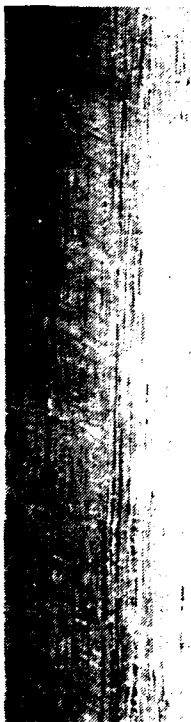
Mechanically induced
crack direction

FIRE RET ENF 160
1-25-88 TASK QNE *CD 88-00154
×2000 30kV 10μm BMT #0003

2,000X

60 degree tilt

FIRE RET ENF 160
1-25-88 TASK QNE *CD 88-00154
×20.0 30kV 1mm BMT #0001

20X

60 degree tilt

FIRE RET ENF 160
1-25-88 TASK QNE *CD 88-00154
×400 30kV 100μm BMT #0002

400X
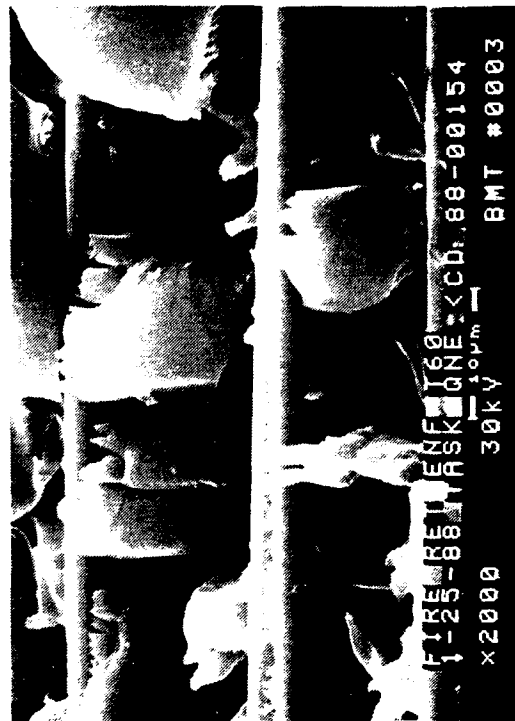
60 degree tilt

Figure 2.4-9. SEM Fractographs of Interlaminar Mode II Shear 0/90 Fracture Exposed to Fire Retardant Foam for 30 Minutes
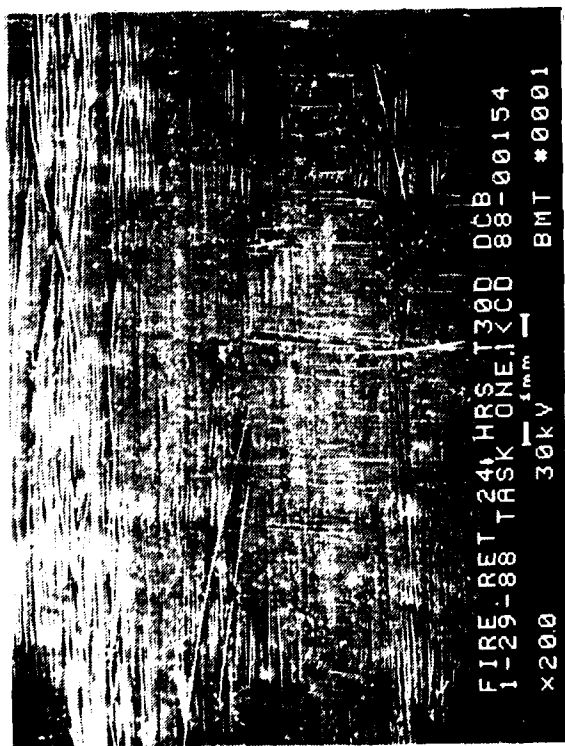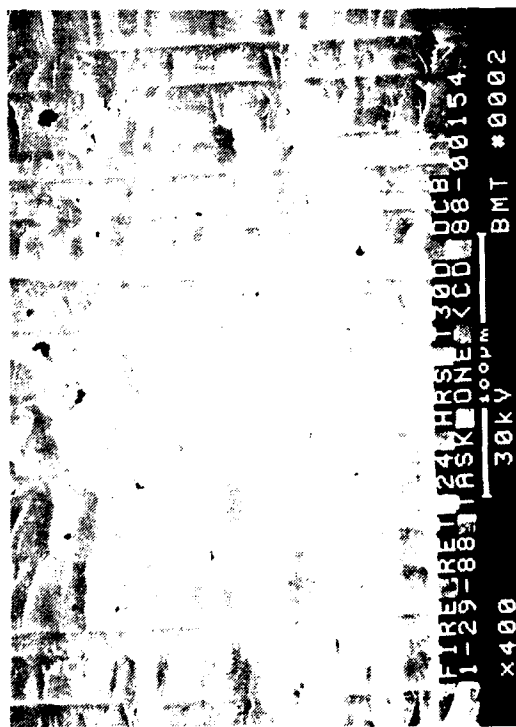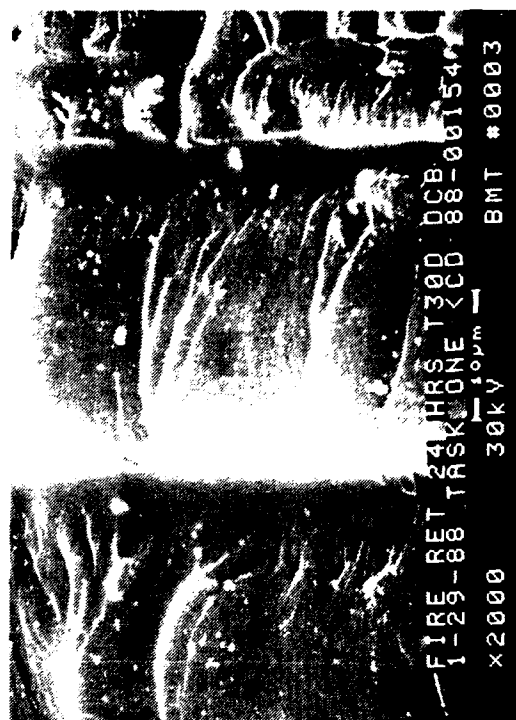
Mechanically induced
crack direction

Figure 2.4-10. SEM Fractographs of Interlaminar Mode I Tension, 0/90 Fracture Exposed to Fire Retardant Foam for 24 Hours

Mechanically induced crack direction →

20X
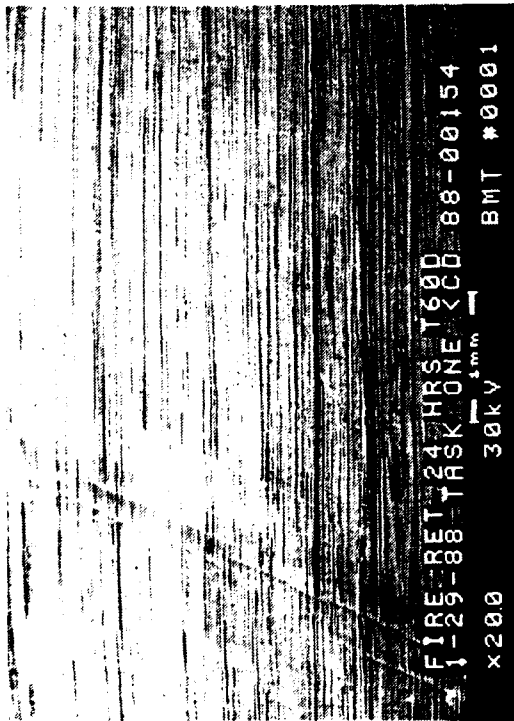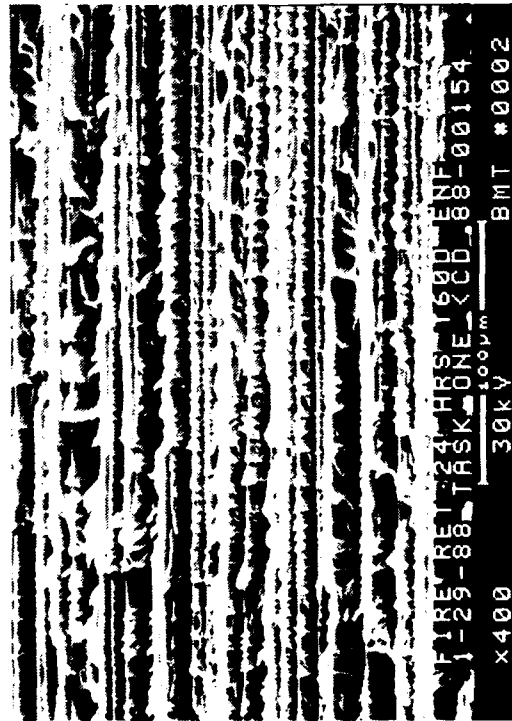
400X

2,000X

60 degree tilt

60 degree tilt

60 degree tilt

Figure 2.4-11. SEM Fractographs of Interlaminar Mode II Shear 0/90 Fracture Exposed to Fire Retardant Foam for 24 Hours
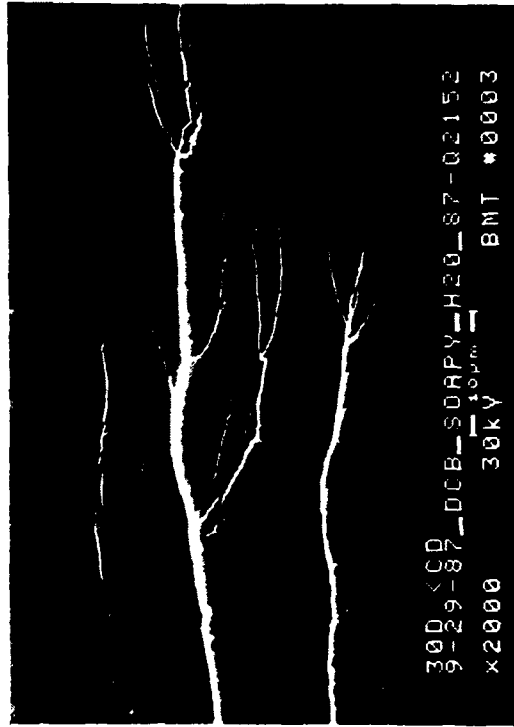
Mechanically induced
crack direction

Figure 2.4-12. SEM Fractographs of Interlaminar Mode I Tension, 0/90 Fracture Exposed to Soapy Water
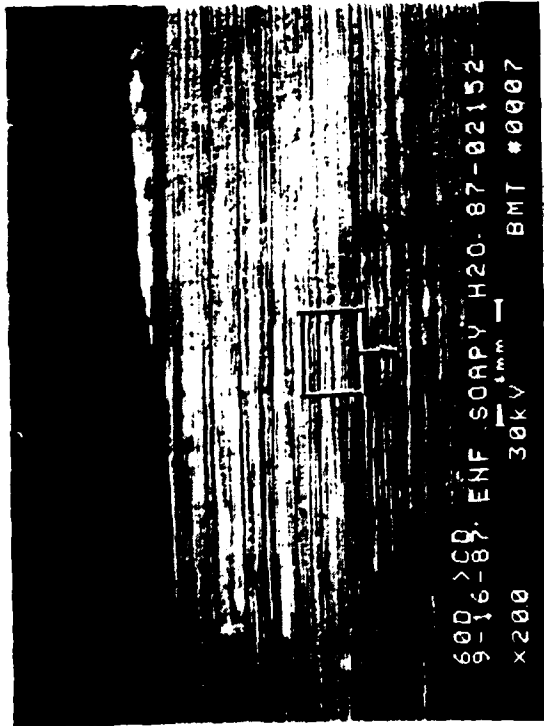
Legend:

F fiber/matrix separation
H hackles
R rivermarks

Mechanically induced
crack direction

20X

400X

2,000X

60 degree tilt
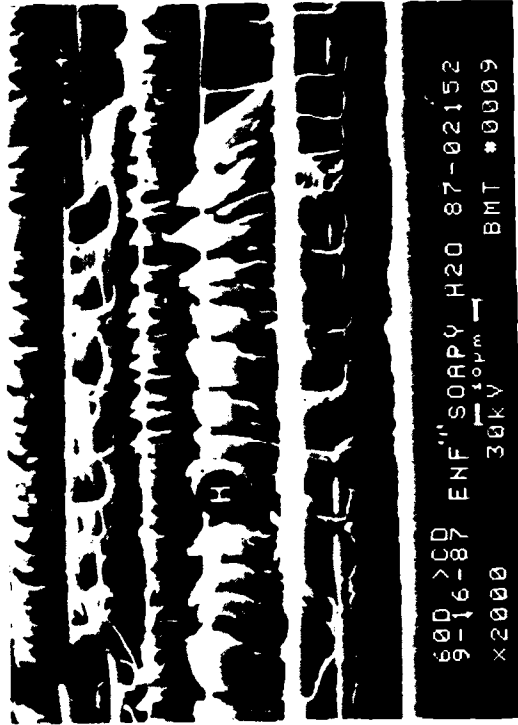
60 degree tilt

60 degree tilt

Figure 2.4-13. SEM Fractographs of Interlaminar Mode II Shear 0/90 Fracture Exposed to Soapy Water
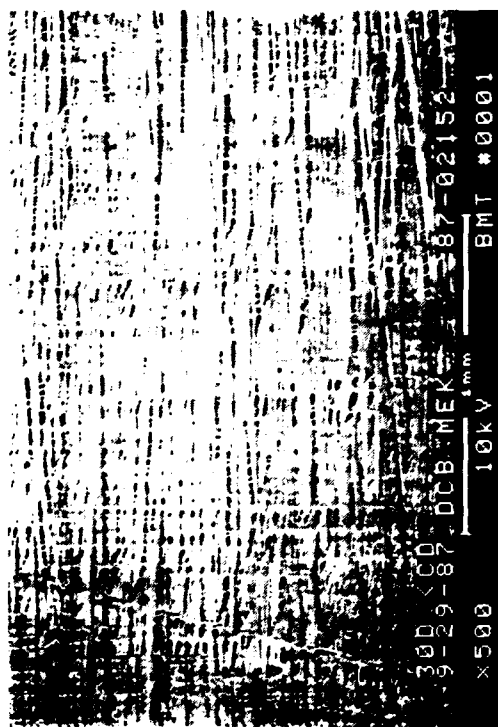
D180-31996-1

27

Mechanically induced
crack direction

50X

400X

2,000X

30 degree tilt

Figure 2.4-14. SEM Fractographs of Interlaminar Mode I Tension, 0/90 Fracture Exposed to MEK
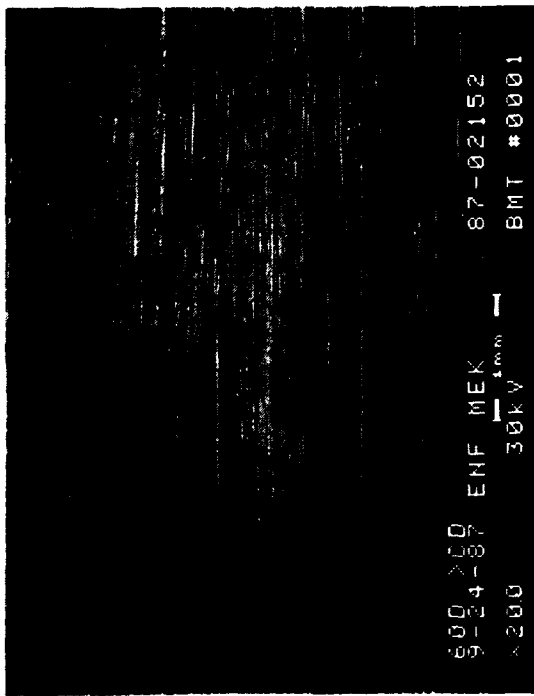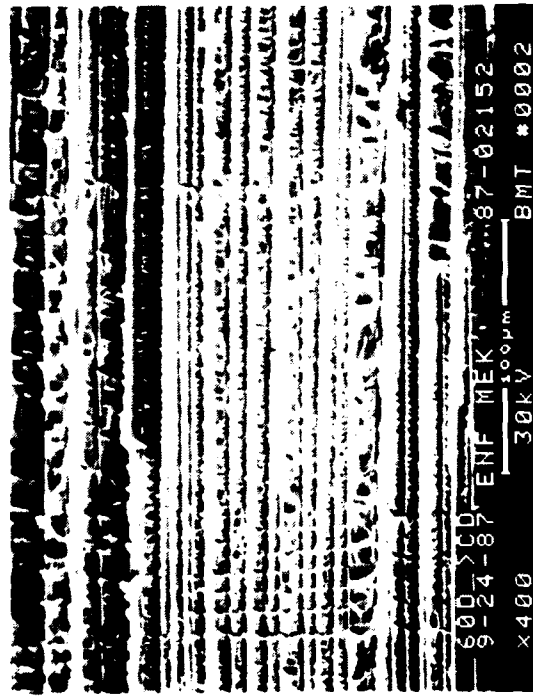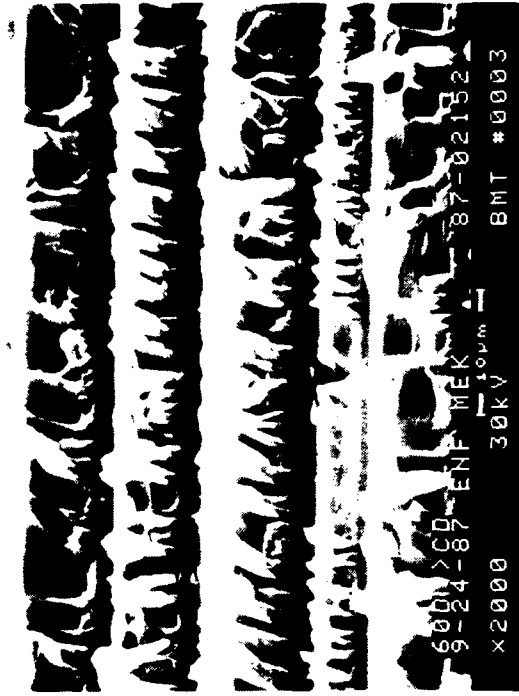
Mechanically induced
crack direction

Figure 2.4-15. SEM Fractographs of Interlaminar Mode II Shear, 0/90 Fracture Exposed to MEK
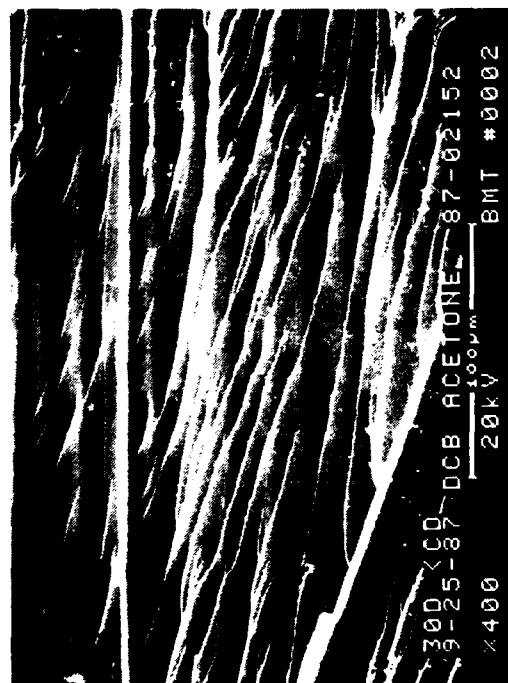
Mechanically induced
crack direction

30 degree tilt   2,000X
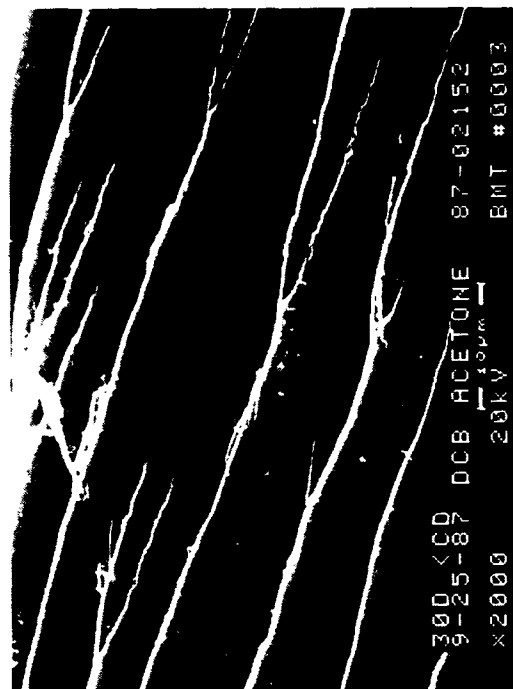
30 degree tilt   20X

30 degree tilt   400X

Figure 2.4-16. SEM Fractographs of Interlaminar Mode I Tension, 0/90 Fracture Exposed to Acetone
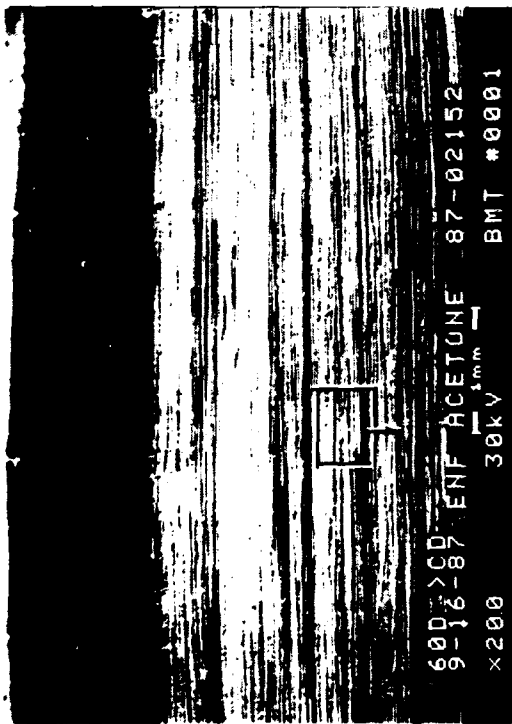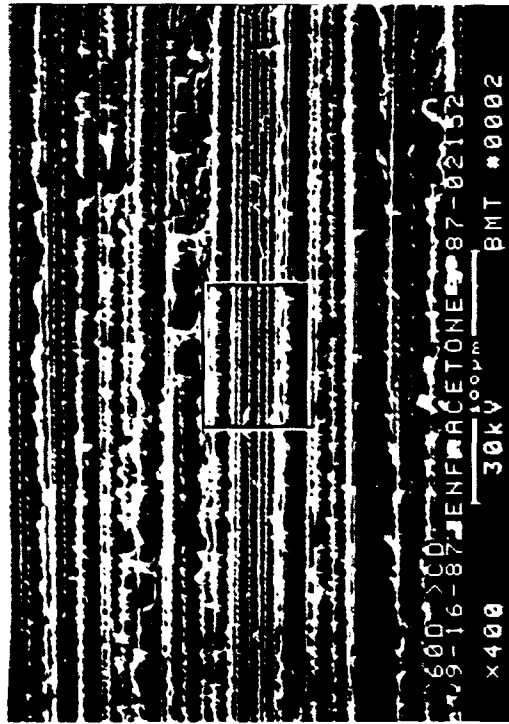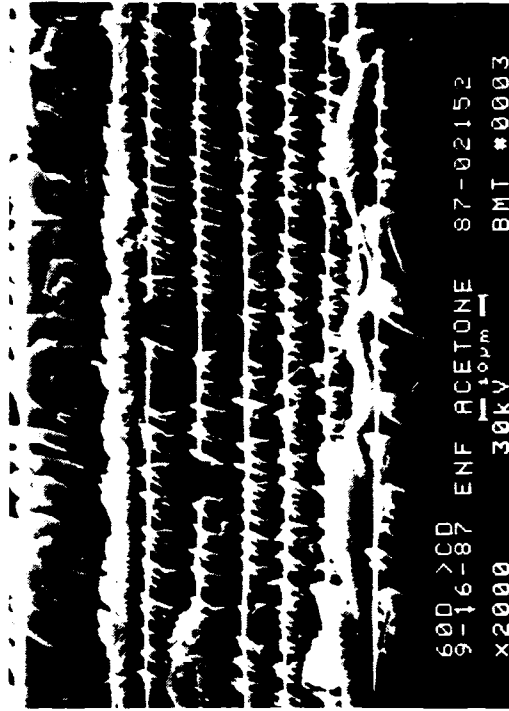
Mechanically induced
crack direction

Figure 2.4-17. SEM Fractographs of Interlaminar Mode II Shear, 0/90 Fracture Exposed to Acetone
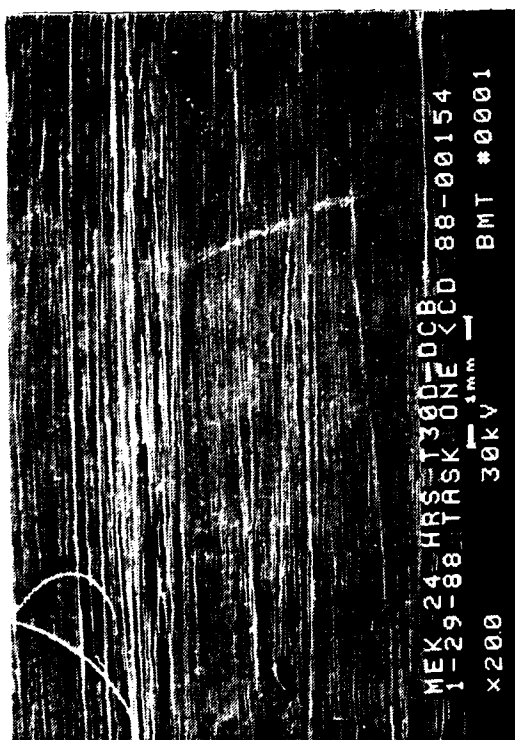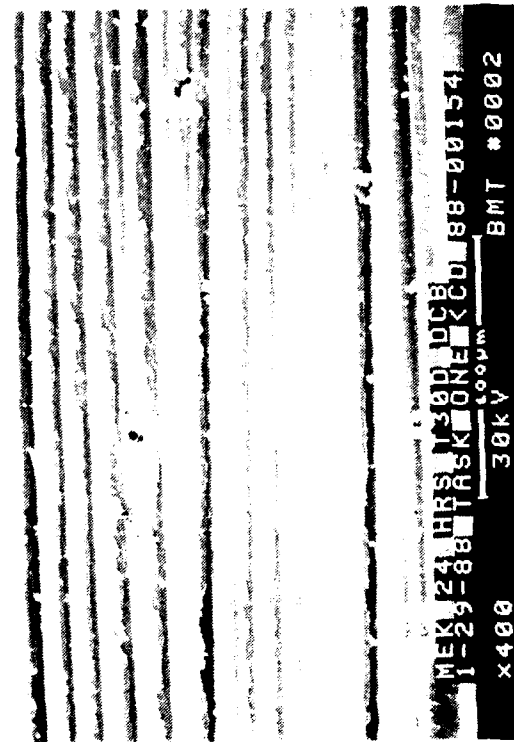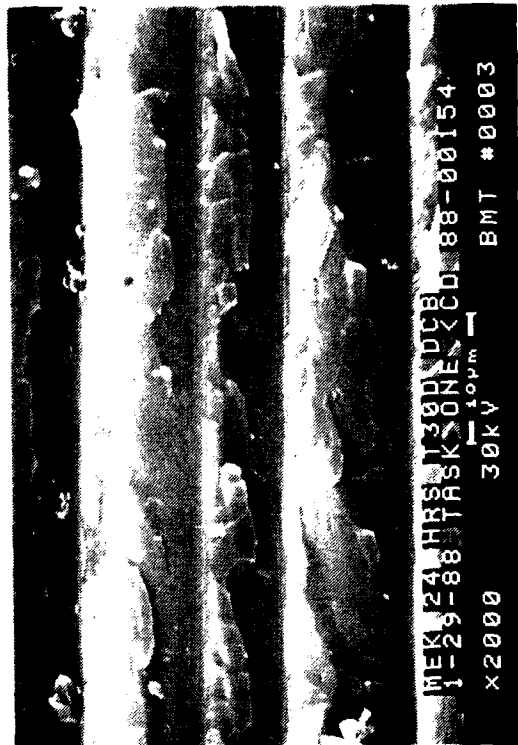
Mechanically induced crack direction →

Figure 2.4-18. SEM Fractographs of Interlaminar Mode I Tension, 0/90 Fracture Exposed to MEK for 24 Hours
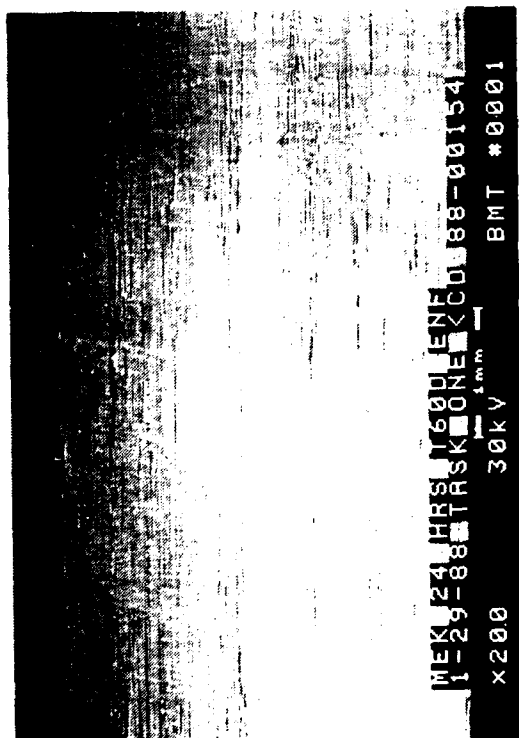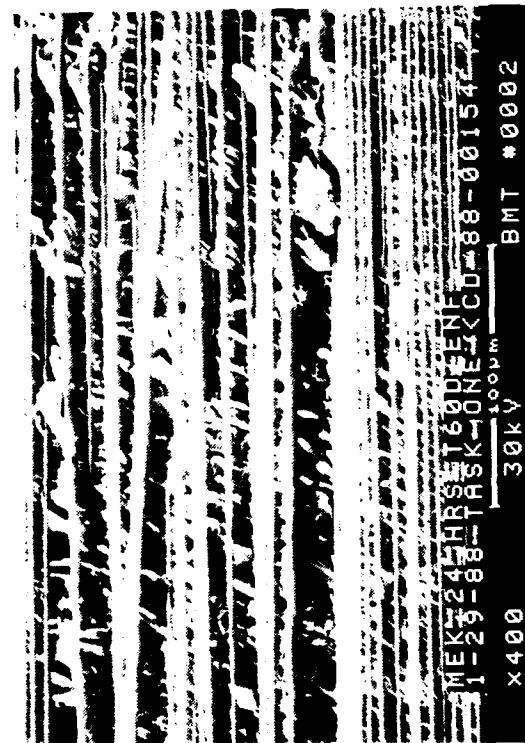
Mechanically induced crack direction

Figure 2.4-19. SEM Fractographs of Interlaminar Mode II Shear, 0/90 Fracture Exposed to MEK for 24 Hours

Note: Both faces A and B are abrasive saw cut
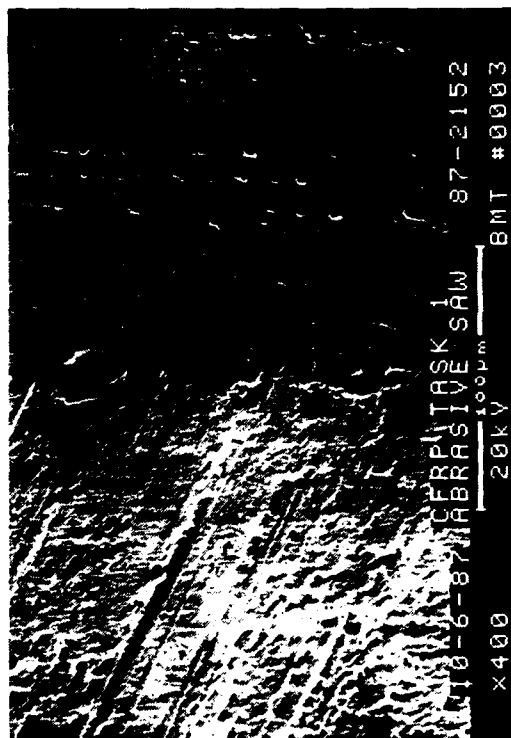
Figure 2.4-20. SEM Fractographs of Abrasive Saw Cut Specimen
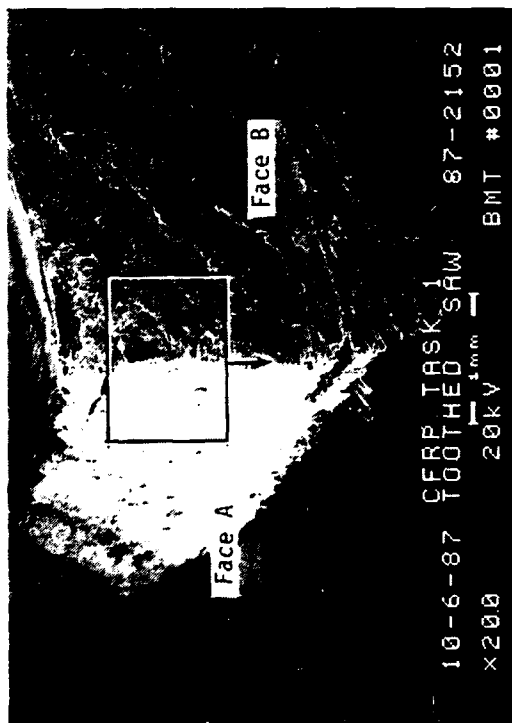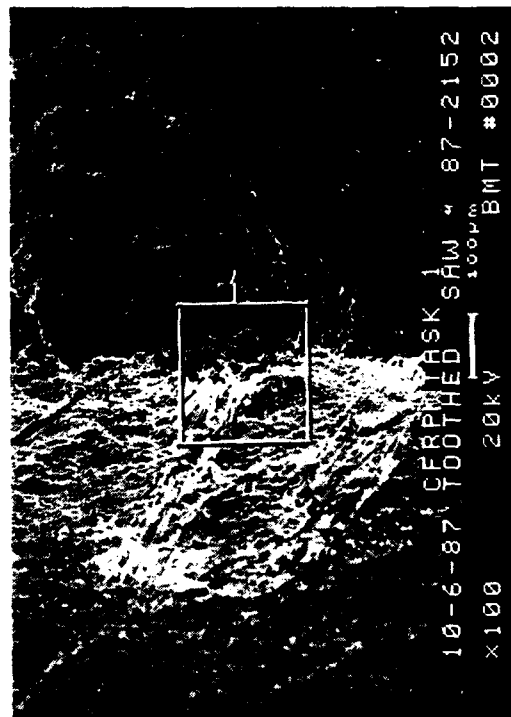
Note: Both faces A and B are toothed saw cut
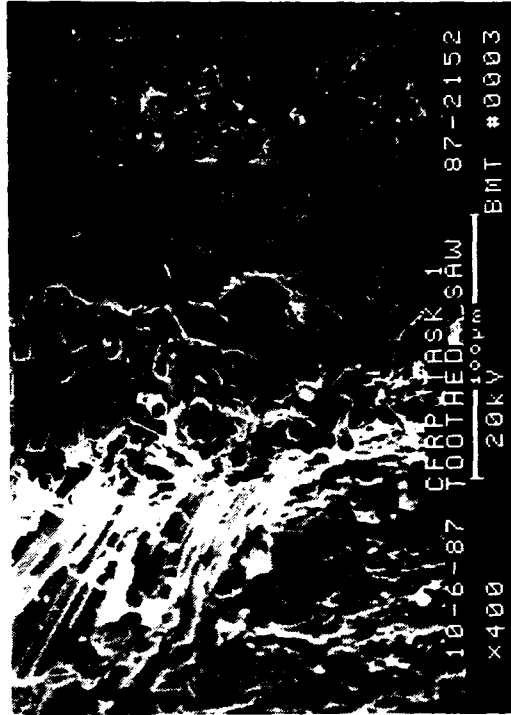
Figure 2.4-21. SEM Fractographs of Toothed Saw Cut Specimen
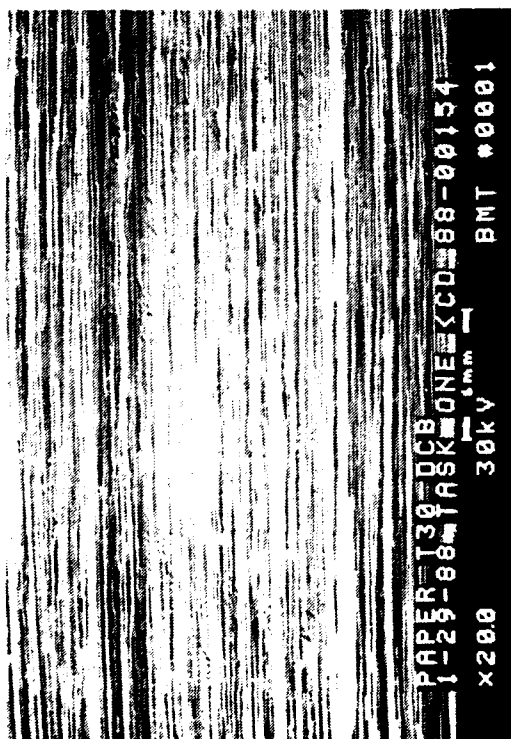
Mechanically induced crack direction
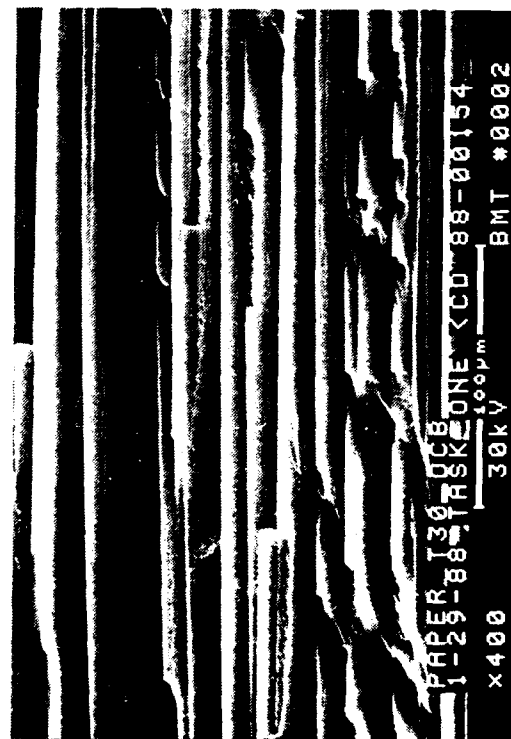
Figure 2.4-22. SEM Fractographs of Interlaminar Mode I Tension, 0/90 Fracture After Packaging with Paper
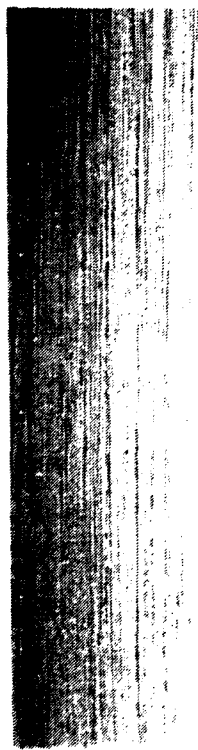
Mechanically induced crack direction
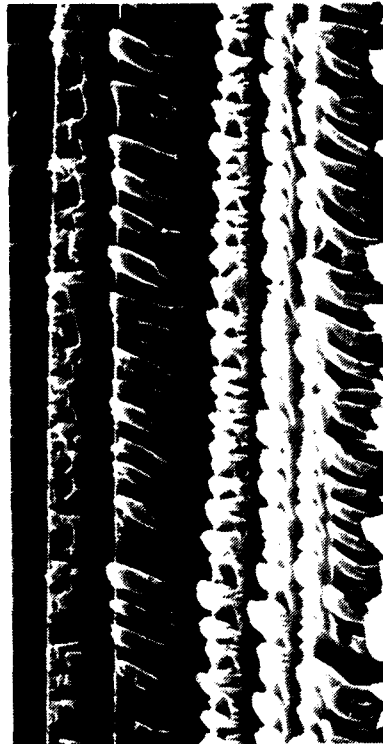
Figure 2.4-23. SEM Fractographs of Interlaminar Mode II Shear, 0/90 Fracture After Packaging with Paper
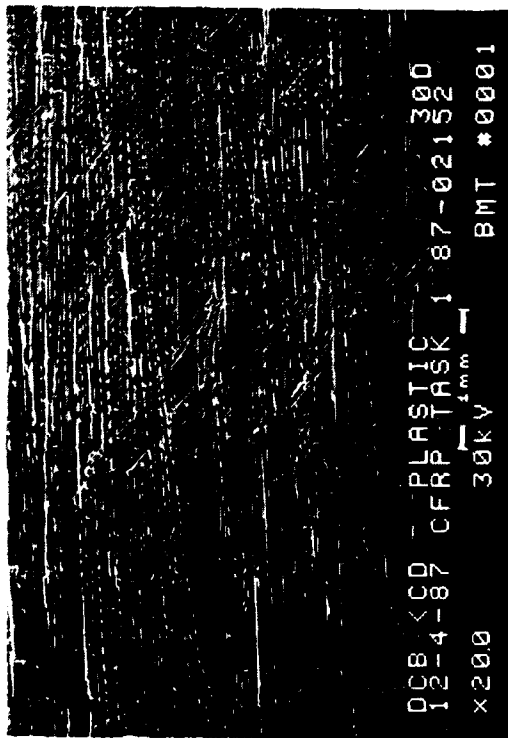
Legend:

R   rivermarks
M   resin microflow

Mechanically induced
crack direction
→
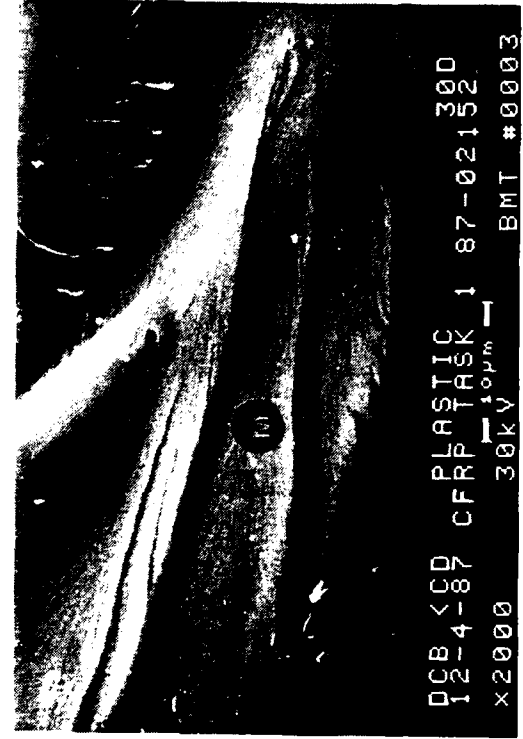
Figure 2.4-24. SEM Fractographs of Interlaminar Mode I Tension, 0/90 Fracture After Packaging with a Plastic Bag
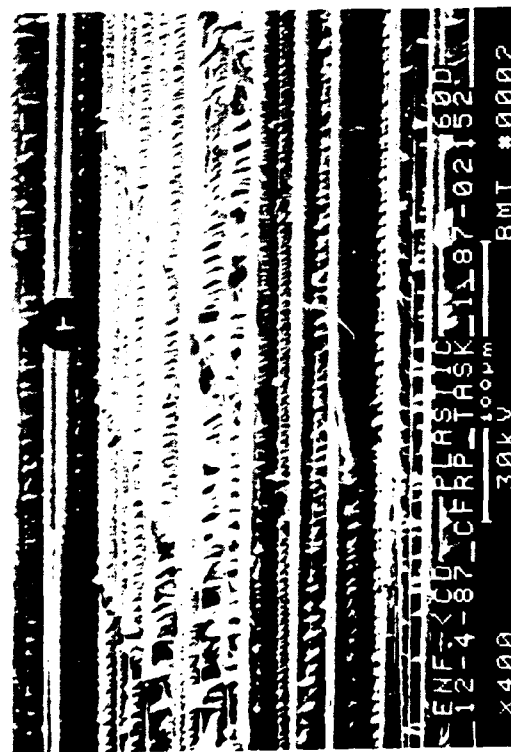
Legend:

H hackles
F fiber/matrix separation
R rivermarks

Mechanically induced
crack direction
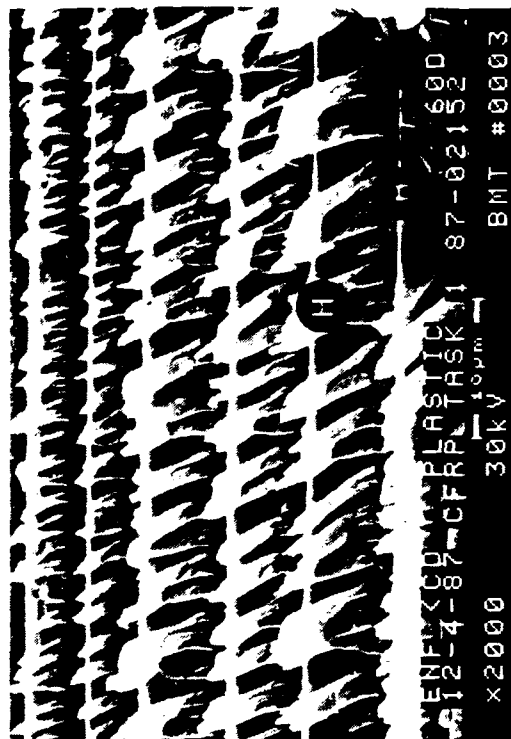
Figure 2.4-25. SEM Fractographs of Interlaminar Mode II Shear, 0/90 Fracture After Packaging with a Plastic Bag

3.0 TASK 2: EXPANSION OF FRACTOGRAPHIC TECHNIQUES IN COMPOSITE FAILURE ANALYSIS

3.1 OBJECTIVE

The objective of this task was to identify, assess, and demonstrate new and advanced failure analysis techniques.

3.2 APPROACH

This task was performed by our subcontractor, General Electric (GE). GE conducted a systematic review to identify new and currently applied fractographic techniques that may be useful for composite failure analysis. These promising techniques were evaluated and the results are provided for incorporation into the handbook. GE provided an independent review of Boeing's FALN as well as additional experience in composite fractography. This ensured continuity with Boeing's existing work and awareness of the methodologies, strengths, and limitations related to this critical analytical discipline. Figure 3.2-1 shows the flow diagram for this task.

3.3 METHODS

In order to evaluate promising fractographic techniques, three subtasks were identified: (1) identification of technique; (2) evaluation and assessment; and (3) technique development. Initially, information was gathered from a literature search, Boeing and GE conferences, and visits to other sites of expertise. This data was then used to select techniques warranting further investigation, which were applied to various controlled failures and evaluated for usefulness in conducting failure analysis investigation.

3.3.1 Identification of Techniques

The literature search was conducted using GE technical internal sources and the Metadex, Compendex, and Aerospace databases. The key words used search were "failure analysis of composites," "failure analysis of fiber reinforced material," and "fractography of composites." The search included material from as far back as 1969, but the main emphasis was on articles from 1980 to 1989 and especially articles that were not reviewed in the previous C-5010 contract.
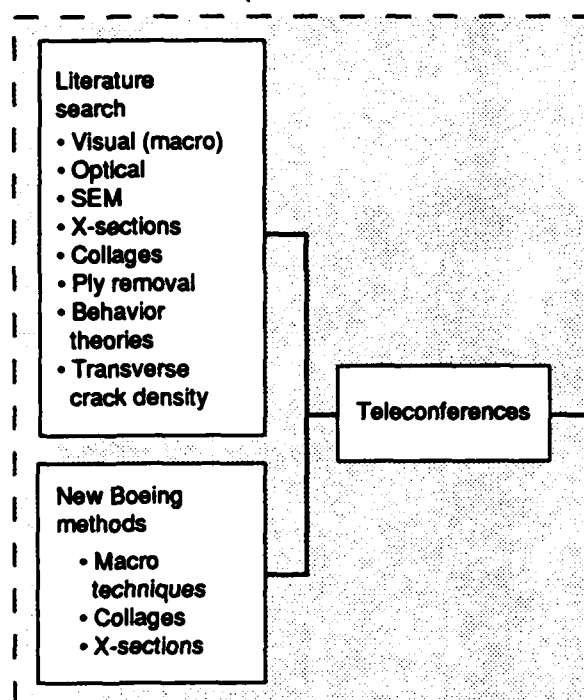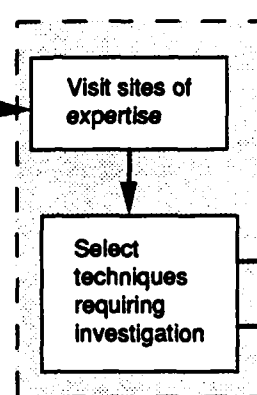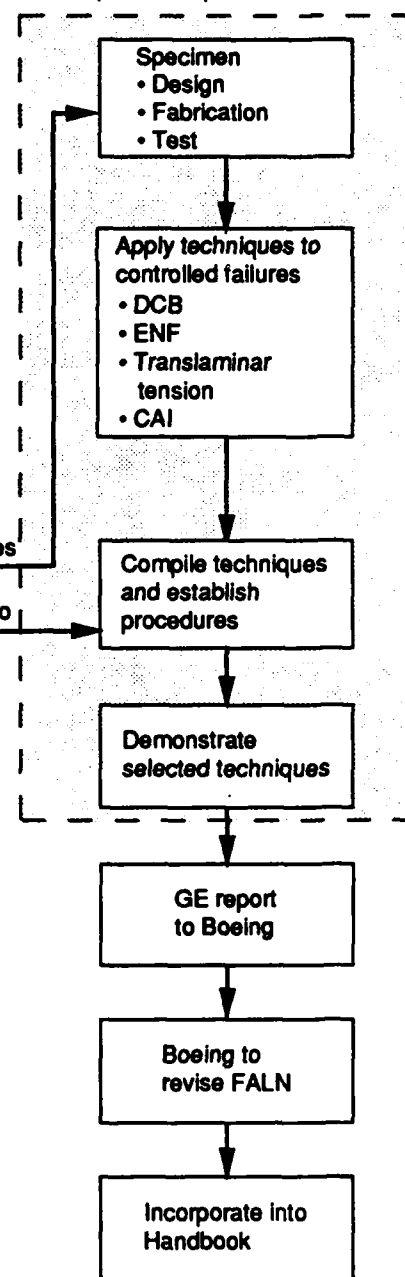
Figure 3.2-1. Task 2 Flow Diagram

3.3.2 Evaluation and Assessment

Sites of expertise were selected by surveying the other aerospace companies to determine if they were active in conducting failure analysis investigations of composite components or subcomponents, had an exclusive composite failure analysis group or expert, and were willing to share their techniques. The following three sites were agreed upon by the Air Force, Boeing, and GE:

a. Lockheed California Company
    Kelly Johnson Research Center
    Rye Canyon, CA
    Contact: Don Petit.

b. United Technologies Corporation
    Sikorsky Aircraft Division
    Stratford, CT
    Contact: Tom Murphy.

c. Royal Aircraft Establishment
    Farnborough, Hants, UK
    Contact: David Purslow.

The visit to Dr. Purslow was later cancelled due to difficulties in placing a purchasing order to a private citizen overseas and unanticipated consultation costs.

3.3.3 Technique Development

Several techniques were identified for evaluation and the AS4/3501-6 material system was selected based on previous experience. The fabrication and test techniques (such as interlaminar Mode I tension, interlaminar Mode II shear, translaminar tension, and translaminar compression tests) were essentially identical to those used in the C-5010 program.

The final test matrix consisted of (1) verification of the fractographic results for interlaminar Mode I tension and Mode II shear and translaminar tension compression on the AS4/3501-6 material system; and (2) development of two deply techniques, thermal oxidative deply (currently used by GE) and cryogenic deply (currently used by Sikorsky), and of the macro-cross sectioning technique (currently used by Lockheed). The three latter techniques were evaluated on an AS4/3501-6 compression-after-impact (CAI) specimen.

3.4 RESULTS

3.4.1 Identification of Techniques

Figure 3.4-1 is a list of articles that were reviewed in detail. The following techniques were identified:

a. Optical microscopy

b. Nondestructive inspection (C-scan, enhanced x-ray, and real-time radiography techniques)

c. Scanning electron microscopy (the most popular technique); stereographic views are used to get the necessary depth of field for fracture surface analysis

d. Two physical deply techniques (peel and abrasion).

3.4.2 Evaluation and Assessment

GE visited Lockheed on 11 September 1987 and Sikorsky on 17 September 1987 to review promising fractographic techniques. The visits included a general discussion of the companies' failure analysis techniques and a detailed tour of their laboratories.

Lockheed California Company. Don Petit, Fatigue and Fracture Mechanics Group Engineer, and George Morse, Non-Metallic and Physics Laboratory Group Engineer, presented their analytical chemistry and metallographic failure analysis techniques. Chemical analysis provides information on material chemistry conformance, presence of oxidation reaction products, and presence of contaminants. Instruments such as the XPS (x-ray photoelectron spectrometer) are used for surface analysis of both polymer-based and metal matrix composites. Chemical and thermal analysis instruments such as the Fourier transform infrared (FTIR) spectrometer, dielectric cure monitoring system, and thermogravimetric analyzer (TGA) are used to determine bulk chemistry, extension of cure, and composite thermal properties. Image analysis is used to determine fiber volume and void content. Lockheed's use of SEM on composite fracture surfaces is limited to the determination of fiber/matrix adhesion and fiber quality. No attempt, other than visual examination, is made to identify failure mode or crack propagation origin or direction. Lockheed has performed failure analysis on unreinforced resin parts and relies heavily on analytical chemistry and metallography in its failure analysis techniques.

Item	Literature
1	Purslow, D., "Matrix Fractography of Fiber-Reinforced Epoxy Composites", <u>Composites</u>, Vol. 17, No. 4, October 1986
2	*Robertson, R. E., et al, "The Stacked Lamellar Texture on the Fracture Surfaces of Fiber Composites", <u>Journal of Material Sciences</u>, Vol. 20, 1985, pp. 2801-2806
3	Johannesson, T., et al, "Influence of Moisture and Resin Ductility on Delamination", <u>Composite Science and Technology</u>, Vol. 24, 1985, pp. 33-46
4	*Robertson, R. E., et al, "Fracture in Epoxy Matrix Resins", <u>Composite Science and Technology</u>, Vol. 22, 1985, pp. 197-207
5	*Purslow, D., et al, "The Effect of Environment on the Compression Strength of Notched CFRP, A Fractographic Investigation" <u>Composites</u>, Vol. 15, No. 2, April 1984
6	*Donaldson, S. L. "Fractography of Mixed Mode I-II Failure in Graphite/Epoxy and Graphite/Thermoplastic Unidirectional Composites", <u>AFWAL-TR-84-4186</u>, June 1985
7	*Purslow, D., "Composites Fractography without a SEM - the Failure Analysis of a CFRP I-beam", <u>Composites</u>, Vol. 15, No. 1, January 1984
8	*Johannesson, T., "The Detailed Structure of Delamination Fracture Surfaces in Graphite/Epoxy Laminates", <u>Journal of Material Science</u>, Vol. 19, 1984, pp. 1171-1177
9	Purslow, D., et al, "The Effect of Pre-Loading on the Environmental Degradation of Carbon Fiber Reinforced Plastics", <u>Composites</u>, Vol. 14, No. 3, July 1983
10	Richards-Frandsen, R., et al, "Fracture Morphology of Graphite/Epoxy Composites", <u>Journal of Composites Materials</u>, Vol. 17, March 1983, pp. 105-113
11	*Purslow, D., "Fractograpahic Analysis of Failures in CFRP", <u>Characterization, Analysis, and Significance of Defects in Composite Materials</u>, AGARD Proceedings No. 355, July 1983
12	*Clements, L. L., et al, "Failure of Morphology of $(0°)_8$ Graphite/Epoxy as Influenced by Environments and Processing", <u>NASA-TM-81318</u>, August 1981
13	Bishop, S. M., "The Significance of Defects on the Failure of Fiber Composites", <u>AGARD-R-690</u>, December 1981
14	Theocaris, P. S., et al, "Crack Propagation in Fiberous Composite Materials Studied by S.E.M.", <u>J. Composite Materials</u>, Vol. 15, March 1981, p. 133
15	Awerbuch, J., et al, "Off-Axis Fatigue of Graphite/Epoxy Composite", <u>Fatigue of Fiberous Composite Materials</u>, ASTM STP 723, 1981, pp. 243-273
16	*Purslow, D., "Some Fundamental Aspects of Composites Fractography", <u>Composites</u>, October 1981, pp. 241-247
17	*Kline, R. A., et al, "Composite Failure Surface Analysis" <u>J. Composite Materials</u>, Vol. 14, October 1980, pp. 315-324
18	Purslow, D., "Further Fractographic Characteristics of Peel Failures in CFRP", <u>Composites</u>, Vol. 18, No. 3, July 1987
19	Morris, G. E., and Hetter, C. M., "Fractographic Studies of Graphite/Epoxy Fatigue Specimens", <u>Damage in Composites Materials</u>, ASTM STP 775, 1982, pp. 27-39
20	Grinty, C. A., Irvine, T. B., "Fracture Surface Characteristics of Notched Angleplied Graphite/Epoxy Composites", <u>NASA-TM-83786</u>, 1984

*Articles reviewed previously by Boeing on the C-5010 contract.

Figure 3.4-1. Articles Reviewed by G. E.

Sikorsky Aircraft Division. Tom Murphy, Material and Process Laboratory Chief Engineer, and Peter Konieczny, Composite Failure Analyst, presented their failure analysis techniques and demonstrated composite hardware. Two carbon/epoxy press-molded spars for tail rotors of the -76 commercial helicopter and the Army Blackhawk helicopter were presented as examples of Sikorsky's defect characterization techniques. The spars were primary rotating structures that have been in service since the mid-1970s. The failure analysis determined that the main causes of failure were manufacturing defects such as wrinkles, voids, improper layup, and poor quality. These defects were caused partly by inappropriate machining and processing.

In one case, the center portion of the press-molded spars contained excessive resin flow causing in-plane and out-of-plane fiber wrinkles. The parts passed C-scan inspection and were released to the field. Two spars failed in the first 100 hours of service because of the defects. Optical microscopic examination of the fracture surfaces revealed the wrinkles, and metallography was used to evaluate the number of plies affected. Sikorsky also machined interlaminar shear and tensile specimens from the hardware and conducted static tests on actual spars to establish strength knockdowns due to the wrinkles. The findings led to modification of Sikorsky's die-closing procedures during press molding and the inclusion of a woven glass scrim (glass tracer) on each ply of carbon/epoxy to allow x-ray inspection. A new specification was established allowing a 1/10 inch peak-to-peak maximum on in-plane wrinkles and no out-of-plane wrinkles.

In another instance, spars were laid up improperly (ply drop-offs were too close together causing interlaminar failure); in yet another, a 70 degree ply was laid up instead of a 20 degree ply causing high interlaminar shear stresses. These defects were found by optical microscopic examination of the fracture surfaces.

Once the defects have been characterized, the laboratory feeds the information back to the stress analyst to recalculate the stresses. The fracture surfaces are not completely separated, but the specimen is deplied by embrittling it in liquid nitrogen and then bench breaking it. However, no analytical techniques or fractography are utilized in the investigation. Generally, Sikorsky relies heavily on low-power optical microscopy and specimen testing to determine causes of failure.

3.4.3 Technique Development

In this subtask, GE verified Boeing fractographic results for the model carbon/epoxy material system AS4/3501-6. New techniques such as the two deply techniques and the macro-cross-sectioning technique were then evaluated on an AS4/3501-6 compression-after-impact specimen.

3.4.3.1 Verification of Boeing Techniques

Room temperature fractographic results were verified for the following known conditions of failure: (1) interlaminar Mode I tension; (2) interlaminar Mode II shear; (3) translaminar tension; and (4) translaminar compression. All fractures were induced under room temperature (RT)/dry conditions.

Interlaminar Mode I Tension. Optical examination revealed a smooth, reflective surface. SEM fractography revealed rivermarks and resin microflow in the matrix rich areas between plies indicating propagation in a direction consistent with the mechanically induced crack direction (Fig. 3.4-2). Fiber/matrix adhesion was good.

Interlaminar Mode II Shear. Visual examination of the Mode II shear surface showed a milky white appearance when the specimen was held at an angle to the light. SEM examination revealed hackles and scallops, indicative of a Mode II shear failure (Fig. 3.4-3). As in the Boeing analysis, the propagation direction could not be determined from these features. The fiber/matrix adhesion was good.

Translaminar Tension. Macroscopically, the fractures were flat and planar. At higher magnifications the edges appeared rough with segregated fiber bundles protruding from the fracture plane. Fiber pullout was observed in varying proportions over the entire fracture. SEM fractography revealed fiber end fractures with fan patterns indicating the propagation through each fiber (Fig. 3.4-4). Fiber end fractures often initiated tangentially to the previous failed fiber and propagated off-axis. The overall propagation direction indicated by the fiber end fractures was consistent with the mechanically induced crack direction.

Translaminar Compression. Macroscopically, the fractures were jagged. At higher magnifications, the compressive region was locally flat with all fibers and the matrix fracture in the same plane. The fracture was littered with debris. Fiber buckling was observed in both the 0 and 90 degree plies. SEM fractography of the compressive region revealed fiber end fractures, each exhibiting a compressive zone and a tensile zone divided by a neutral axis (Fig. 3.4-5).
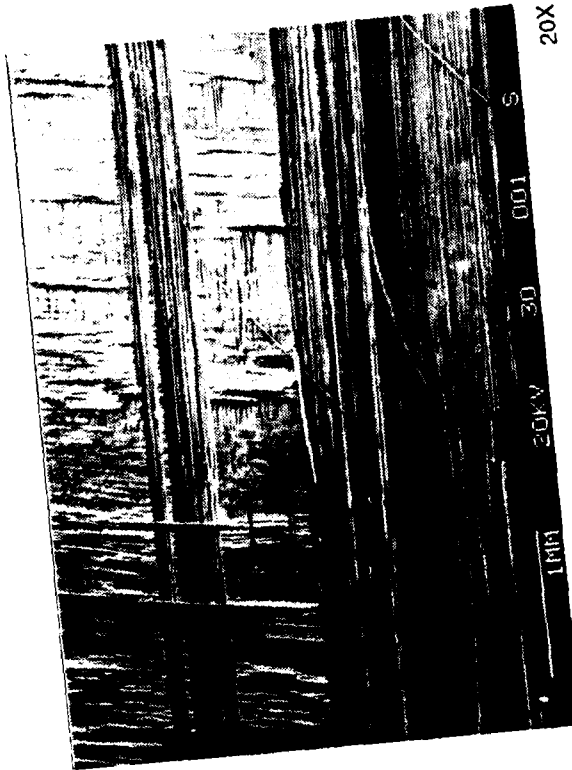
Legend:
F fiber/matrix separation
R rivermarks

Mechanically induced
crack direction
→
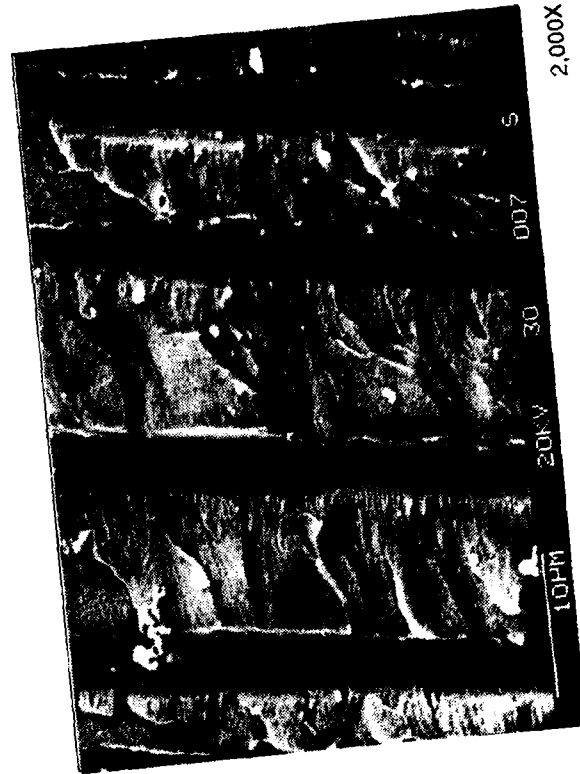
Figure 3.4-2.   SEM Fractographs of Interlaminar Mode I Tension, Room Temperature, 0/90
                 Fracture in AS-4/3501-6
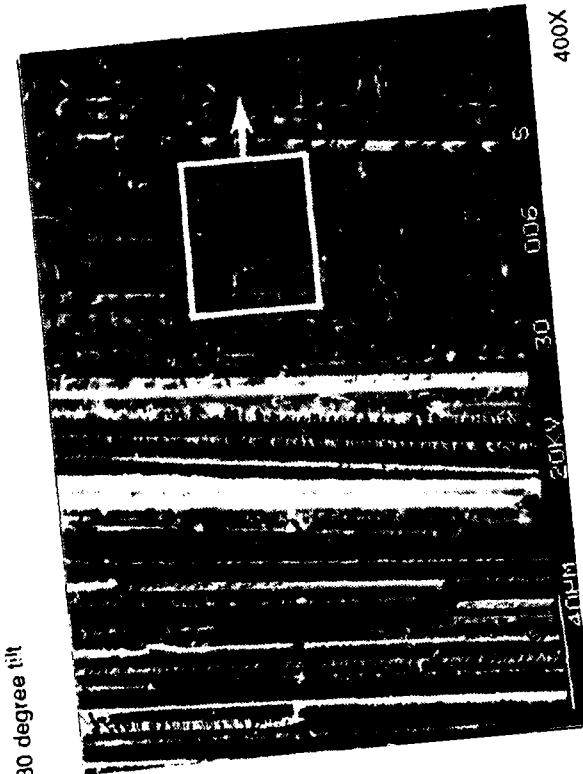
Legend:

F fiber/matrix separation
H hackle
S scallop

Mechanically induced
crack direction

Area a—60 degree tilt

60 degree tilt

Figure 3.4-3. SEM Fractographs of Interlaminar Mode II Shear, Room Temperature, 0/90 Fracture in AS-4/3501-6
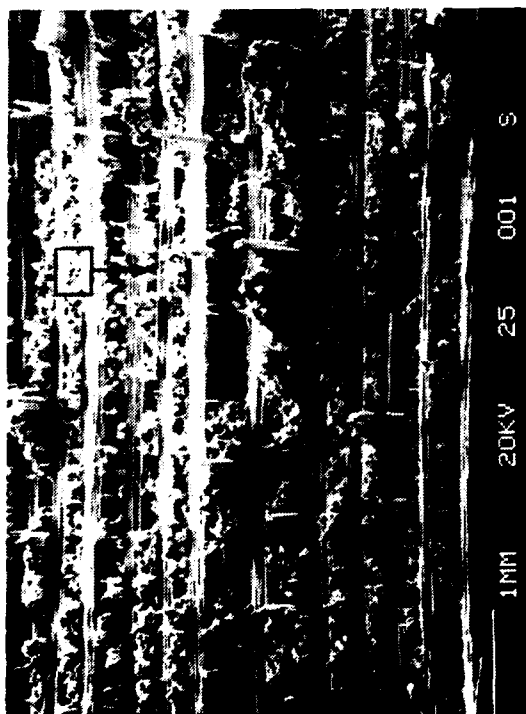
Mechanically induced crack direction
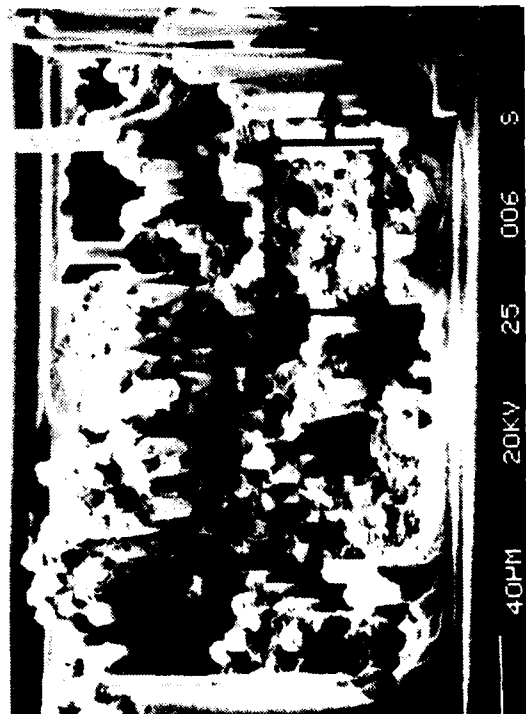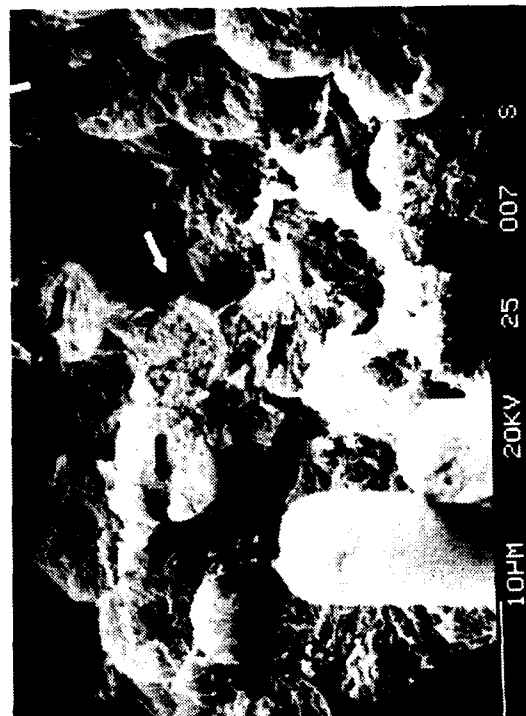
Figure 3.4.4. SEM Fractographs of Translaminar Tension, Room Temperature Fracture in AS-4/3501-6
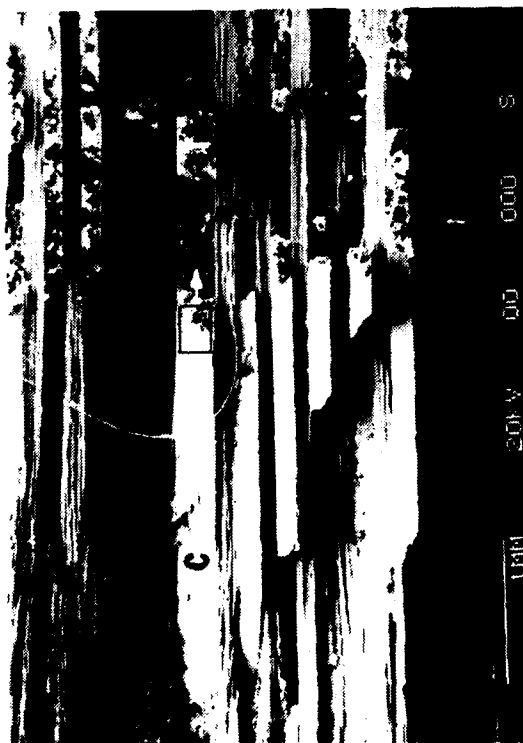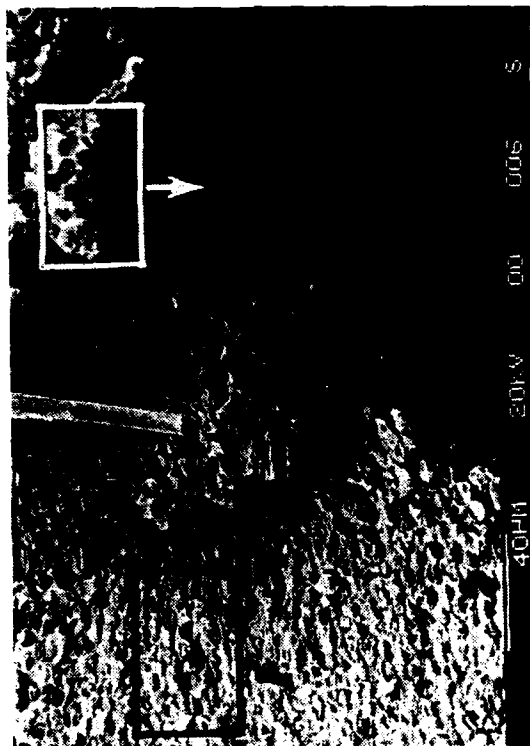
Legend:

C   compression zone
T   tension zone
N   neutral axis

Mechanically induced
crack direction
———————→

Figure 3.4.5. SEM Fractographs of Translaminar Compression, Room Temperature Fracture in AS-4/3501-6

In summary, GE fractographic results for Mode I tension, Mode II shear, translaminar tension, and translaminar compression agreed with those derived from Boeing techniques developed under the C-5010 program.

3.4.3.2 Investigation of New Techniques

Three techniques currently used by the industry were examined: (1) macro-cross sectioning, used by Lockheed; (2) thermal oxidative deply, used by GE; and (3) cryogenic deply, used by Sikorsky. The new techniques were evaluated on an AS4/3501-6 compression-after-impact specimen.

The compression-after-impact specimen was quartered through the impact site and the various techniques were employed on the separate quarters (Fig. 3.4-6 and 3.4-7).

Macro-Cross-Sectioning. Two metallographic sections were taken to observe the crack patterns surrounding the damage zone from two orientations. The lengthwise cross-section includes the actual point of impact and shows the main crack path to the back surface. The damage spreadout conically from the impact site to the back surface of the specimen, as indicated by the small translaminar cracks (Fig. 3.4-8 and 3.4-9). By aligning these small cracks, the location of the impact could be determined. The number and size of delaminations increased toward the back of the specimen. The transverse cross-section was taken adjacent to the impact site to determine damage effects near to the impact (Fig. 3.4-10). As in the lengthwise section, the size and number of delaminations increased toward the back surface. The damage was more severe at the edge of the specimen than at the center. This edge showed evidence of interlaminar fracture, translaminar fracture, intralaminar fracture, and microbuckling (Fig. 3.4-11 and 3.4-12).

Thermal Oxidative Deply. Thermal-oxidative deply was performed on a third quarter. The sample was heated in air at 600F for 12 hours. During heating, the specimen expanded due to the gases evolved. Deply was then performed at room temperature by peeling the layers apart with tweezers and carefully placing them in correct order (Fig. 3.4-13 through 3.4-15). All layers were deplied. It was observed that colored bands were produced during the heat cycle, but these bands did not seem to correspond with prior delaminations. However, several plies exhibited lighter colored, less reflective areas that did align with the delaminations indicated by ultrasonic and X-ray inspection. Fractography of these regions was not performed.
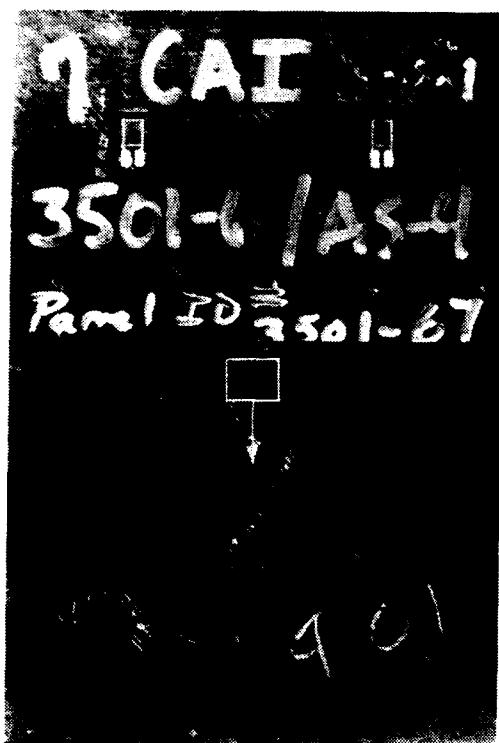
CAI AS-4/3501-6   2/3X   2/3X
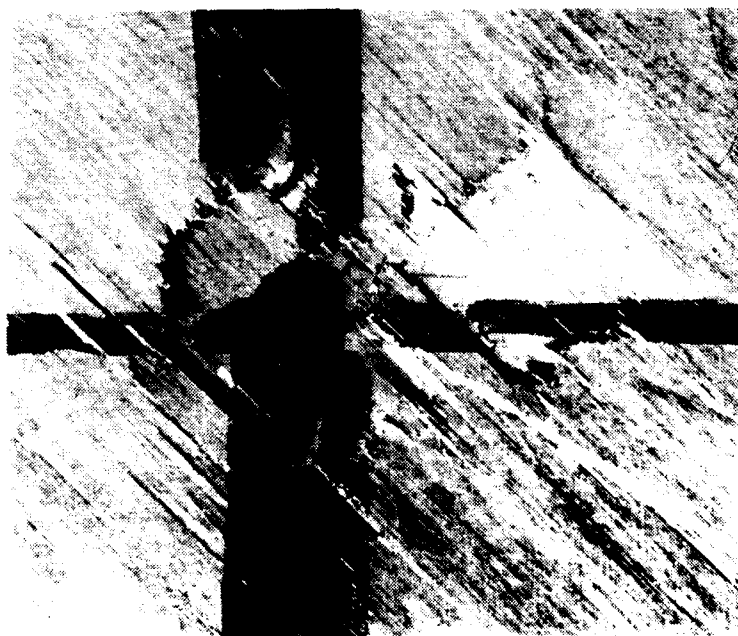
Point of Impact   10X

Figure 3.4-6. Photomacrographs of AS-4/3501-6 Compression-After-Impact Specimen

2/3X

Thermal-oxidative deply

Cryogenic deply

10X
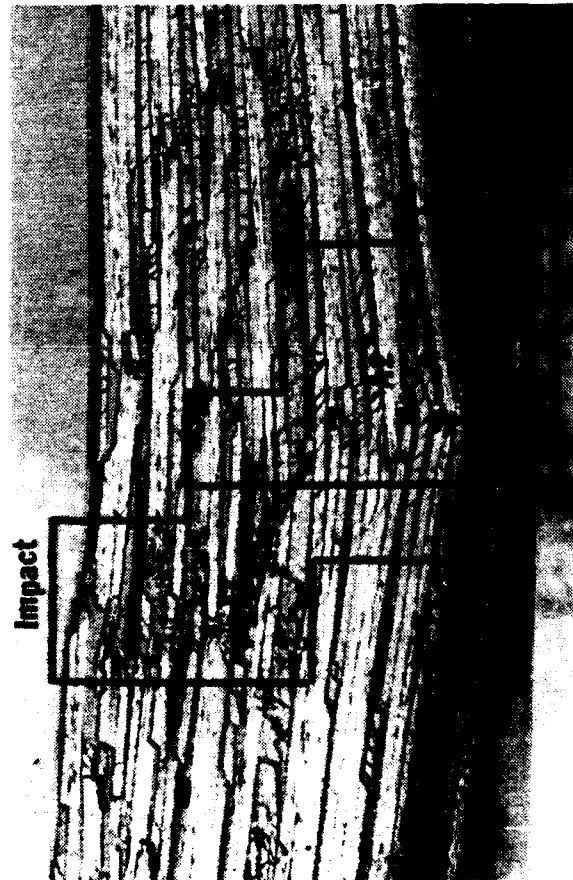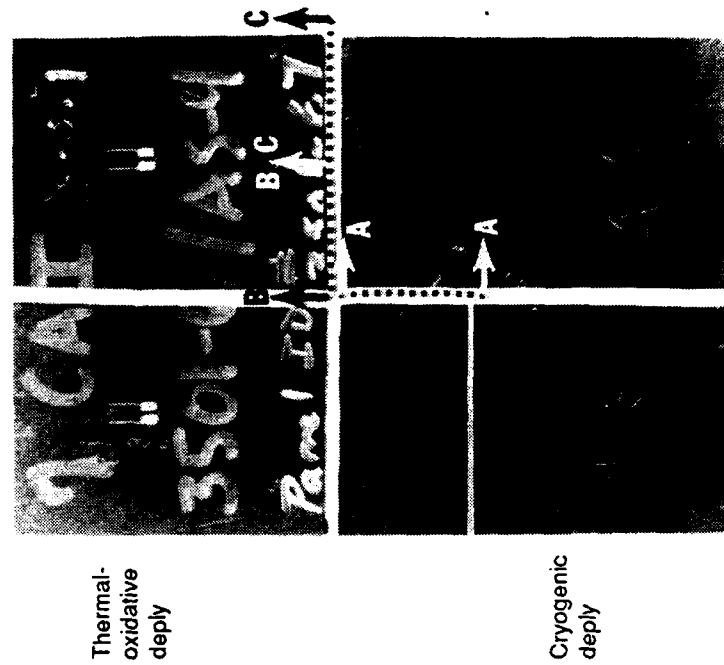
Section A-A

Figure 3.4-7. Photomacrograph and Photomicrograph of AS-4/3501-6 Compression-After-Impact Specimen, Section A-A
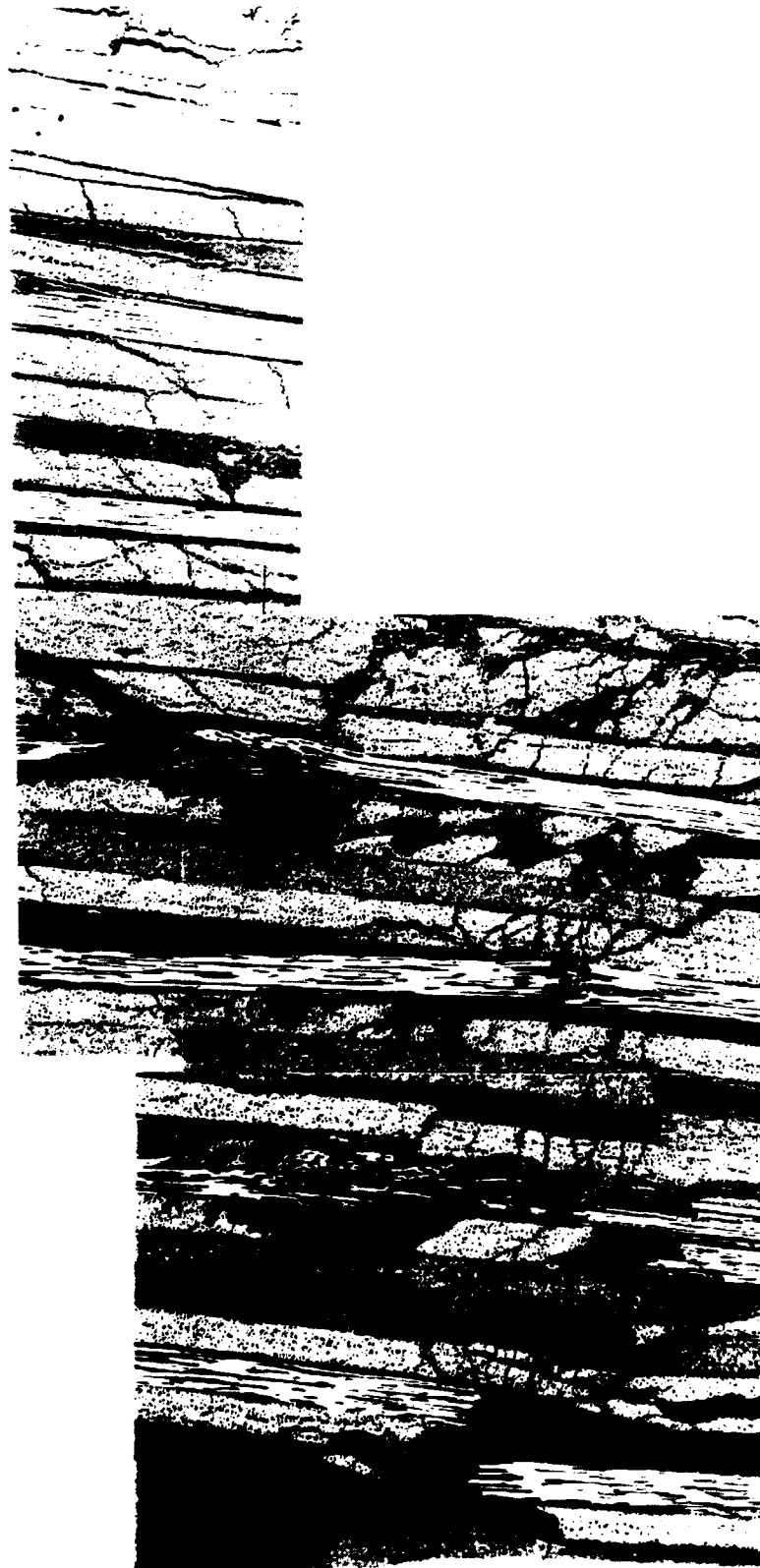
Figure 3.4-8. Photomicrograph of AS-4/3501-6 Compression-After-Impact Specimen, Section A1

50X

A1
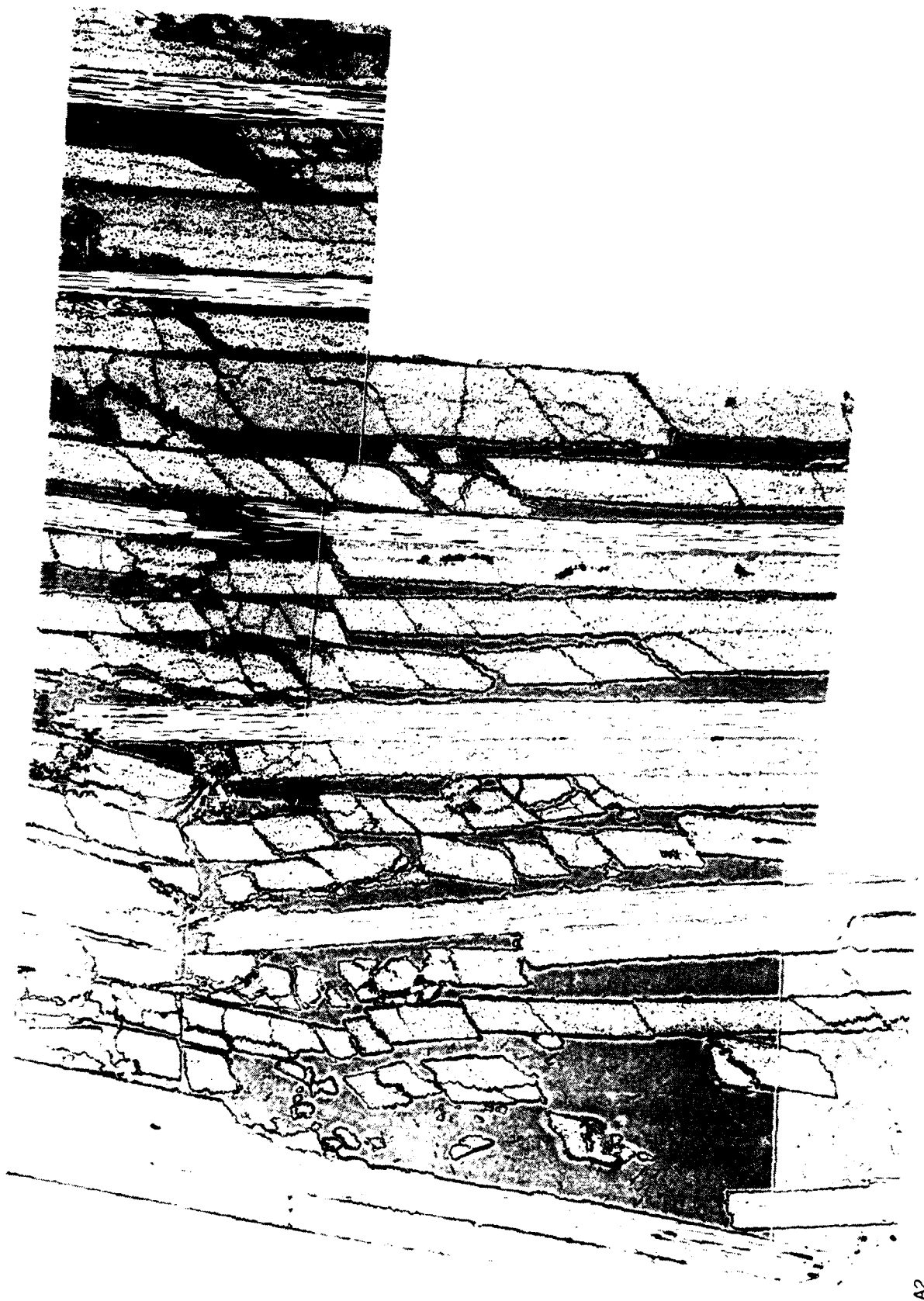
Figure 3.4-9. Photomicrograph of AS-4/3501-6 Compression-After-Impact Specimen, Section A2

50X

A2

Figure 3.4-10. Photomicrograph of AS-4/3501-6 Compression-After-Impact Specimen, Section B-B

Section B-B

10X

Figure 3.4-11. Photomicrograph of AS-4/3501-6 Compression-After-Impact Specimen, Section B1

40X

B1

Section C-C

10X

50X

C1
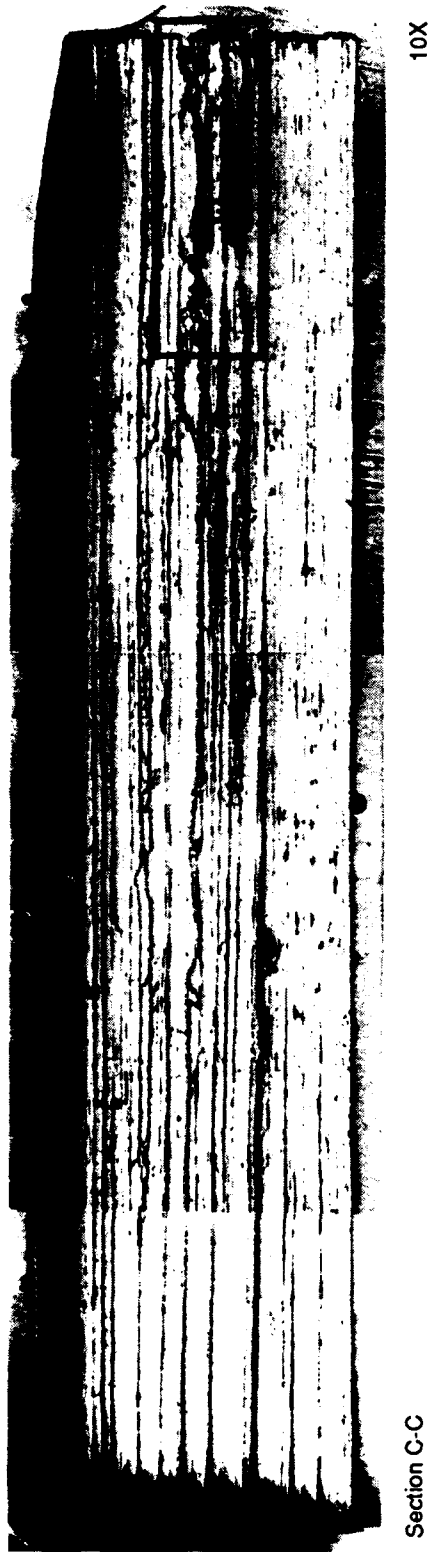
Figure 3.4-12. Photomicrograph of AS-4/3501-6 Compression-After-Impact Specimen, Section C-C

Thermal-oxidative deply 3/4X
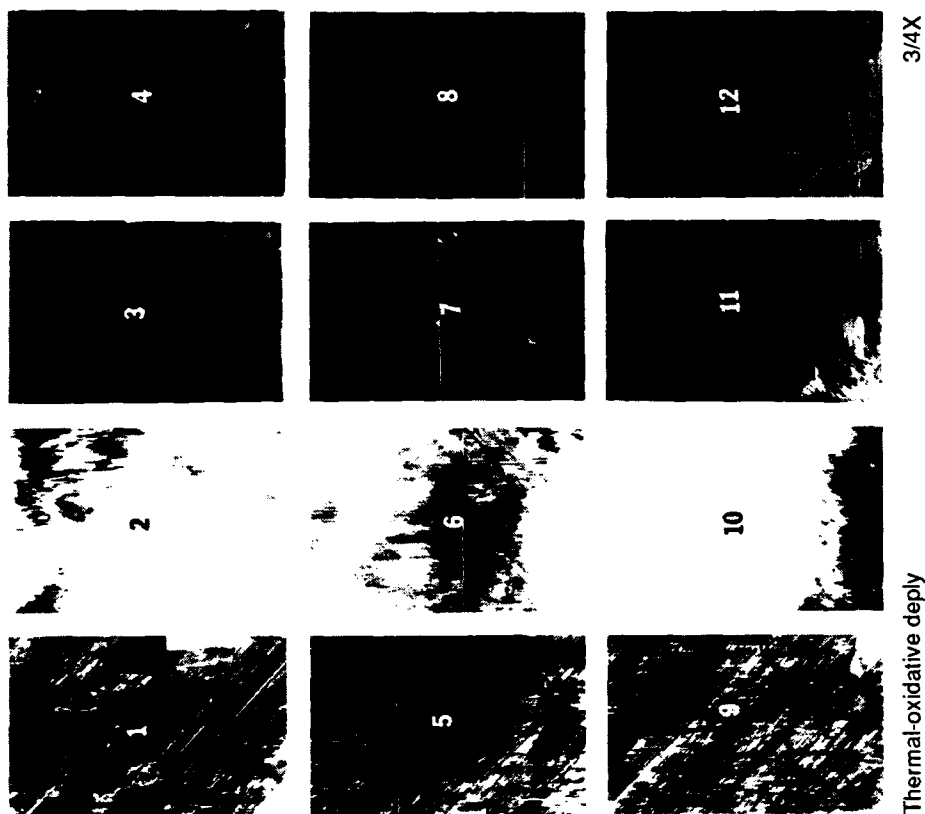
Figure 3.4-13. Photomacrograph of AS-4/3501-6 Compression-After-Impact Specimen After Thermal-Oxidative Deply, Sections 1-12
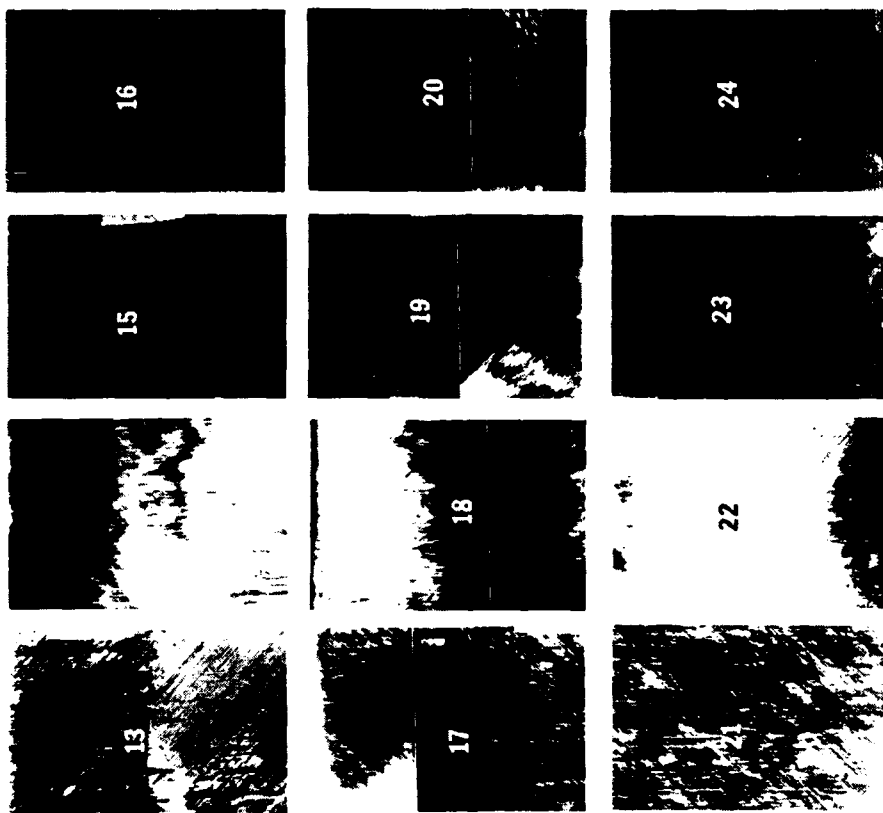
Thermal-oxidative deply

3/4X

Figure 3.4-14. Photomacrograph of AS-4/3501-6 Compression-After-Impact Specimen After Thermal-Oxidative Deply, Sections 13-24
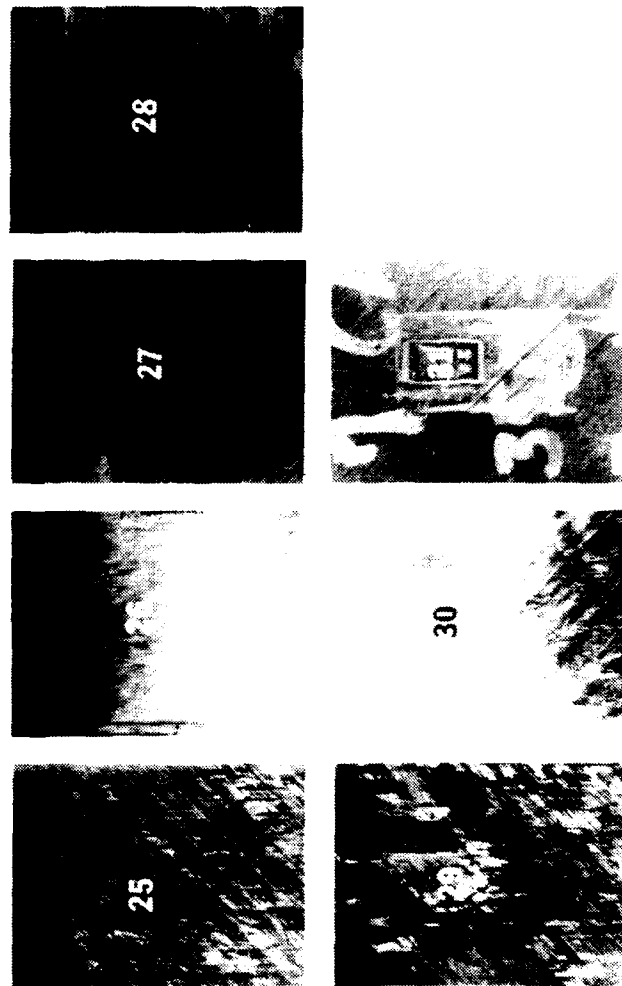
Thermal-oxidative deply

3/4X

Figure 3.4-15. Photomacrograph of AS-4/3501-6 Compression-After-Impact Specimen After Thermal-Oxidative Deply, Sections 25-31

Cryogenic Deply. The last quarter was used for cryogenic deply and prepared by soaking in liquid nitrogen prior to peeling the layers with tweezers. Only the existing delaminations were peeled apart. Examination of these layers revealed light colored, less reflective regions similar to those observed in the thermal oxidative deply (Fig. 3.4-16). These regions correspond to the expected delamination locations. Fractography was not performed on these regions.

Of the fractographic methods tested, the macro-cross-sectioning technique provided the most information, detailing the amount of matrix cracking, the number of delamination planes, and the areas of fiber breakage. Of the deply techniques, GE's thermal oxidative deply technique gave the clearest indication of previous delamination planes.
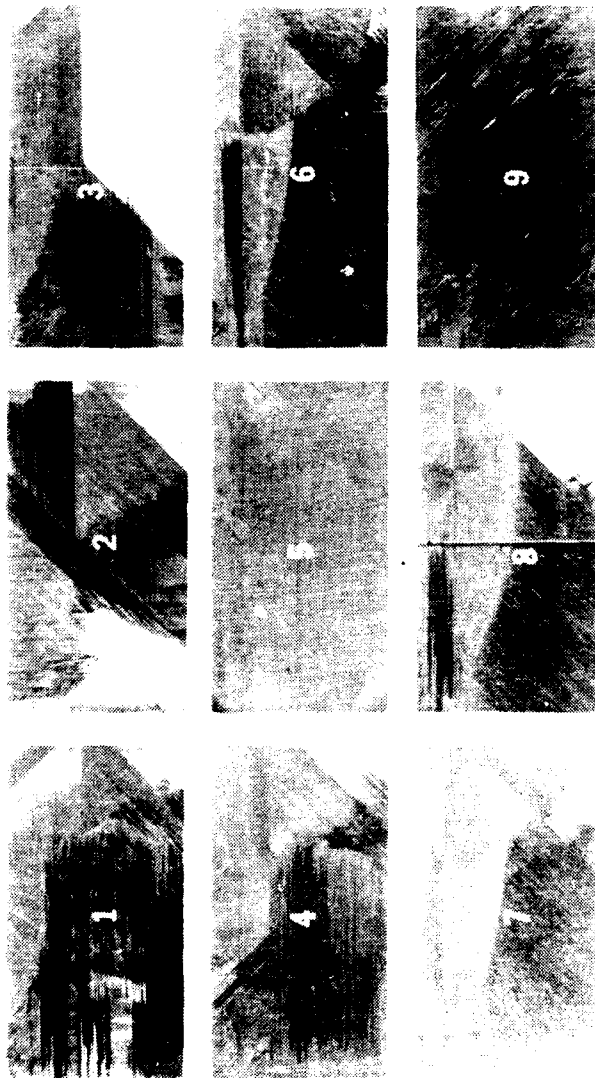
Cryogenic deply

Figure 3.4-16. Photomacrograph of AS-4/3501-6 Compression-After-Impact Specimen After Cryogenic Deply

1X

4.0 TASK 3: EXPANSION OF THE FRACTOGRAPHIC DATABASE

4.1 OBJECTIVE

The objective of this task was to build a comprehensive database for the model system studied under the previous C-5010 program in Task 3A, and using this information and the experience gained from the C-5010 program, develop a database for other composite materials. The completed task provided a larger database for the model system and formed a set of findings from which failure conditions and tests for materials other than the model AS4/3501-6 system could be selected.

4.2 APPROACH

This task was divided into two subtask: 3A, an expansion of the AS4/3501-6 database evaluated in C-5010 program (Fig. 4.2-1); and 3B, a compilation of a similar database for other carbon-based and epoxy-based material systems (Fig. 4.2-2). The database developed for AS4/3501-6 was reviewed and additional conditions of failure were identified. From this information a new test matrix was developed for Task 3A (Fig. 4.2-3). The parameters examined in this subtask were:

a. Stress/loading conditions

b. Environmental effects

c. Process deficiencies

d. Product forms

Test specimens were fabricated and tested with known conditions of failure. Subsequently, the morphological fracture features were analyzed fractographically.

Based on the AS4/3501-6 database developed in Task 3A, a reduced test matrix was developed for the other material systems (Fig. 4.2-4). Six material systems that are currently or soon to be in service were evaluated: carbon/PEEK, carbon/PMR-15, carbon/8551-7, boron/epoxy, Kevlar/epoxy, and glass/epoxy. To provide direct comparison against AS4/3501-6, the material systems were divided into carbon-based and epoxy-based categories.

Step 1-model system data review

Model system review

Industry review/inputs

Select parameters for investigation

Step 2-matrix development

- C-5010 extended tests

  - K_t effects
  - Fire

  - New tests

  - Rate sensitivity
  - Environmental effects
  - Forms
  - Impact
  - Process deficiencies

Submit general test plan for A/F review and approval
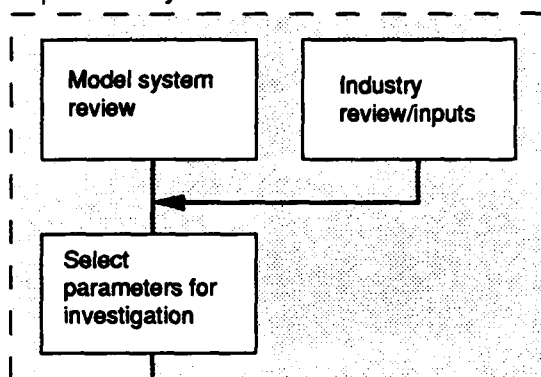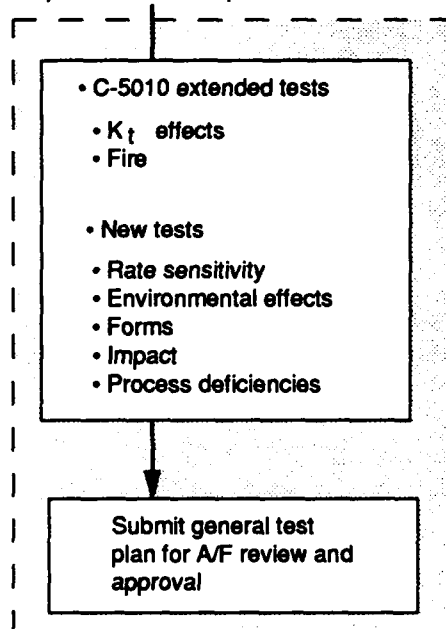
Step 3-fabrication and test

Specimen fabrication and NDE

Environmental preconditioning

Testing

Interlaminar

Translaminar

Complex
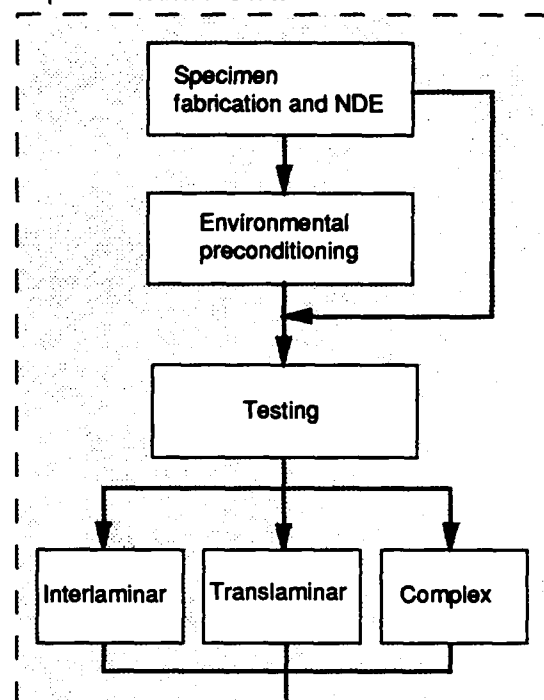
Step 4- fractographic analysis

- Visual
- Optical
- SEM
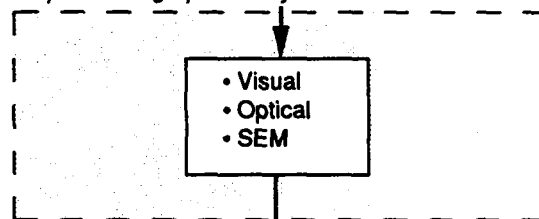
Step 5-database review and incorporation

Compile and summarize

Revise and review FALN

Incorporate into Handbook
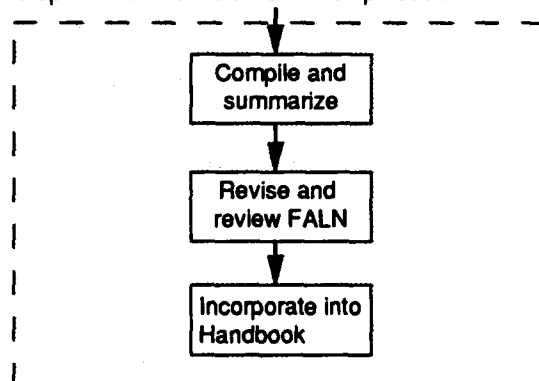
Figure 4.2-1. Task 3A Flow Diagram
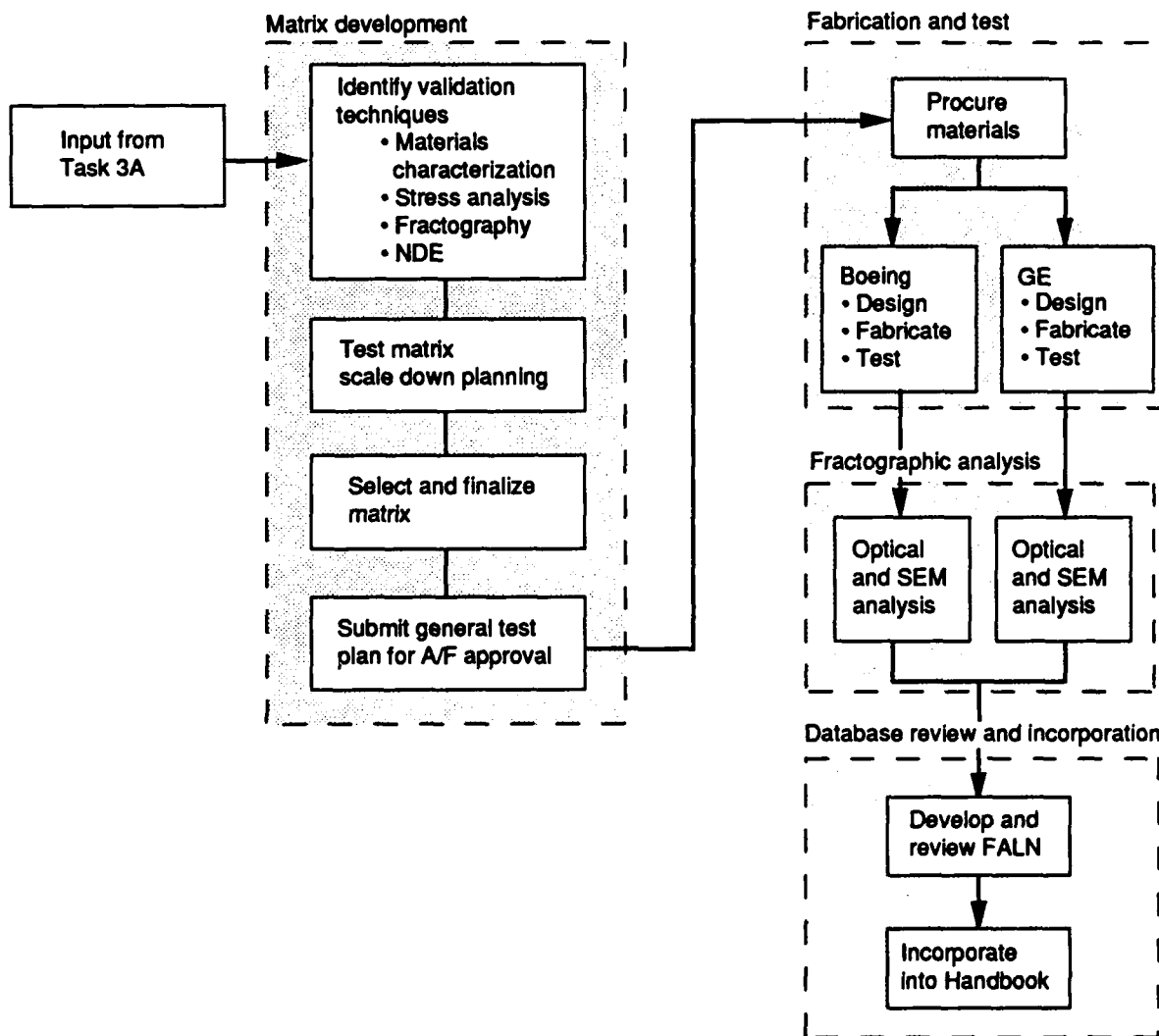
Figure 4.2-2. Task 3B Flow Diagram
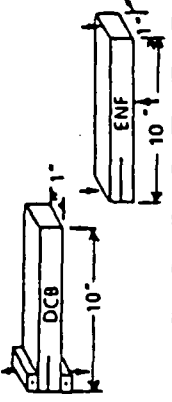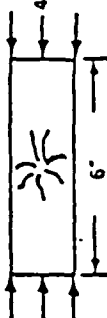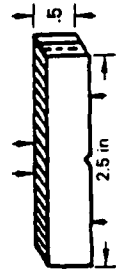
Figure 4.2-3. Task 3A Test Matrix

PARAMETERS AND FRACTURE TYPE	SPECIMEN TYPES		PLY LAYUP/NO OF PLIES	NO OF SPECIMENS	SPECIMEN CONFIGURATION	COMMENTS
STRESS/LOADING CONDITIONS						
K_1 • Translaminar • Small K_1 • Large K_1	Open Hole Tension	—	(0) 12 (±45) 6s	2 each	Open Hole Tension	Hole Diameter K_1 large = 0.5 in K_1 small = 0.10 in
Rate sensitivity • Interlaminar • Creep 70°F 270°F • High rate 70°F 270°F	DCB	ENF	(0/90) 6s	2 each	DCB / ENF	Creep @ sustained load; High rate with gas gun
Impact • Interlaminar	Compression After Impact (CAI)	—	(0/+45/90/-45)4s	2 each		Impacted at 1200 in-lbs
ENVIRONMENTAL CONDITIONS						
Elevated Temperatures • Interlaminar • Translaminar	DCB	ENF, Notched 4 Pt Tension (N 4 pt T)	(0/90) 6s (0/90) 8s	2 each		2000°F Exposure for 5 minutes
Immersion • Interlaminar • Translaminar	DCB	ENF, N 4 pt T	(0/90) 6s (0/90) 8s	2 each	DCB and ENF Translaminar Tension	Hanging 160°F 100% RH for 4 wks Immersion for 4 wks @ 160°F
Humidity • Interlaminar • Translaminar	DCB	ENF, N 4 pt T	(0/90) 6s (0/90) 8s	2 each	DCB and ENF Translaminar Tension	Hanging 160°F 100% RH for 4 wks Immersion for 4 wks @ 160°F

PARAMETERS AND FRACTURE TYPE	SPECIMEN TYPES			PLY LAYUP/NO OF PLIES	NO OF SPECIMENS	SPECIMEN CONFIGURATION	COMMENTS
PROCESS DEFICIENCIES	DCB	ENF	N 4 pt T				
Undercure • Interlaminar • Translaminar	DCB	ENF	N 4 pt T	(0/90) 6S (0/90) 8S	2 each	DCB and ENF Translaminar Tension	Cure two 350°F system at 250°F
Double-cured • Interlaminar • Translaminar	DCB	ENF	N 4 pt T	(0/90) 6S (0/90) 8S	2 each	DCB and ENF Translaminar Tension	Cure for Two 350°F Cure Cycles
High resin content • Interlaminar • Translaminar	DCB	ENF	N 4 pt T	(0/90) 6S (0/90) 8S	2 each	DCB and ENF Translaminar Tension	Angled pressure on tool for > 40% resin content
Low resin content • Interlaminar • Translaminar	DCB	ENF	N 4 pt T	(0/90) 6S (0/90) 8S	2 each	DCB and ENF Translaminar Tension	Angled pressure on tool for < 30% resin content
PRODUCT FORMS Fabric • Interlaminar • Translaminar	DCB	ENF	N 4 pt T	(0/90) 6S (0/90) 8S	2 each	DCB and ENF Translaminar Tension	24 plies PW-3K-70
Filament winding • Interlaminar • Translaminar	DCB	ENF	N 4 pt T	Unidirectional	2 each	DCB and ENF Translaminar Tension	Flat tooling 0 1 in thick
Stitched • Complex fracture	CAI	–	–	(±45/0/45/90) 4S	2 each	CAI	4 x 8 stitch patterns with Kevlar 29

(1 of 2)

Figure 4.2-3. Task 3A Test Matrix (Concluded)

	Material system	Specimen types	Environment at fracture	Layup	No. of specimens	Comments
Graphite based	PEEK/graphite tape grade 145 APC-2/AS4	1,2,3	70°F/dry, 270°F/wet	(0/90)s	2 each	No 4 due to post-failure damage of graphite fibers
	PMR-15/graphite fabric C3000 8H satin grade 145	1,2,3	70°F/dry, 500°F/dry	(0/90)s	2 each	Same as above
	Multiphase resin/graphite X8551/IM7 350°F tape grade 145	1,2,3	70°F/dry, 270°F/wet	(0/90)s	2 each	Same as above
Epoxy based	Boron/epoxy tape	1,2,3,4	70°F/dry, 270°F/wet	(0/90)s	2 each	
	Kevlar/epoxy fabric style 285 BMS 8-219 250°F Kevlar 49/F155	1,2,3,4	70°F/dry, 200°F/wet	(0/90)s	2 each	
	Fiberglass/epoxy fabric style 181-150 BMS 8-79 250°F S-glass	1,2,3,4	70°F/dry, 200°F/wet	(0/90)s	2 each	Same as above

Legend:

1 Double cantilever beam (DCB)

2 End notched flexure (ENF)

3 Translaminar tension notched 4 - pt load

4 Translaminar compression notched 4-pt load
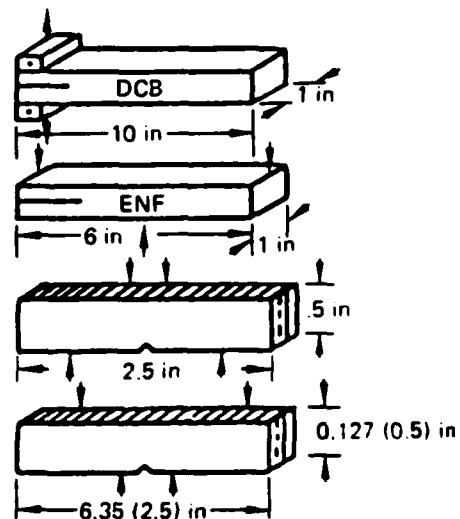
Figure 4.2-4. Task 3B Test Matrix

4.3 METHODS

4.3.1 Fabrication Procedures for Task 3A

To evaluate anomalous conditions known to typically cause premature failure of structures, specimens were fabricated as follows:

Low Resin Content. One ply of Mochburg W 1850 polyester bleeder mat was applied for every two plies of prepreg. This technique reduced the nominal resin content of 35% by approximately 7% to produce a laminate with 28% resin.

High Resin Content. A film stacking method was used to increase the resin content by 7% 3501-6 neat resin films were cut and sandwiched between prepreg plies to achieve a 42% resin content laminate.

Undercured. Specimens were cured at $260^\circ F$ and 45 psi for a dwell time of one hour; the standard cure cycle is $355^\circ F$ and 85 psi for two hours.

Double-cured. Laminates were cured at the standard cycle, debagged, rebagged, and cured again at the same cycle.

4.3.2 Hot/Wet Preconditioning

Prior to mechanical testing, specimens that required hot/wet preconditioning were placed in the environmental chamber and subjected to 100% relative humidity at $160^\circ F$ for 4 weeks.

4.3.3 Mechanical Testing

Seven mechanical tests were used to create fracture surfaces with known failure conditions.

K_t, **Stress Concentration Factor.** K_t is the ratio of the maximum stress in the region of a stress concentrator (such as a hole) to the stress in a similar strained area without the stress concentrator. The open hole tension test was used to simulate fractures under large and small K_t conditions. Eight one by ten inch AS4/3501-6 specimens were fabricated, half with a $(0)_{24}$ stacking sequence and the other half with $(\pm45)_{12s}$. Two large and two small K_t tests were simulated for each layup type. For the large K_t test, a 0.5 inch diameter hole was drilled at the center of the specimen. Simililarly, a 0.1 inch diameter hole was used to simulate a small K_t. Specimens were mechanically tested in

tension at an approximate deflection rate of 0.05 inch/min. All tests were conducted at RT.

Interlaminar Mode I Tension (DCB). Interlaminar Mode I tension fractures were produced using a DCB specimen geometry as shown in Figure 4.2-5. In this test, interlaminar tension conditions are generated at the specimen midplane by deflecting two halves of the beam at one end of the specimen. This was made possible by inserting a release film, fluorinated ethylene propylene (FEP). The specimen configuration is illustrated in Figure 4.2-6. Special fixtures were developed for this specimen to allow free-pin rotation at the beam end and mechanical grip attachment. The triangular specimen grips were wedged into the crack tip formed by the FEP insert (Fig. 4.2-7). This resulted in an opening displacement at the beam end prior to mechanical testing. Any precrack observed during clamping was marked on the specimen edge. The specimen was loaded under deflection control on a mechanical testing system servohydraulic load frame with the rate of cross-head deflection adjusted during the test to produce a relatively constant rate of crack growth of about 1.27 to 2.54 cm (0.5 to 1.0 inch)/min. Cross-head deflection rates ranged from 0.25 to 0.51 cm (0.1 to 0.2 inch)/min.

Interlaminar Mode II Shear (ENF). Interlaminar Mode II shear fractures were produced using the modified end-notched flexural specimen geometry shown in Figure 4.2-8. FEP was again used as a crack starter. Tests were carried out using a cantilever geometry fixture that allows the uncracked end to move horizontally but prevents it from rotating or moving vertically so that no extraneous (vertical) loads will be introduced as the beam shortens under deflection. With this geometry the top surface of the specimen is loaded in pure compression, while the bottom surface is in pure tension. The result is pure shear at the crack tip. During testing, cracks typically propagated rapidly along the midplane of the specimen for the first 60% of the test span, generally followed by a series of slower growth episodes. Full monitoring of the direction of cracking was precluded during the period of rapid growth; however, during the periods of slow, stable growth crack extension proceeded as expected, away from the FEP crack starter and toward the cantilever beam support fixture.

Creep Testing. Four tapered specimens were tested under creep condition: two specimens under interlaminar Mode I tension at RT and at 270°F, and two under interlaminar Mode II shear at the same temperatures. Specimens were tested in a Satec
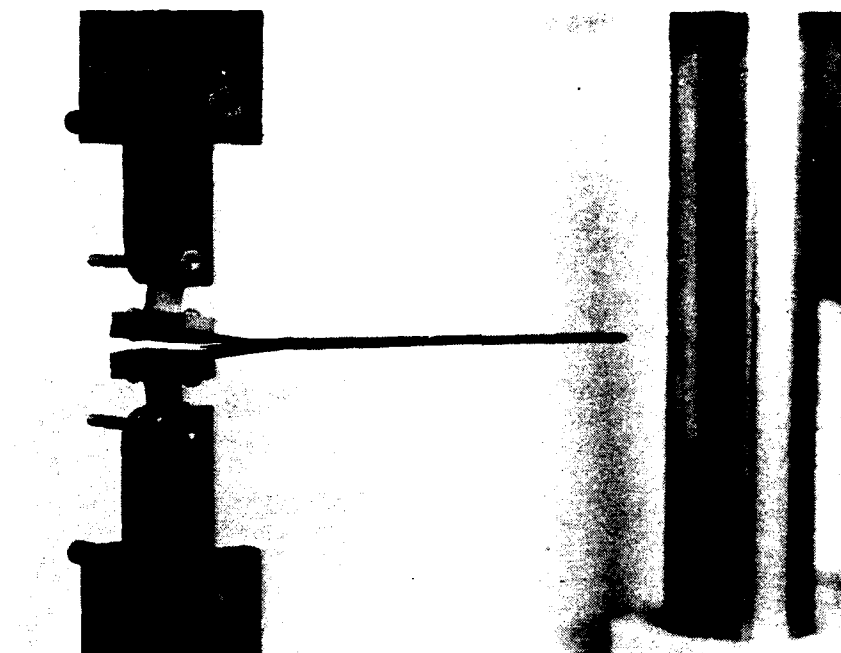
Figure 4.2-5. Double Cantilever Beam Specimen Geometry
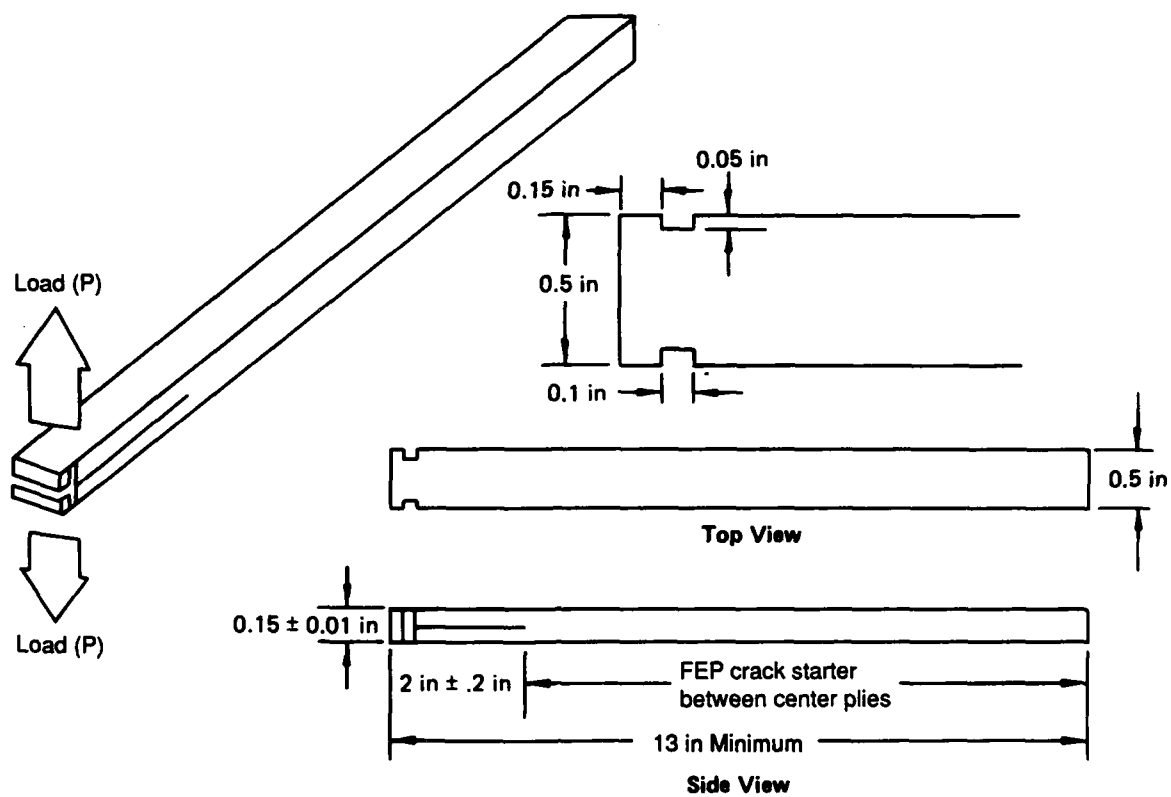
Figure 4.2-6. Double Cantilever Beam Specimen
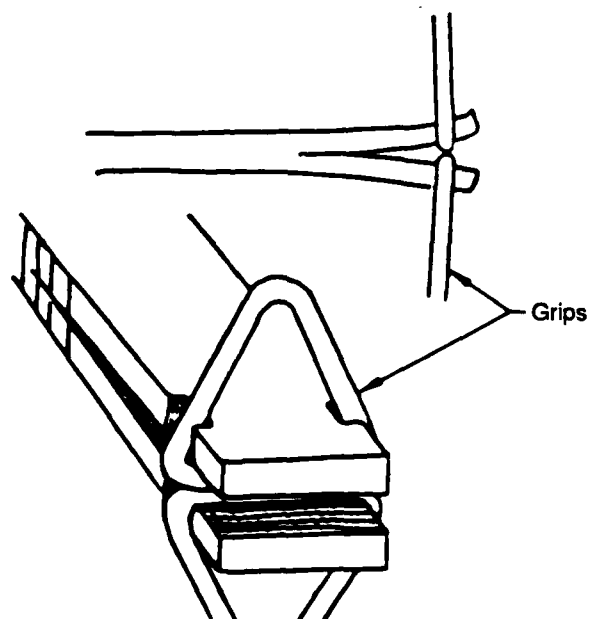
Figure 4.2-7. Double Cantilever Beam Grip Fixture
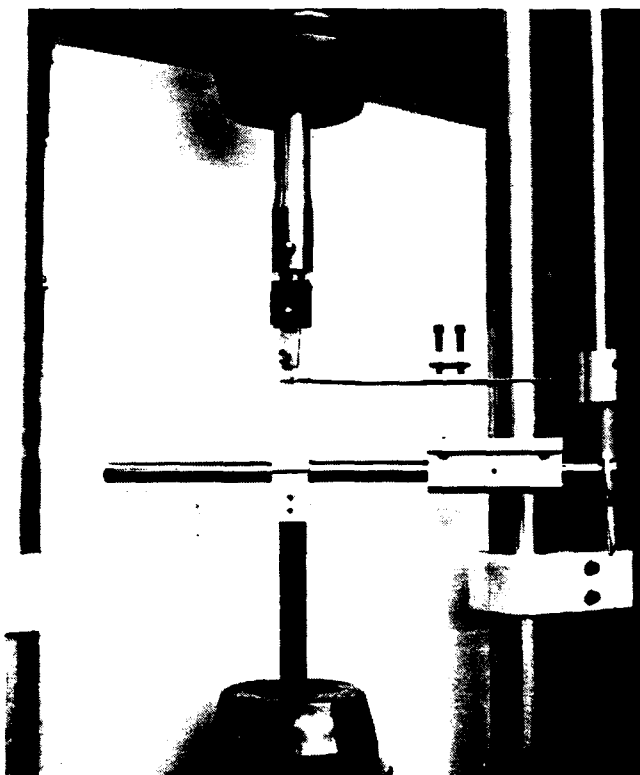
Figure 4.2-8. End-Notched Flexure Specimen Geometry

25,000-lb capacity Universal test machine with the crosshead speed set at .001 in/min. Deflection was measured at the crosshead using a motion transducer. Load versus time and deflection versus time curves were recorded on a Soltec recorder.

For the elevated temperature tests, a Watlow rubber strip heater was used as the heat source. Silicone adhesive was used to adhere the flexible silicone rubber heater to the specimen. Thermocouples were located throughout the specimen to assure maintenance of the 270° test temperature.

High-Rate Sensitivity. To create RT high-rate Mode I tension and Mode II shear fractures, projectiles were shot into a 1-inch by 10-inch specimen protected by an aluminum plate at the location of penetration. For DCB specimens, a 1/2-inch thick aluminum plate was double-back taped to a cutout as shown in Figure 4.2-9. A vise was used to hold one end of the specimen. The aluminum plate served as a shooting target deflecting the back half of the laminate away from the front half. This created a Mode I tension fracture. The interlaminar Mode II shear fracture was created by shooting a projectile at an aluminum target plate attached to the forward face of the specimen. The force of the impact deflected both halves of the laminate. FEP crack starter initiated crack propagation by the sliding of the two halves of the laminate, creating a Mode II shear fracture.

Translaminar Tension and Compression (Notched Four Point Tension (N4PtT) and Notched Four Point Compression (N4PtC)). Controlled translaminar tension and compression failures were generated using a four-point beam apparatus. The specimen has a notched-bend-bar geometry. The position of a chevron-shaped notch in the specimen determined the type of load the specimen experienced; when the notch was placed across from the beam's lower surface, the specimen was in tension (Fig. 4.2-10), while a specimen with its notch across from the beam's upper surface was in compression (Fig. 4.2-11).

Compression After Impact (CAI). Compression testing was performed on a 4-inch by 6-inch laminate. The specimen was first centrally mounted on an impact support fixture (Fig. 4.2-12) and impacted on the tool side by an indenter with a 0.62 inch hemispherical tip at 1200 inch lbs/inch. After impact, the specimen was examined using through transmission ultrasonic (TTU) techniques. The specimen was then placed on a 50 kip servohydraulic machine with a deflectometer and loaded to failure with a displacement of 0.05 inch/min.
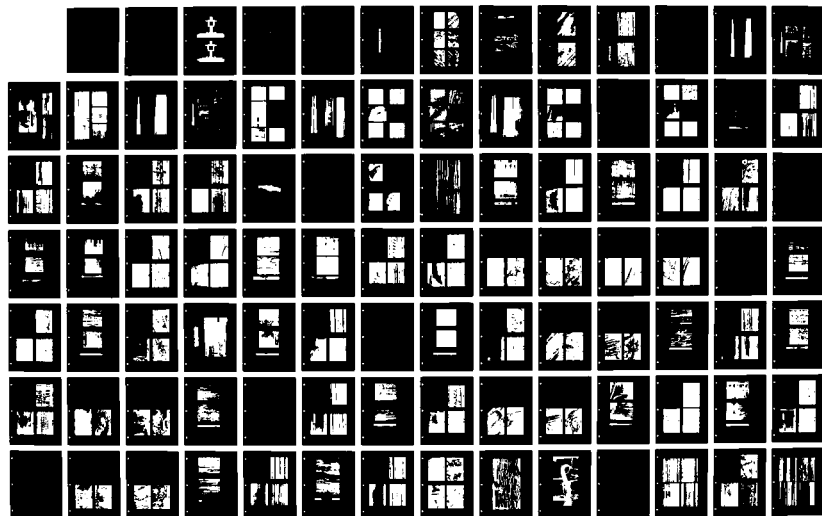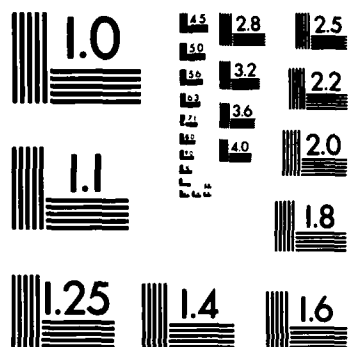
MICROCOPY RESOLUTION TEST CHART
NATIONAL BUREAU OF STANDARDS
STANDARD REFERENCE MATERIAL 1010a
(ANSI and ISO TEST CHART No. 2)
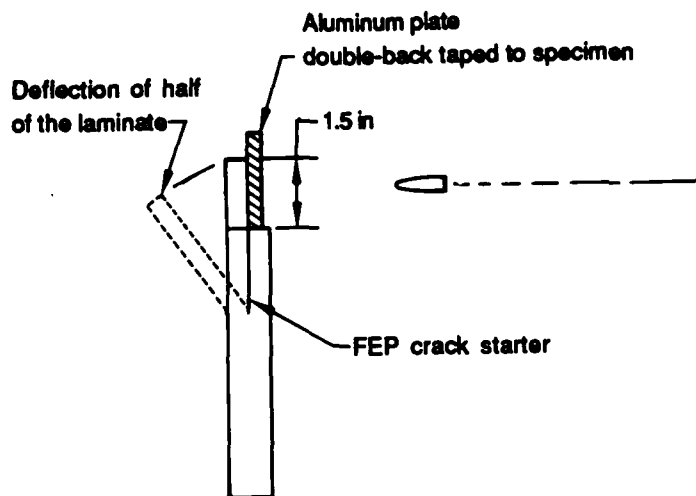
(a) High-rate fracture simulation for double cantilever beam (DCB), Mode I tension specimen
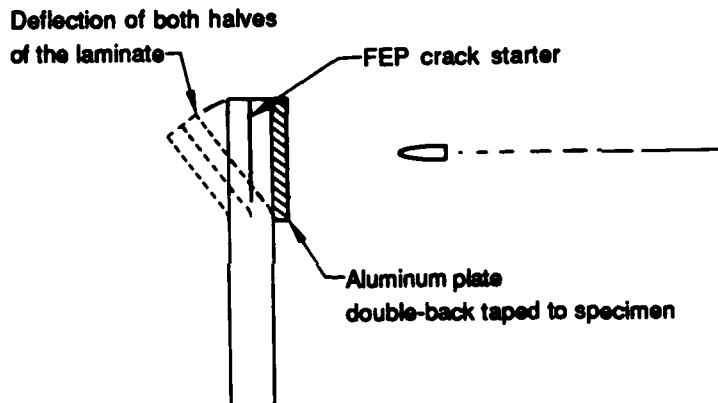
(b) High-rate fracture simulation for end-notched flexure (ENF), Mode II shear specimen

Figure 4.2-9. High-Rate Fracture Simulation
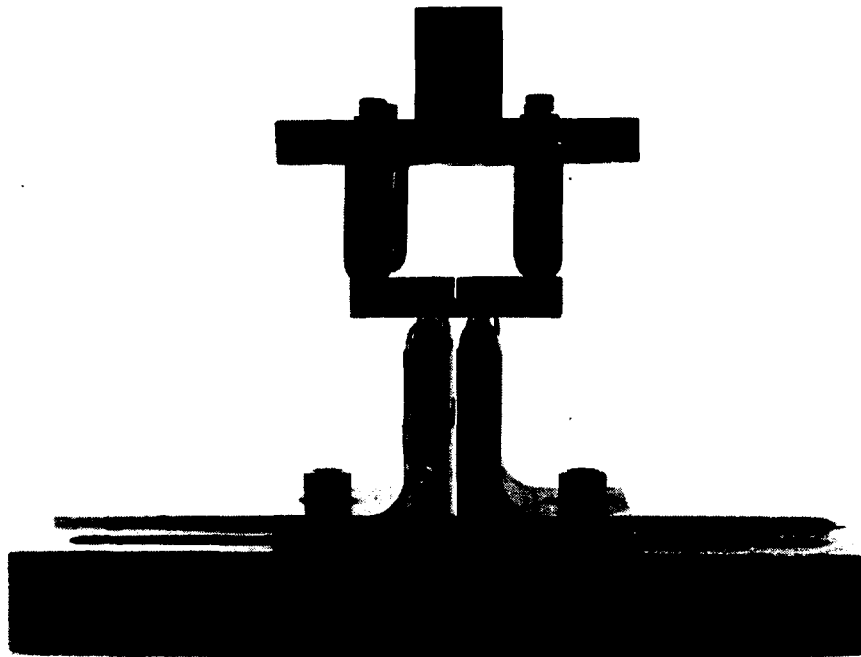
Figure 4.2-10. Notched Bend Bar Tension Specimen Geometry
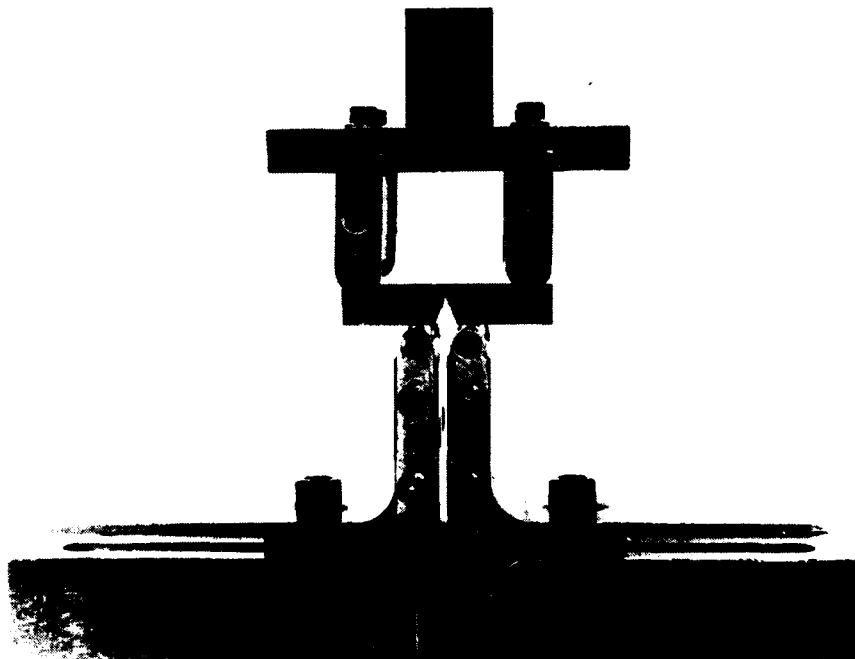
Figure 4.2-11. Notched Bend Bar Compression Specimen Geometry
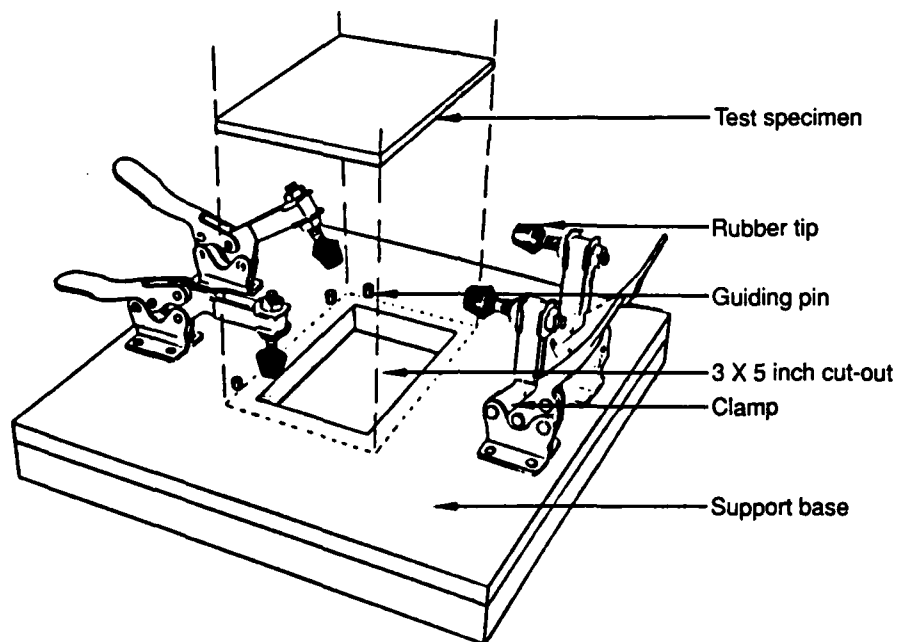
Figure 4.2-12. Compression-After-Impact Support Fixture

4.4 RESULTS

4.4.1 Task 3A: Model System

4.4.1.1 Stress/Loading Conditions

K_t.   Specimens with ±45 degree and 0 degree layups and with large and small diameter holes were subjected to open hole tension tests.

In the large K_t, ±45 degree layup specimen, visual observation revealed an elongated hole in the loading direction. This hole was caused by loading the ±45 degree ply layup in 0 degree tension. The specimen did not produce a translaminar fracture as it would have with a 0/90 degree ply layup. Rather, there were two fractures, originating from the sharp radius of the hole and propagating in opposite directions to one another. Three locations were examined to determine the fracture modes and origins (Fig. 4.4-13). Removing the delaminated surface ply revealed rivermarks in two locations indicating the crack propagated toward the outer edge of the specimen. The cracks initiated near a third location, under Mode II shear (Fig. 4.4-14).

In the large K_t, 0 degree layup specimen, two main fractures occurred in the intralaminar region.   They originated at opposite edges of the hole and propagated outward and parallel to one another (Fig. 4.4-15a). One crack was examined optically; it had occurred under Mode II shear (Fig. 4.4-15b).

The fracture of the small K_t, ±45 degree layup specimen produced delamination approximately 0.5 inch to both sides of the open hole (Fig. 4.4-16a). The microscopic examination of the delamination revealed that the fracture was created predominately in almost pure Mode II shear (Fig. 4.4-16b). However, a Mode I tension fracture occurred near the outermost region of the delamination (Fig. 4.4-16c).

In the small K_t, 0 degree layup, the fractures occurred in the intralaminar region. Fractography was performed on two fracture surfaces: one near to the hole and the other toward the outer edge (Fig. 4.4-17a). It was revealed in the optical examination that the fractures occurred by pure Mode II shear, as evidenced by the presence of hackle formations (Figs. 4.4-17b and c). In contrast to the small K_t, ±45 degree layup specimen, the hole was enlarged by at least five-times.
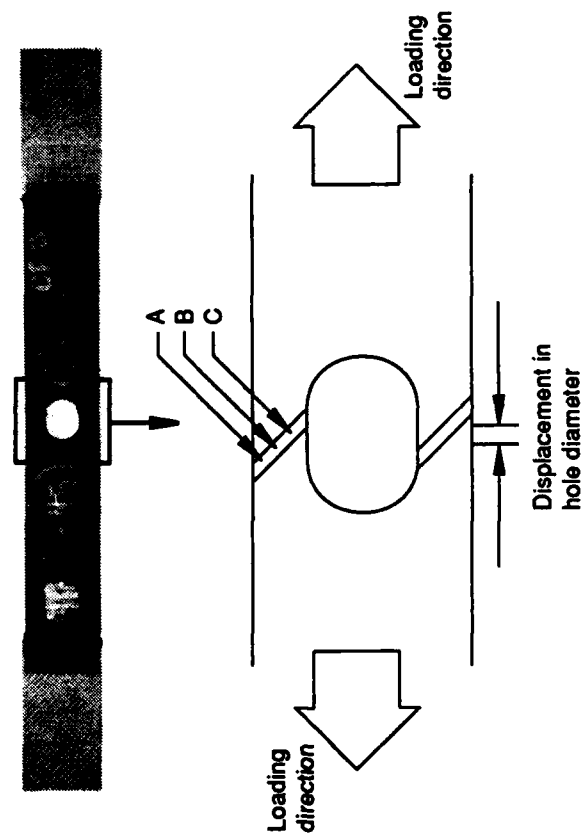
Figure 4.4-13. Open Hole Tension Specimen (Large K_t) with Locations of Optical Photomicrographs

Location A —
near the outer edge

Location B —
at the center

Location C —
near the hole edge
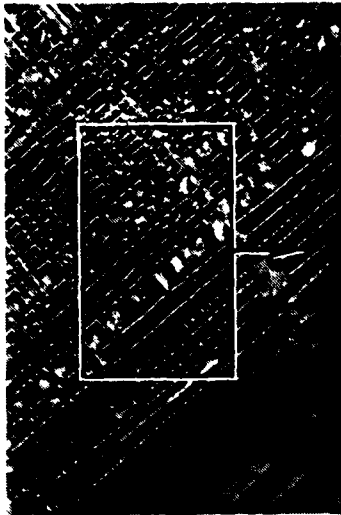
200X

200X

200X

400X

400X

400X

Legend:
R river marks
H hackles

Figure 4.4-14. Optical Photomicrographs of the Open Hole Tension Fracture Surface; ± 45 Degree Layup, Large K_t
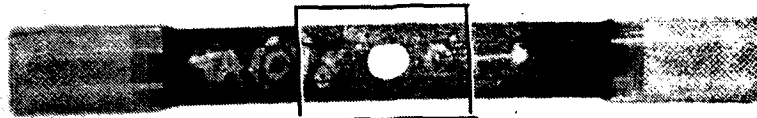
Photomacrograph of sample; fracture area shown below

(a) Diagram of fracture area

(b) Optical photomicrograph of fracture
surface, location a-a; magnified 400X

Legend:
H hackles

Figure 4.4-15. Open Hole Tension Fracture; 0 Degree Layup, Large K_t

Loading direction

Loading direction

Diagram of fracture area

(a)

Photomacrograph of sample

(b) Optical photomicrograph of location A, near the hole edge; magnified 400X

(c) Optical photomicrograph of location B, at the center of delamination; magnified 400X

Figure 4.4-16. Open Hole Tension Fracture; ±45 Degree Layup, Small K_t
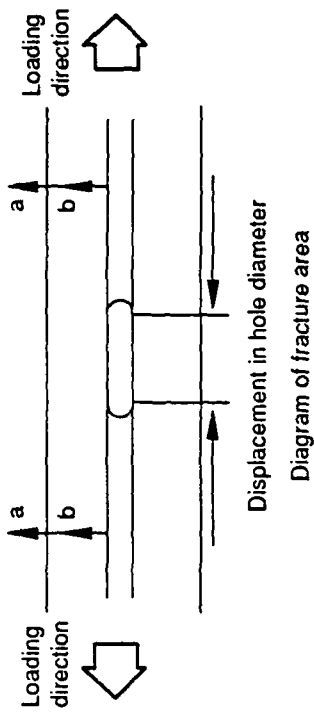
Legend:
H hackles
R rivermarks

Loading
direction

Displacement in hole diameter

Diagram of fracture area

(a)

Photomacrograph of sample

(b) Optical photomicrograph of fracture
surface, location a-a; magnified 400X
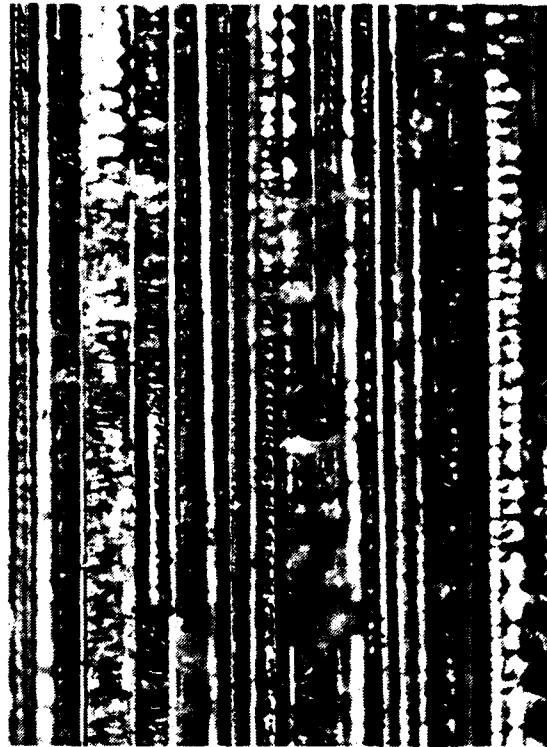
(c) Optical photomicrograph of fracture
surface, location b-b; magnified 400X

Figure 4.4-17. Open Hole Tension Fracture; 0 Degree Layup, Small K_t

Legend:
H hackles

Creep. RT/Dry and elevated temperature/dry creep specimens were tested under tension and shear.

Interlaminar Mode I Tension, RT/Dry. Visual observation revealed a smooth, glassy surface typical of an interlaminar Mode I tension fracture. There were visible crack arrest marks ("beach marks") running perpendicular to the mechanically induced crack direction (Fig. 4.4-18). The spacing between these marks was quite consistent due to the constant loading rate throughout the creep test. Optical fractography focused on what appeared to be a stripped fracture region. Due to the re-initiation of the crack, the location just after crack arrest appeared much rougher than the region just prior to it (Fig. 4.4-19). The rivermarks were more readily observed in the region prior to the crack arrest.

SEM fractographs were taken of the three regions of fracture, including the location of the crack arrest (Fig. 4.4-20). The fracture topography was smooth with distinct rivermarks just prior to the periodic crack arrest; after reinitiation of the crack, the fracture appeared uneven with very fine rivermarks (Fig. 4.4-21).

Interlaminar Mode I Tension, 270°F/Dry. Visual observation revealed a smooth, glassy fracture surface similar to that of the RT specimen. Crack arrest marks were again observed (Fig. 4.4-22). However, there were fragments of loose fibers on the fracture surface. These fibers may have separated from the resin matrix prematurely due to poor adhesion. The fracture topography at the region before and after the crack arrest was smooth (Fig. 4.4-23), unlike that of the fracture created at RT. The difference between the RT and 270°F fractures may be due to lower resistance to crack propagation in the 270°F specimen. The SEM analysis confirmed the observations made during the optical analysis (Fig. 4.4-24).

Interlaminar Mode II Shear, RT/Dry. Visually, the mating fracture surfaces looked somewhat different: one surface smooth and glassy, the other rough and dull (Fig. 4.4-25). Crack arrest marks were observed on the fracture surfaces at the ends of the specimen and at the center. SEM fractographs revealed that the glassy surface consisted largely of scallops (with some hackles) (Fig. 4.4-26) and the rough surface exhibited mainly hackles (with some scallops) (Fig. 4.4-27).

Interlaminar Mode II Shear, 270°F. Visual examination revealed a fracture with smooth and glassy surface on one of the mating sides and rough and dull on the other (Fig. 4.4-28). This was similar to the fracture surfaces created at room temperature. The glassy surface exhibited mostly of scallops (with some hackles) (Fig. 4.4-29), and the

FEP crack starter

End of controlled test

Mechanically induced crack direction

(a) Full view

Stroke marks

(b) Close-up view
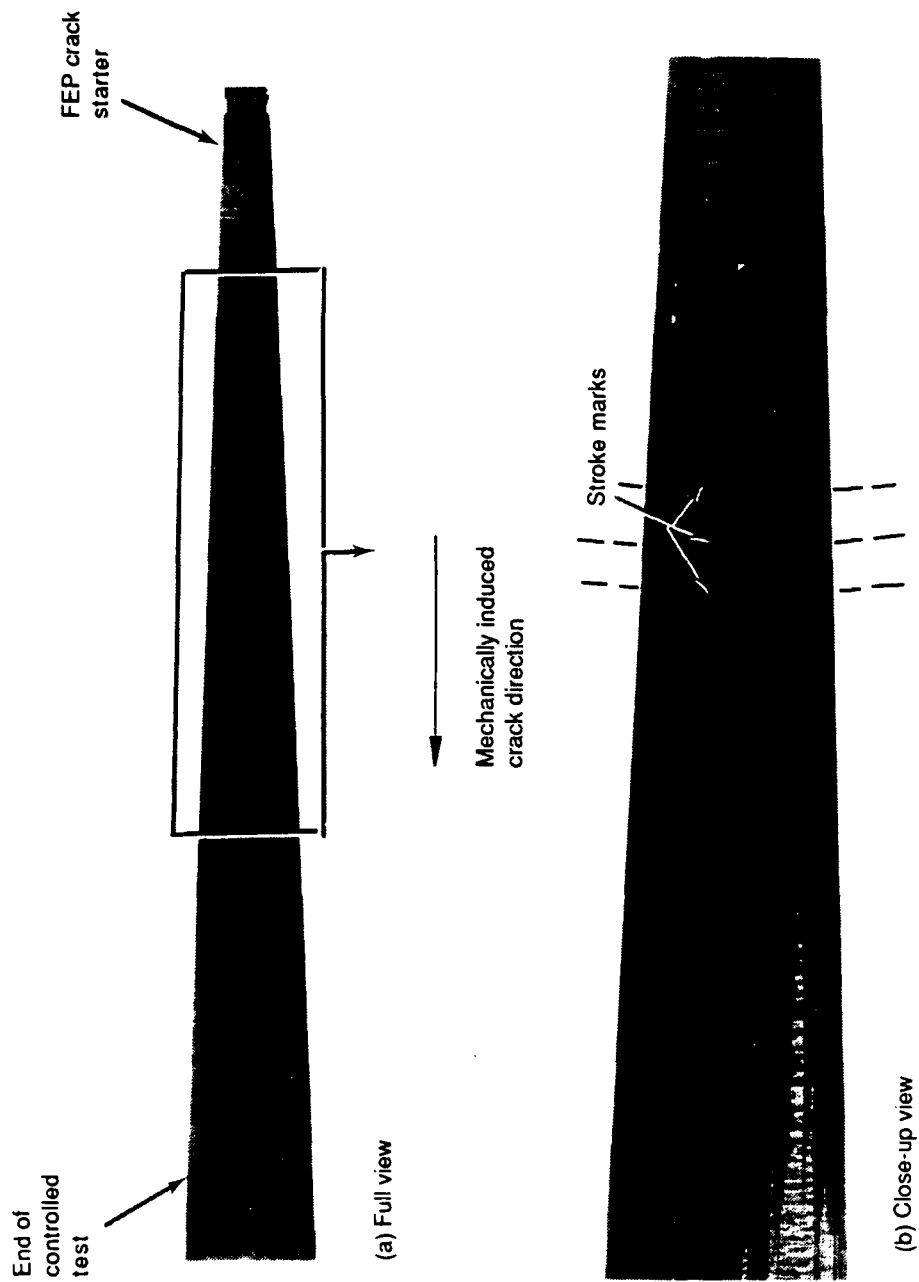
Figure 4.4-18. Photomacrographs of Interlaminar Mode I Tension, RT/Dry Creep Fracture
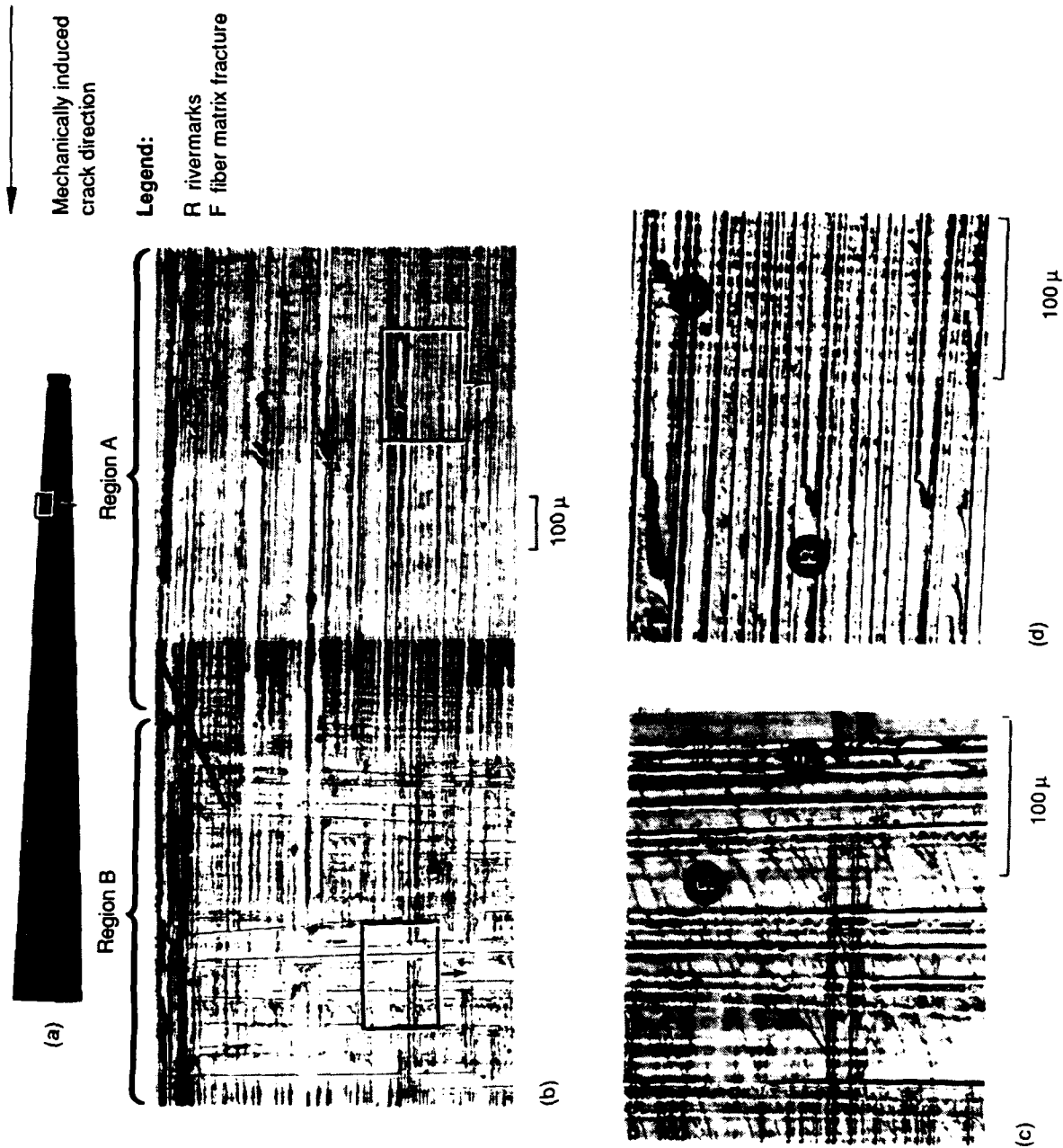
Figure 4.4-19. *Optical Photomicrographs of Interlaminar Mode I Tension, RT/Dry Creep Fracture*
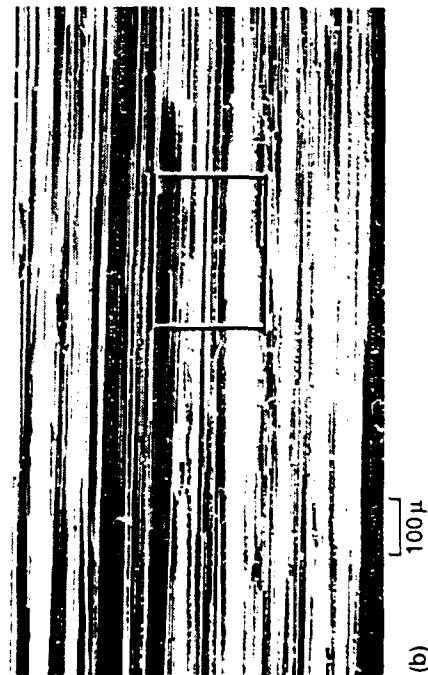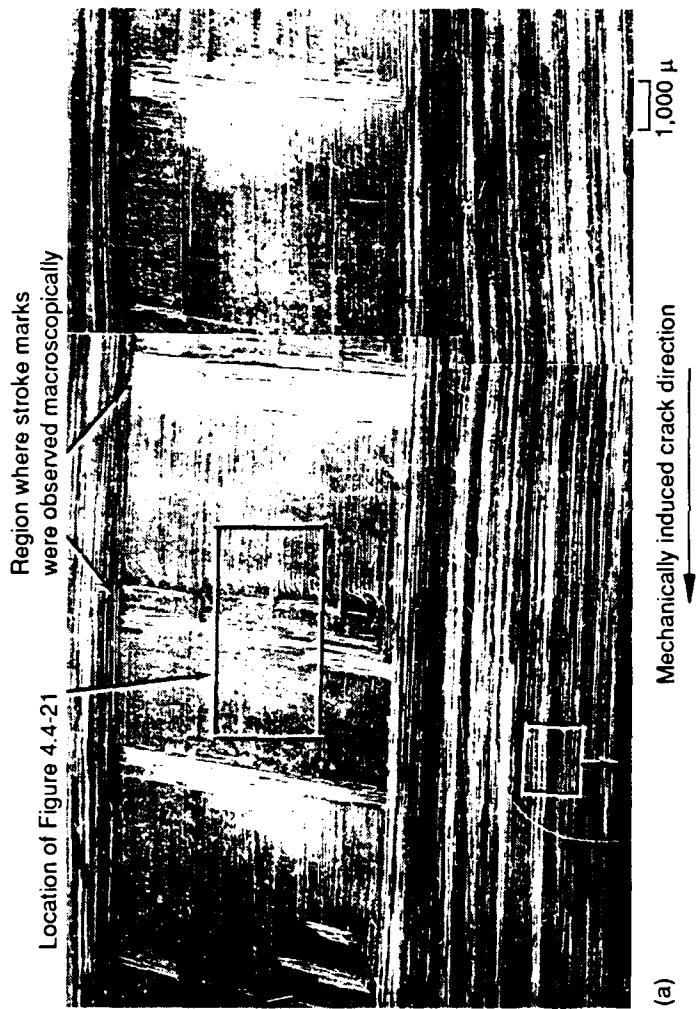
Figure 4.4-20. *SEM Fractographs of Interlaminar Mode I Tension, RT/Dry Creep Fracture*
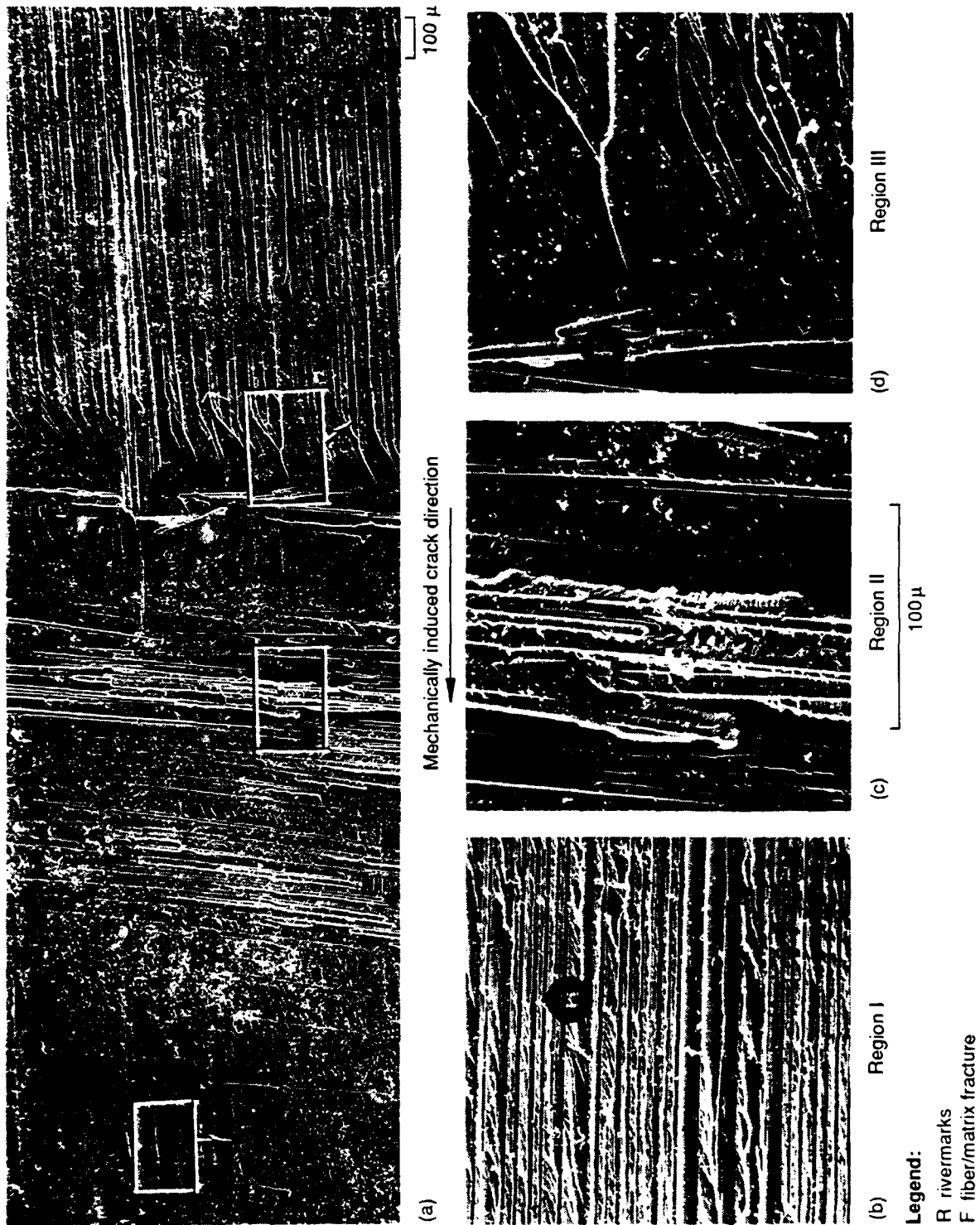
Figure 4.4-21. SEM Fractographs of Interlaminar Mode I Tension, RT/Dry Fracture

Legend:
R rivermarks
F fiber/matrix fracture

FEP crack starter

Mechanically induced crack direction

(a) Full view

Stroke (crack arrest) marks

Stray fibers

(b) Closeup view
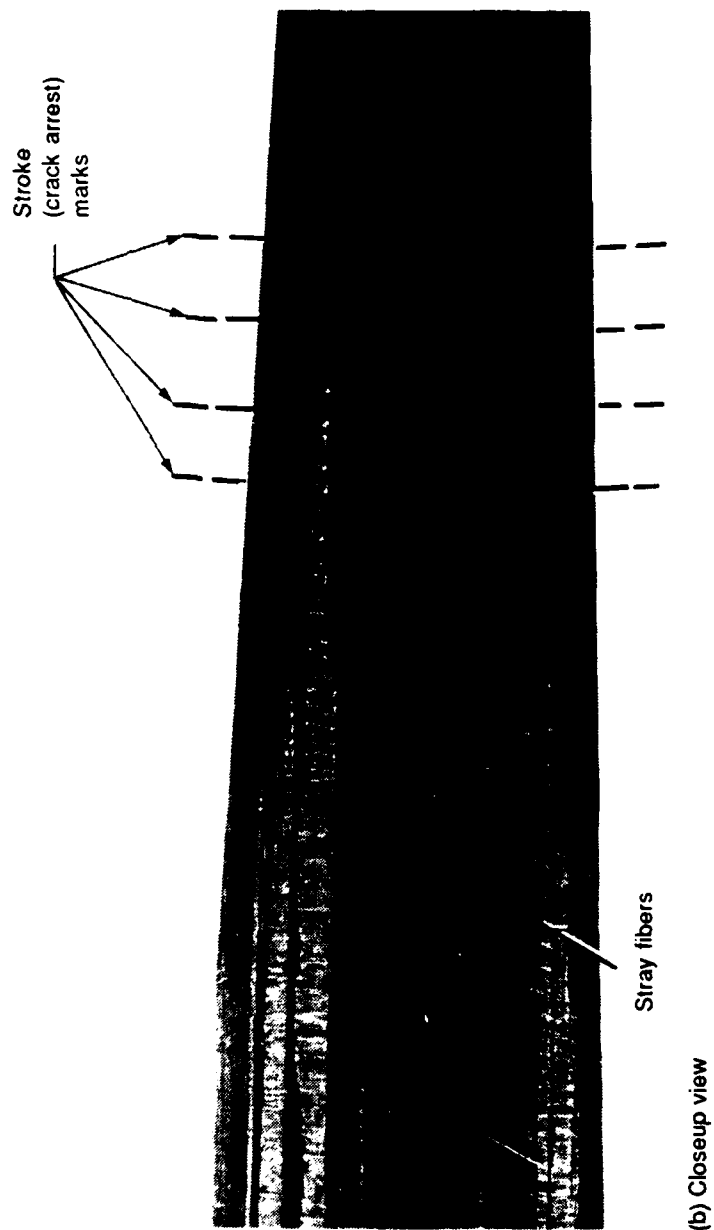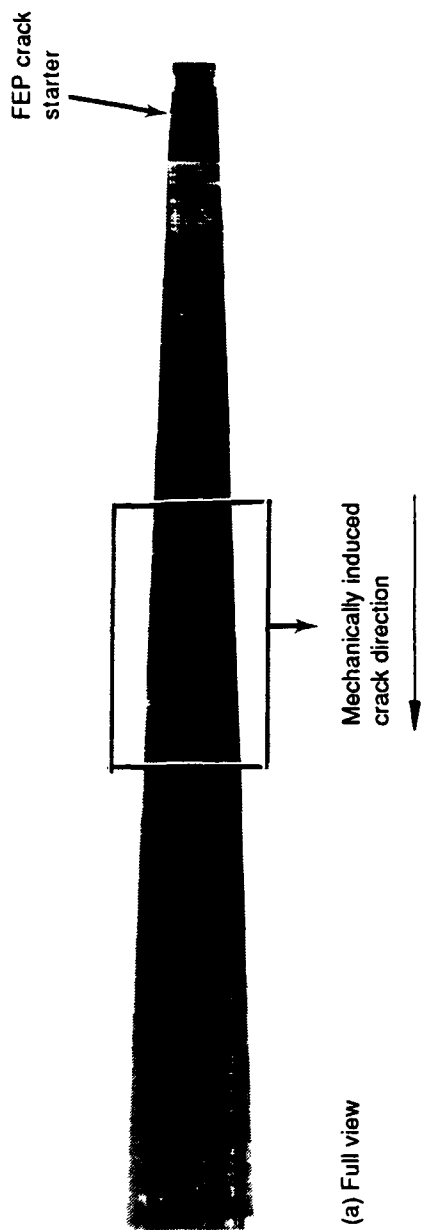
Figure 4.4-22. Photomacrographs of Interlaminar Mode I Tension, 270 F/Dry Creep Fracture

(a)

(b)

(c)

(d)

Crack arrest

Legend:
R rivermarks

Mechanically induced
crack direction

100 μ
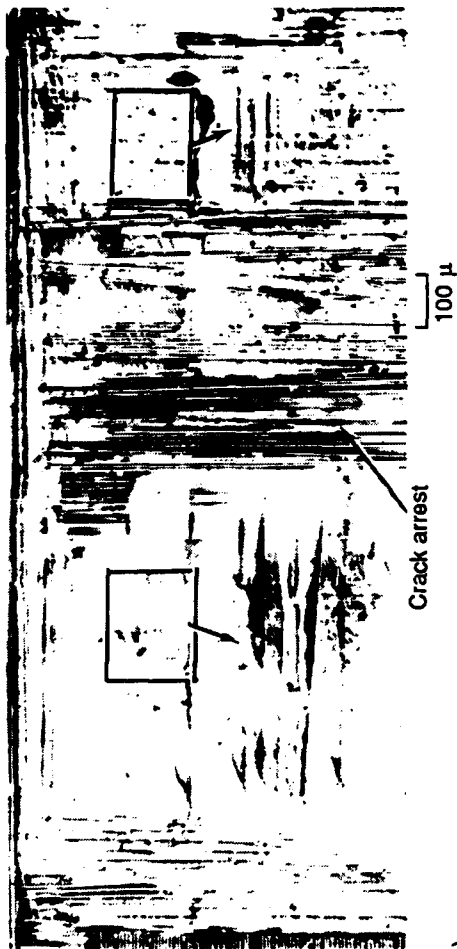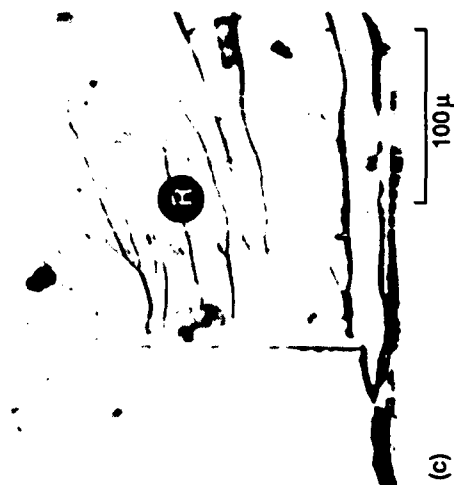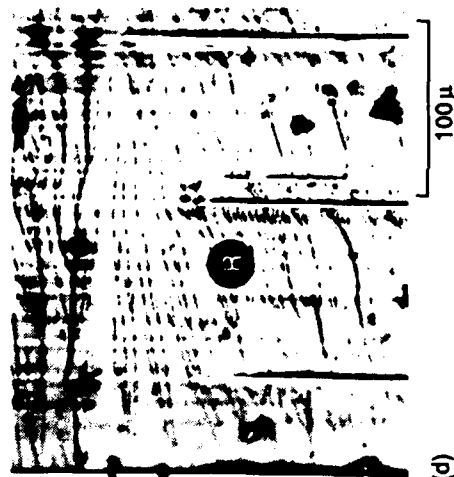
Figure 4.4-23. Optical Photomicrographs of Interlaminar Mode I Tension, 270 F/Dry Creep Fracture

(c)

(e)

100 μ

(b)

1,000 μ

Legend:

R rivermarks
F fiber/matrix fracture

Mechanically induced
crack direction

(a)

(d)

100 μ
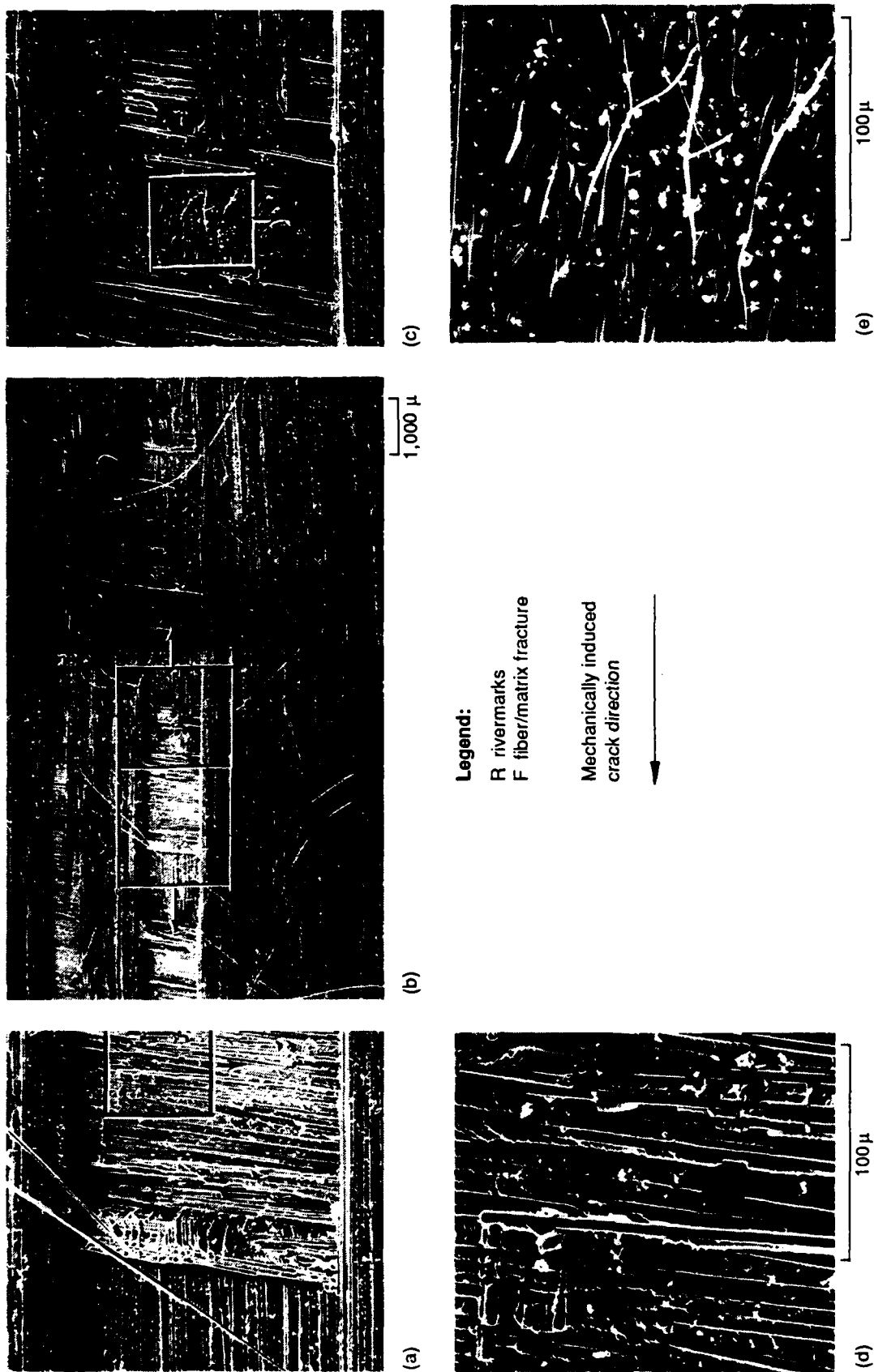
Figure 4.4-24. SEM Fractographs of Interlaminar Mode I Tension, 270 F/Dry Creep Fracture
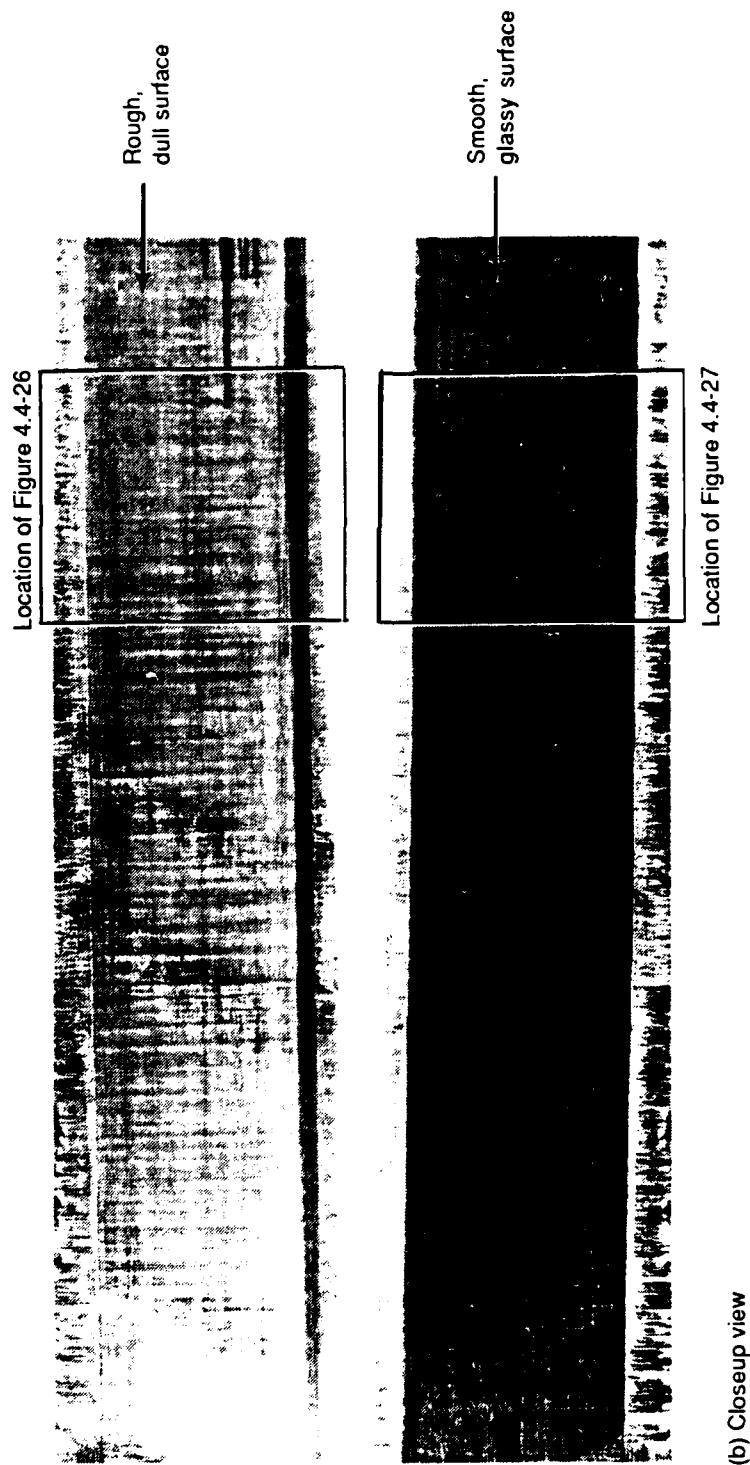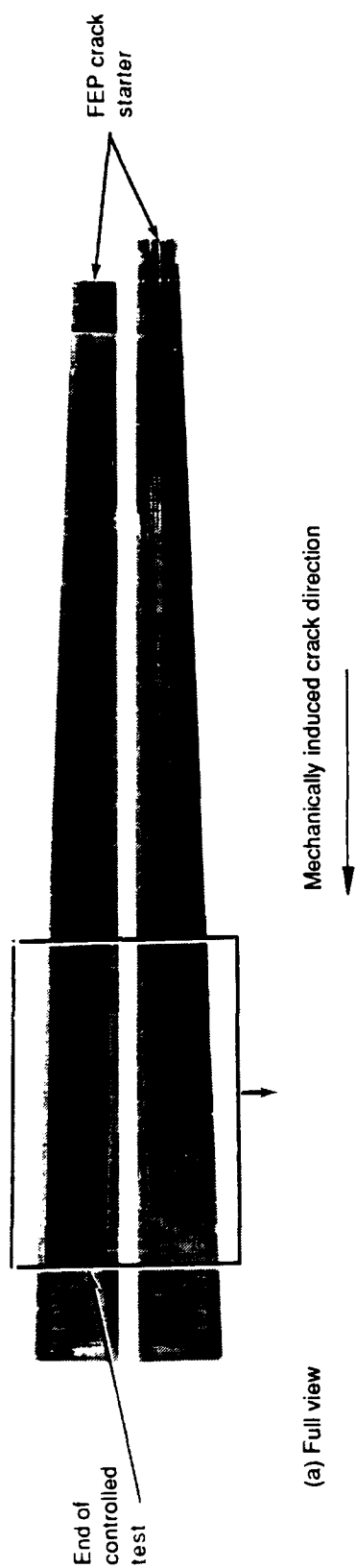
FEP crack starter

End of controlled test

Mechanically induced crack direction

(a) Full view

Rough, dull surface

Location of Figure 4.4-26

Smooth, glassy surface

Location of Figure 4.4-27

(b) Closeup view

Figure 4.4-25. Photomacrographs of Interlaminar Mode II Shear, RT/Dry Creep Fracture

D180-31996-1

93

(c)

100 μ

(b)

1,000 μ

Legend:

H hackles
F fiber/matrix separation
S scallops

Mechanically induced
crack direction

(a)

100 μ

(e)

100 μ

(d)

100 μ
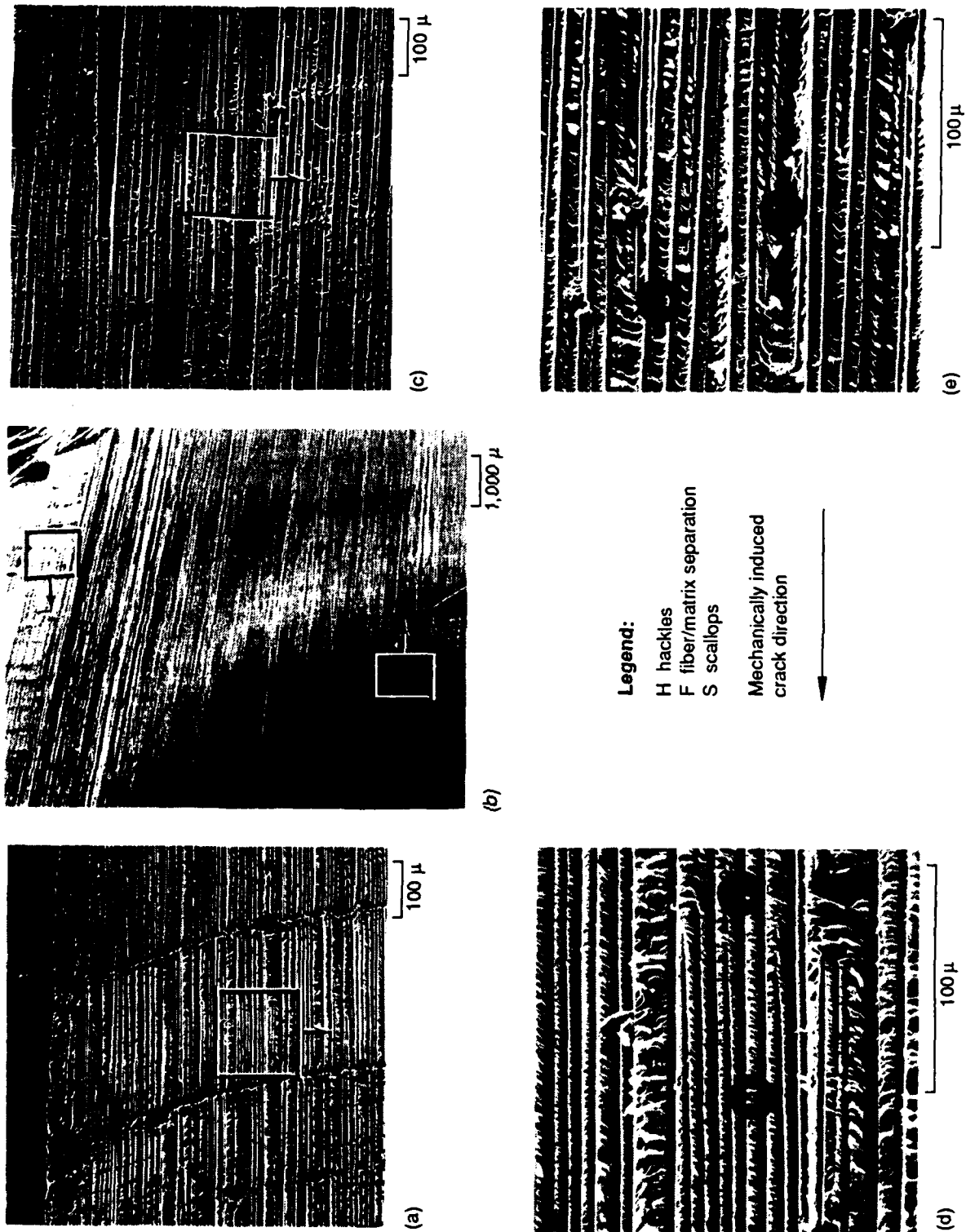
Figure 4.4-26. SEM Fractographs of Interlaminar Mode II Shear, RT/Dry Creep Fracture Showing Glassy Surface
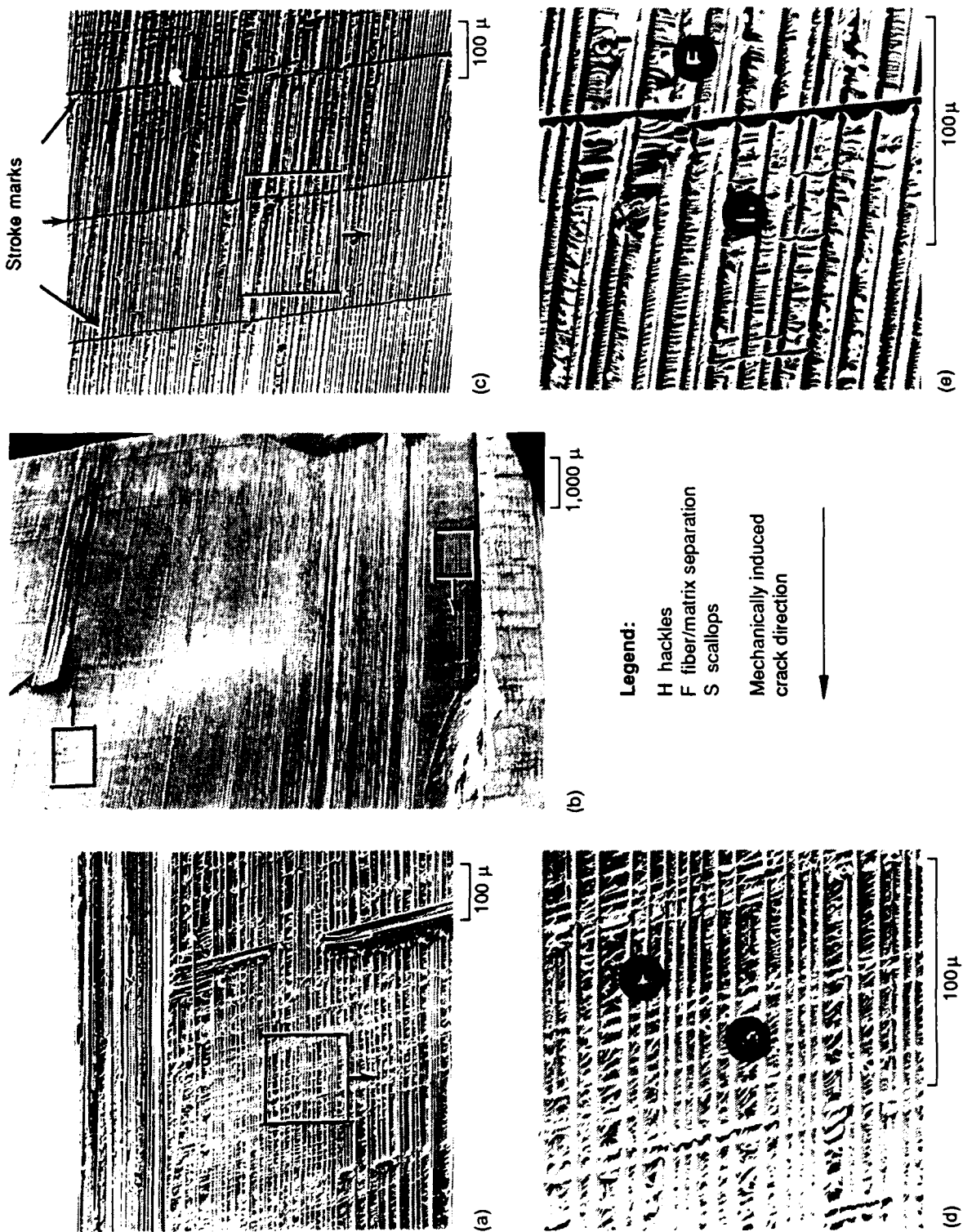
Figure 4.4-27. SEM Fractographs of Interlaminar Mode II Shear, RT/Dry Creep Fracture Showing Rough Surface

Stroke marks

Legend:
H hackles
F fiber/matrix separation
S scallops

Mechanically induced
crack direction

(a) (b) (c) (d) (e)

100 μ   1,000 μ   100 μ

FEP crack starter

End of controlled test

Mechanically induced crack direction

(a) Full view

Smooth, glassy surface

Rough, dull surface

Location of Figure 4.4-29

Location of Figure 4.4-30

(b) Closeup view
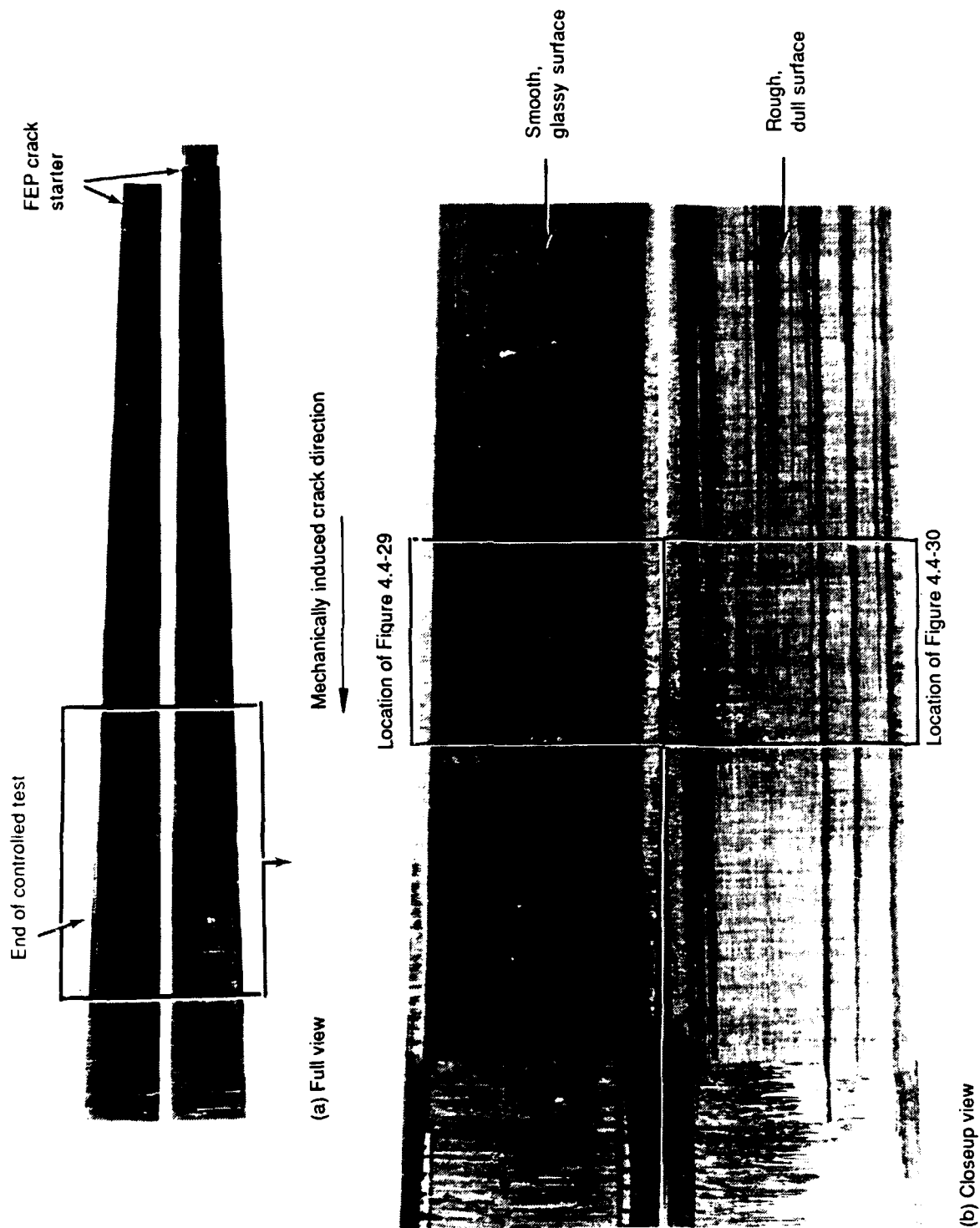
Figure 4.4-28. Photomacrographs of Interlaminar Mode II Shear, 270 F/Dry Creep Fracture

Legend:

H hackles
F fiber/matrix separation
S scallops

Mechanically induced
crack direction

Figure 4.4-29. SEM Fractographs of Interlaminar Mode II Shear, 270 F/Dry Creep Fracture Showing Glassy Surface
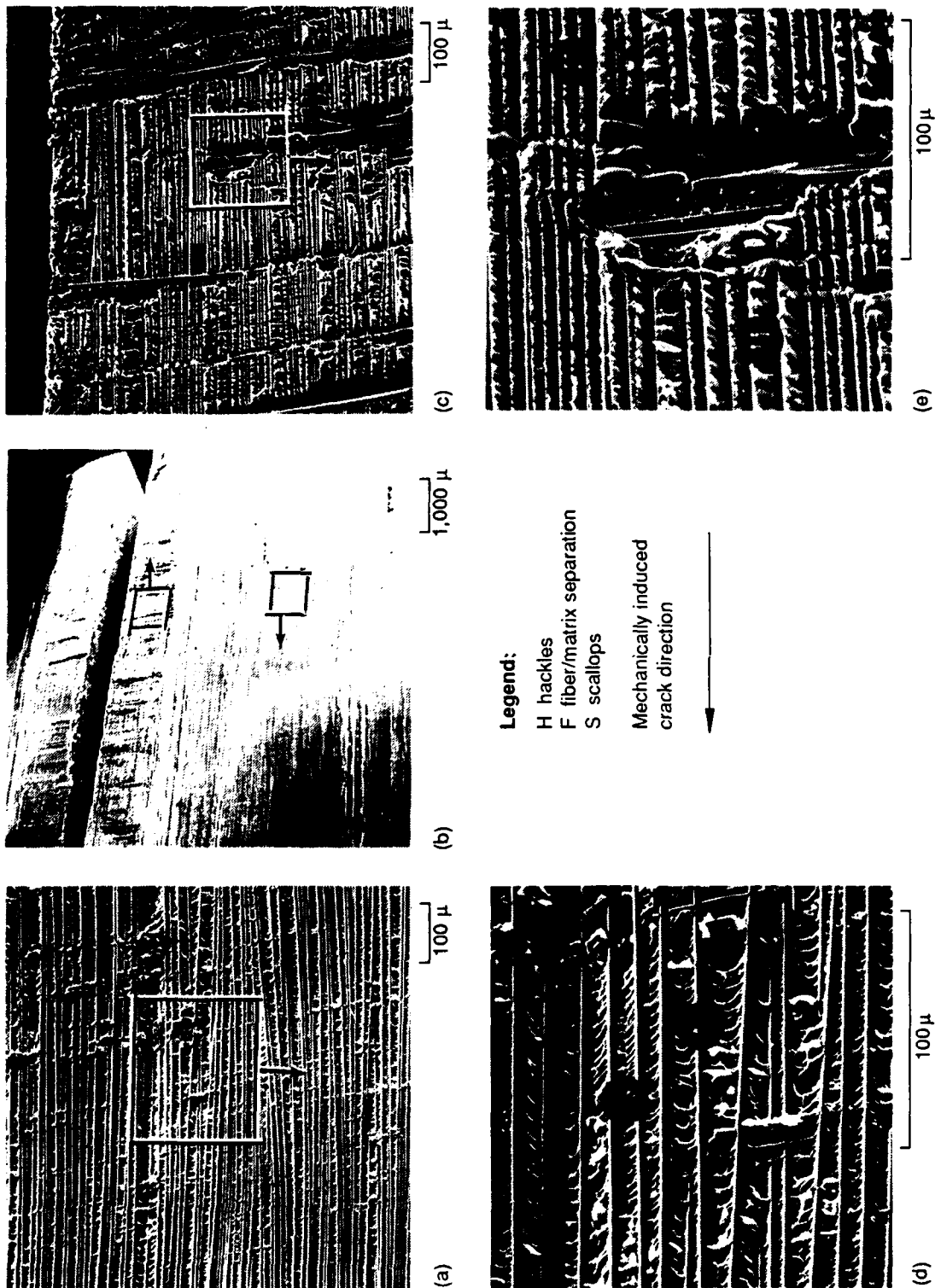
rough surface consisted mostly of hackles (with some scallops) (Fig. 4.4-30). Optical and SEM analyses showed no significant features to distinguish the RT and 270°F creep specimens.

High Rate RT/Dry. Specimens were shot with a projectile to produce high rate DCB and ENF-type fractures.

<u>Interlaminar Mode I Tension, RT/Dry</u>. Visual observation of the RT, DCB Mode I tension specimen, tested under conditions resulting in a high rate of fracture, revealed fractures somewhat different from those in a DCB/RT Mode I tension specimen tested at constant rate. Due to the very rapid crack propagation, the fracture surface did not exhibit the clear macroscopic crack arrest marks which are characteristic of slow crack growth. In some locations, fiber splinters were peeled away from the matrix.

Under the optical microscope, a cleavage fracture was observed with numerous rivermarks showing an overall crack direction (Fig. 4.4-31).

To illustrate the different rates of fracture, two regions on the specimen were documented and analyzed. Region I was created by the initial projectile; Region II was created by a second projectile penetration.

SEM analysis showed that Region I experienced a lower energy fracture than Region II, as evidenced by its rougher surface and more mixed mode fracture (Fig. 4.4-32). This may be a result of the initially delaminated portion driving the crack at a higher rate. There were also many fiber splinters in Region II (Fig. 4.4-33).

<u>Interlaminar Mode II Shear, RT/Dry</u>. Visual observation revealed a fracture surface similar to a typical interlaminar Mode II shear specimen tested at constant rate; the only noticeable difference was the fiber splinters seen on the high load rate specimen.

Optical microscopy of the fracture surface showed a difference between the high rate specimen and the typical ENF specimen tested at constant rate (Fig. 4.4-34). Due to the very rapid fracture, hackles were formed in various tilts and shapes; at slower crack growth rates, the hackles tend to form parallel to one another. As noted previously on Mode I specimens, regions created by initial and secondary projectile penetration (resulting in different crack growth rates) exhibited no distinctly different features (Fig. 4.4-35 and 4.4-36).

Compression After Impact. Visual inspection revealed extensive buckling damage around the point of impact. Failure of the panel occurred in a band approximately 1.0 to 1.5 inch wide across the full width of the panel (Fig. 4.4-37). TTU indicated a
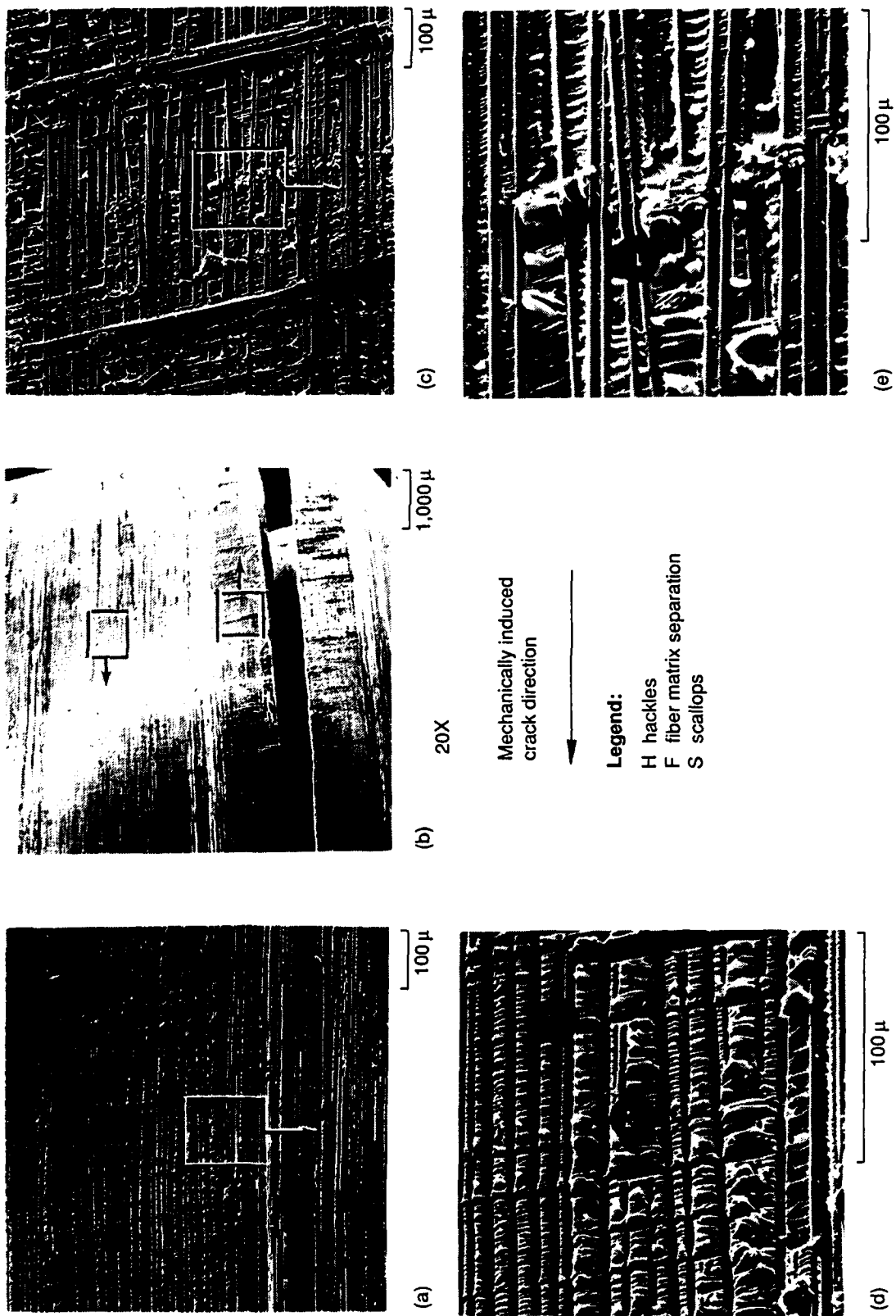
Figure 4.4-30. SEM Fractographs of Interlaminar Mode II Shear, 270 F/Dry Creep Fracture Showing Rough Surface

400X

100X

Figure 4.4-31. Optical Photomicrographs of Interlaminar Mode I Tension, High Rate, Room Temperature Fracture Between the 0/90 Plies

FEP crack starter region

Region I

Region II

End of controlled fracture

Mechanically induced crack growth direction
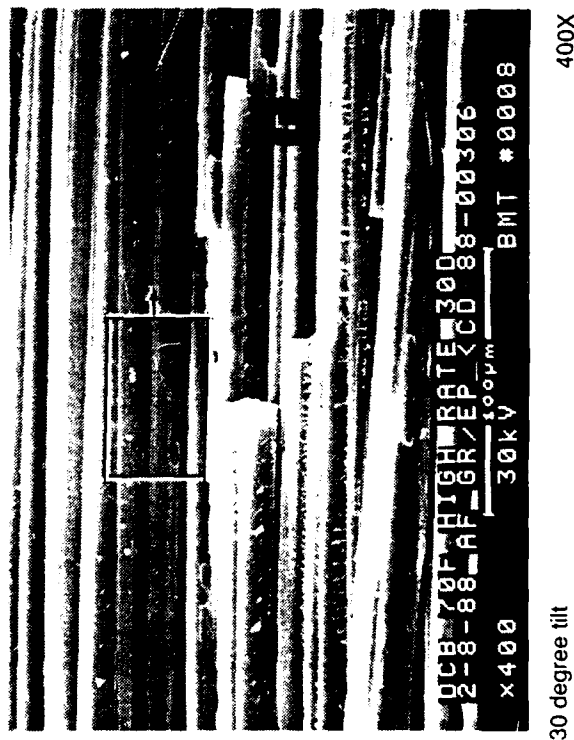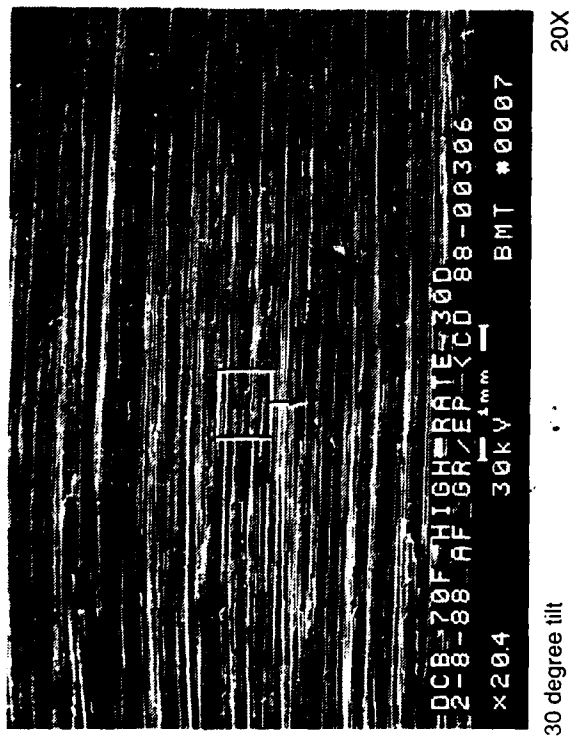
Legend:

F fiber matrix
R rivermark
M matrix fracture

Mechanically induced
crack direction
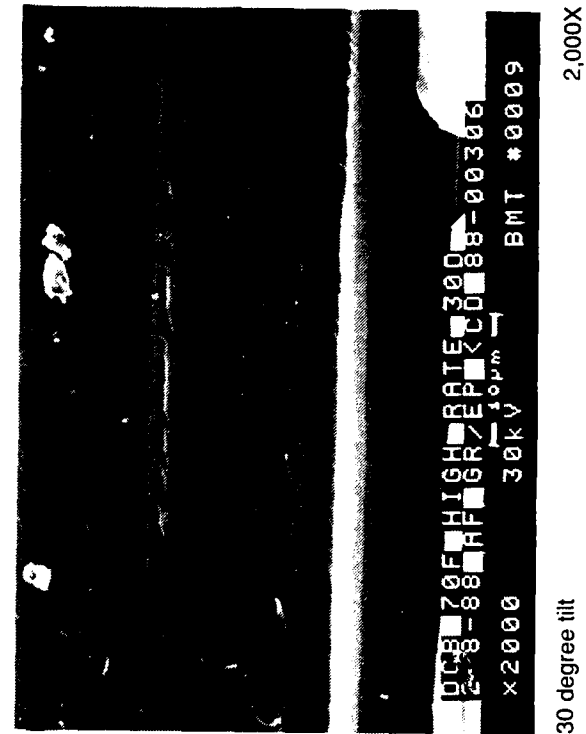
Figure 4.4-32. SEM Fractographs of Interlaminar Mode I Tension, High Rate, Room Temperature Fracture (Region I)
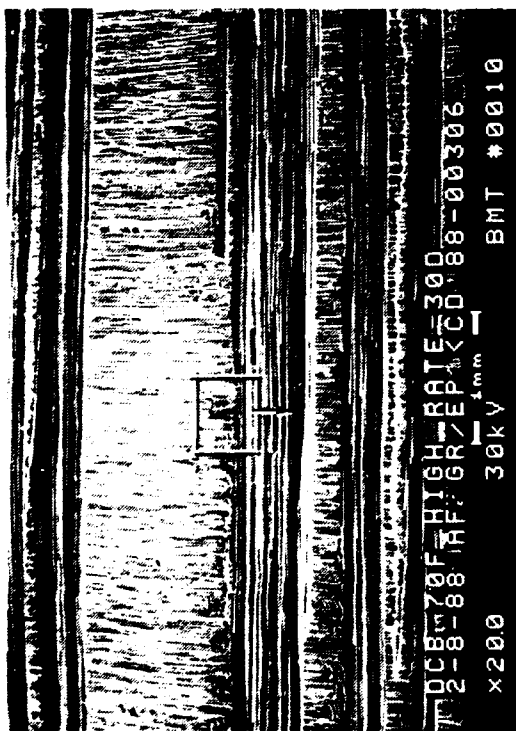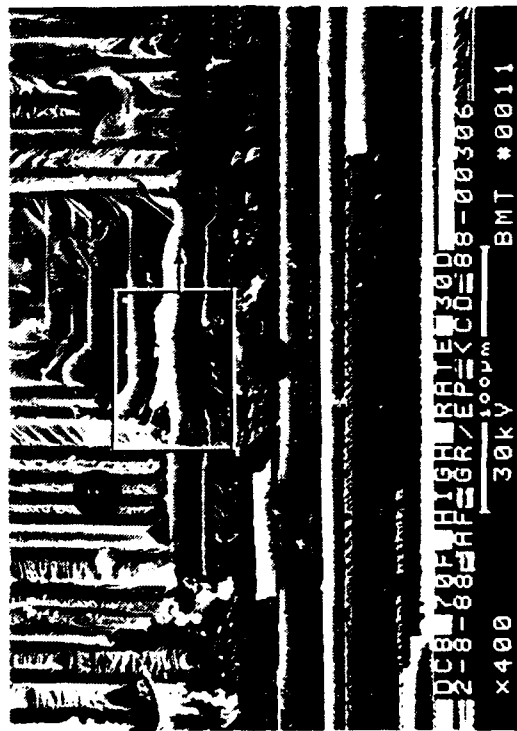
Legend:

R rivermark
H hackle
F fiber matrix separation
M matrix fracture

Mechanically induced
crack direction

Figure 4.4-33. SEM Fractographs of Interlaminar Mode I Tension, High Rate, Room Temperature Fracture (Region II)

400X

100X

FEP crack
starter
region

Region I

Region II

Mechanically
induced
crack
growth
direction

End of
controlled
fracture
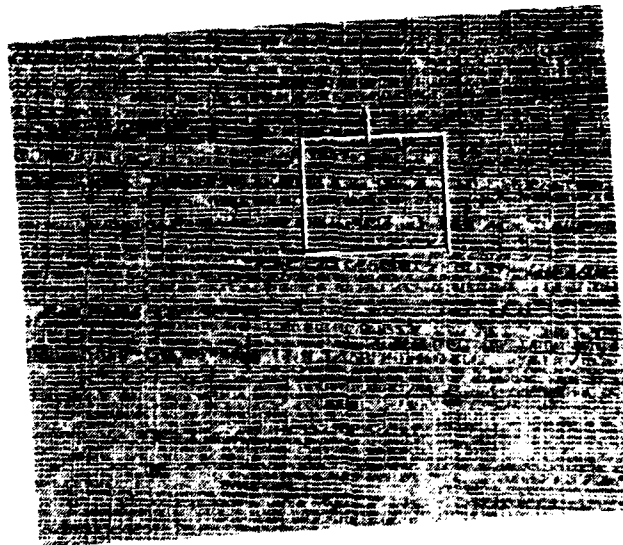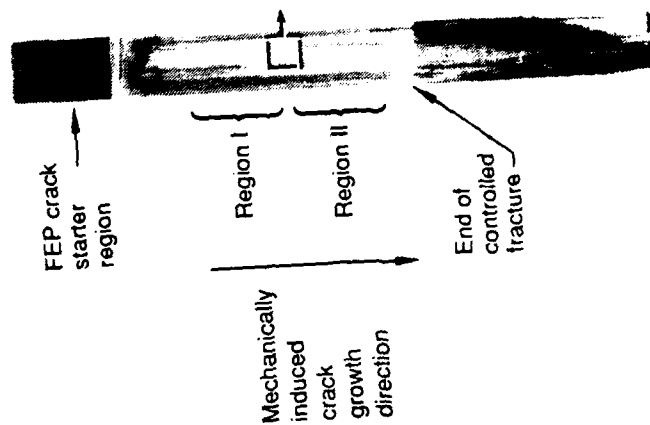
Figure 4.4-34. Optical Photomicrographs of Interlaminar Mode II Shear, High Rate, Room Temperature Fracture Between the 0/90 Plies
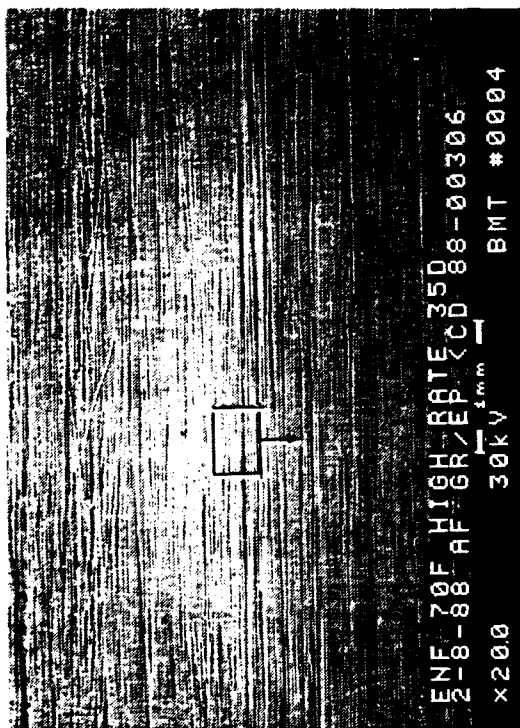
Legend:

F fiber matrix separation
H hackle
S scallop
M matrix fracture

Mechanically induced
crack direction

Figure 4.4-35. SEM Fractographs of Interlaminar Mode II Shear, Room Temperature, High Rate Fracture (Region I)
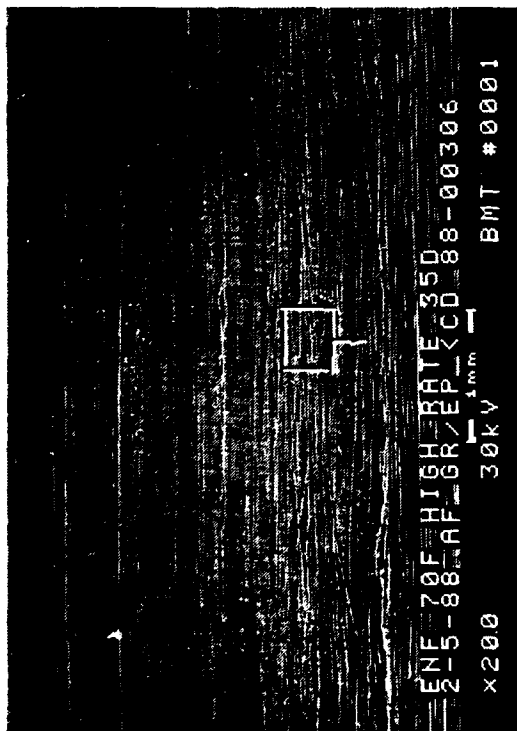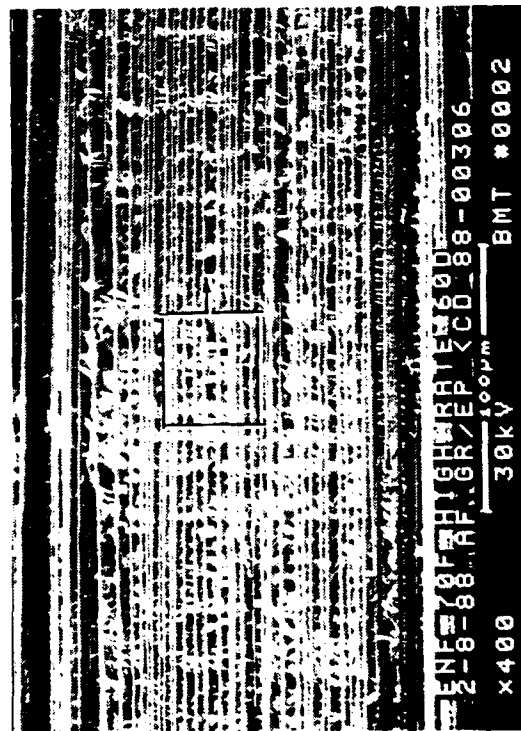
Legend:

F fiber matrix separation
H hackle
S scallop
M matrix fracture

Mechanically induced
crack direction

Figure 4.4-36. SEM Fractographs of Interlaminar Mode II Shear, Room Temperature, High Rate Fracture (Region II)

Figure 4.4-37. Extent of Impact Damage Identified by Through Transmission of Ultrasonic (TTU) Scan of Impact Specimen (AS-4/3501-6)

delamination which was exposed for further examination to determine the mode of failure in the vicinity of the impacted area. An examination was conducted under the optical microscope. In the region immediately surrounding the impact site (0.3 inch in diameter), the features were predominately hackle formations indicating Mode II shear failure. The outer perimeter of the impact site was predominately covered with rivermarks and resin microflow indicating Mode I tension failure mode (Fig. 4.4-38). The crack initiated at the impact site and propagated radially through the specimen from the tool side in both interlaminar and translaminar fracture modes (Fig. 4.4-39).

4.4.1.2 Environmental Conditions

Elevated Temperature Exposure. DCB, ENF, and N4PtT specimens were exposed to a 2000°F flame for 5 minutes.

Interlaminar Mode I Tension. Visual observation revealed feather-like, resin-starved carbon fibers on the outermost ply, which was the first exposed to the flame. The remaining 23 plies delaminated, but were kept intact by residual resin. The fracture surface created prior to exposure to the elevated temperature, appeared quite low in resin content, as evidenced by the unfilled regions between the fibers, and exhibited the smooth, glassy surface typical of Mode I tension fractures.

Optical examination showed that the fibers had just enough resin to hold them together. Due to the minimal resin content, there were no signs of rivermarks or resin microflow to indicate crack propagation direction (Fig. 4.4-40).

SEM analysis confirmed the optical results. The fibers were resin-starved to the point that individual fibers were clearly visible (Fig. 4.4-41).

Interlaminar Mode II Shear. Visual, optical, and SEM analyses revealed the same results as the interlaminar Mode I tension specimen (Figs. 4.4-42 and 4.4-43).

Translaminar Tension. Visual observation of the translaminar tension fracture surface exposed to 2000°F flame revealed a surface with rows of bare fibers. Most of the resin matrix was burned off near the fracture surface.

The bare fibers were especially visible in the SEM fractographs. Radial patterns typically seen under translaminar tension failure mode were observed on the fiber ends prior to the flame test was no longer present afterwards (Fig. 4.4-44). Instead, the fibers showed extensive cracking on their end surfaces.

(b) Crack propagation direction   400X

Key to crack growth direction arrows:
→ Mode I tension
⇄ Mode II shear
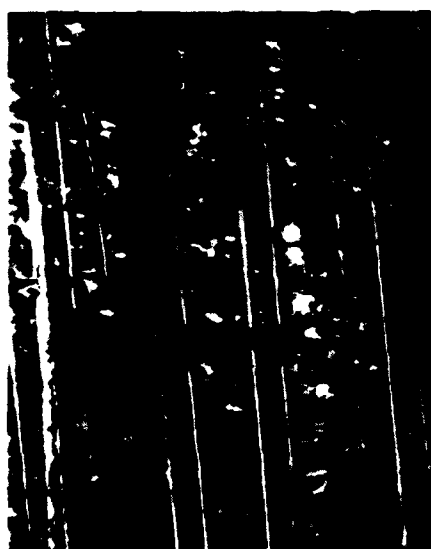
(a) Crack propagation direction   400X

(c) Crack propagation direction   400X
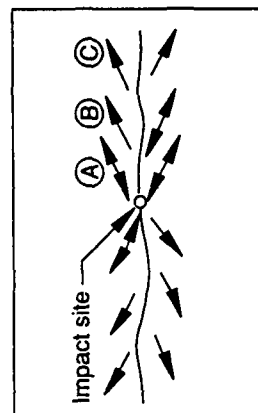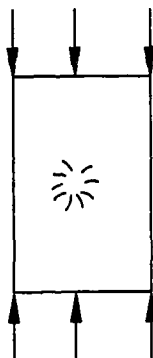
Figure 4.4-38. Optical Photomicrographs of Interlaminar Fracture of Compression-After-Impact, RT/Dry Specimen (AS-4/3501-6)

Impact site
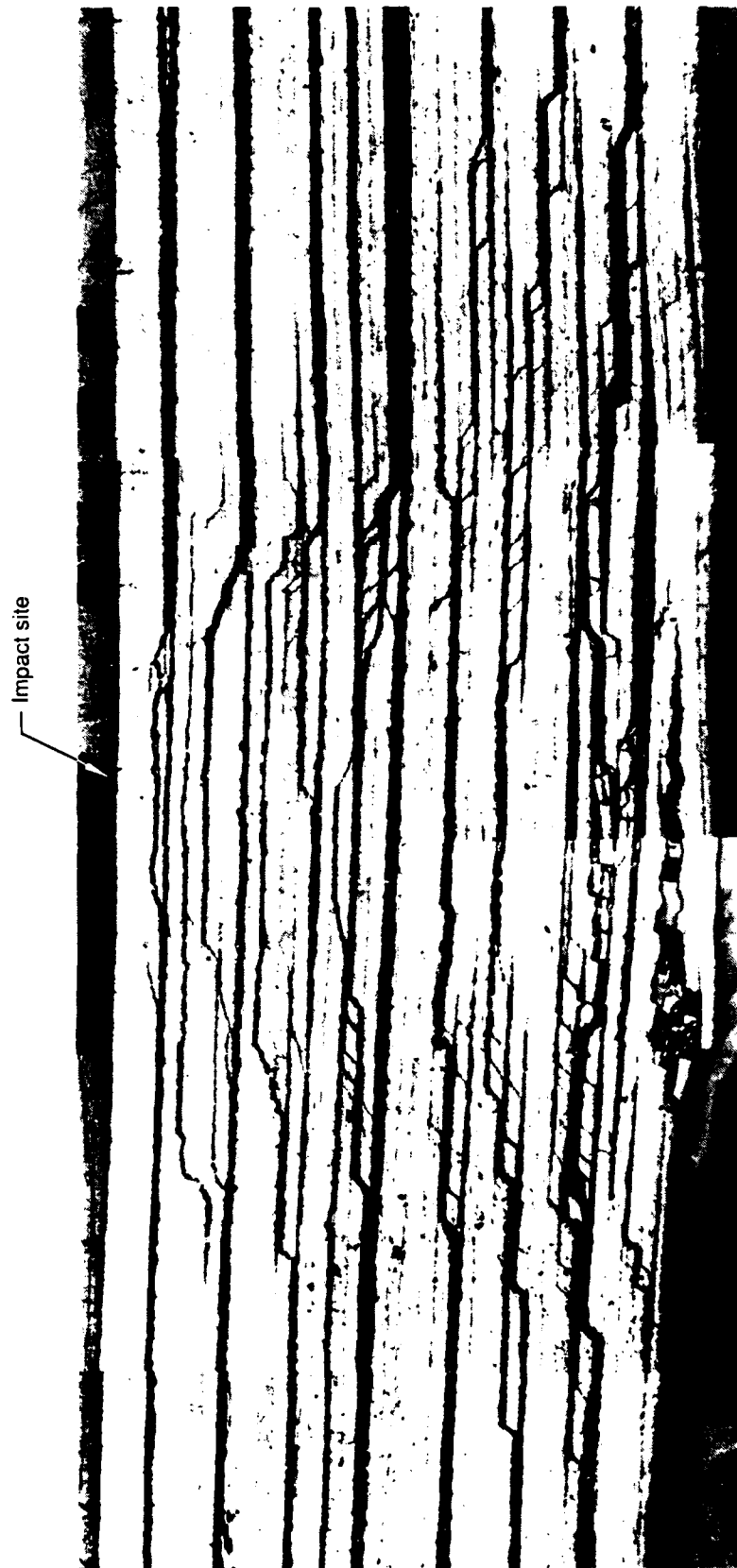
16X

Figure 4.4-39. Cross-Sectional View of Compression-After-Impact, RT/Dry Specimen (AS-4/3501-6)

FEP crack starter region

Crack growth direction
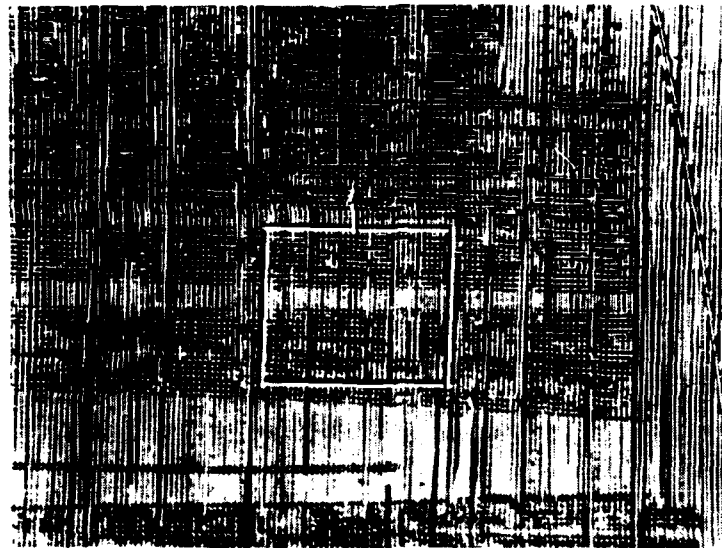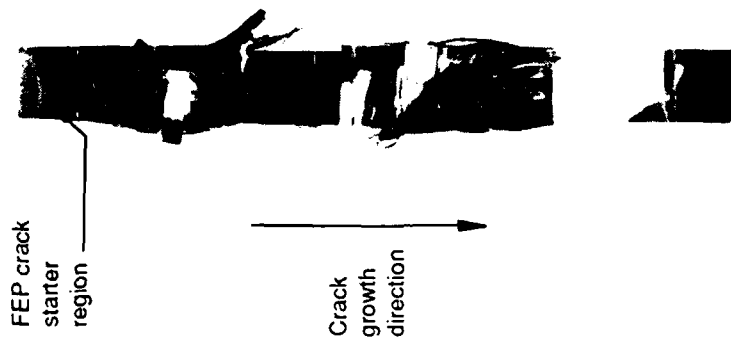
400X

400X

Figure 4.4-40. Optical Photomicrographs of Interlaminar Mode I Tension, Elevated Temperature, 0/90 Fracture
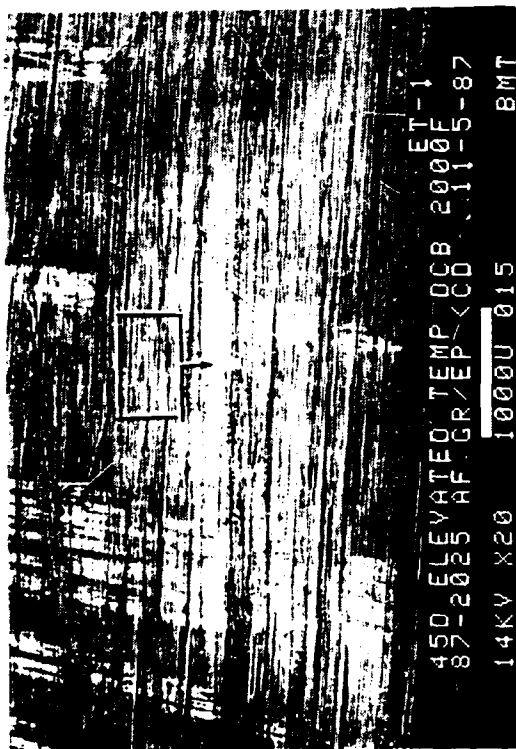
Mechanically induced crack direction
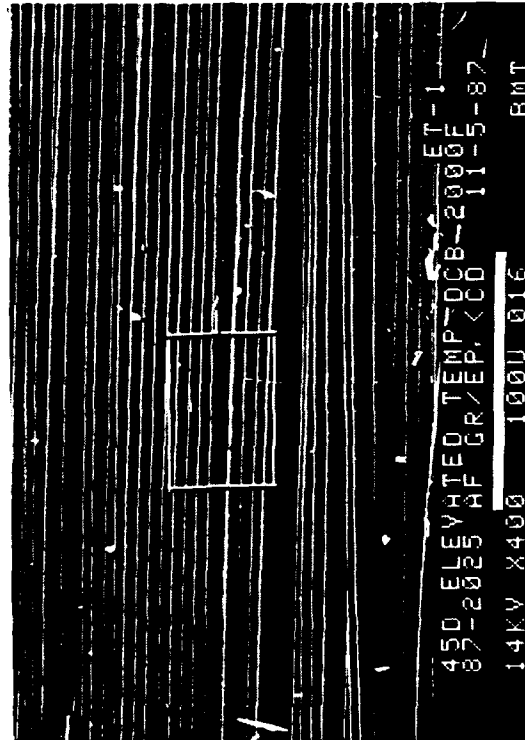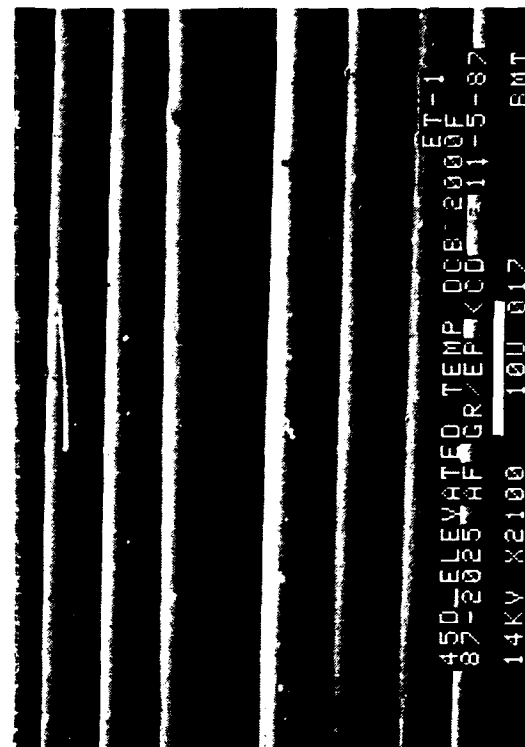
Figure 4.4.41. SEM Fractographs of Interlaminar Mode I Tension, Elevated Temperature, 0/90 Fracture
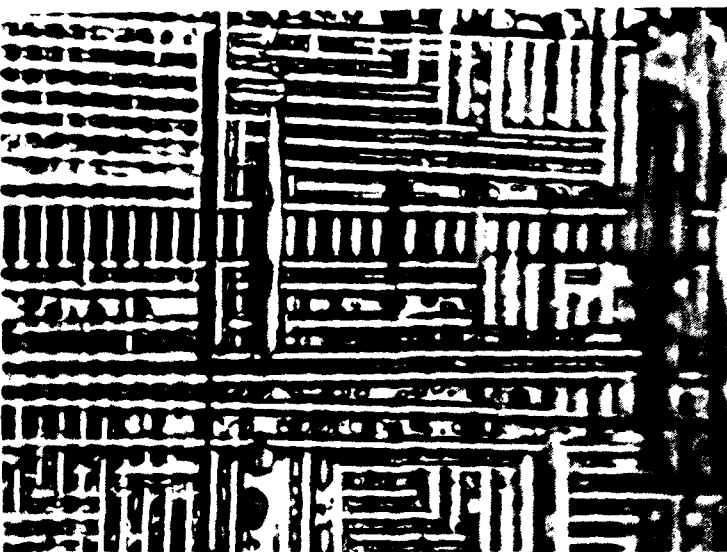
400X
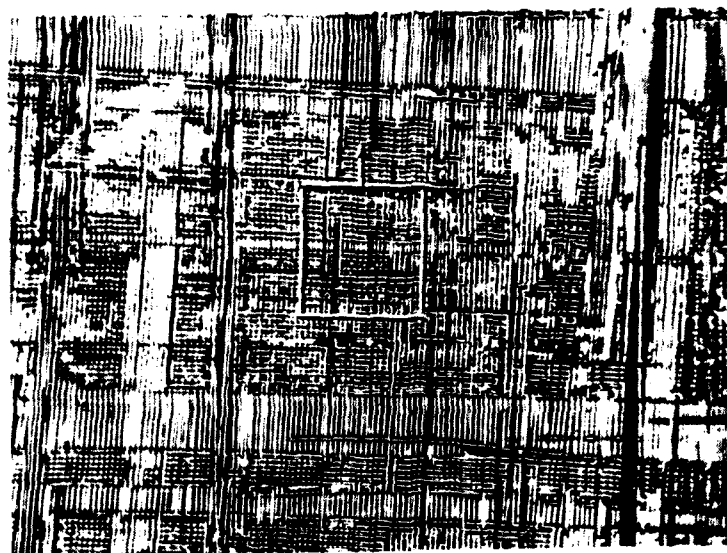
400X

FEP crack starter region

Crack growth direction

Figure 4.4-42. Optical Photomicrographs of Interlaminar Mode II Shear, Elevated Temperature, 0/90 Fracture
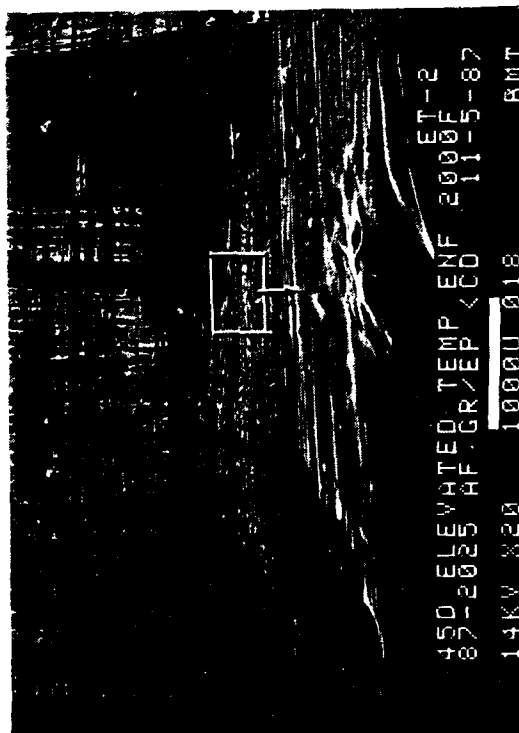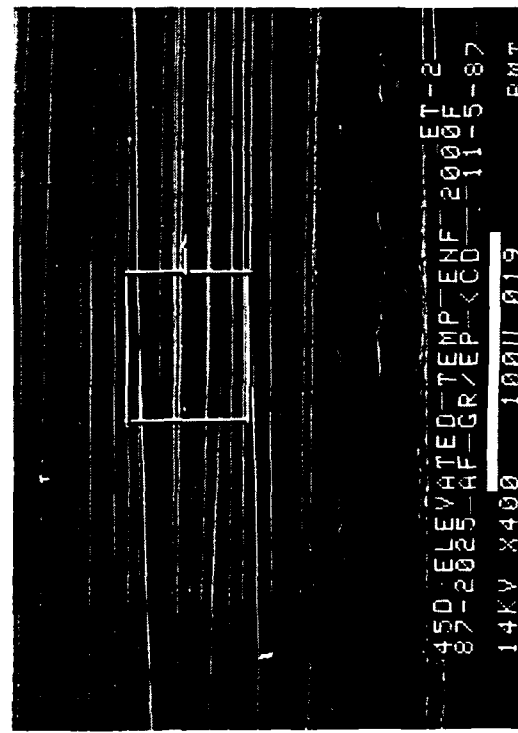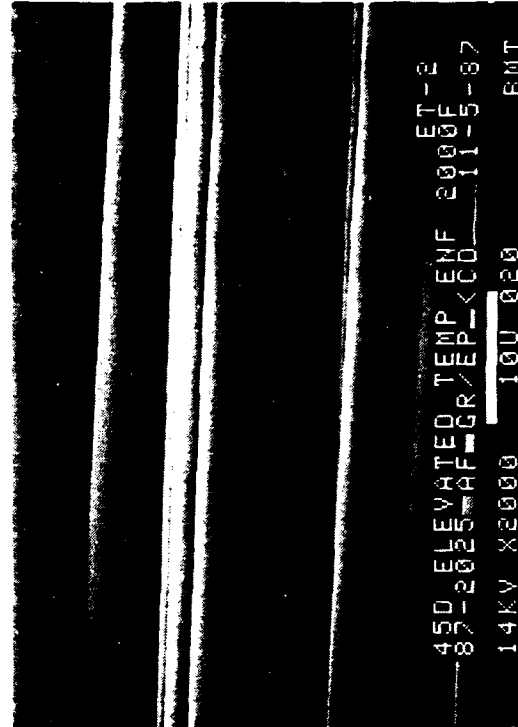
Mechanically induced crack direction

Figure 4.4-43. SEM Fractographs of Interlaminar Mode II Shear, Elevated Temperature, 0/90 Fracture
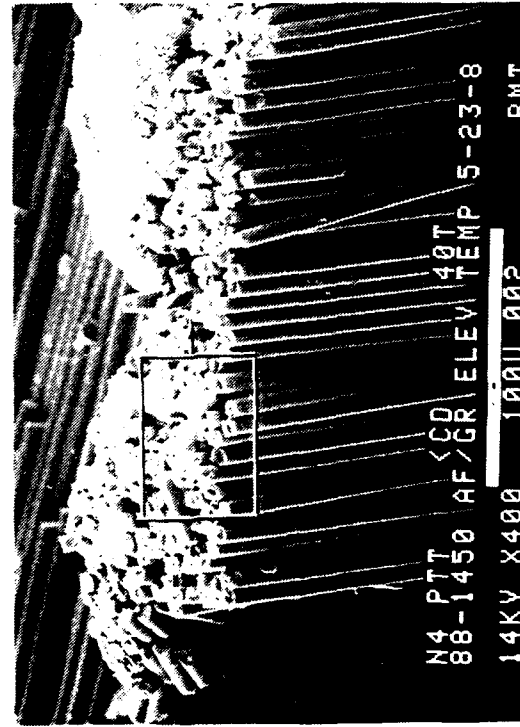
Mechanically induced
crack direction →

(a) 40 degree tilt 20X

(b) 40 degree tilt 400X

(c) 0 degree tilt 2,000X

Figure 4.4-44. SEM Fractographs of Elevated Temperature, Translaminar Tension Fracture

Water Immersion and Humidity. DCB, ENF, and N4PtT specimens were immersed in water at 160°F for 4 weeks; similar specimens were subjected to 100% relative humidity (RH) at 160°F for 4 weeks.

Interlaminar Mode I Tension. Visual observation of the water immersion and high humidity specimens revealed smooth glassy fracture surfaces as commonly seen in interlaminar Mode I tension specimens at RT/dry conditions (Fig. 4.4-45 and 4.4-46). At higher magnifications under the optical microscope, rivermarks and resin microflow were seen. Work done in the previous contract, C-5010, determined that these features reveal an overall crack propagation direction. However, it was noted that the rivermarks in these specimens were not as distinct as they were in the RT/dry specimens (Fig. 4.4-47 and 4.4-48). In general, the humidity and water immersion specimens exhibited nearly identical fracture characteristics.

Interlaminar Mode II Shear. Visual observation of the fracture surface revealed a flat but milky appearance when the specimen was held at an angle to the light. The milky appearance is due to the hackles created by the shear loading and observed both optically (Figs. 4.4-49 and 4.4-50) and with the SEM. Under higher magnification (SEM), the hackles were seen to lack consistency in their shape (Fig. 4.4-51 and 4.4-52). Under dry conditions, the platelets were tilted in a single direction and had a similar shape, but in these wet specimens the features varied depending on their location.

Translaminar Tension. Visual and optical observations revealed little except for evidence that the fibers were protruding from the through-thickness fracture. SEM analysis of these fiber ends was performed. At high magnification the fiber ends exhibited the unique radial patterns observed in the previous program. These radial patterns indicate the localized crack direction for each individual fiber (Fig. 4.4-53 through 4.4-54). The sum of the individual fiber end radial patterns provides an overall crack propagation direction. There were some indications of fiber pullout, but in general, the fiber/matrix interface showed good adhesion.

4.4.1.3 Process Deficiencies

Undercured. Undercured DCB, ENF, and N4PtT specimens were examined visually, optically and under the SEM.

Interlaminar Mode I Tension. Visual observation of the fracture surface revealed the same smooth, glassy fracture surface commonly seen in interlaminar Mode I tension specimens at RT/dry conditions. The laminate showed poor quality in its fiber/matrix

400X

100X

0.42X

FEP crack
starter
region

Crack
growth
direction

End of
controlled
fracture
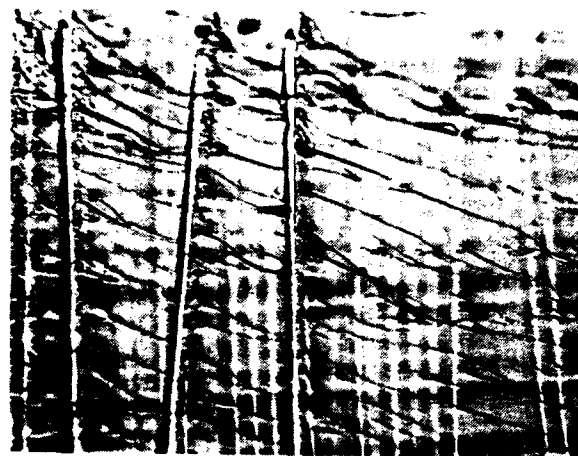
Figure 4.4-45. Optical Photomicrographs of Interlaminar Mode I Tension, 0/90 Fracture After Water Immersion (160 F)

FEP crack
starter
region

Mechanically
induced crack
growth direction

End of
controlled
fracture

0.42X

100X
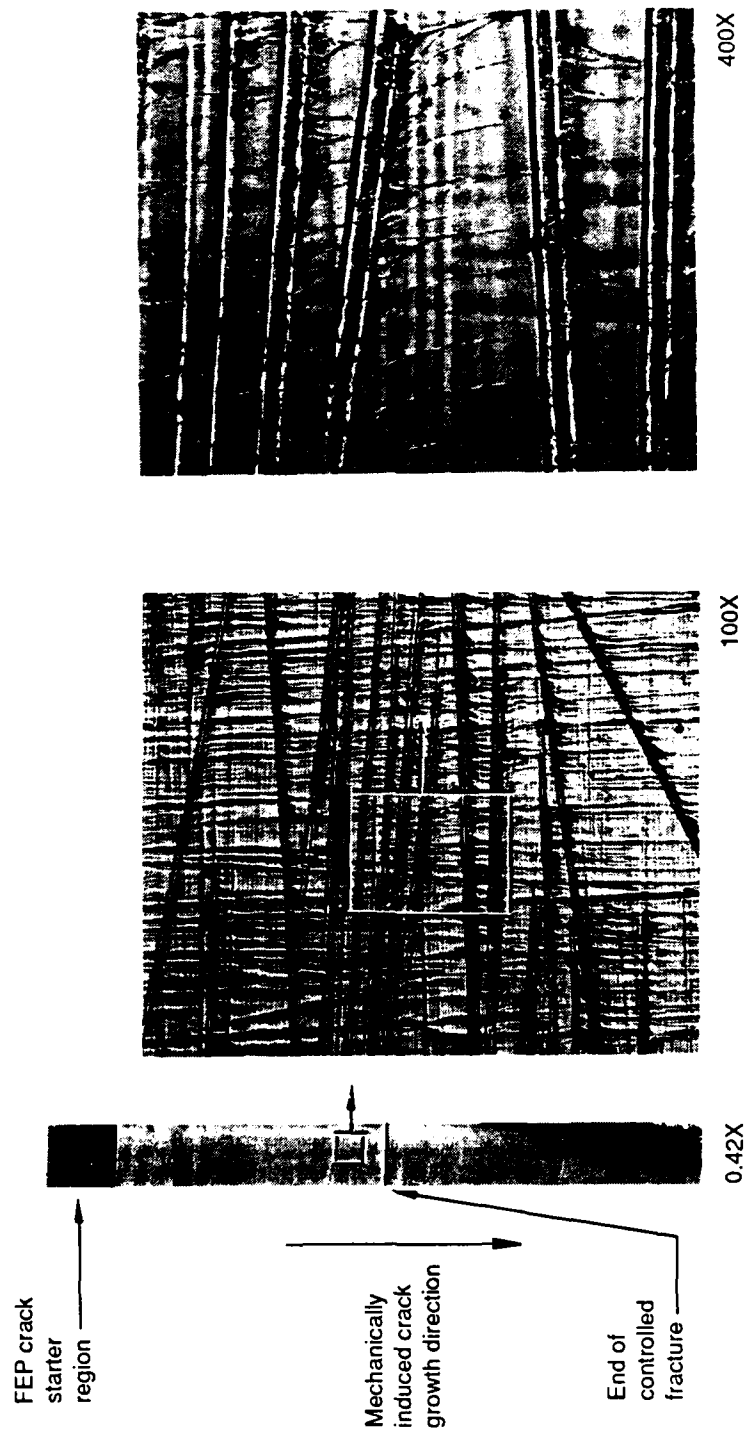
400X

Figure 4.4-46. Optical Photomicrographs of Interlaminar Mode I Tension, 0/90 Fracture After Exposure to Humidity (160 F)
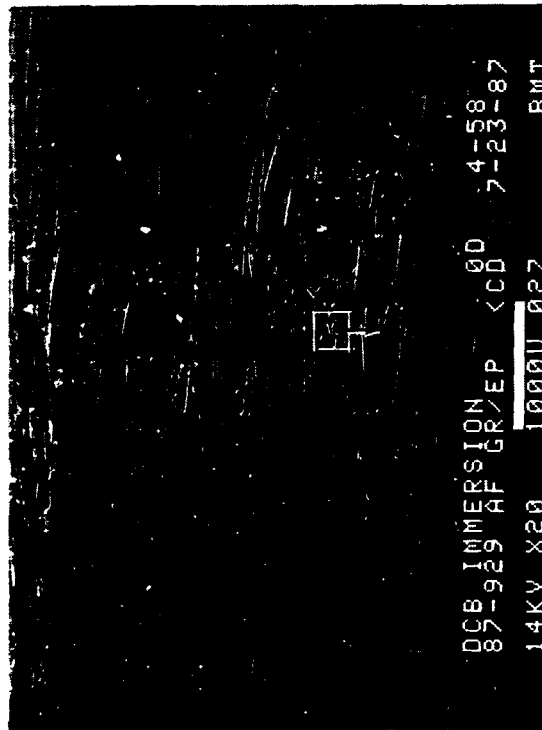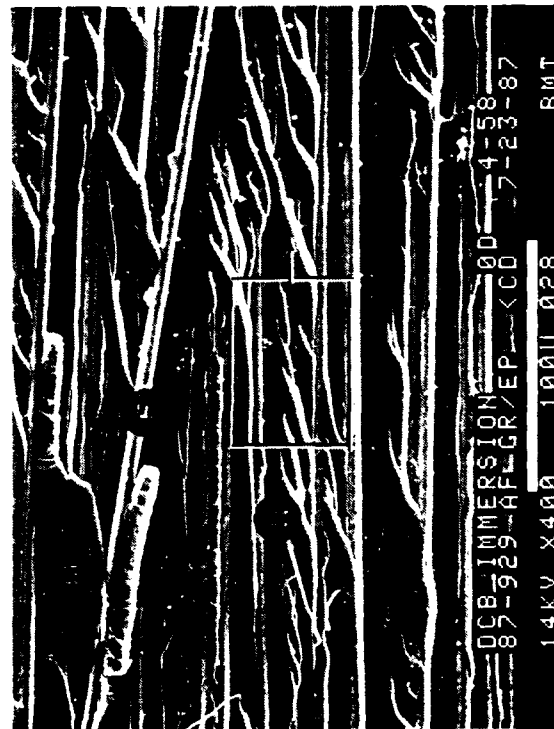
Legend:

M matrix fracture
F fiber matrix separation
R rivermarks

Mechanically induced
crack direction

Figure 4.4-47. SEM Fractographs of Interlaminar Mode I Tension, 0/90 Fracture After Water Immersion (160 F)
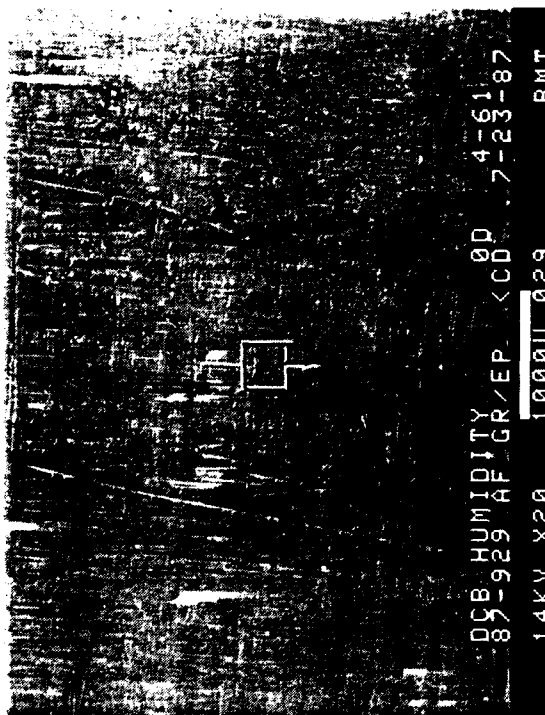
Legend:

M matrix fracture
F fiber matrix separation
R rivermarks

Mechanically induced
crack direction
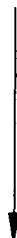
Figure 4.4-48. SEM Fractographs of Interlaminar Mode I Tension, 0/90 Fracture After Exposure to Humidity (160 F)

400X

100X

0.55X

FEP crack starter region

Mechanically induced crack growth direction

End of controlled fracture
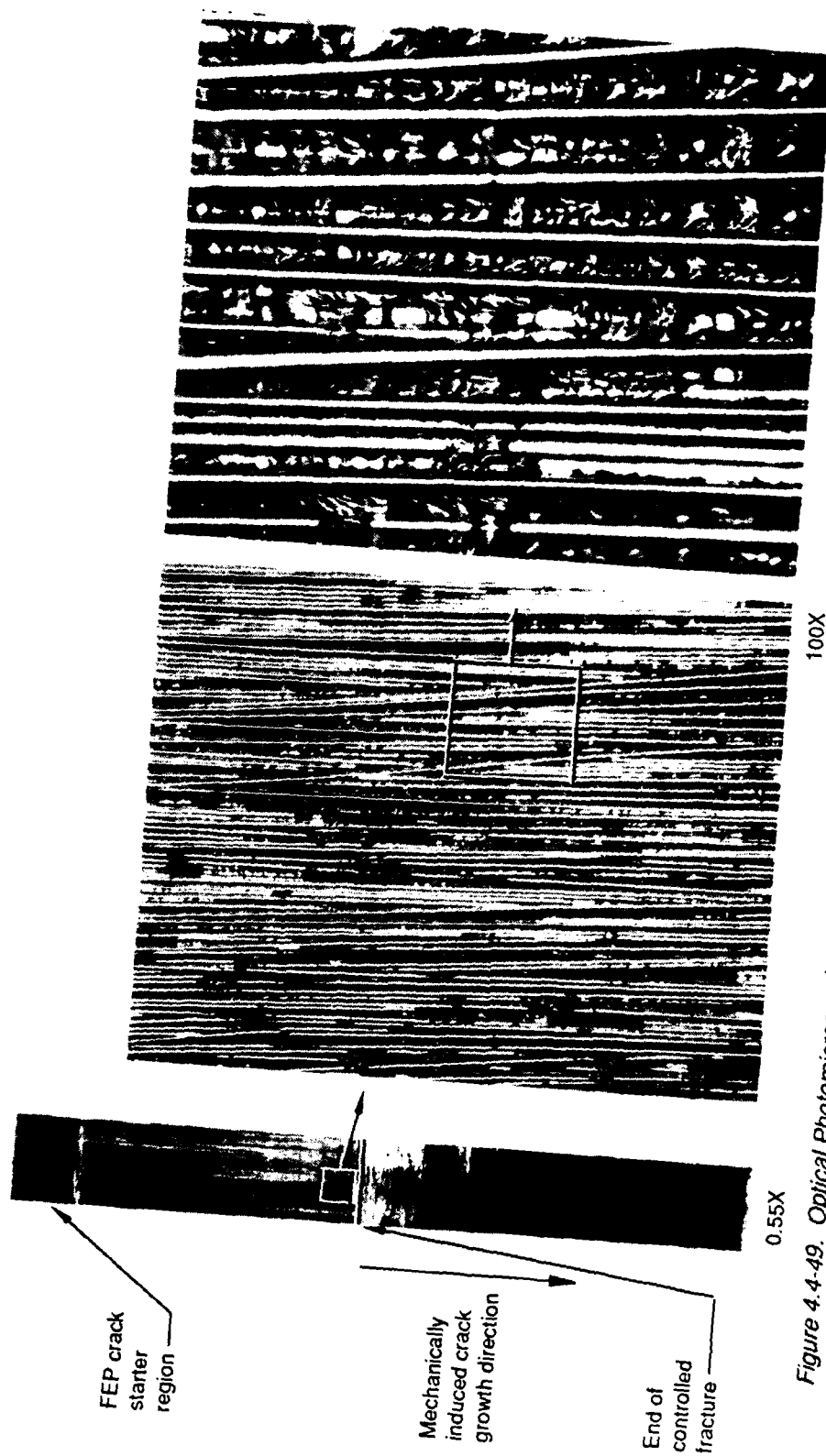
Figure 4.4-49. Optical Photomicrographs of Interlaminar Mode II Shear, 0/90 Fracture After Water Immersion (160 F)

400X

100X

0.44X

FEP crack
starter
region

Mechanically
induced crack
growth direction

End of
controlled
fracture
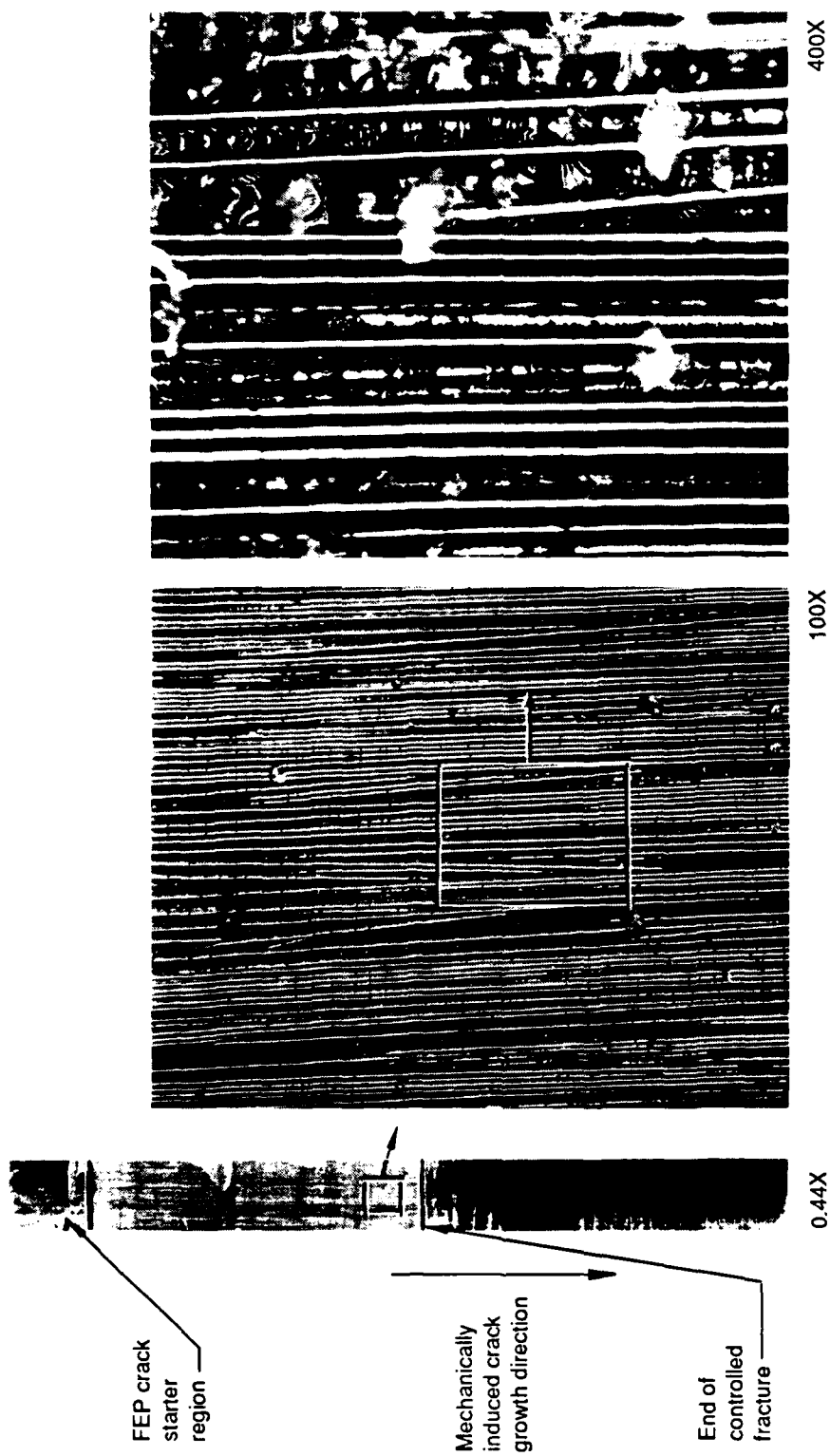
Figure 4.4-50. Optical Photomicrographs of Interlaminar Mode II Shear, 0/90 Fracture After Exposure to Humidity (160 F)

Legend:

F fiber matrix separation
H hackles
R rivermarks
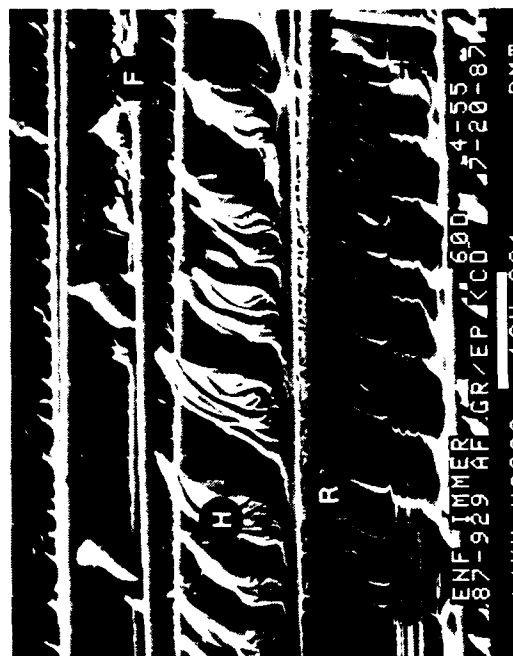
Mechanically induced
crack direction →

Figure 4.4-51. SEM Fractographs of Interlaminar Mode II Shear, 0/90 Fracture After Water Immersion (160 F)

Legend:

F fiber matrix separation
H hackles
R rivermarks

Mechanically induced
crack direction ⟶
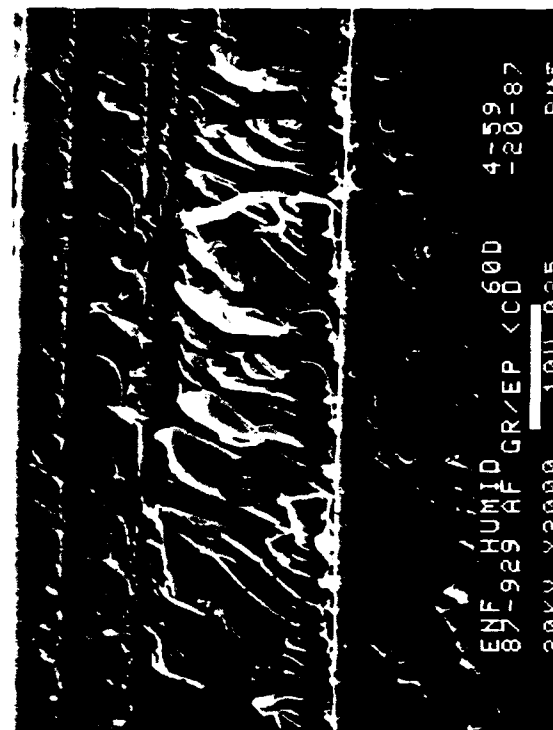
Figure 4.4-52. SEM Fractographs of Interlaminar Mode II Shear, 0/90 Fracture After Exposure to Humidity (160 F)
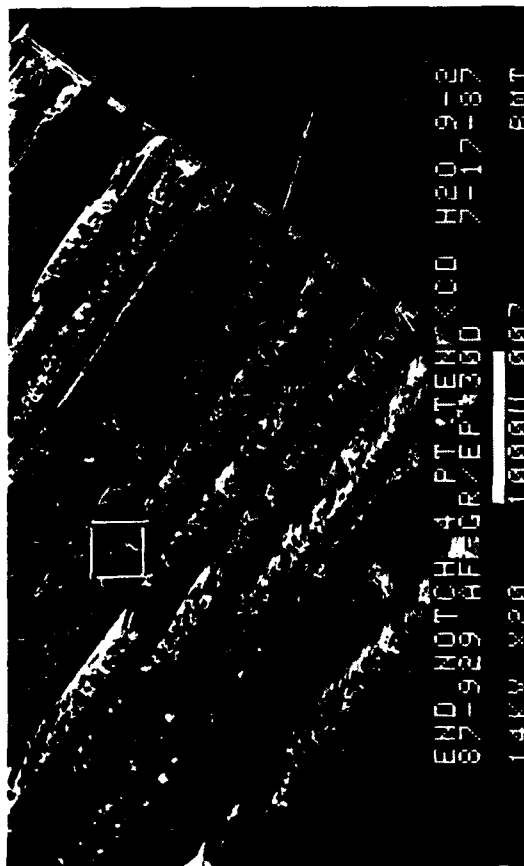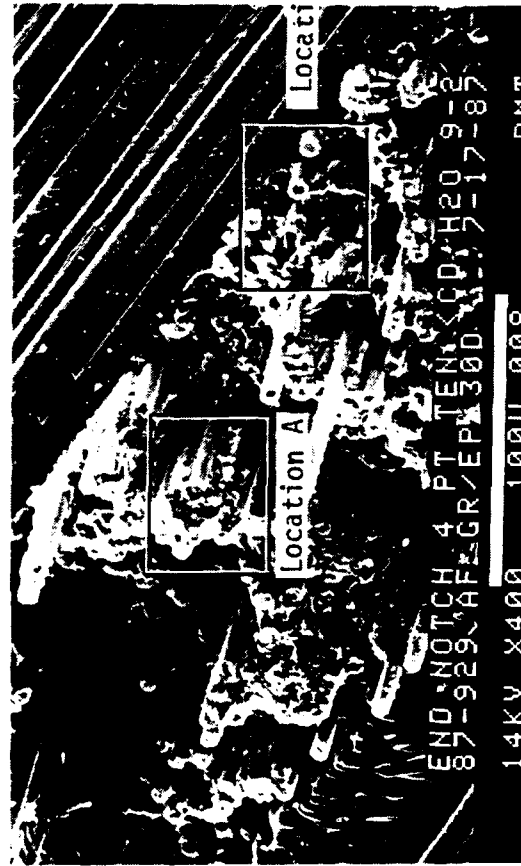
Note:
Location a is magnified in (c)
Location b is magnified in (d)

Mechanically induced
crack direction

(a)

20X

30 degree tilt

Location B

Location A

(b)

400X

30 degree tilt

Figure 4.4-53. SEM Fractographs of Translaminar Tension Fracture After Water Immersion (160 F)

Mechanically induced crack direction

(c) Typical fracture along the fibers

30 degree tilt

(d) Illustration of crack mapping using the radial patterns on the fiber ends

30 degree tilt

Figure 4.4-53. *SEM Fractographs of Translaminar Tension Fracture After Water Immersion (160 F) (Concluded)*
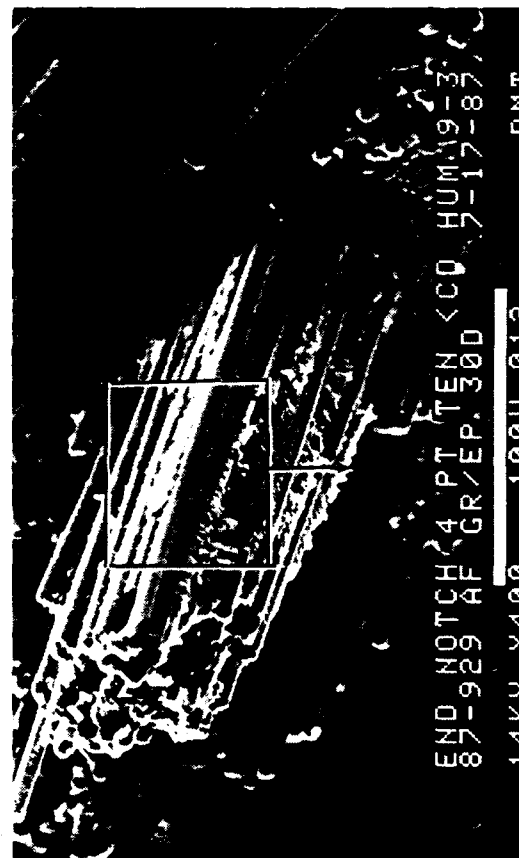
Illustration of crack mapping using the radial patterns on the fiber ends

Mechanically induced crack direction

(a)

20X

30 degree tilt

(b)

400X

30 degree tilt

Figure 4.4-54. SEM Fractographs of Translaminar Tension Fracture After Exposure to 100% Relative Humidity (160 F)

Illustration of crack mapping using
the radial patterns on the fiber ends

Mechanically induced
crack direction

2,000X

(c)

30 degree tilt

2,000X

(d)

30 degree tilt

Figure 4.4-54. SEM Fractographs of Translaminar Tension Fracture After Exposure to 100% Relative Humidity (160 F) (Concluded)

adhesion. The fibers were easily separated from each other and exhibited a feathery texture. Because of the undercuring process, some of the fibers never reached the state of wetting, causing loose fibers within the laminate. At higher magnifications, rivermarks and resin microflow were seen (Fig. 4.4-55).

The SEM analysis revealed a fracture surface typically seen in an RT/dry specimen (Fig. 4.4-56). However, optical observation showed many stray fibers indicating the lack of fiber wetting from the undercuring process. The rivermarks were clearly observed and showed the overall crack propagation direction.

<u>Interlaminar Mode II Shear</u>. Visual observation of the fracture surface revealed a flat but milky appearance when the specimen was held at an angle to the light. Like the interlaminar Mode I tension specimen, the fibers appeared to have a feathery texture and the laminate quality was poor. At higher magnifications, hackles were observed (Fig. 4.4-57).

The SEM analysis revealed a fracture surface with fiber/matrix separation characterized by an adhesive-type fracture (Fig. 4.4-58). This was evidenced by the practically featureless surface. As in the Mode I tension specimens, the lack of fiber wetting caused loose fibers to occur along the fracture surface.

<u>Translaminar Tension</u>. The specimens did not fracture as intended but rather buckled. The undercuring caused insufficient cross linking in the polymer which lessened the ability of the matrix to support the fiber (Fig. 4.4-59).

Double-cured. DCB, ENF, and N4ptT specimens prepared by double curing, were examined visually, optically, and under the SEM.

<u>Interlaminar Mode I Tension</u>. Visual observation of the fracture surface revealed the smooth, glassy fracture surface typical of an interlaminar Mode I tension specimen at RT/dry conditions. At higher magnifications, rivermarks and resin microflow were seen (Fig. 4.4-60).

The SEM analysis revealed a typical RT/dry fracture surface. It is thought that additional cross-linking occurs in double-cured specimens causing the material to become brittle (Fig. 4.4-61). The visual observation of the fracture was inconclusive although it revealed a dry surface characteristic of a brittle material. The rivermarks were clearly observed and showed the overall crack propagation direction.

<u>Interlaminar Mode II Shear</u>. Visual observation of the fracture surface revealed the typical flat but milky appearance when the sample was held at an angle to the light. At

400X

100X

.38X

FEP crack starter region

Mechanically induced crack growth direction

End of controlled fracture
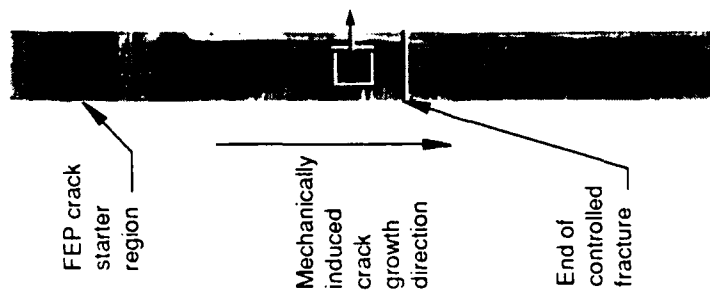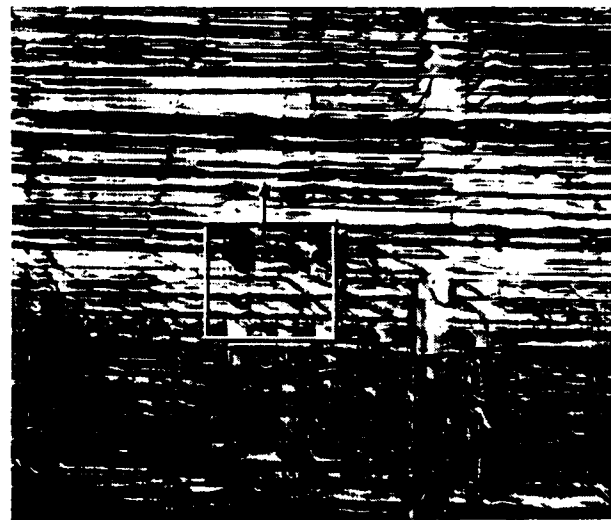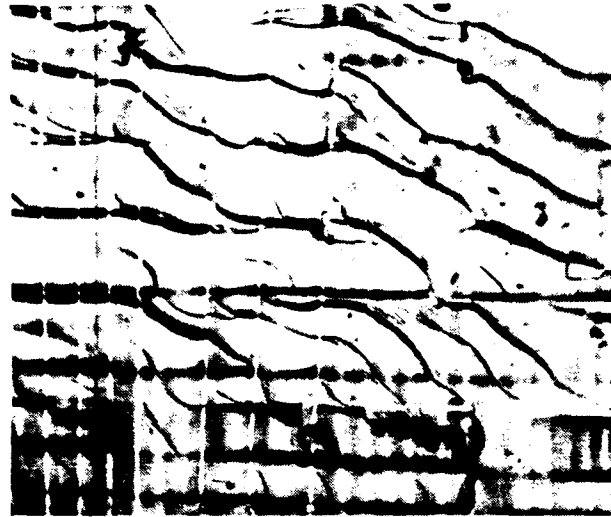
Figure 4.4-55. Optical Photomicrographs of Interlaminar Mode I Tension, 0/90 Fracture of Undercured Specimen
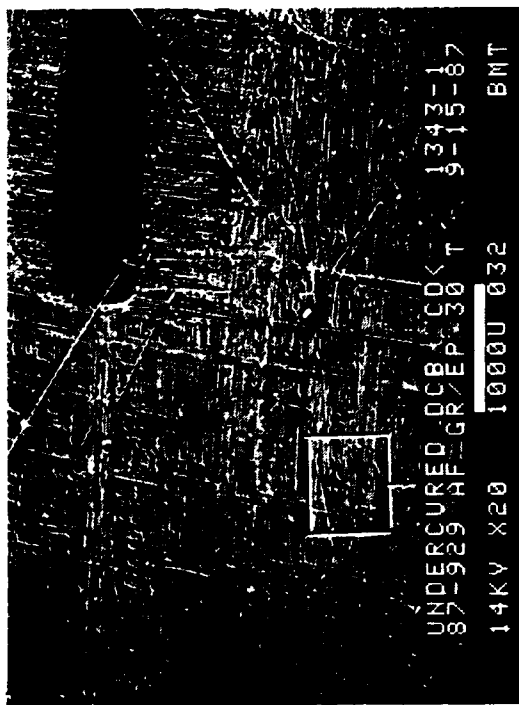
Legend:

F   fiber matrix separation
H   hackles
R   rivermarks

Mechanically induced
crack direction
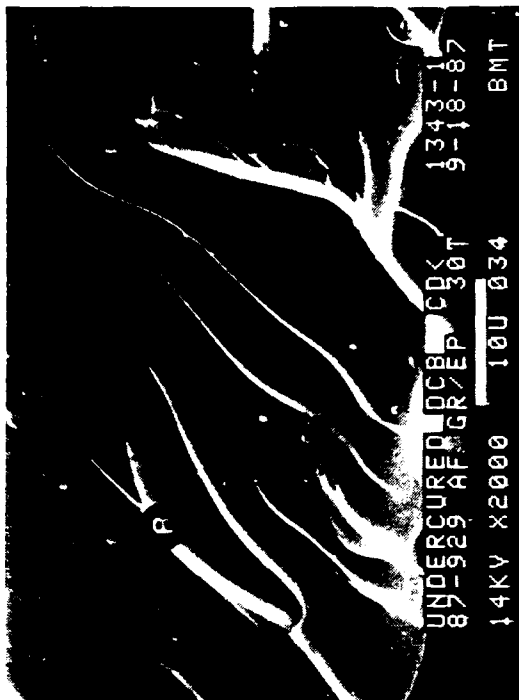
Figure 4.4-56. SEM Fractographs of Interlaminar Mode I Tension, 0/90 Fracture of Undercured Specimen
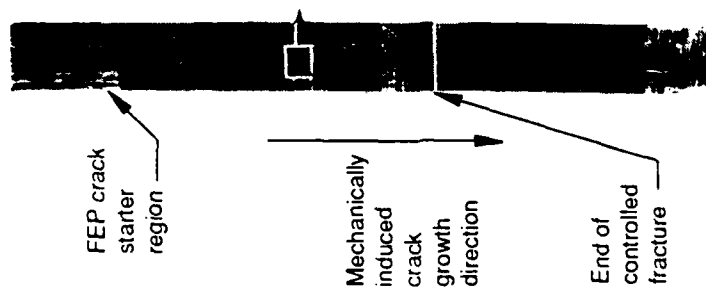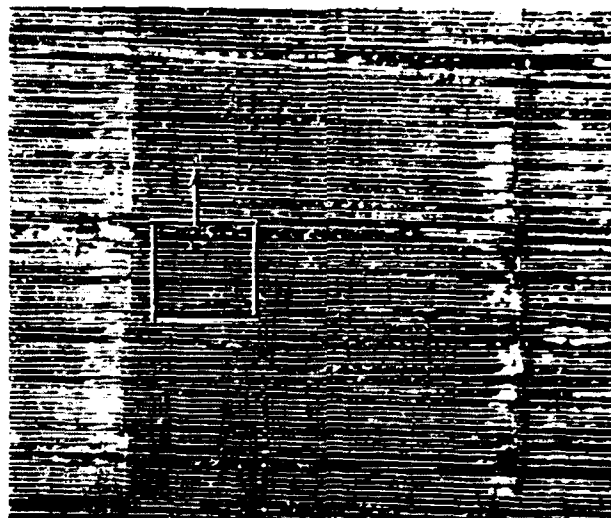
Figure 4.4-57. Optical Photomicrographs of Interlaminar Mode II Shear, 0/90 Fracture of Undercured Specimen

FEP crack
starter
region

Mechanically
induced
crack
growth
direction

End of
controlled
fracture

400X

100X
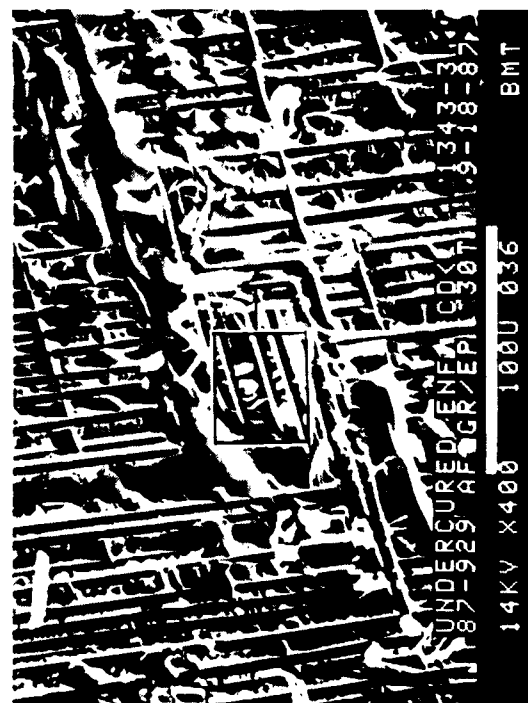
.38X

Legend:

F fiber matrix separation
H hackles
R rivermarks

Mechanically induced
crack direction →

Figure 4.4-58. SEM Fractographs of Interlaminar Mode II Shear, 0/90 Fracture of Undercured Specimen

Location of expanded figure (b)

1.6X

(a) Overview

Delamination and
intra-ply cracks

16X

Overlapping fibers indicate
compression buckling
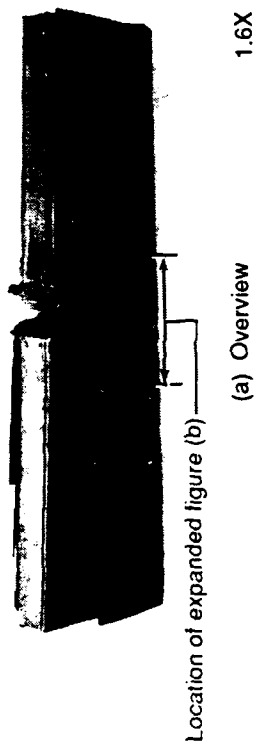
(b) Region on the edge opposite to the notched side

Figure 4.4-59. Optical Photomicrographs of Damaged Region of Translaminar Tension Fracture of Undercured Laminate
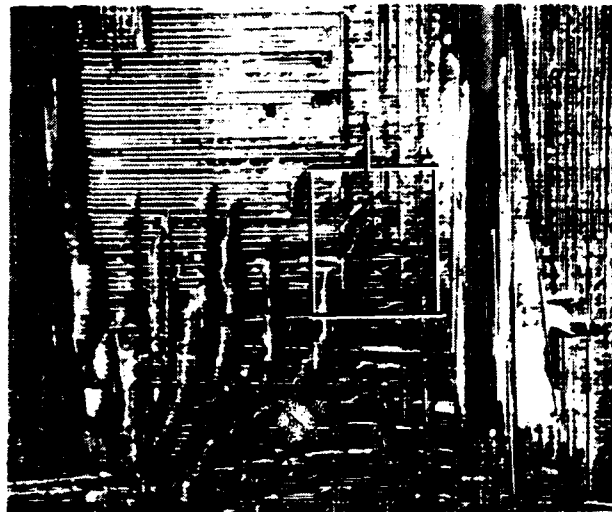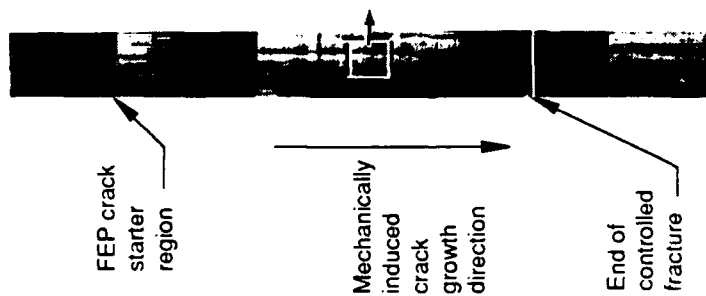
400X

100X
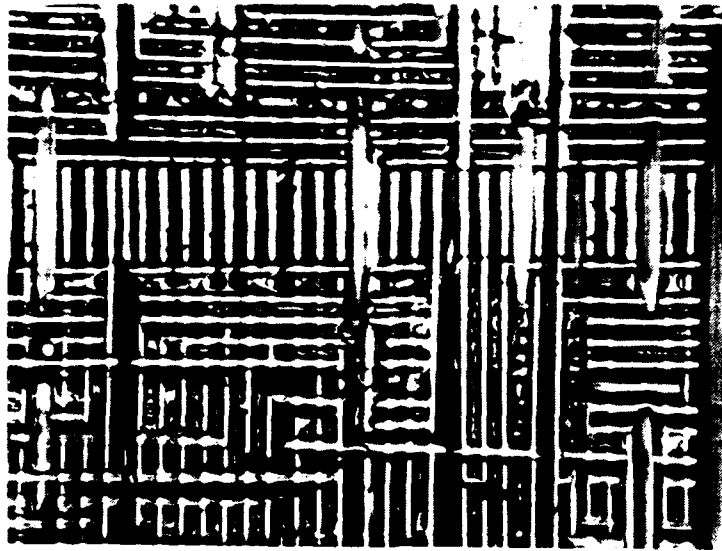
Figure 4.4-60. Optical Photomicrographs of Interlaminar Mode I Tension, 0/90 Fracture of Overcured Specimen

FEP crack starter region

Mechanically induced crack growth direction

End of controlled fracture
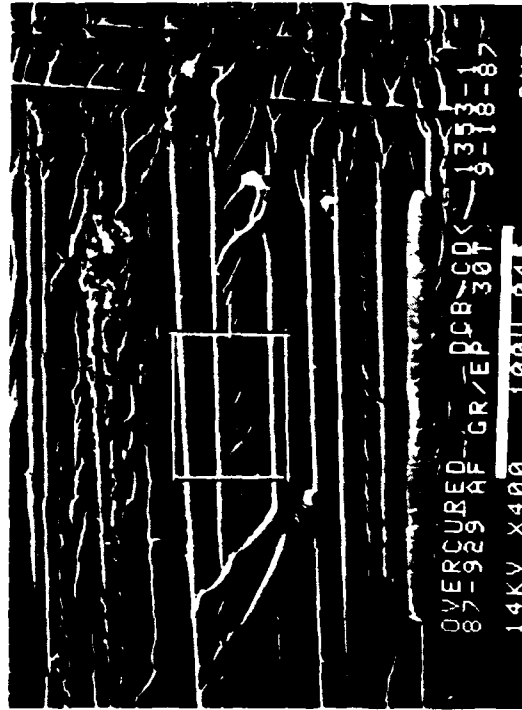
Legend:

F fiber matrix separation
H hackles
R rivermarks

Mechanically induced
crack direction
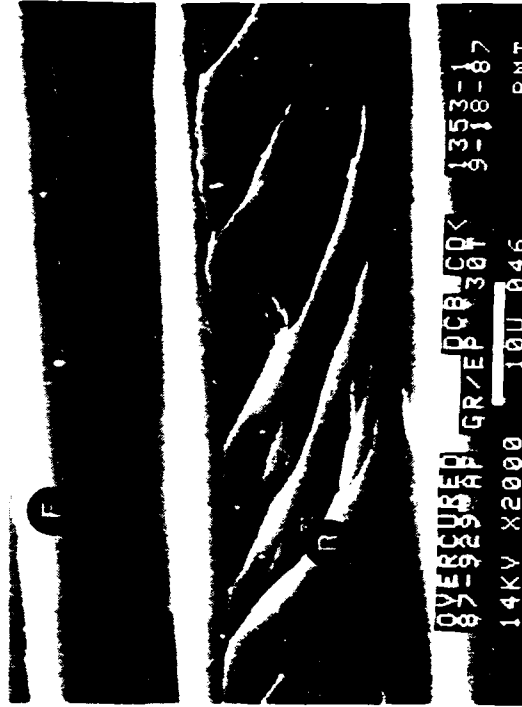
Figure 4.4-61. SEM Fractographs of Interlaminar Mode I Tension, 0/90 Fracture of Overcured Specimen

higher magnifications, hackles were observed (Fig. 4.4-62).

The SEM analysis revealed a typical RT/dry fracture surface with many hackles between the fibers. The hackles were scattered along the fracture surface without any orderly arrangement (Fig. 4.4-63).

Translaminar Tension. Visual and optical observations revealed a typical translaminar fracture with protruding fibers. The fiber/matrix interface showed good adhesion. The radial patterns on the fiber ends were clearly seen and the crack direction was easily determined (Fig. 4.4-64).

High Resin Content. DCB, ENF, and N4ptT fractures of samples with higher than normal resin content were tested.

Interlaminar Mode I Tension. Visual observation of the fracture surface revealed a typical smooth, glassy fracture commonly seen in interlaminar Mode I tension specimens at RT/dry condition as shown in Figure 4.4-65. At higher magnification, rivermarks and resin mircoflow were seen. The SEM analysis revealed a fracture surface with rivermarks as typically observed in RT/Dry specimens (Fig. 4.4-66).

Interlaminar Mode II Shear. Visual observation of the fracture surface revealed a flat, milky appearance when held at an angle to the light. Unlike the low resin content specimens, these specimens showed complete wet-out at the resin/matrix interface (Fig. 4.4-67).

The SEM analysis revealed a fracture surface typically observed in RT/dry specimens (Fig. 4.4-68).

Translaminar Mode I Tension. Visual and optical observations revealed large fiber pullout regions due to uneven distribution of the added resin film. SEM fractograph showed a cohesive resin fracture at the fiber/matrix interface due to the excessive resin content. The radial patterns on the fiber ends were clearly seen (Fig. 4.4-69).

Low Resin Content. DCB, ENF, and N4ptT fractures of samples with low resin content were examined as with other processing deficient samples.

Interlaminar Mode I Tension. Visual observation of the fracture surface revealed the smooth, glassy fracture surface typical of interlaminar Mode I tension specimens at RT/dry. The only noticeable difference was the fiber splinters resulting from the insufficient degree of resin wet-out at the fiber/matrix interface. At higher magnification under the optical microscope, a typical region of low resin content showed lack of fracture features such as rivermarks to indicate the overall crack direction (Fig. 4.4-70).

400X

100X

Figure 4.4-62. Optical Photomicrographs of Interlaminar Mode II Shear, 0/90 Fracture of Overcured Specimen

FEP crack starter region

Mechanically induced crack growth direction
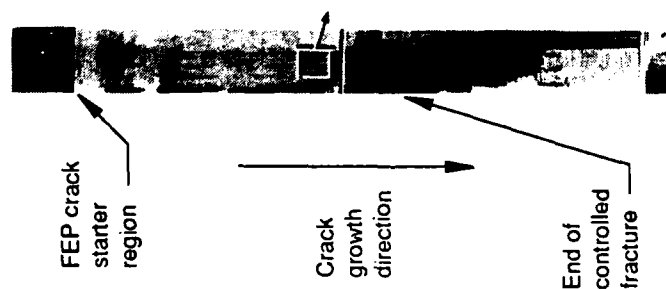
End of controlled fracture

Legend:

F fiber matrix separation
H hackles
R rivermarks

Mechanically induced
crack direction

Figure 4.4-63. Sem Fractographs of Interlaminar Mode II Shear, 0/90 Fracture of Overcured Specimen

Mechanically induced crack direction

(a)

40 degree tilt

20X

(b)

40 degree tilt

400X

Figure 4.4-64. SEM Fractographs of Translaminar Tension Fracture of Overcured Specimen
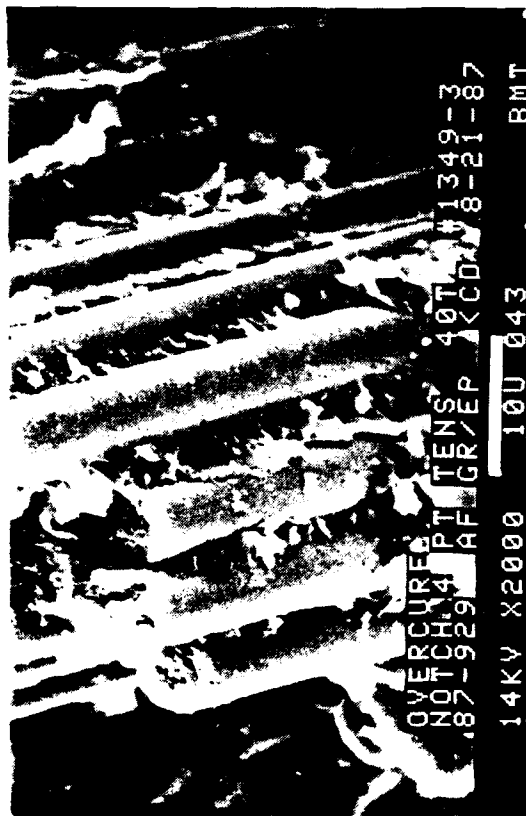
Mechanically induced crack direction

(c) Typical fracture along the fibers
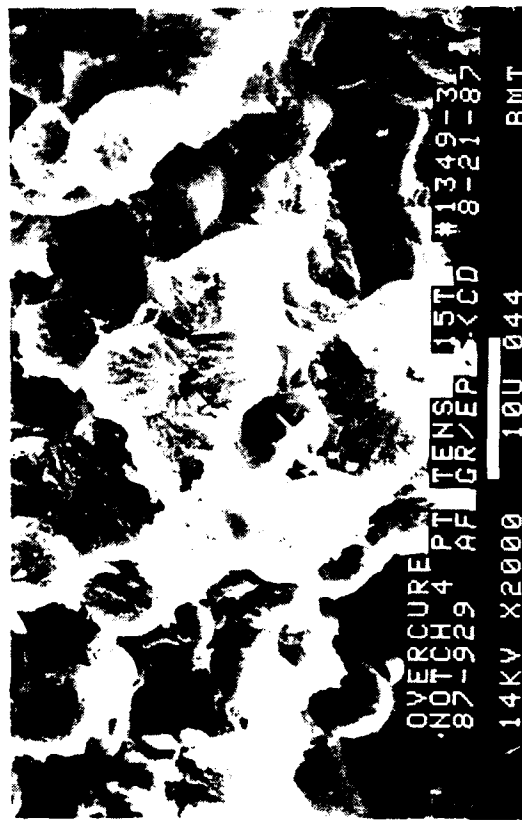
40 degree tilt

(d) Illustration of crack mapping using the radial patterns on the fiber ends

15 degree tilt

Figure 4.4-64. SEM Fractographs of Translaminar Tension Fracture of Overcured Specimen (Concluded)

400X

100X

FEP crack starter region

Mechanically induced crack growth direction

End of controlled fracture

Figure 4.4-65. Optical Photomicrographs of Interlaminar Mode I Tension, 0/90 Fracture of High Resin Content Specimen

Legend:

M matrix fracture
F fiber/matrix separation
R rivermarks

Mechanically induced
crack direction

30 degree tilt

20X

400X

30 degree tilt

30 degree tilt

Figure 4.4-66. *SEM Fractographs of Interlaminar Mode I Tension, 0/90 Fracture of High Resin Content Specimen*

400X

100X

FEP crack starter region

Mechanically induced crack growth direction

End of controlled fracture
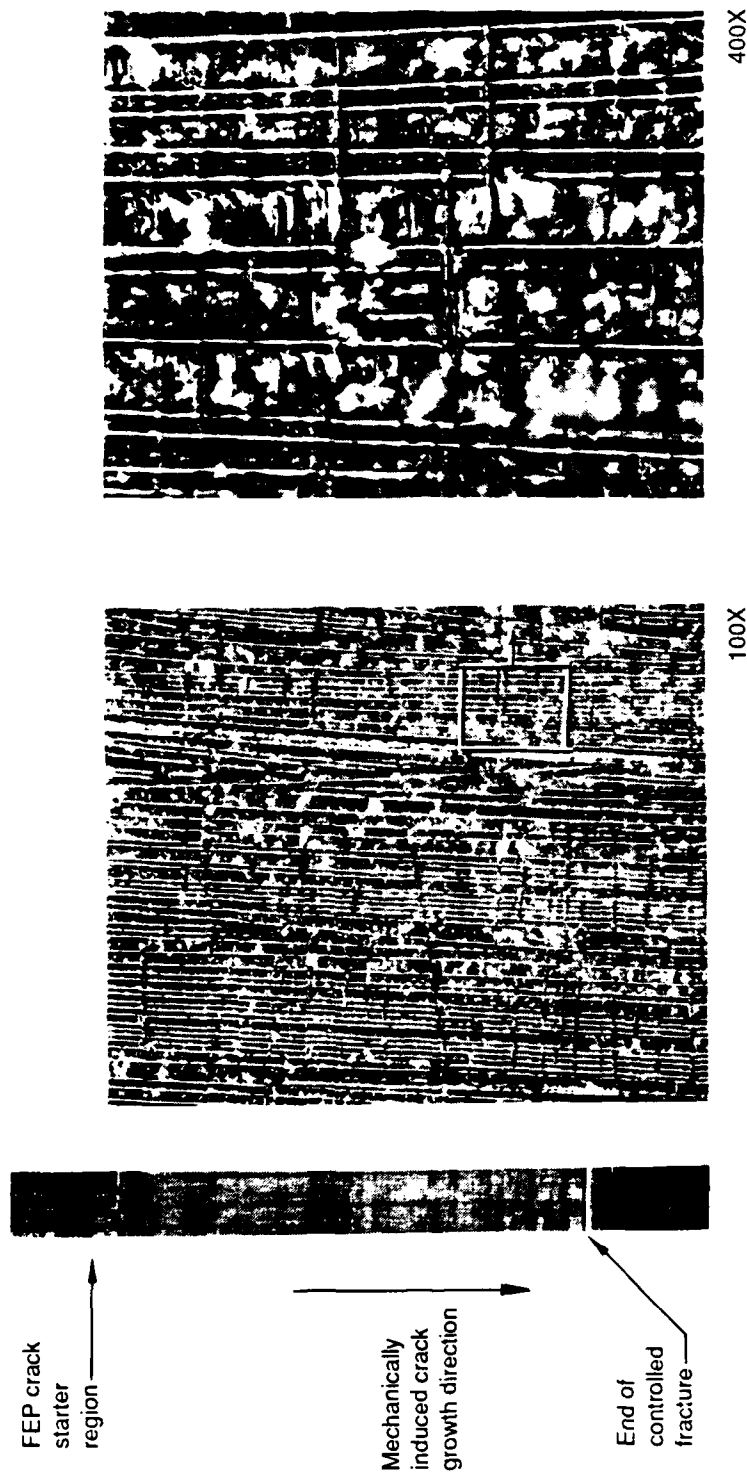
Figure 4.4-67. Optical Photomicrographs of Interlaminar Mode II Shear, 0/90 Fracture of High Resin Content Specimen
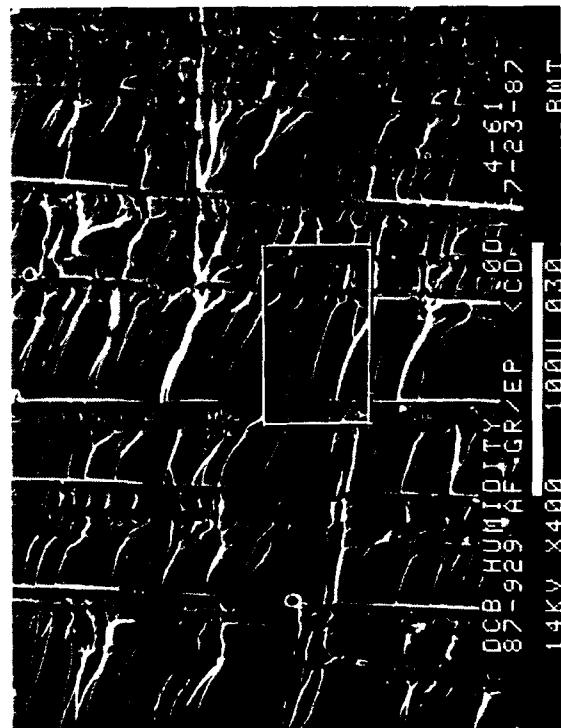
Legend:

F fiber matrix separation
H hackles
R rivermarks

Mechanically induced
crack direction
→

Figure 4.4-68. SEM Fractographs of Interlaminar Mode II Shear, 0/90 Fracture of High Resin Content Specimen
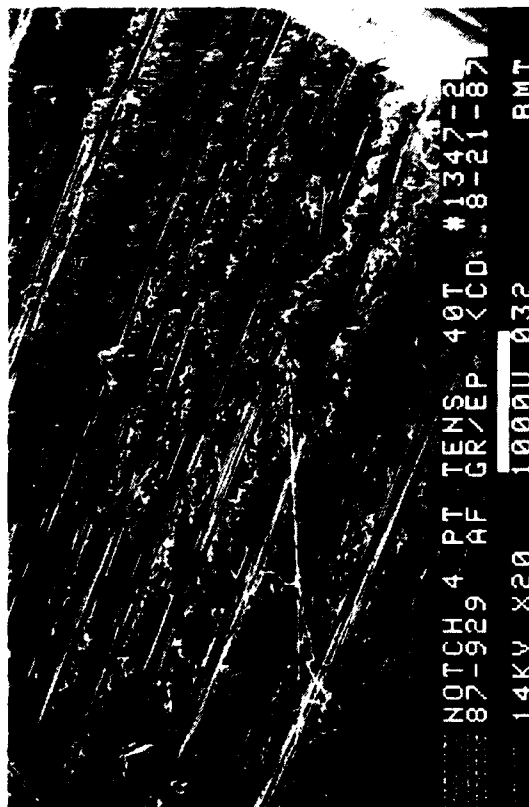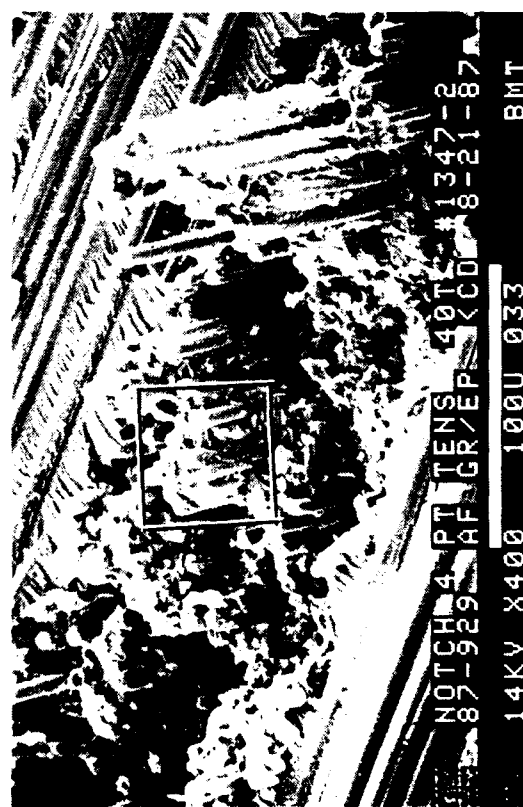
Note:

Higher magnification of the boxed region is shown in (c) and (d)

Mechanically induced crack direction

40 degree tilt

NOTCH 4 PT TENS 40T #1347-2
87-929 AF GR/EP <CO .8-21-87
14KV X20   1000U 032   BMT

20X

(a)

40 degree tilt

NOTCH 4 PT TENS 40T #1347-2
87-929 AF GR/EP <CO .8-21-87
14KV X400   100U 033   BMT

400X

(b)

Figure 4.4-69. SEM Fractographs of Translaminar Tension Fracture of High Resin Content Specimen

Mechanically induced crack direction

(c)
40 degree tilt

(d)
15 degree tilt

Figure 4.4-69. SEM Fractographs of Translaminar Tension Fracture of High Resin Content Specimen (Concluded)

400X

100X

FEP CRACK
STARTER
REGION

Mechanically
induced
crack growth
direction

END OF
CONTROLLED
FRACTURE
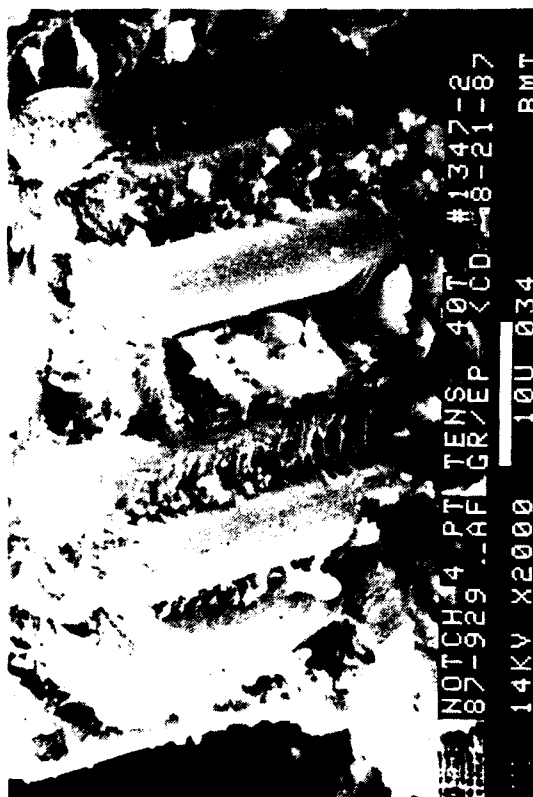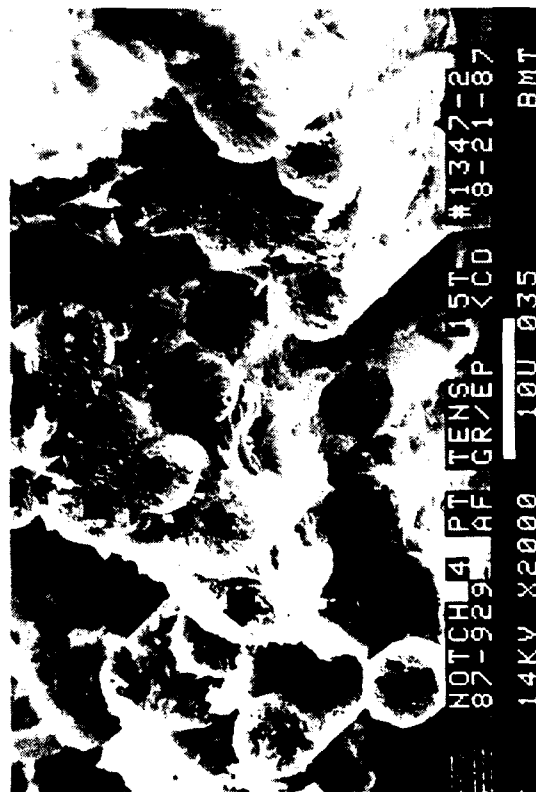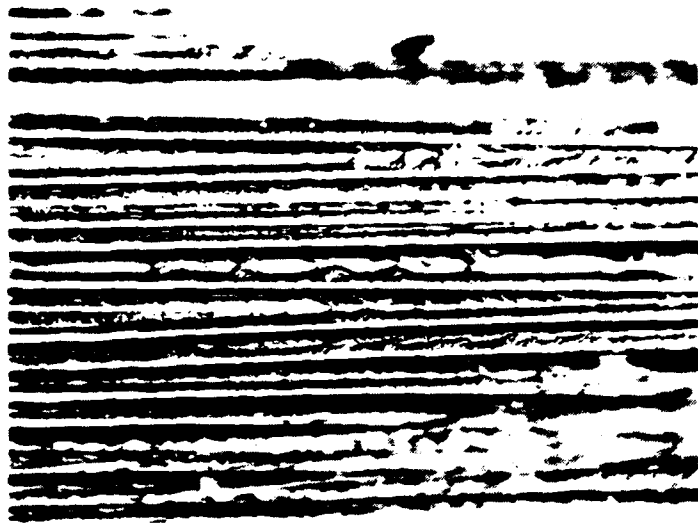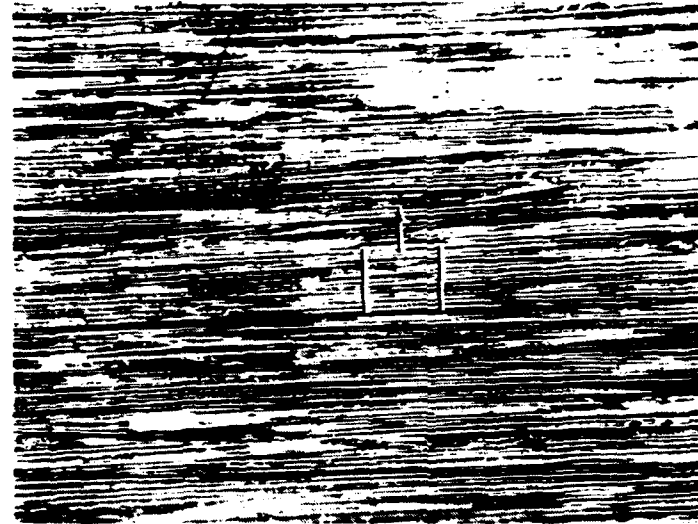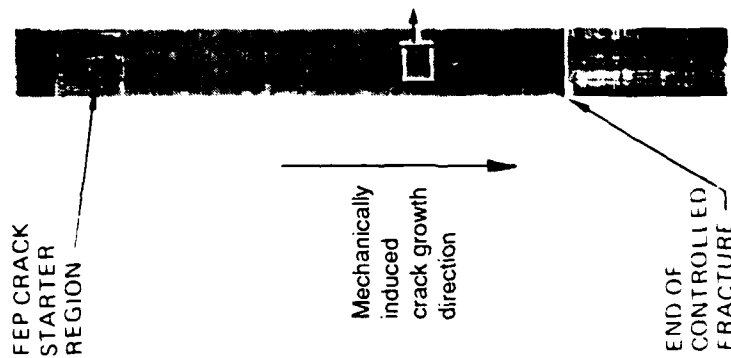
Figure 4.4-70. Optical Photomicrographs of Interlaminar Mode I Tension, 0/90 Fracture of Low Resin Content Specimen

The SEM analysis revealed a featureless fracture surface (Fig. 4.4-71).

Interlaminar Mode II Shear. Visual observation of the fracture surface revealed a flat but milky appearance when the sample was held at an angle to the light. In some locations on the specimen, there were dark spots indicating voids caused by resin starvation between plies. Although the hackles were present, fine details were difficult to resolve (Fig. 4.4-72).

The SEM revealed a fracture surface with features typically seen in RT/dry specimens, such as hackles and scallops. However, between these hackles, there were many valleys which seemed to have been caused by resin starvation (Fig. 4.4-73).

Translaminar Tension. Visual, optical, and SEM observations revealed localized fiber pullouts; the protruding fibers were unevenly distributed on the fracture surface. The fiber/matrix adhesion seemed poor as evidenced by the lack of resin fracture along the sides of the fibers. However, the radial patterns essential for determining the crack direction were clearly seen (Fig. 4.4-74).

4.4.1.4 Product Forms

Fabric. Interlaminar Mode I tension and Mode II shear and translaminar tension test were conducted on carbon/epoxy fabric.

Interlaminar Mode I Tension. Visual inspection revealed a flat, smooth surface. However, because of the weave pattern, the fracture surface appeared less reflective or glassy than unidirectional tape.

Optical examination revealed rivermarks and resin microflow especially in the resin-rich regions at the nodes where weaves overlap (Fig. 4.4-75).

SEM analysis confirmed the optical results. However, because the rivermarks in a single region are not always consistent with those in other regions, several resin-rich regions should be observed before making any conclusions on the crack propagation direction (Fig. 4.4-76).

Interlaminar Mode II Shear. Visual inspection revealed a dull, rough surface. Optical examination showed hackles not only at the nodes, but also at other regions of the weave (Fig. 4.4-77).

SEM analysis confirmed the optical results. The hackles were in various shapes and sizes (Fig. 4.4-78); as with the fracture surface created with a tape layup, these hackles are not indicators of crack propagation direction.

Legend:

M matrix fracture
F fiber/matrix separation
R rivermarks

Mechanically induced
crack direction
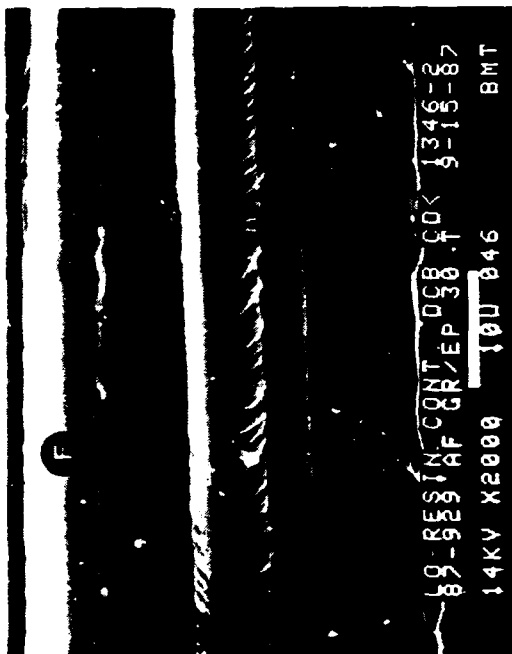
Figure 4.4-71. SEM Fractographs of Interlaminar Mode I Tension, 0/90 Fracture of Low Resin Content Specimen

400X

100X

FEP crack starter region

Mechanically induced crack growth direction

End of controlled fracture
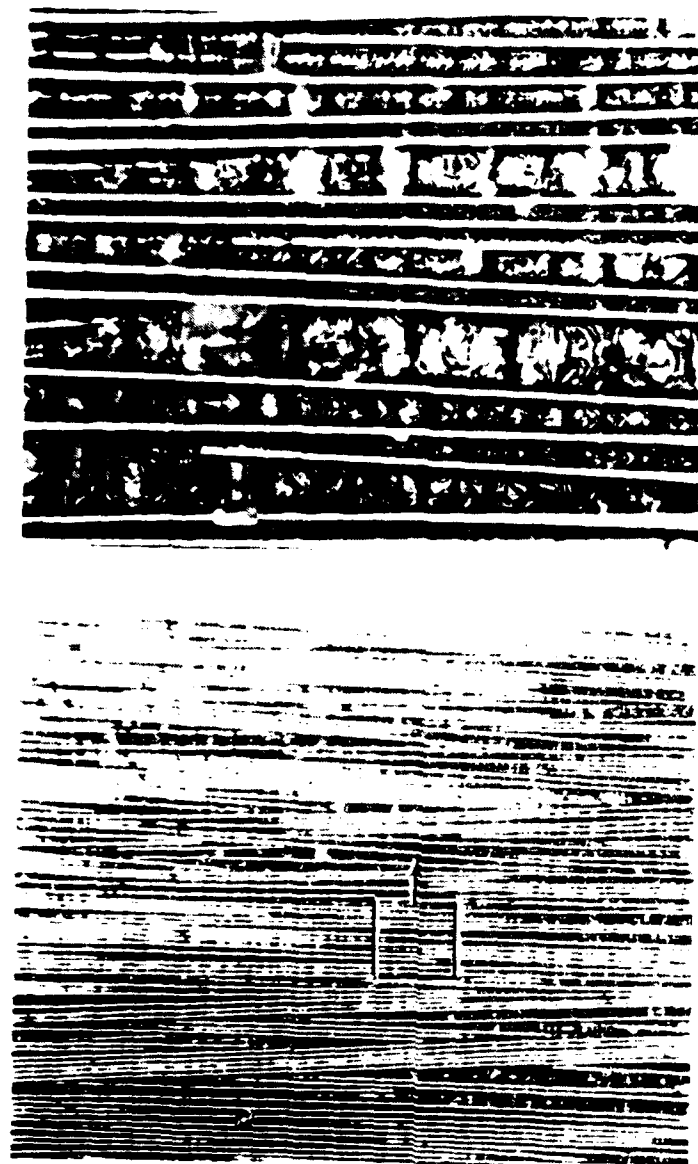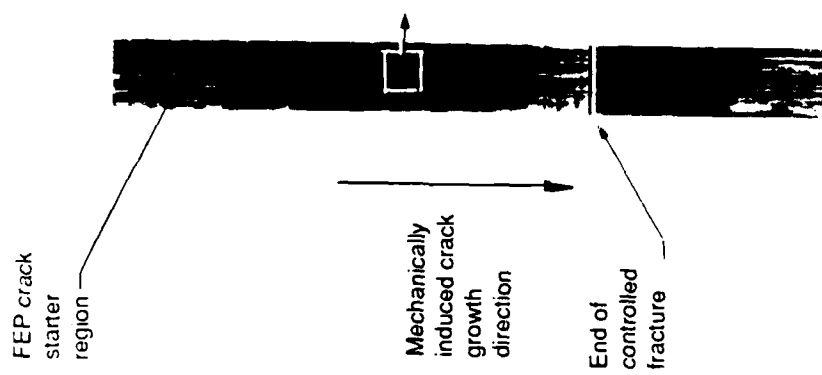
Figure 4.4-72. Optical Photomicrographs of Interlaminar Mode II Shear, 0/90 Fracture of Low Resin Content Specimen
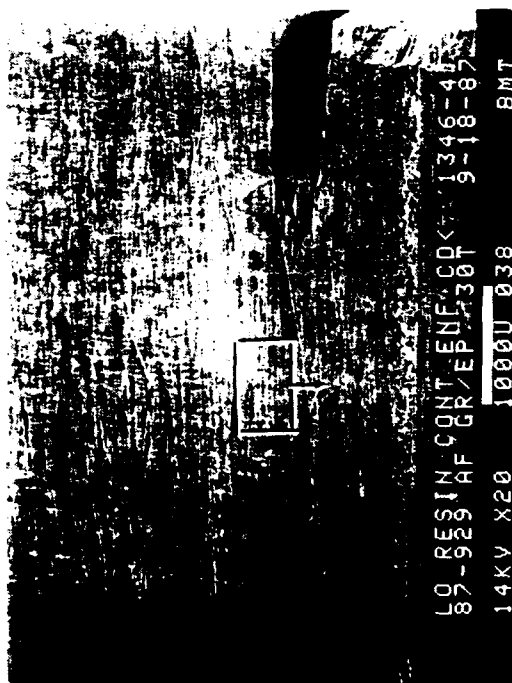
Legend:

F fiber/matrix separation
H hackles
R rivermarks

Mechanically induced
crack direction →

Figure 4.4-73. SEM Fractographs of Interlaminar Mode II Shear, 0/90 Fracture of Low Resin Content Specimen

Mechanically induced crack direction

(a) 20X

40 degree tilt

(b) 400X

40 degree tilt

Figure 4.4-74. SEM Fractographs of Translaminar Tension Fracture of Low Resin Content Specimen

Mechanically induced crack direction

14KV X2000 10U 038
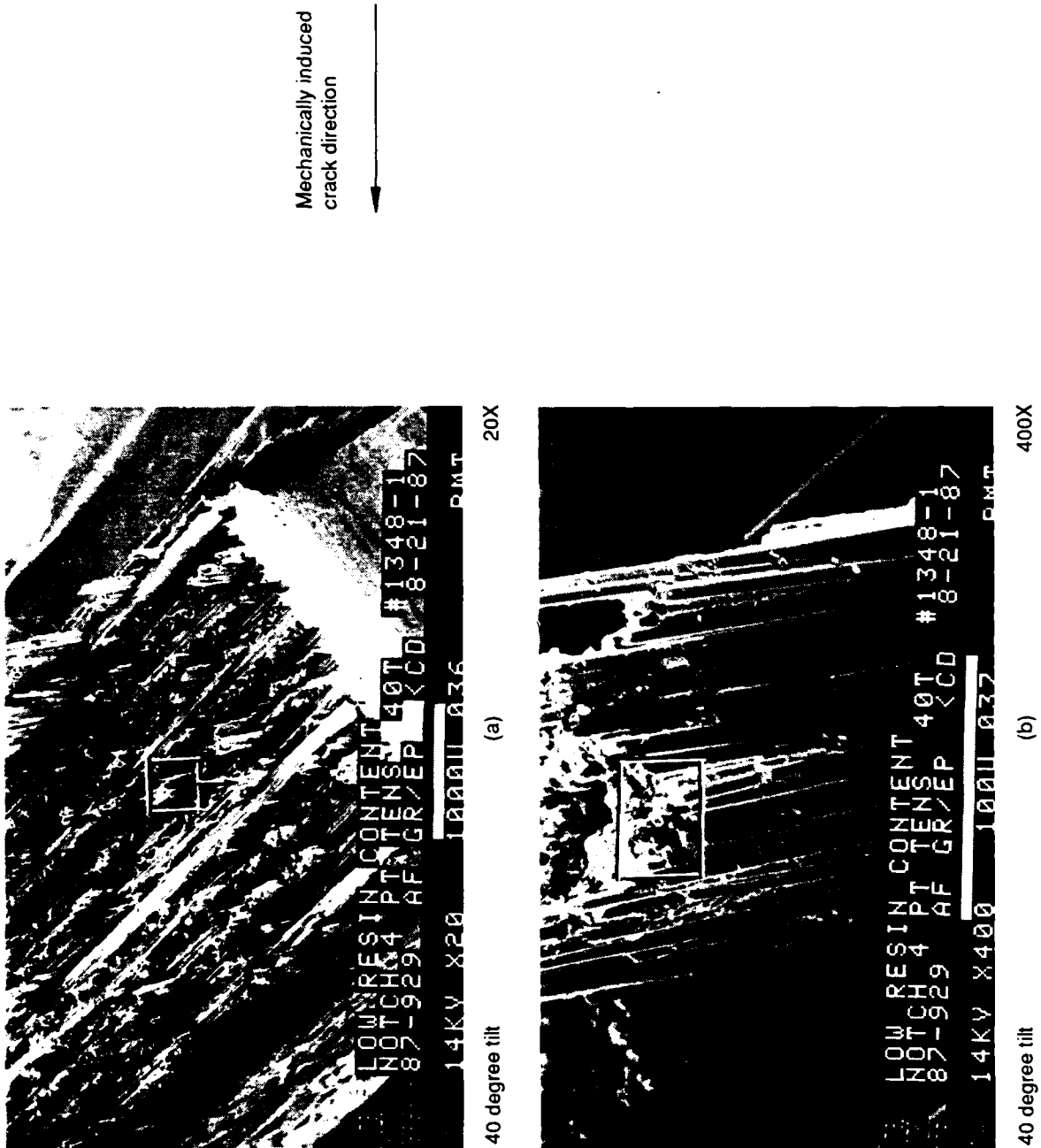
LOW RESIN CONTENT
NOTCH 4 PT TENS 40TL #1348-1
87-929 AF GR/EP <CD 8-21-87
BMT
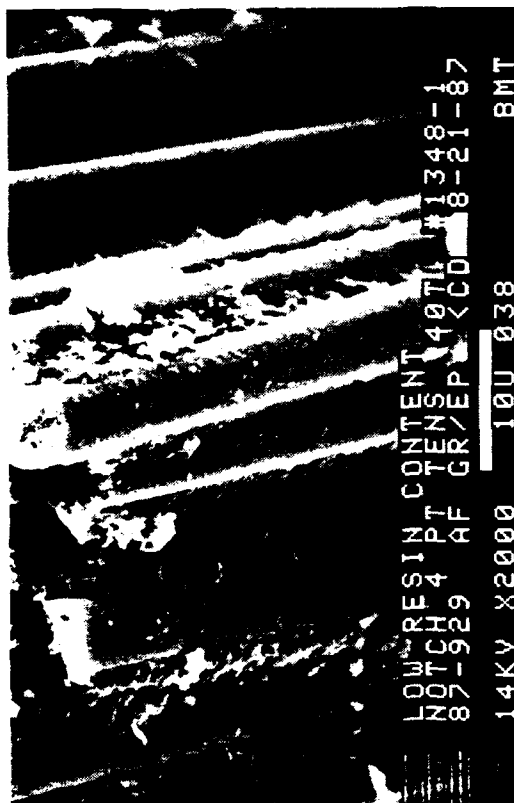
2,000X

40 degree tilt

(c) Typical fracture along the fibers

14KV X2000 10U 040

LOW RESIN CONTENT
NOTCH 4 PT TENS 15T #1348-1
87-929 AFL GR/EP <CD 8-21-87
BMT

2,000X

15 degree tilt

(d) Illustration of crack mapping using the radial patterns on the fiber ends

Figure 4.4-74. SEM Fractographs of Translaminar Tension Fracture of Low Reain Content Specimen (Concluded)

FEP CRACK
STARTER
REGION

Mechanically
induced
crack growth
direction

100X
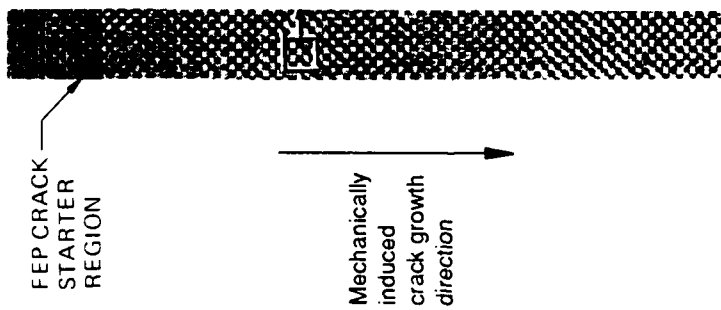
400X

Figure 4.4-75. Optical Photomicrographs of Interlaminar Mode I Tension, Room Temperature, Fabric Fracture
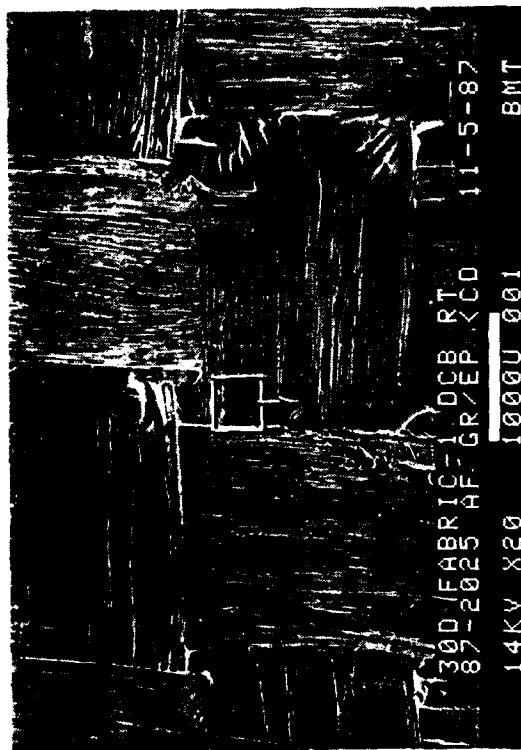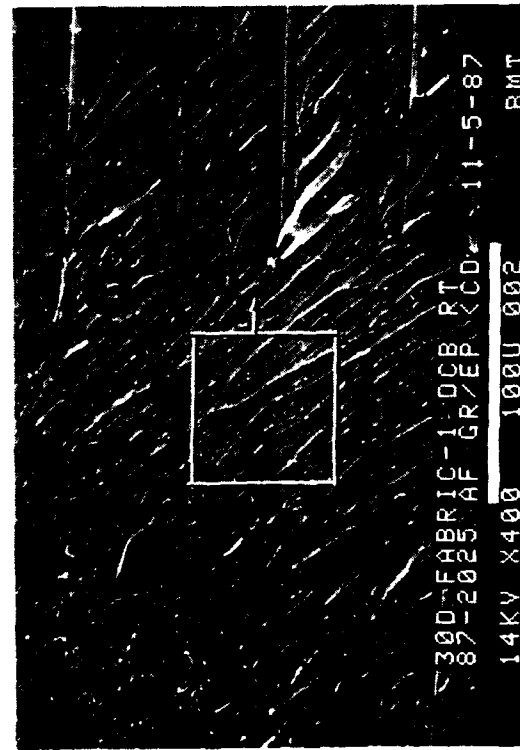
Legend:

R rivermarks
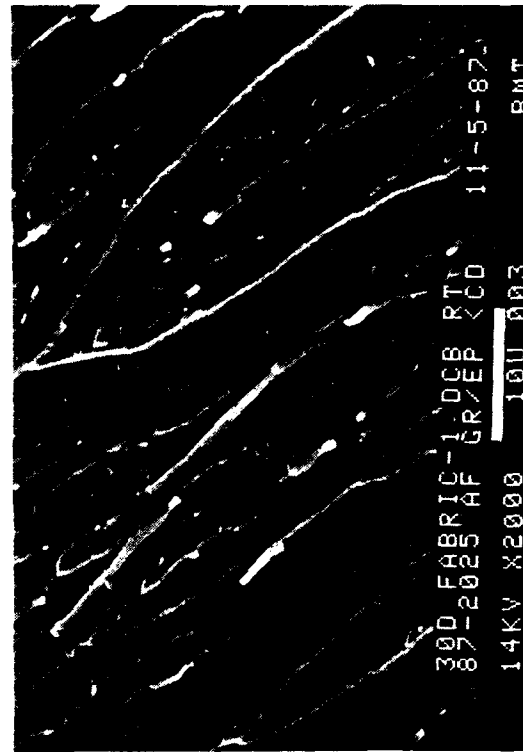
Mechanically induced crack direction →

30 degree tilt | 20X

30 degree tilt | 2,000X

30 degree tilt | 400X

Figure 4.4-76. SEM Fractographs of Interlaminar Mode I Tension, Room Temperature, Fabric Fracture

400X

100X

FEP crack
starter
region

Mechanically
induced crack
growth direction
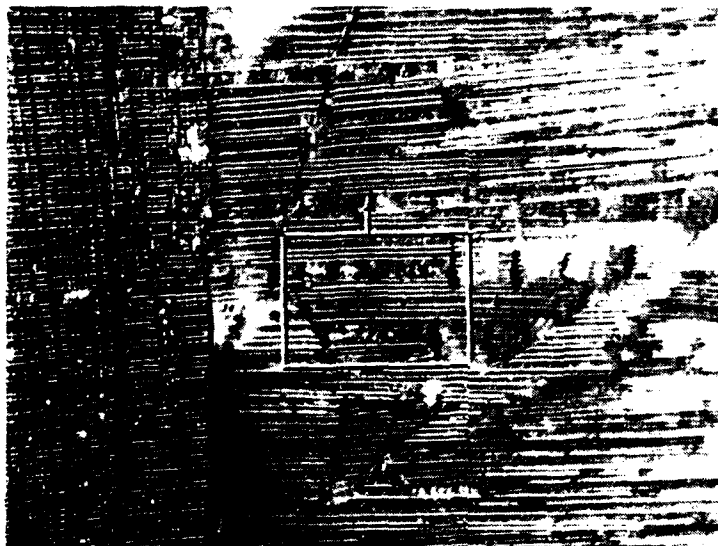
Figure 4.4-77. Optical Photomicrographs of Interlaminar Mode II Shear, Room Temperature, 0/90 Fabric Fracture
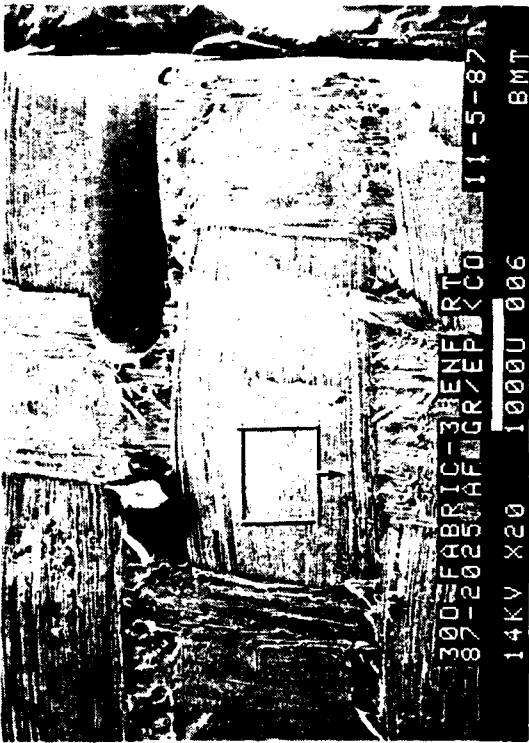
Legend:

H hackles
S scallops

Mechanically induced
crack direction

20X
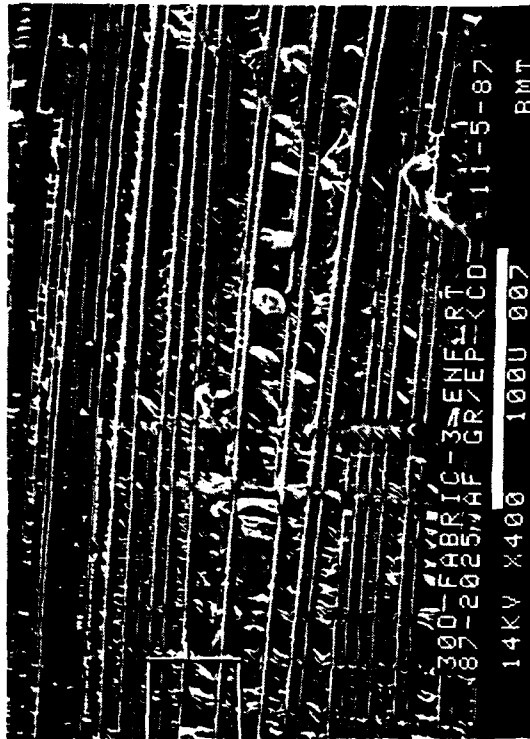
30 degree tilt

400X
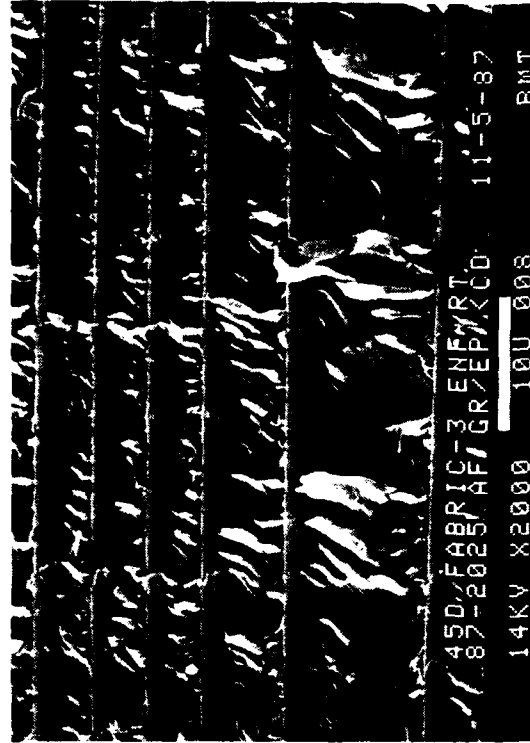
30 degree tilt

2,000X

45 degree tilt

Figure 4.4-78. SEM Fractographs of Interlaminar Mode II Shear, Room Temperature, Fabric Fracture

Translaminar Tension. Visual inspection revealed a fracture surface with protruding fibers. There seemed to be resin-rich regions between the fiber bundles.

SEM analysis showed resin-rich regions between protruding fiber bundles. The fiber/matrix adhesion was good. Radial patterns on the fiber ends were observed (Fig. 4.4-79).

Filament Wound. A filament wound carbon/epoxy specimen was subjected to DCB, ENF, and translaminar tension tests.

Interlaminar Mode I Tension. Visual observation of the fracture surface revealed a flat, glassy surface similar to that of the unidirectional tape specimen under the same conditions. There was evidence of loose fibers resulting from the low resin content of the AS4/3501-6 prepreg tow.

In optical photomicrographs fracture features were very difficult to identify due to the low resin content. However, at high magnification, fine rivermarks were observed (Fig. 4.4-80).

These fine rivermarks were also observed under SEM. Due to the lack of resin surrounding the fibers, the fiber/matrix adhesion was rather poor as evidenced by the stray fibers on the fracture surface (Fig. 4.4-81).

Interlaminar Mode II Shear. Visual observation revealed a rough, dull fracture surface similar to that of the unidirectional tape specimen under the same conditions.

Under optical microscopy, hackles were observed only at locations where there was a sufficient amount of resin between the fibers (Fig. 4.4-82). The hackles observed under the SEM were very small due to the low resin content. The fiber/matrix adhesion seemed to be poor at resin-starved regions as evidenced by bare fibers (Fig. 4.4-83).

Translaminar Tension. The fiber/matrix adhesion was good and radial patterns commonly observed in carbon fibers were present on the fiber ends. From these patterns, it was possible to obtain the overall crack propagation direction (Fig. 4.4-84).

Stitch (CAI). An AS4/35601-6 specimen was stitched with Kevlar 29. Fractographs of the specimen tested under CAI were documented. The ply-by-ply crack propagation showed an irregularly arranged, complex pattern (Fig. 4.4-85). The damage around the Kevlar 29 stitch was composed of interlaminar and translaminar cracks (Fig. 4.4-86).

Crack mapping of the delamination near the vicinity of the impact site was impossible because of the complex fracture mode.

Mechanically induced crack direction

(a) 20X

(b) 400X

45 degree tilt

Figure 4.4-79. SEM Fractographs of Translaminar Tension, Room Temperature, Fabric Fracture

Mechanically induced crack direction

(c) Typical fracture along the fibers

45 degree tilt

(d) Illustration of crack mapping using the radial patterns on the fiber ends

0 degree tilt

Figure 4.4-79. SEM Fractographs of Translaminar Tension, Room Temperature, Fabric Fracture (Concluded)

400X

100X

FEP crack
starter
region

Mechanically
induced crack
growth direction
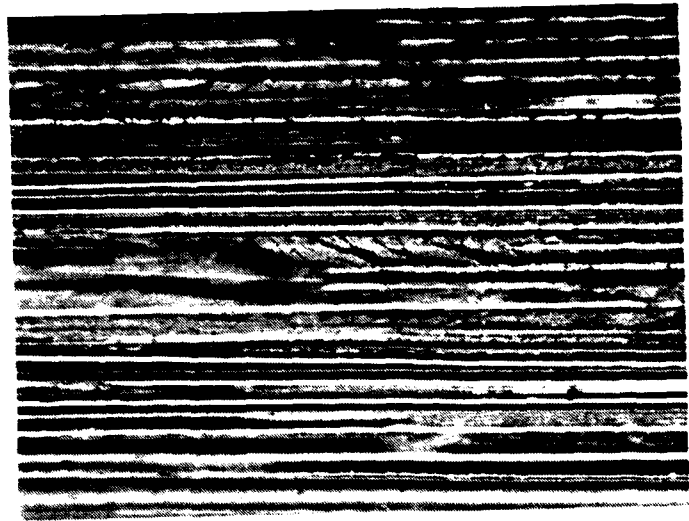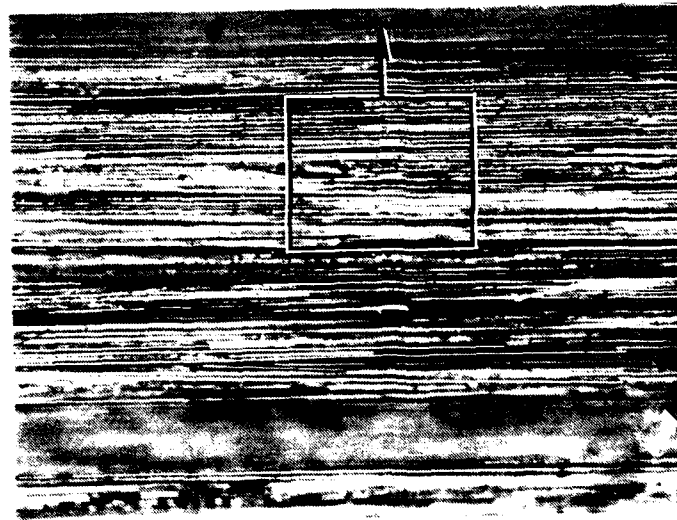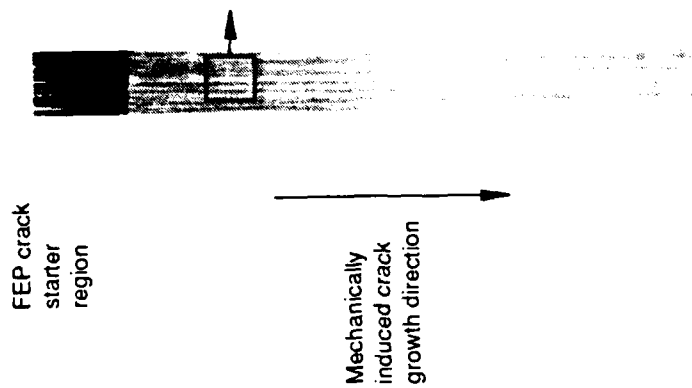
Figure 4.4-80. Optical Photomicrographs of Interlaminar Mode I Tension, 0/0 Fracture of a Filament Wound Specimen
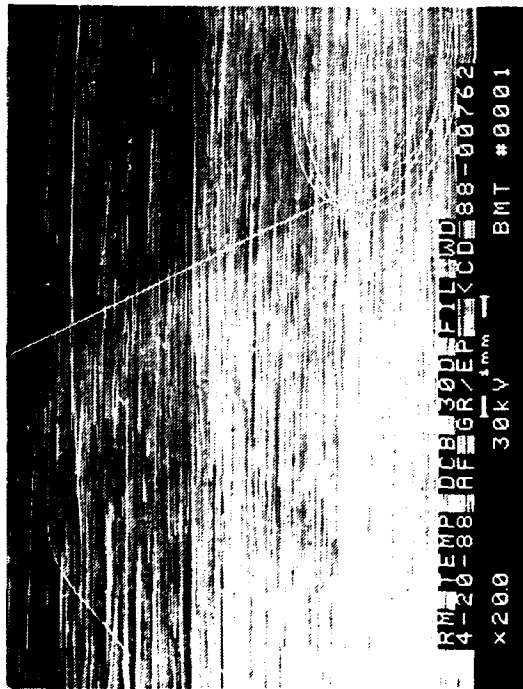
Mechanically induced crack direction →
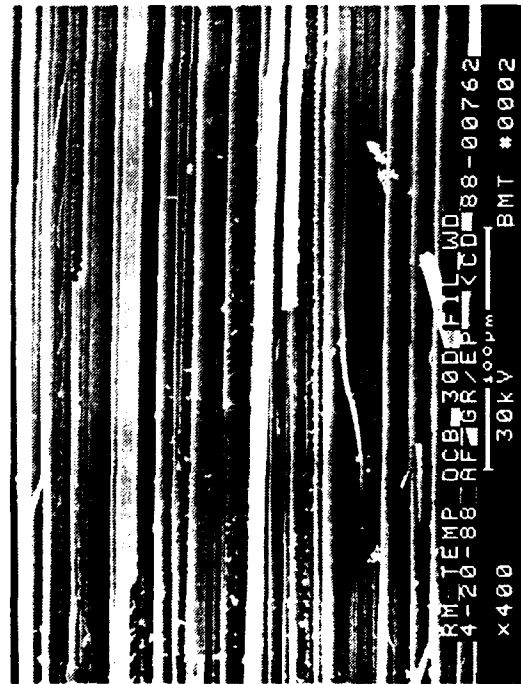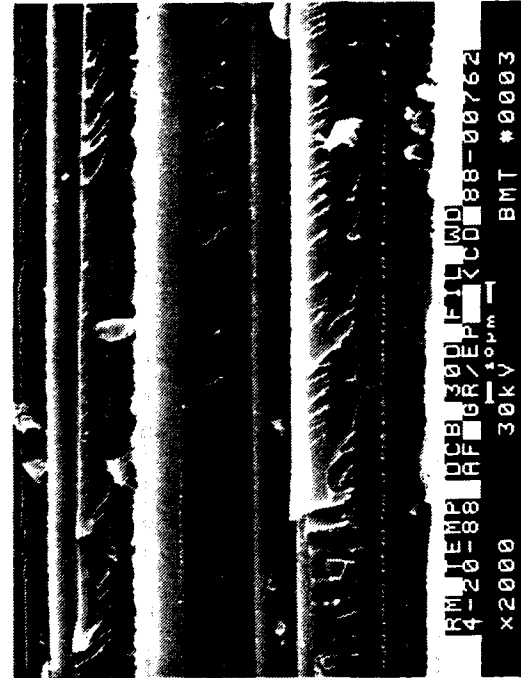
Figure 4.4-81. SEM Fractographs of Interlaminar Mode I, 0/0 Fracture of Filament Wound Specimen
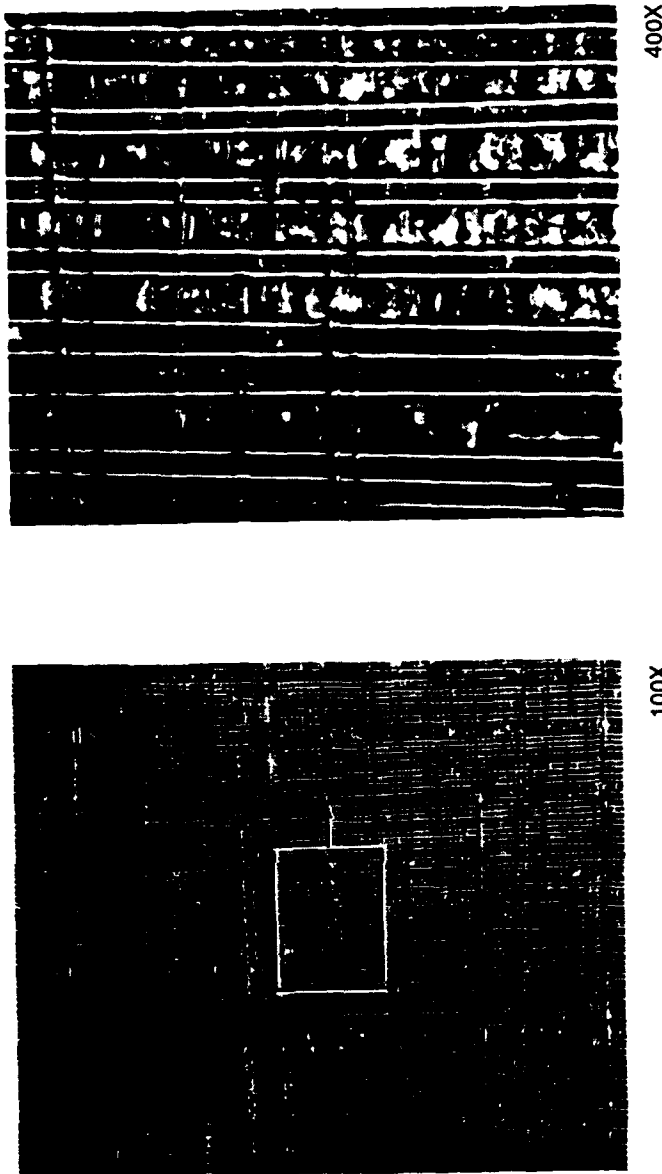
400X

100X
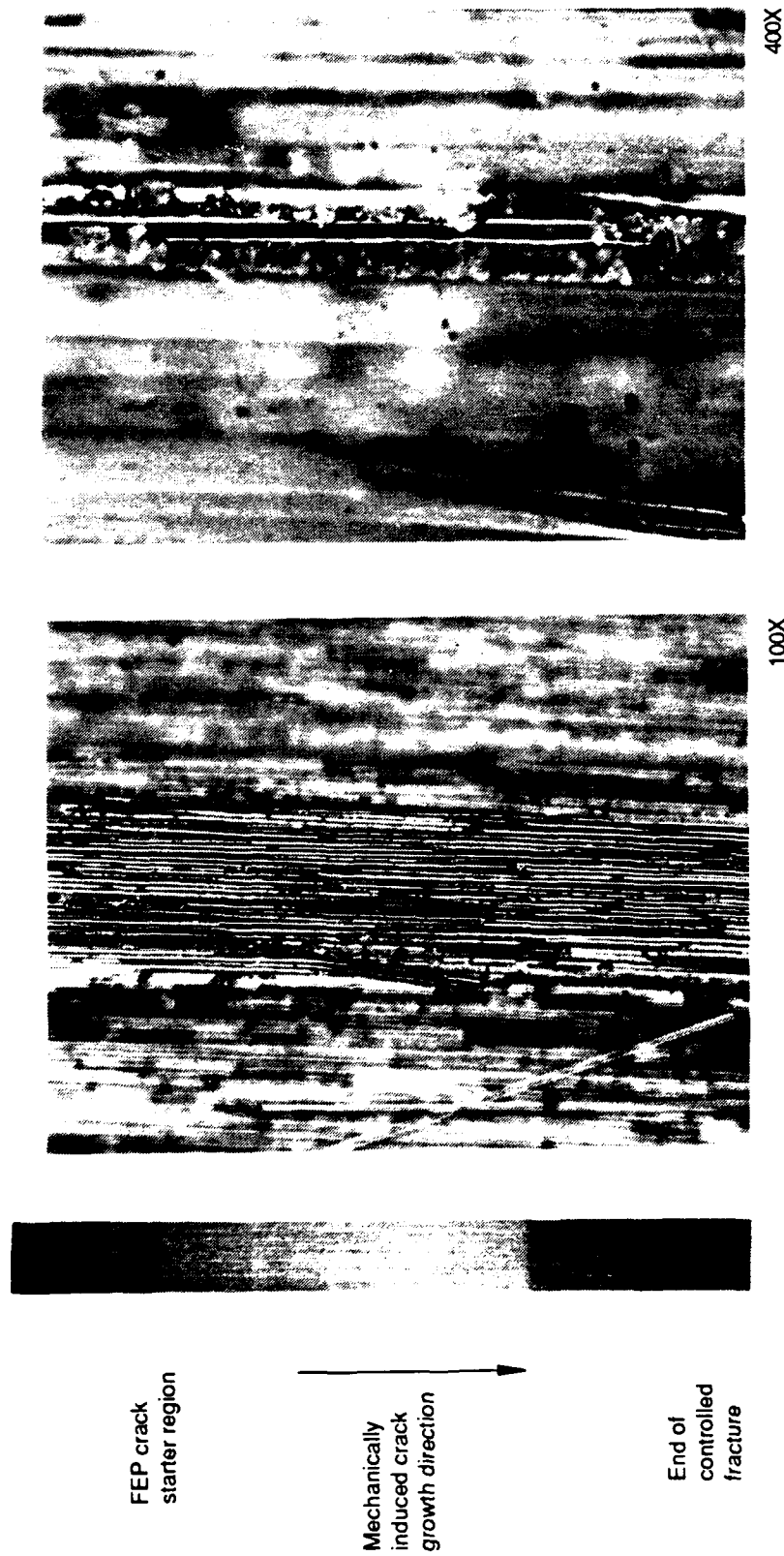
Figure 4.4-82. Optical Photomicrographs of Interlaminar ModeII, 0/0 Fracture of Filament Wound Specimen

FEP crack
starter region

Mechanically
induced crack
growth direction

End of
controlled
fracture
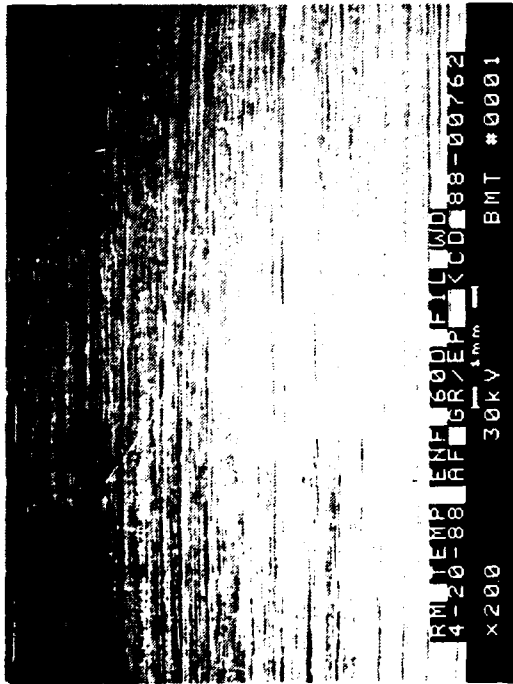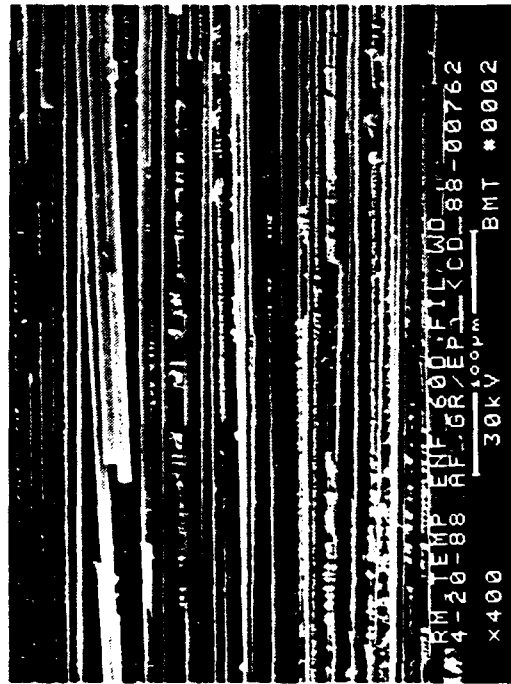
Mechanically induced
crack direction

Figure 4.4-83. SEM Fractographs of Interlaminar Mode II Shear, 0/0Fracture of Filament Wound Specimen

(b) Protruding fibers 400X

(d) Radial patterns on fiber ends 2,000X

Mechanically induced crack direction

(a) Overall view 20X

(c) Good fiber/matrix adhesion 2,000X

Figure 4.4-84. SEM Fractographs of Translaminar Tension Fracture of Filament Wound Specimen

Optical photomicrograph

16X

Impact site

Figure 4.4-85. Cross-Sectional View of Compression-After-Impact Fracture of AS-4/3501-6 Stitched with Kevlar 29

Figure 4.4-86. Damage Around Kevlar 29 Stitch

4.4.2 Task 3B: Other Systems

Carbon/PEEK, carbon/PMR-15, carbon/8551-7, boron/epoxy, Kevlar/epoxy, and glass/epoxy were evaluated. The material systems mentioned are currently or soon to be in service. The material systems were divided into two categories, carbon fiber based materials and epoxy based materials.

4.4.2.1 Carbon-Fiber Based Materials.

Carbon/PEEK (AS4/APC-2), carbon/PMR-15 (Celion 3000 8H Satin), and carbon/multi-phase resin (IM7/8551) were evaluated under the carbon-fiber materials category.

Carbon/PEEK, (AS4/APC-2). Interlaminar Mode I and II fractures were examined after exposure to RT/dry and 270°F/wet conditions.

Interlaminar Mode I Tension. RT/Dry. Optical examination revealed a dull, matte interlaminar surface, unlike the reflective Mode I fractures observed in carbon/epoxy. SEM examination revealed features similar to ductile overload dimples observed in metals (Fig. 4.4-87). These were found in radial patterns due to the influence of semi-crystalline formations, termed spherulites, within the PEEK matrix. The fractographs are indicative of a fast, brittle fracture. A slow fracture is characterized by high ductility. No overall crack propagation direction could be determined. Fiber/matrix adhesion was good.

Interlaminar Mode I Tension, 270°F/Wet. Optical examination revealed a white fracture surface due to the presence of ductile tufts of material. SEM examination revealed ductile matrix fracture, showing the small tufts of matrix which were drawn perpendicularly to the fracture plane (Fig. 4.4-88). This morphology is typical of a slow, ductile fracture in PEEK matrix. Overall crack propagation direction could not be determined. Fiber/matrix adhesion was good.

Interlaminar Mode II Shear, RT/Dry. Optical examination revealed a distinct transition point from the Mode I precrack to Mode II shear propagation. SEM examination revealed ductile shear dimples similar to those observed in metals (Fig. 4.4-89). Unlike hackles, these features make it possible to determine the relative shear directions of the mating fractures. Resin-rich areas between plies revealed mixed features of ductile overload and ductile shear. Fiber/matrix adhesion was good.
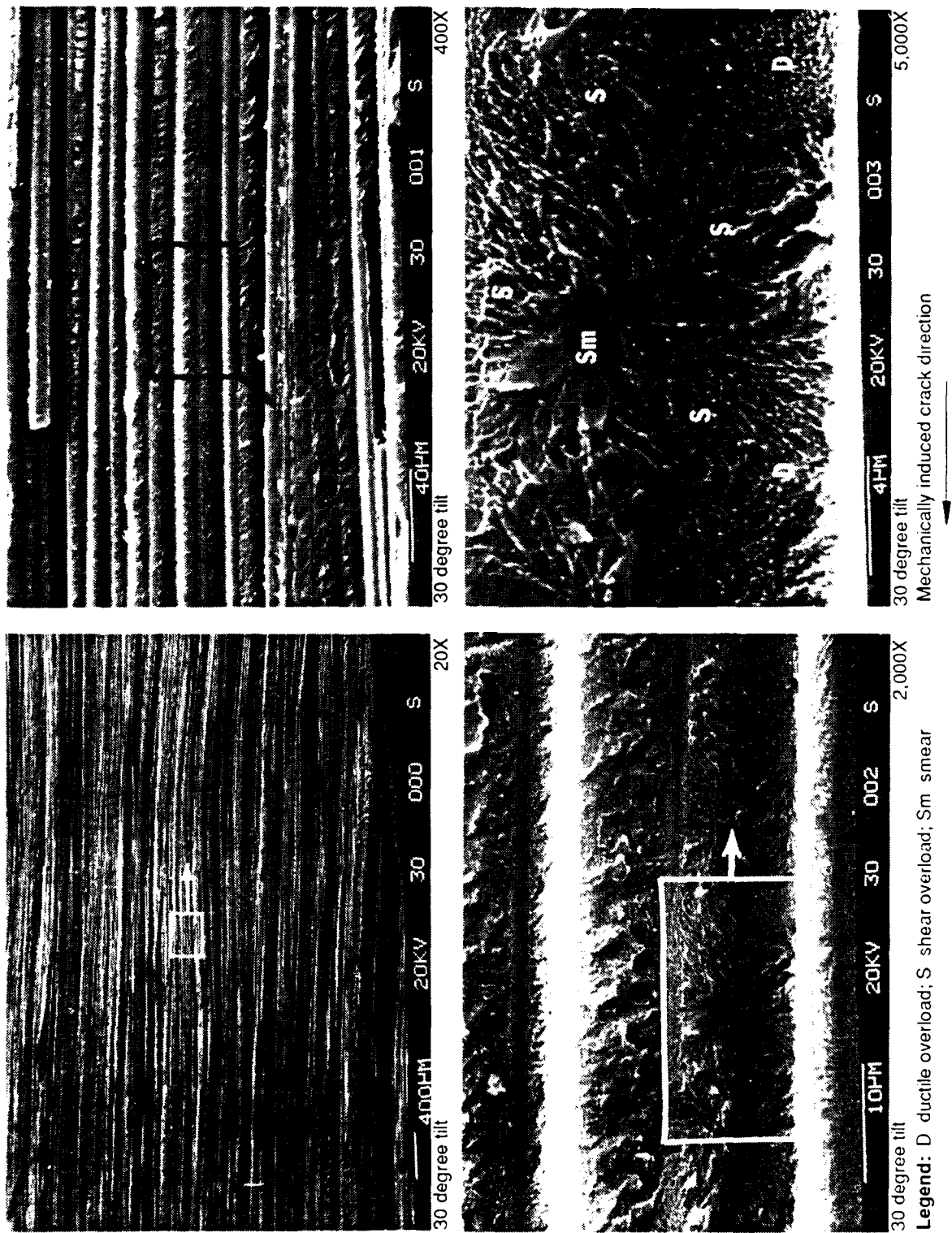
Figure 4.4-87. SEM Fractographs of Room Temperature, Interlaminar Mode I Fracture in AS-4/APC-2

Legend: D ductile overload; S shear overload; Sm smear
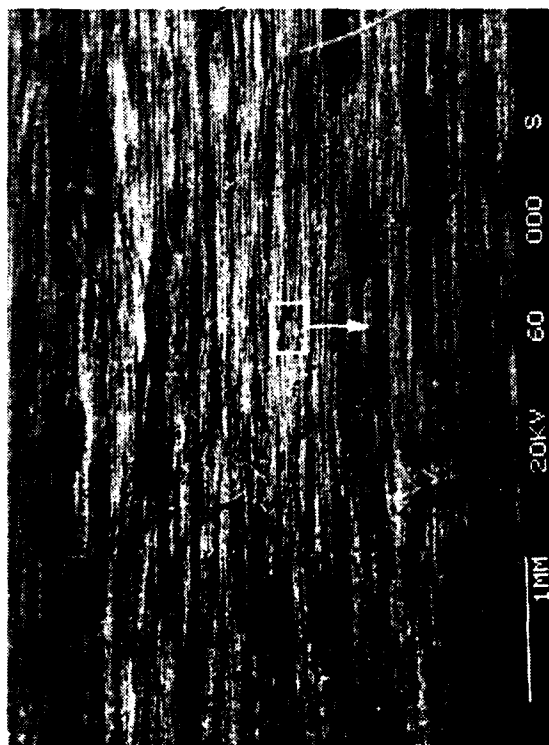
Legend:
D ductile matrix fracture
F fiber

Mechanically induced
crack direction
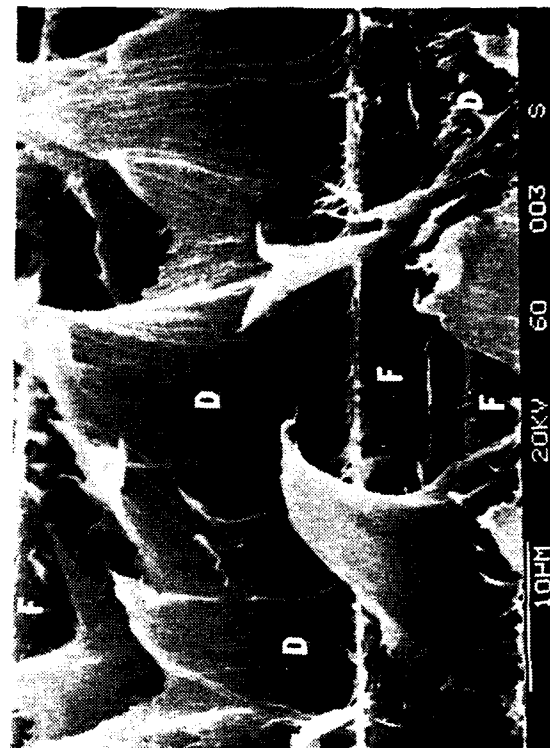
Figure 4.4-88. SEM Fractographs of 270 F/Wet, Interlaminar Mode I Tension Fracture in AS-4/APC-2

Figure 4.4-89. SEM Fractographs of Room Temperature, Interlaminar Mode II Fracture in AS-4/APC-2
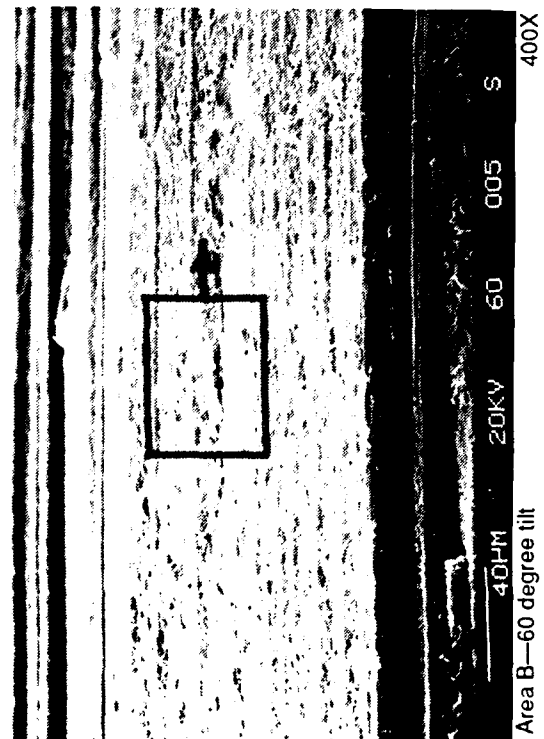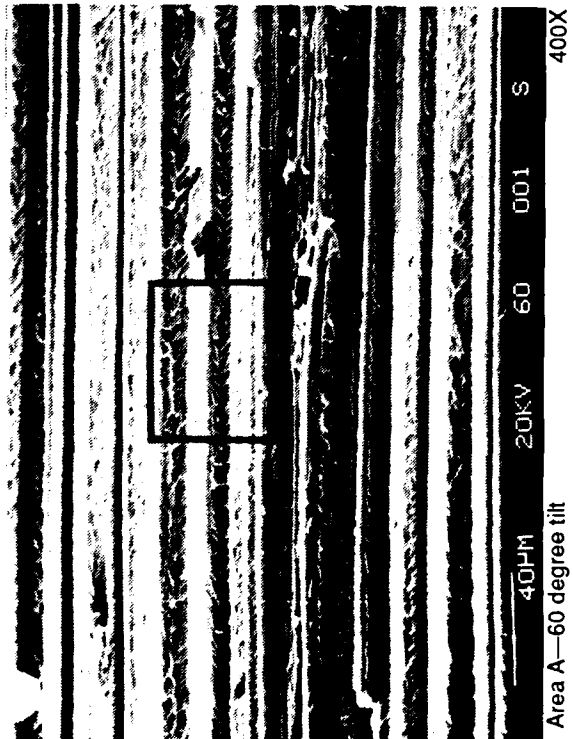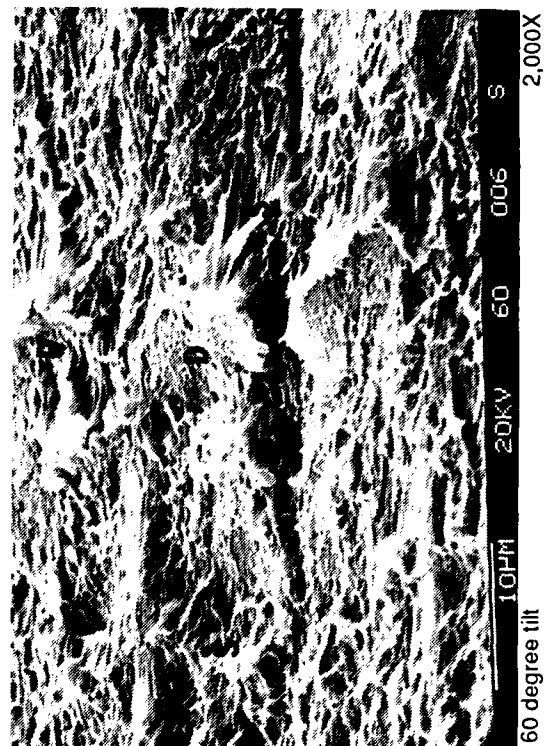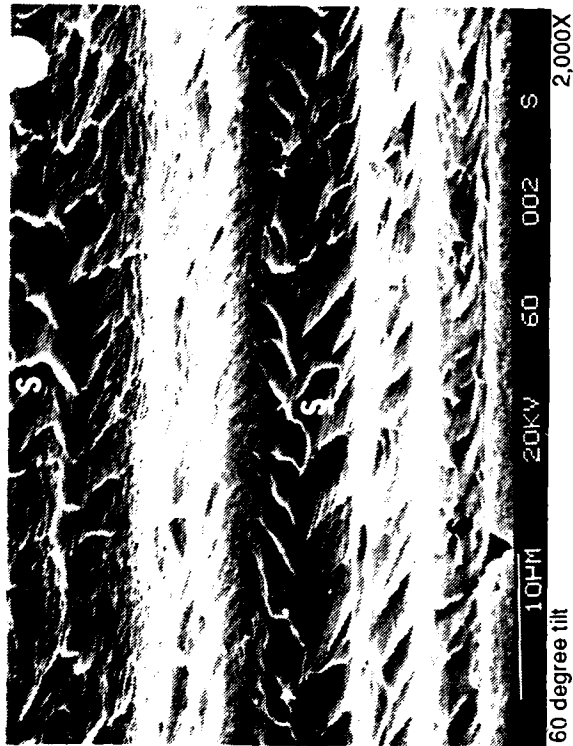
Legend: D ductile overload; S ductile shear

Area A—60 degree tilt

Area B—60 degree tilt

Mechanically induced crack direction
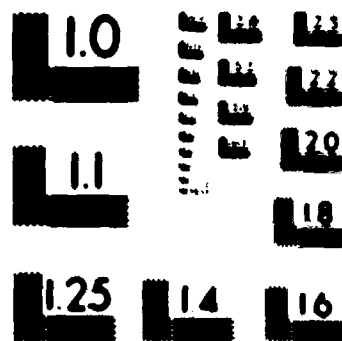
MICROCOPY RESOLUTION TEST CHART
NATIONAL BUREAU OF STANDARDS
STANDARD REFERENCE MATERIAL 1010a
(ANSI and ISO TEST CHART No. 2)

Interlaminar Mode II Shear, 270°F/Wet. Optical examination of the fracture did not reveal a distinct transition from the Mode I precrack to Mode II shear propagation. SEM fractography revealed hackles covered with features similar to ductile overload dimples (Fig. 4.4-90). The direction of crack propagation could not be determined from these features. However, the axis of propagation indicated by shear hackles was consistent with the mechanically induced crack direction. Fiber/matrix adhesion was good.

Translaminar Tension, RT/Dry. Optical examination revealed a planar fracture with typical fiber pullout. Only a thin compressive zone (approximately 6% of the fracture) was observed on the end opposite the notch. SEM examination revealed radial patterns on fiber ends which indicated a propagation direction consistent with the mechanically induced crack direction (Fig. 4.4-91). Fiber/matrix adhesion was good.

Translaminar Tension, 270°F/Wet. Optical examination revealed a relatively flat fracture with no significant buckling on the compressive surface. The fracture was almost exclusively tensile, and significant fiber pullout was observed. SEM fractography revealed small bundles of fibers all in the same plane (Fig. 4.4-92). Radial patterns found on fiber end fractures indicated crack growth consistent with the mechanically induced crack growth direction. Fiber/matrix adhesion was good.

Translaminar Compression, RT/Dry. Optical examination revealed a rough surface. Compressive fracture occurred on only 30% of the surface. Fiber end fractures in the compressive portion of the fracture revealed a tensile zone, a compressive zone, and a neutral axis on each fiber end (Fig. 4.4-93). Matrix ductility was observed between fiber end fractures. As in the translaminar tension specimen, the matrix fracture in the 90 degree plies revealed ductile overload dimples. Fiber/matrix adhesion was good.

Translaminar Compression, 270°F/Wet. Optical examination revealed approximately 50% compressive and 50% tensile fracture. SEM examination of the compressive zone revealed fiber end fractures having tensile, compressive, and neutral zones typical of compressive fractures (Fig. 4.4-94). Fiber/matrix adhesion was good.

Carbon/PMR-15 (Celion 3000 8H Satin). Interlaminar Mode I and II and translaminar tension and compression specimens were exposed to RT/dry and 500°F/dry conditions.

Interlaminar Mode I Tension, RT/Dry. Optical examination revealed a reflective interlaminar surface. SEM fractography of tows perpendicular to the crack propagation direction revealed rivermarks indicating propagation consistent with the mechanically induced crack direction (Fig. 4.4-95). Fractography of tows parallel to the crack propagation direction revealed a mixed-mode morphology with poorly formed hackles

Legend:

D ductile overload
H hackle
S ductile shear

Mechanically induced
crack direction

Figure 4.4-90. SEM Fractographs of 270 F/Wet, Interlaminar Mode II Shear Fracture in AS-4/APC-2

Mechanically induced crack direction

60 degree tilt 2,000X

30 degree tilt 400X

Figure 4.4.91 SEM Fractographs of Room Temperature, Transverse Tension Fracture in AS-4/APC-2

Mechanically induced crack direction

30 degree tilt X 60

10 degree tilt X 1000

30 degree tilt X 1000

Figure 4-132 SEM Fractographs of Room Temperature Transverse Compression Failure in AS4/APC-2

Mechanically induced crack direction
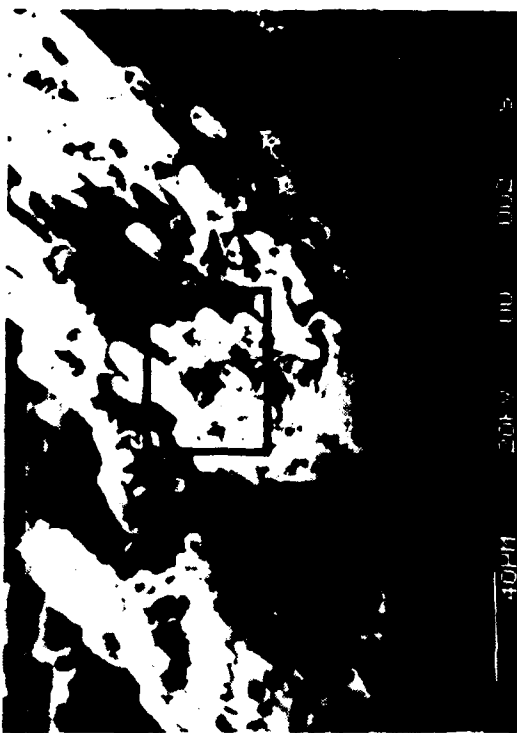
20X 30 degree tilt

2,000X 0 degree tilt

400X 0 degree tilt

Figure 4.4.93. SEM Fractographs of 270 F/Wet, Translaminar Tension Fracture in AS-4/APC-2

Mechanically induced crack direction →
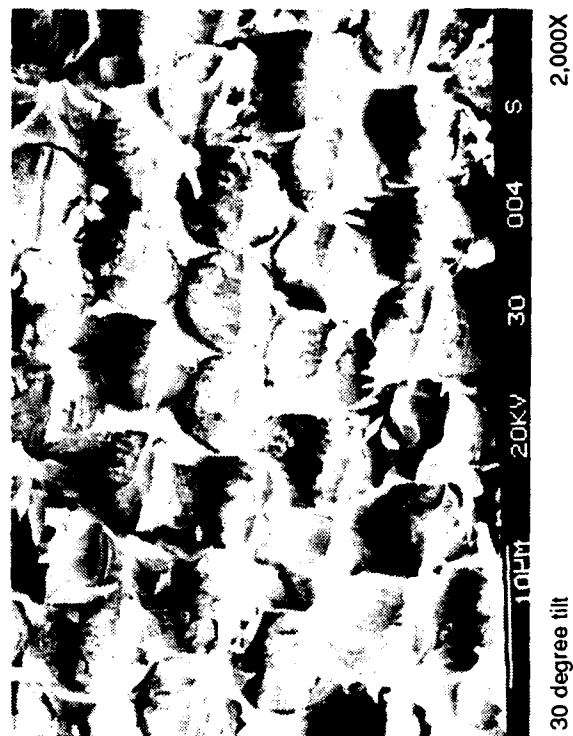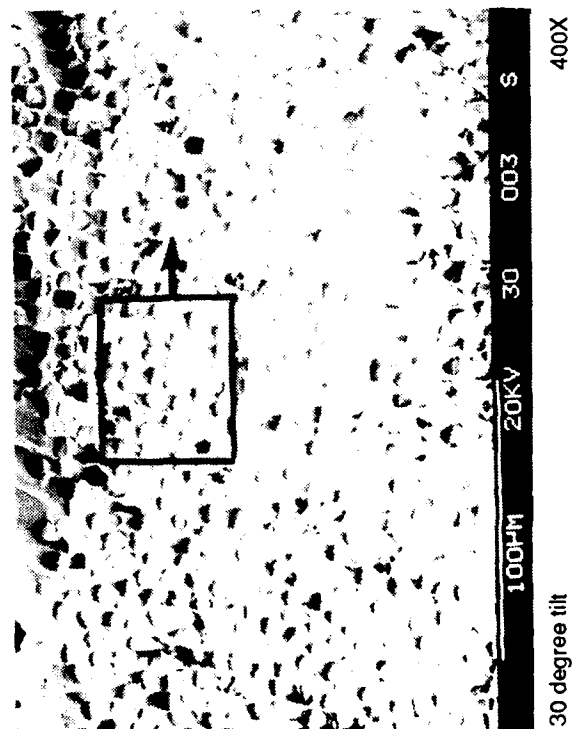
Figure 4.4.94. *SEM Fractographs of 270 F/Wet, Translaminar Compression Fracture in AS-4/APC-2*
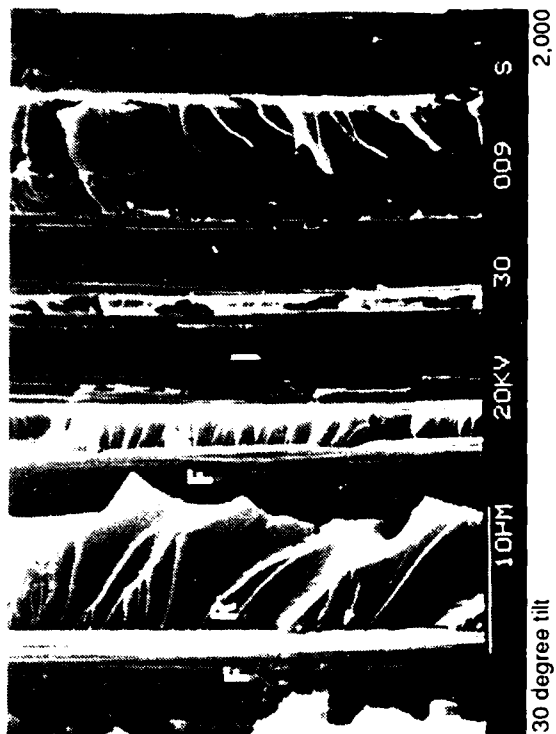
Legend: F fiber, H hackle, I fiber imprint, R rivermarks.
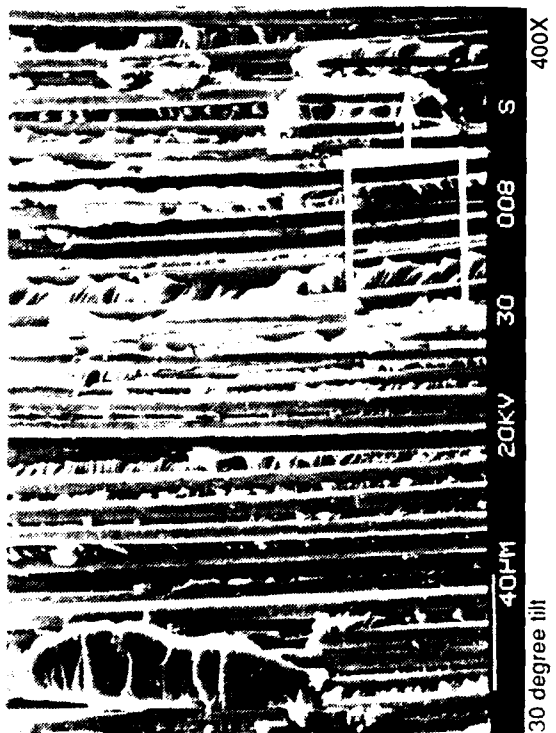
Mechanically induced crack direction

Figure 4.4-95. SEM Fractographs of Room Temperature, Mode I Fracture in C3K 8 HS PMR 15

indicating shear propagation due to the influence of fabric reinforcement. Fractography of resin-rich regions between tows revealed propagation toward the center of the adjacent tow, regardless of direction. Fiber/matrix adhesion was poor, as most fibers were bare.

Interlaminar Mode I Tension, 500°F/Dry. Optical examination revealed a slightly reflective interlaminar surface. SEM fractography of tows perpendicular to the crack propagation direction revealed rivermarks indicating propagation in directions both consistent with and opposite to the overall propagation direction (Fig. 4.4-96). Fractography of tows parallel to the crack propagation direction revealed a featureless matrix fracture having the appearance of shear failure. Fiber/matrix adhesion was good.

Interlaminar Mode II Shear, RT/Dry. Optical examination revealed a matte surface corresponding to the shear fracture. SEM fractography of tows parallel to the mechanically induced crack revealed hackles and scallops, indicative of shear fracture (Fig. 4.4-97). Fractography of tows perpendicular to crack propagation revealed a mixed-mode morphology. The cleavage features associated with the observed hackles did not indicate crack propagation in the induced direction. The fiber/matrix adhesion was poor.

Interlaminar Mode II Shear, 500°F/Dry. Optical magnification of the interlaminar shear fracture did not reveal the regular dull, matte surface or milky white appearance associated with Mode II shear fractures. SEM fractography revealed hackles and scallops on both the parallel and perpendicular tows (Fig. 4.4-98). Crack propagation direction could not be determined. Fiber/matrix adhesion was good.

Translaminar Tension, RT/Dry. Visual examination revealed tensile failure. SEM fractography of the tensile portion revealed fiber end features with fan patterns showing an overall propagation direction consistent with the mechanically induced crack direction (Fig. 4.4-99). Rivermarks and resin microflow in the resin-rich areas of the tensile zone also indicated crack growth direction consistent with the mechanically induced crack direction.

The carbon/PMR-15 specimens used for the translaminar tension and translaminar compression test were produced from quasi-isotropic laminates, unlike the 0/90 degree specimens used for the AS4/APC-2 and the IM7/8551 tests. Therefore, the carbon/PMR-15 specimen fractures reveal 45 degree plies not present in the other fractures.

Legend: F fiber; M matrix failure; R rivermarks
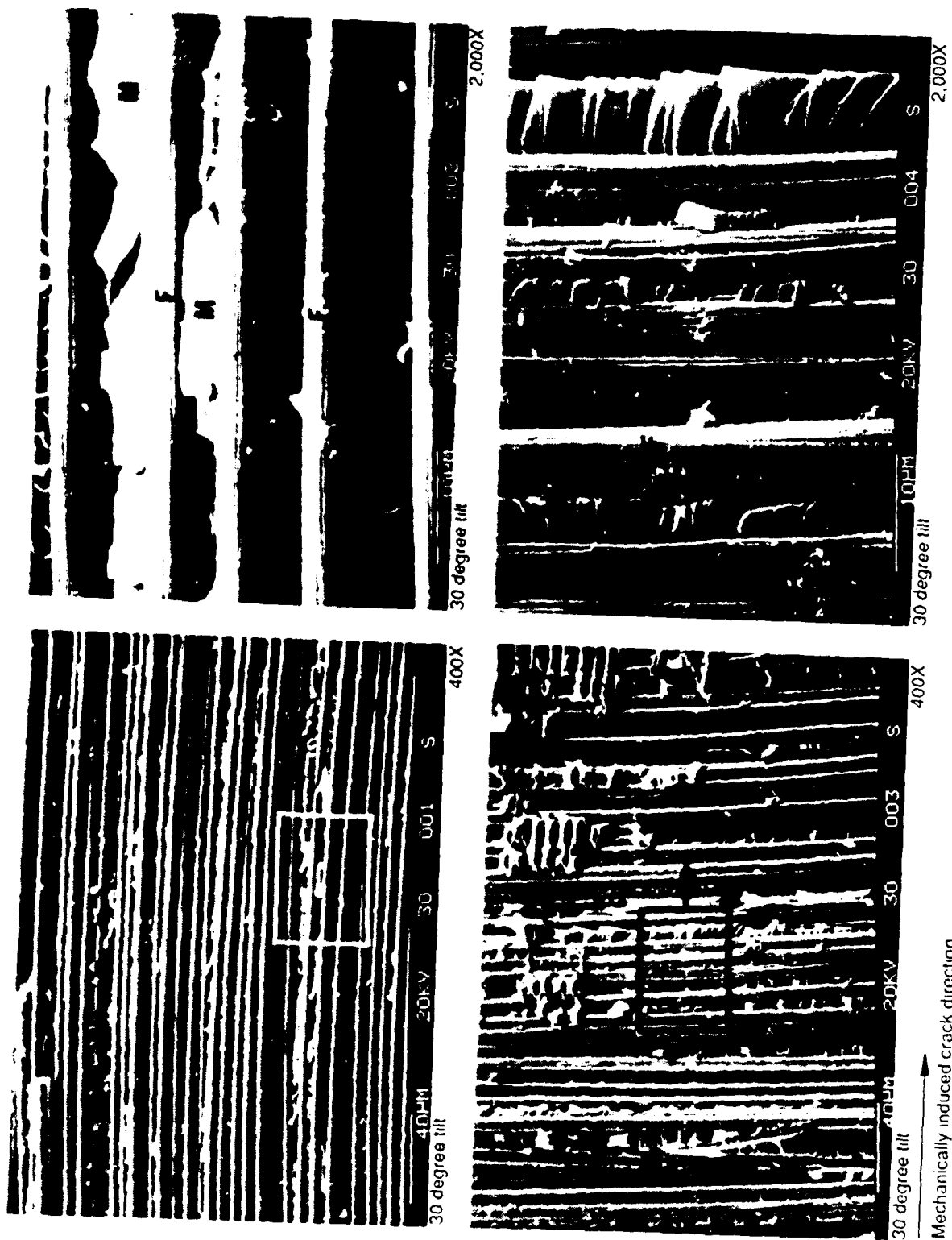
Figure 4.4-96. SEM Fractographs of 500 F/Dry, Mode I Fracture in C3K 8-HS/PMR-15

Legend: F fiber; H hackle; R rivermark

Mechanically induced crack direction
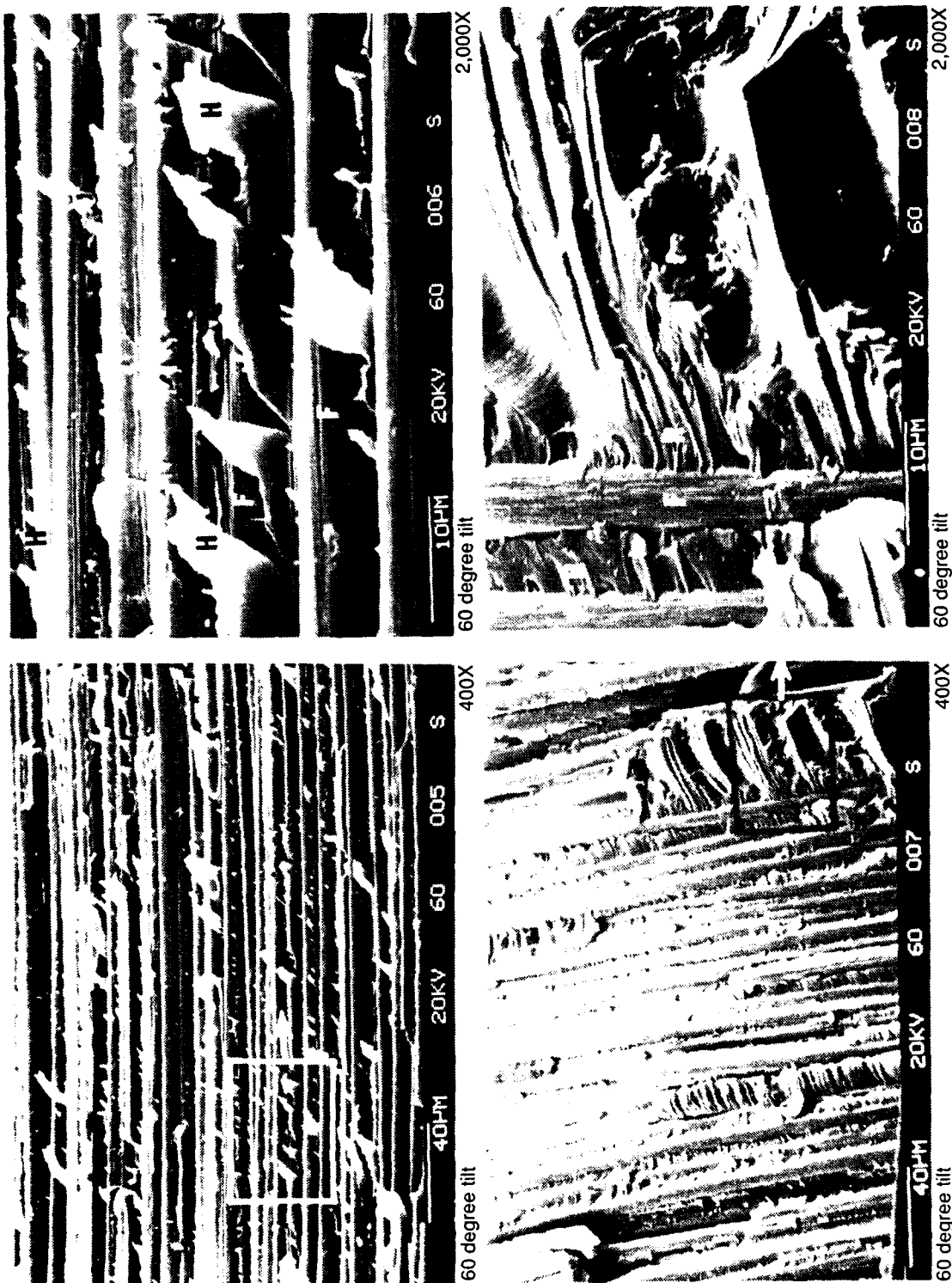
Figure 4.4-97 SEM Fractographs of Room Temperature, Mode II Fracture in C3K 8-HS/PMR-15

Legend:

F fiber matrix separation
H hackle

Mechanically induced
crack direction

Figure 4.4-98. SEM Fractographs of 500 F/Dry, Mode II Fracture in C3K 8-HS/PMR-15

Legend:

F   fiber fracture
M   matrix fracture

Mechanically induced
crack direction
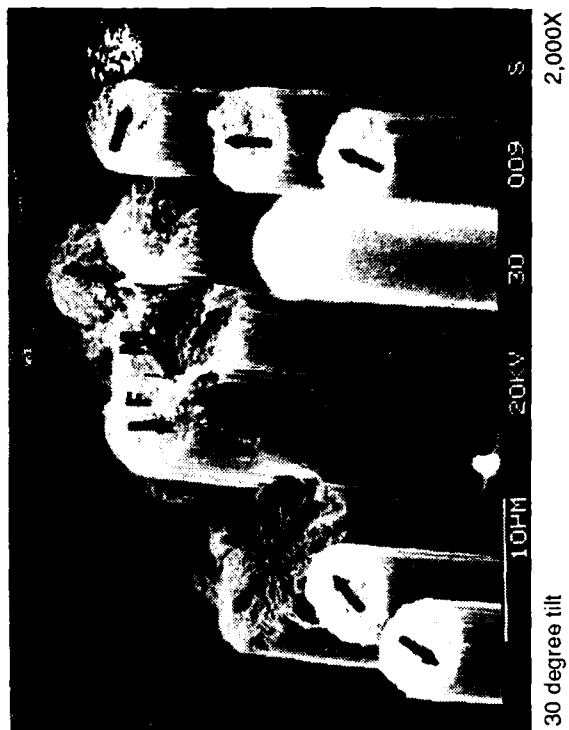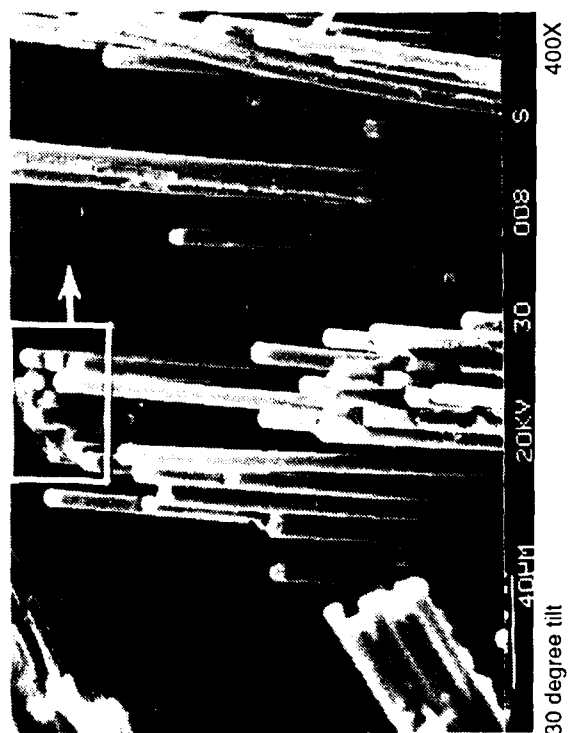
Figure 4.4-99. SEM Fractographs of Room Temperature/Dry, Translaminar Tension Fracture in C3K 8-HS/PMR-15

A substantial amount of 45 degree fibers were observed protruding from the surfaces. Fibers oriented at +45 degree were observed from one fracture surface and -45 degree fibers from the mating fracture surface. This condition is expected with tensile loading.

Macroscopically, the fractures appeared jagged due to the protruding plies. The most outstanding feature was the multitude of individual fibers protruding from the tensile loading. Due to the high fiber content utilized in carbon/PMR 15, fiber/matrix adhesion was poor and extensive fiber pullout was observed.

Translaminar Tension, 500°F/Dry. Optical examination revealed a rough translaminar surface. Only a quarter of the fracture was tensile, with the remainder being compressive. SEM fractography of the tensile region revealed small bundles of fibers on the fracture plane, due to fiber pullout, making determination of a propagation direction difficult (Fig. 4.4-100). However, the direction indicated by radial patterns found on fiber end fractures was consistent with the mechanically induced crack growth direction. Microbuckling and typical compressive fiber end fractures were observed on the compressive portion of the fracture. Fiber/matrix adhesion was fair.

Translaminar Compression, RT/Dry. Optical examination revealed both tensile and compressive regions, as was found on the translaminar tension specimens (Fig. 4.4-101). The compressive zone in this specimen was approximately a third of the fracture surface with the remainder being tensile. The compressive loading appeared to have initiated a tensile crack on the opposite surface which propagated toward the notch and intersected the compressive damage; SEM examination of the tensile portion revealed fiber end fractures that indicated propagation toward the opposite side. (In these specimens, the specified mechanically induced crack direction is from the notch outward). The compressive region revealed a debris-covered surface with fiber end fractures containing both tensile and compressive zones. Resin-rich fractures in the tensile zone revealed rivermarks, indicating propagation opposite to the mechanically induced crack direction, as expected.

As in the translaminar tension specimens, plies oriented at 45 degree were observed protruding from the fracture surface. However, plies oriented at both +45 and -45 were observed on each fracture surface, with the +45 degree plies dominating. Delaminations were observed in these protruding plies.

Macroscopically, the fractures were jagged due to protruding plies. The most outstanding features were the delaminated 45 degree plies which gave the appearance of

Mechanically induced
crack direction

30 degree tilt   2,000X

30 degree tilt   20X

30 degree tilt   400X

Figure 4.4.100   SEM Fractographs of 500 F Dry Transfamilar Tension Fracture in C3K 8 HS PMR 15
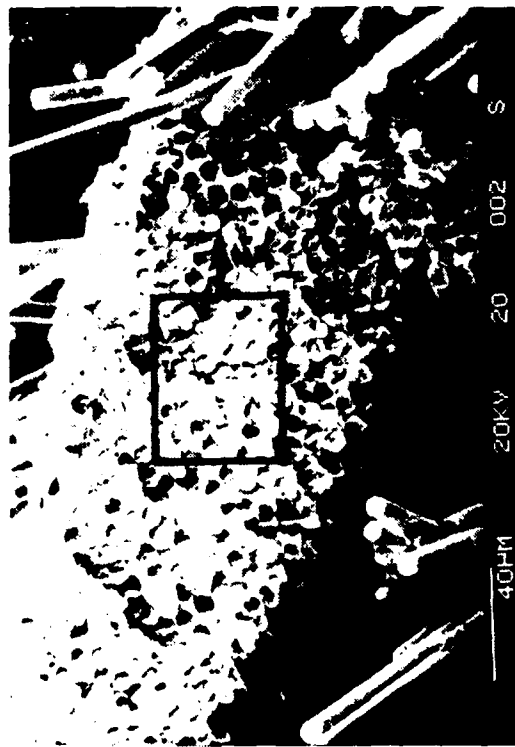
Legend:

C   compression
N   neutral axis
T   tension

Mechanically induced
crack direction

20X

20 degree tilt

400X

20 degree tilt

2,000X

20 degree tilt

Figure 4.4-101. SEM Fractographs of Room Temperature/Dry, Translaminar Compression Fracture in C3K 8-HS/PMR-15

strips of material. Fiber/matrix adhesion was poor, but fiber pullout was less pronounced than in the translaminar tension specimens.

Translaminar Compression, 500°F/Dry. Optical examination revealed a rough, partly compressive and partly shear fracture. Compressive failure was found on approximately half of the fracture and was located on the notched portion (as intended). Compressive fracture occurred predominantly on the 0 and 90 degree plies, while the shear portion of the fracture occurred on the 45 degree plies. SEM examination of the compression portion of the fracture revealed fiber end fractures which had been obliterated by fracture debris (Fig. 4.4-102). Microbuckling was observed. Hackles were found on the shear portion of the fracture. Fiber/matrix adhesion was poor.

Similarities between the carbon/PMR-15 and the AS4/3501-6 specimens examined under Tasks 2 and 3A include the presence of rivermarks and microflow in the resin-rich fracture, fan patterns on the fiber end fractures in the tensile zone (indicating crack growth direction), and the flat, debris covered surfaces on compressive failures.

The most striking difference, due to the presence of 45 degree plies, was the protruding off-axis fibers in the carbon/PMR-15 composite, which produced a more jagged surface. The relative sizes of the tensile and compressive zones on the fracture surfaces were strikingly dissimilar.

Multiphase Carbon/Resin (IM7/8551). Tests were conducted on IM7/8551 at RT/dry and hot/wet conditions.

Interlaminar Mode I Tension, RT/Dry. Optical examination revealed a smooth, reflective, mostly interlaminar fracture surface. Between plies, the epoxy and toughening phases were distinguishable. SEM fractography revealed rivermarks between fibers that had a longitudinal component consistent with the mechanically induced crack direction (Fig. 4.4-103). Fractography of the resin-rich region between plies revealed rivermarks in the epoxy, propagating around toughener particles. These rivermarks indicated crack growth consistent with the mechanically induced crack direction. The toughener particles did not reveal indications of crack growth direction. Some evidence of ductile fracture was observed adjacent to the toughener particles. Fiber/matrix adhesion appeared to be good.

Interlaminar Mode I Tension, 270°F/Wet. Optical examination of the fracture revealed a reflective surface, typical of Mode I fractures. SEM examination revealed rivermarks between fibers indicating propagation consistent with the mechanically

Mechanically induced
crack direction

30 degree tilt   20X
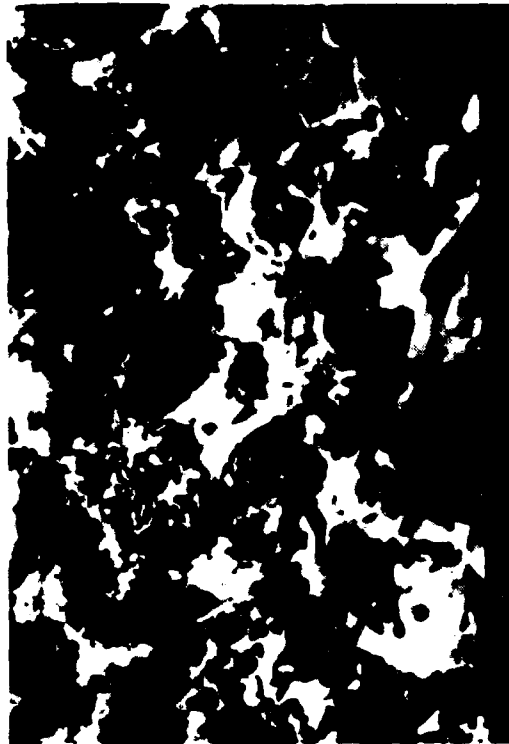
30 degree tilt   30 degree tilt
400X   2,000X

Figure 4.4.102. SEM Fractographs of 500 F Dry, Translaminar Compression Fracture in C3K 8 HS PMR 15.
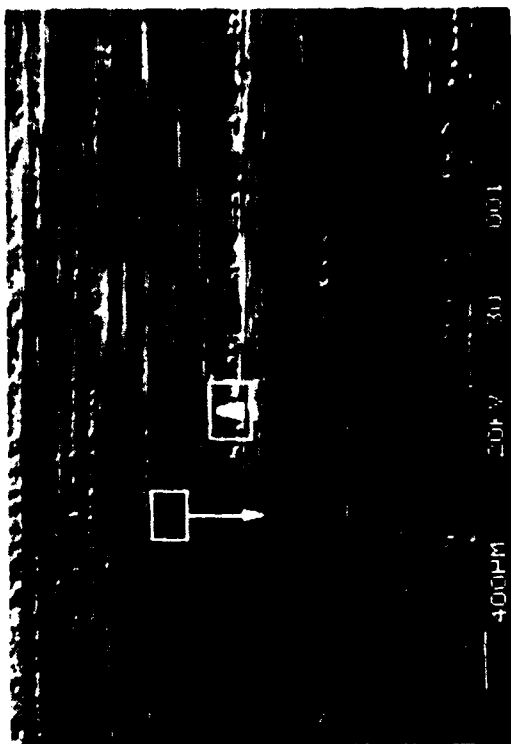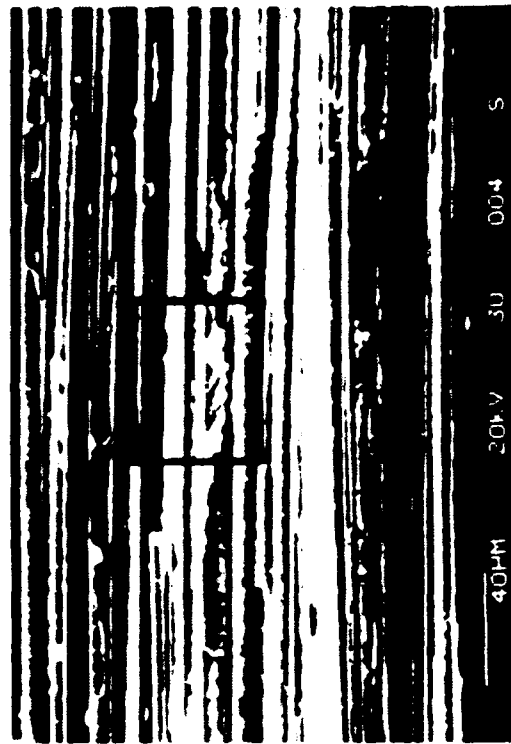
Legend:
F fiber
M matrix fracture
R rivermarks

Mechanically induced
crack direction

20X
30 degree tilt

400X
30 degree tilt

2,000X
30 degree tilt

Figure 4.4-103. SEM Fractographs of Room Temperature/Dry, Interlaminar Mode I Tension Fracture in IM 7/8551

induced crack direction (Fig. 4.4.-104). Rivermarks found in the resin-rich areas between plies also indicated a propagation consistent with the mechanically induced crack propagation. Fiber/matrix adhesion was good.

Interlaminar Mode II Shear, RT/Dry. Optical examination revealed typical Mode II shear fracture features. SEM fractography revealed hackles also typical of Mode II propagation (Fig. 4.4-105). Resin-rich regions between plies contained rivermarks indicating crack propagation in a direction consistent with the mechanically induced direction. These rivermarks are apparently the result of cracking through the ply due to offset crack planes. Bare fibers and matrix separation are normal for a shear failure.

Interlaminar Mode II Shear, 270°F/Wet. Optical examination revealed a typical Mode II shear fracture. SEM examination of the fracture revealed hackles and scallops typical of Mode II fractures (Fig. 4.4-106). The direction of mechanically induced crack propagation could not be determined.

Translaminar Tension, RT/Dry. Optical examination revealed a rough surface due to typical fiber pullout. SEM fractography revealed radial patterns on the fiber ends indicating a resultant crack direction consistent with the mechanically induced direction (Fig. 4.4-107). Fiber/matrix adhesion was good.

Translaminar Tension, 270°F/Wet. At 270°F/wet, the toughened epoxy became very ductile. The matrix was not stiff enough to support the fiber system. Rather than producing a translaminar fracture as intended, these specimens buckled to the extent that the test could not be continued. Therefore, fractography could not be performed.

Translaminar Compression, RT/Dry. Optical examination revealed a rough surface comprising approximately 55% compressive failure and 45% tensile failure. Large sections of the 0 degree plies were observed protruding from the compressive portion of the fracture surface. The individual fiber end fractures revealed a compressive zone, a tensile zone, and a neutral axis (Fig. 4.4-108). Fiber end fractures in the generated tensile crack revealed radial patterns which indicated crack direction consistent with the mechanically induced tensile crack direction. Fracture along the 90 degree plies produced some rivermarks with a longitudinal component also indicating crack propagation direction consistent with the mechanically induced direction. Fiber/matrix adhesion was good.

Translaminar Compression, 270°F/Wet. Optical examination of the fracture revealed approximately 70% compressive and 30% tensile zones. SEM examination of

Area A—30 degree tilt
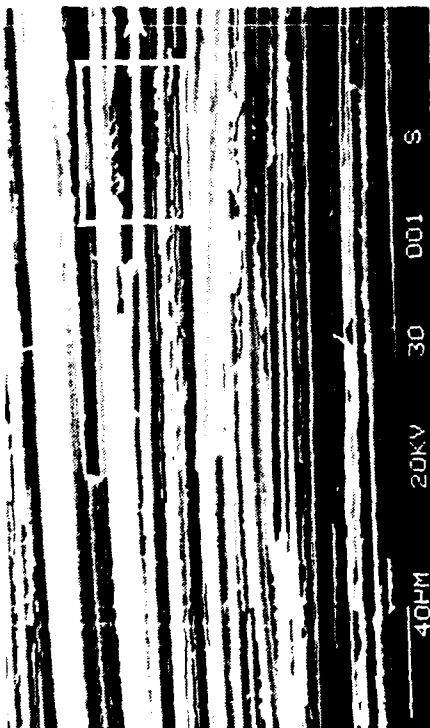
Area B—30 degree tilt

Mechanically induced crack direction

Legend: F fiber; R rivermarks; T toughener

Figure 4.4-104. SEM Fractographs of 270 F/Wet, Interlaminar Mode I Tension Fracture in IM-7/8551
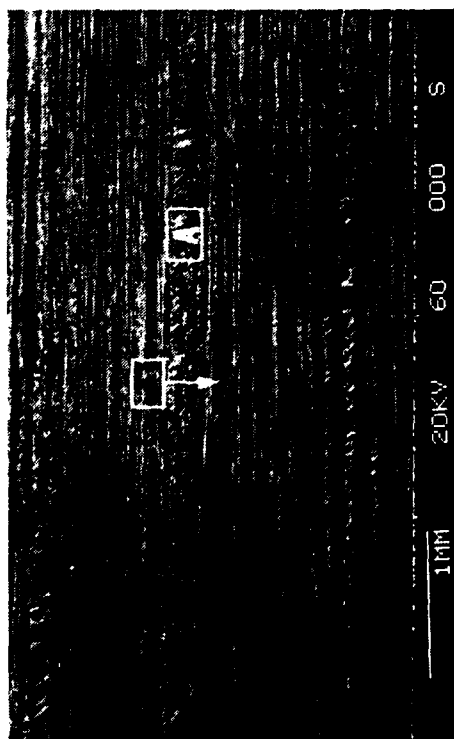
Legend:

F fiber
H hackle

Mechanically induced
crack direction

Figure 4.4-105. SEM Fractographs of Room Temperature, Interlaminar Mode II Shear Fracture in IM-7/8551

Mechanically induced crack direction

60 degree tilt

2,000X

60 degree tilt

20X

60 degree tilt

400X
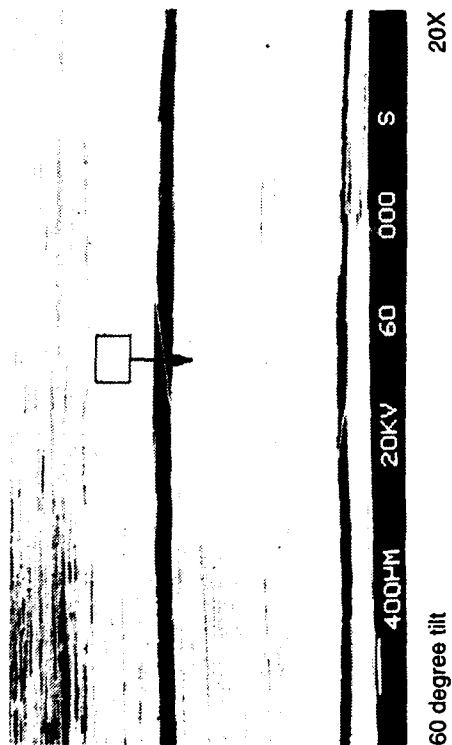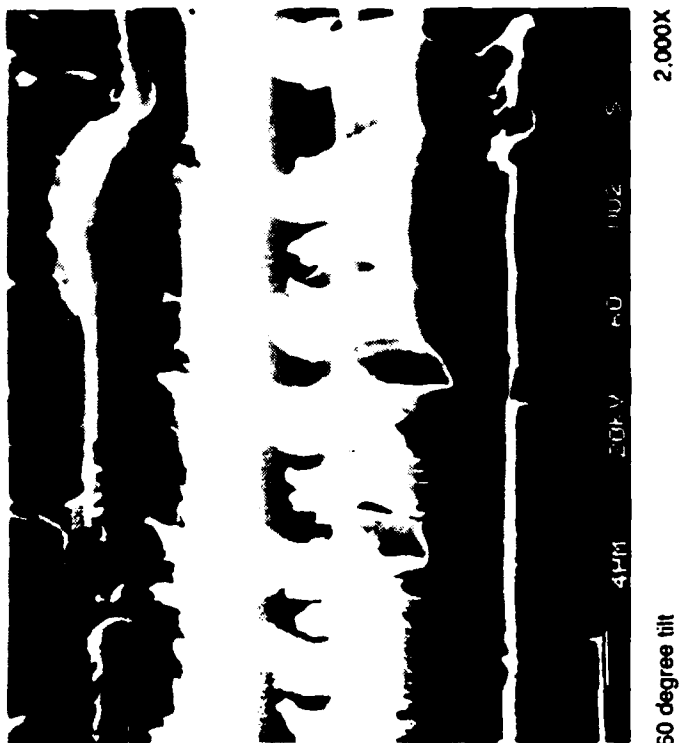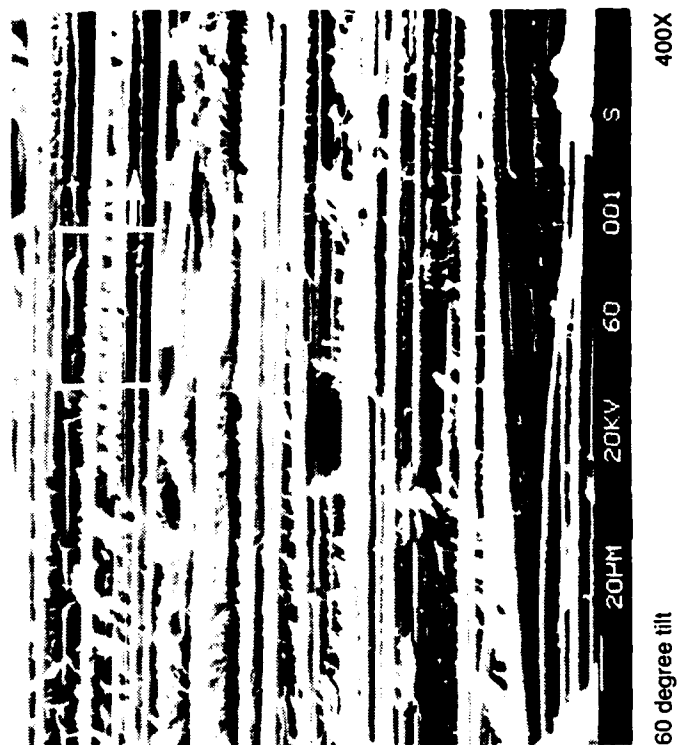
Figure 4.4-106. SEM Fractographs of 270 F/Wet, Interlaminar Mode II Shear Fracture in IM-7/8551
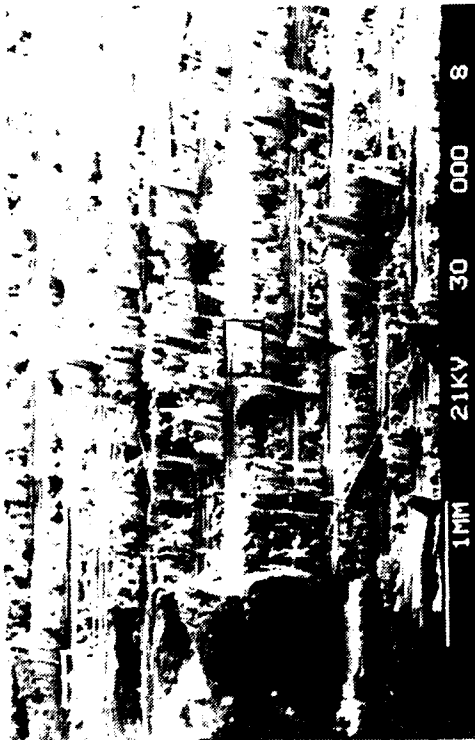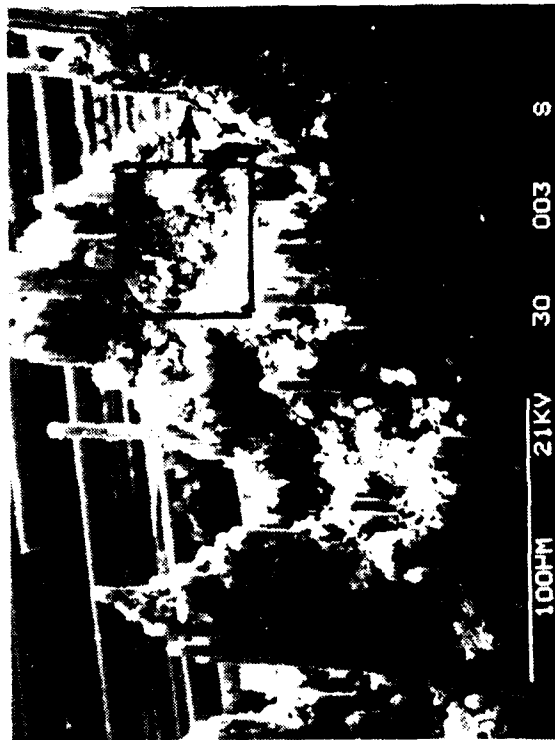
Mechanically induced crack direction

15 degree tilt

2,000X

30 degree tilt

400X

20X

30 degree tilt

100X

Figure 4.4-107. SEM Fractographs of Room Temperature, Translaminar Tension Fracture in IM-7/8551
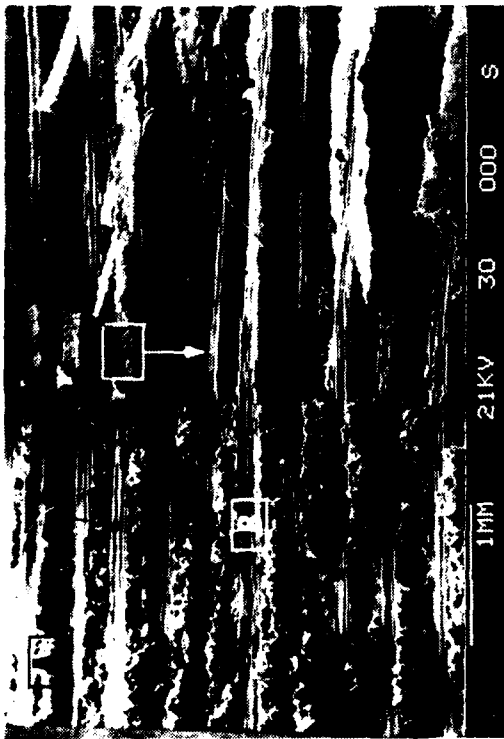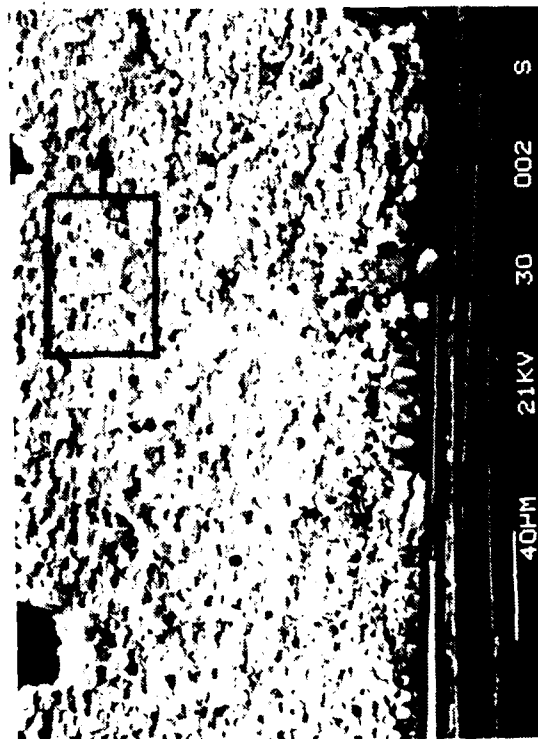
Legend:
N   neutral axis

Mechanically induced
crack direction

Figure 4.4-108. SEM Fractographs of Room Temperature, Translaminar Compression Fracture in IM-7/8551

the compressive region revealed typical fiber end fractures having tensile, compressive, and neutral zones (Fig. 4.4-109). The tensile portion of the fracture revealed substantial fiber pullout and it was not possible to examine enough fiber ends on a single plane to determine crack growth direction. Fiber/matrix adhesion was poor, as evidenced by the fiber pullout.

4.4.2.2 Epoxy-Based Materials

Boron/epoxy, Kevlar/epoxy, and glass/epoxy materials were evaluated. The materials were selected due to their current usage in production mode. Keeping the epoxy constituent constant and changing only the fiber type permitted determination of the effects of various fiber types on fracture surfaces.

Boron/Epoxy (Avco 5505/4). Various types of fractures produced under RT/dry and 270°F/wet conditions were examined.

Interlaminar Mode I Tension, RT/Dry. Visual observation of the fracture surface revealed five distinguishable planes of fracture leading to failure at the outer ply. The overall fracture surface span was only 2.5 inches from the crack initiation site. The boron/epoxy laminate exhibited a more complex crack path than those in carbon and glass fiber-reinforced epoxy laminates, mainly due to the resistance of the boron filaments to the crack front.

The fracture feature most frequently observed under the optical microscope was a resin flow line indicating the overall crack growth direction. This feature was similar to a rivermark (Fig. 4.4-110). The reflection of light from the boron-tungsten filament made it difficult to see some of the fine details of the critical fracture features.

SEM analysis showed both rivermarks and resin microflow lines on the fracture surface (Fig. 4.4-111). This indicated that the crack direction could be identified from these microscopic features.

Interlaminar Mode I Tension, 270°F/Wet. Visual examination revealed a fracture surface on only one or two stepped planes. This was in contrast to the RT specimen, which fractured over many stepped planes. The 270°F/wet condition made the resin ductile and prevented a multiple-plane fracture. The optical photomicrograph showed resin microflow lines similar to those observed in the RT/dry specimen (Fig. 4.4-112).

Figure 4.4-113 shows the SEM fractographs of the interlaminar Mode I tension specimen exposed to humidity and tested at 270°F. The fracture surface showed

Mechanically induced
crack direction
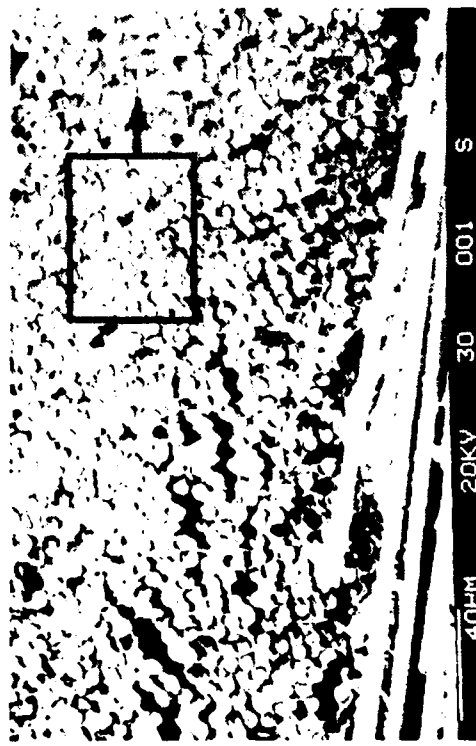
30 degree tilt

Figure 4.4-109. SEM Fractographs of 270 F/Wet, Translaminar Compression Fracture in IM-7/8551

400X

100X

FEP crack
starter region

End of
controlled
fracture

Mechanically
induced
crack
direction
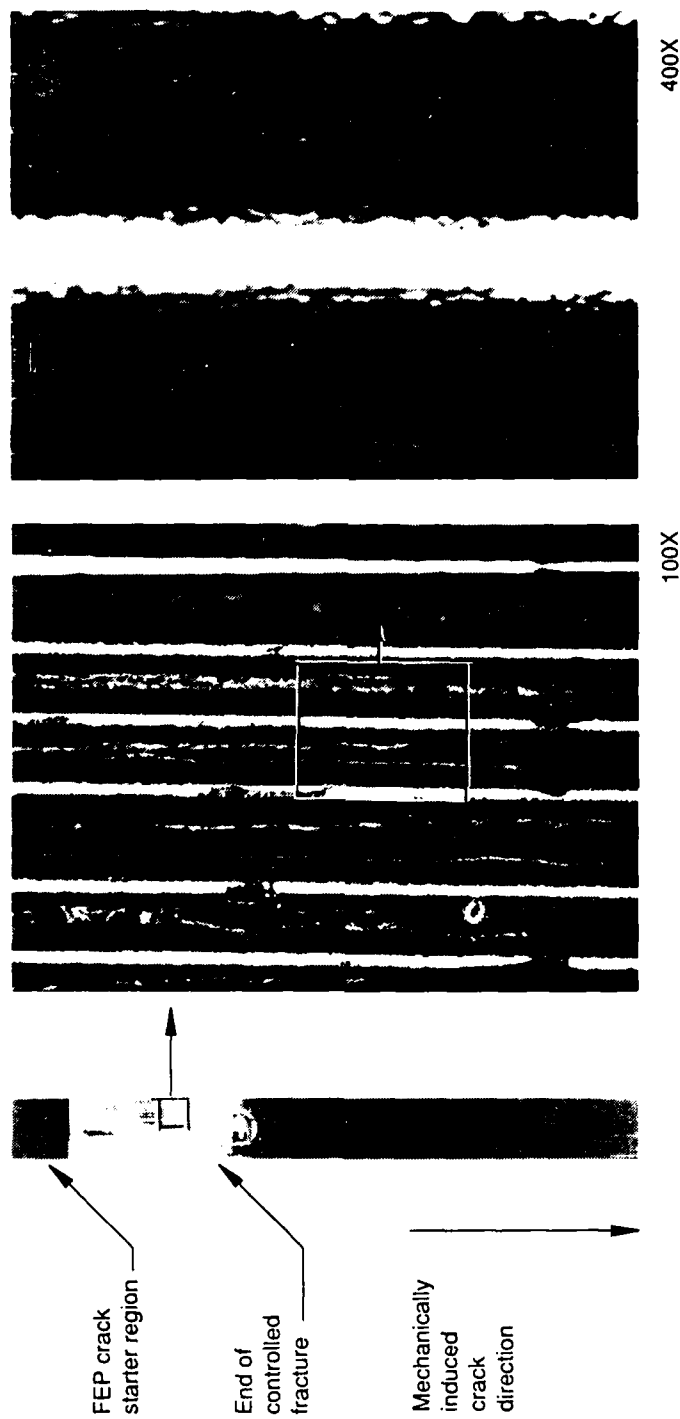
Figure 4.4-110. Optical Photomicrographs of Room Temperature, Interlaminar Mode I Tension, 0/90 Fracture in Boron/Epoxy
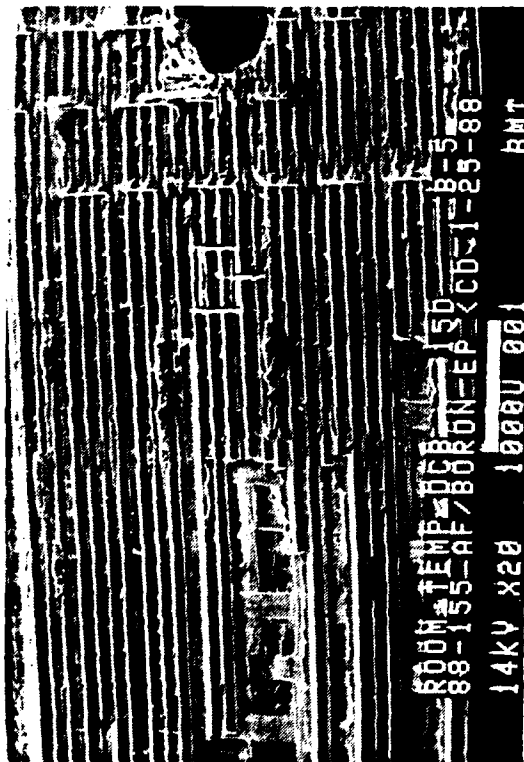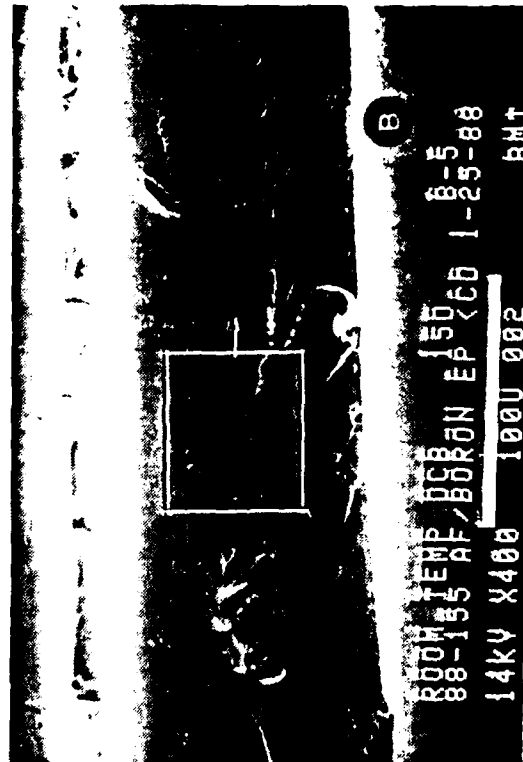
Legend:

B boron tungsten filament
R rivermark

Mechanically induced
crack direction
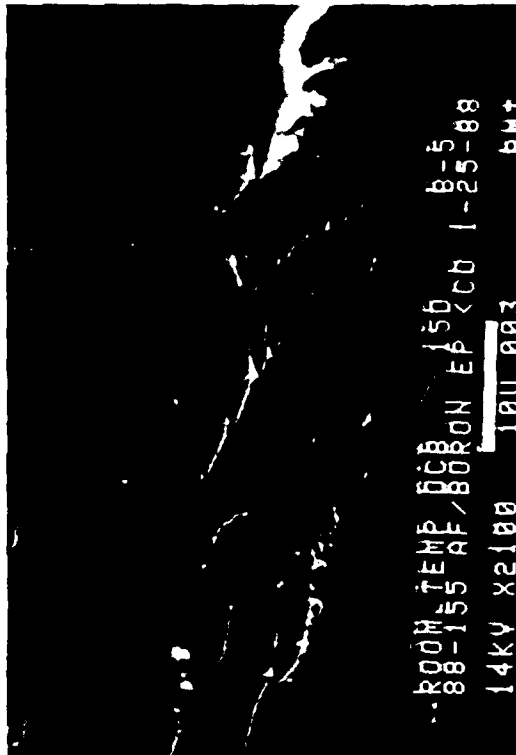
Figure 4.4-111. SEM Fractographs of Room Temperature, Interlaminar Mode I Tension Fracture in Boron Epoxy

400X

100X

Mechanically induced
crack growth direction

FEP crack
starter region

End of
controlled
fracture

Figure 4.4-112. Optical Photomicrographs of 270 F/Wet, Interlaminar Mode I Tension, 0/90 Fracture in Boron/Epoxy
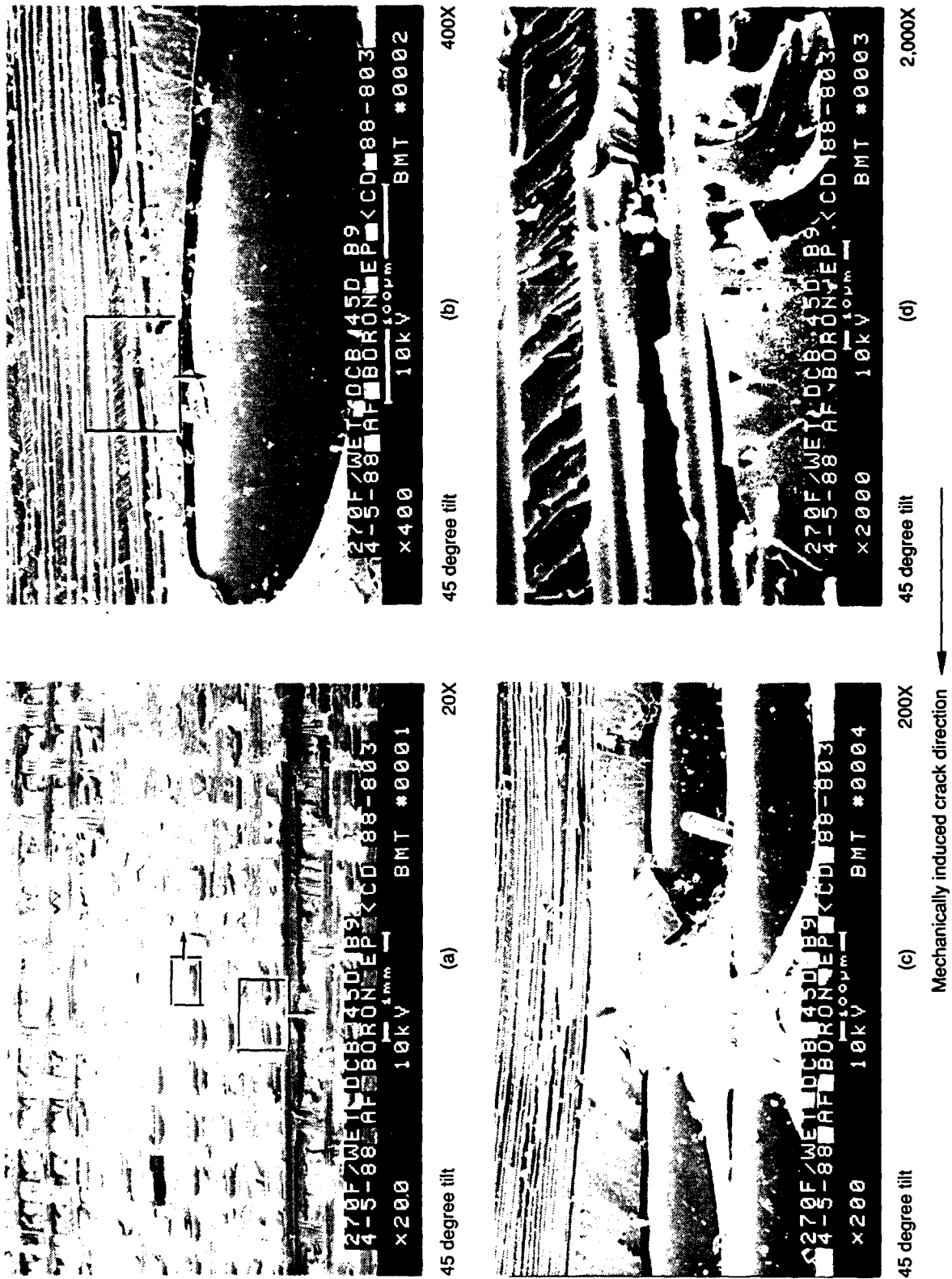
Figure 4.4-113. SEM Fractographs of 270 F/Wet, Interlaminar Mode I Tension Fracture in Boron/Epoxy

rivermarks in some regions. The major difference between the RT/dry and 270°F/wet specimens was the latter's very poor adhesion at the fiber/matrix interface.

Interlaminar Mode II Shear, RT/Dry. Under visual examination, the fracture surface was dull and milky due to the formation of hackles. This appearance was similar to that observed in previous work on the carbon-fiber reinforced epoxy system. Due to difficulties in creating a large area of interlaminar Mode II shear fracture surface for this material system, we were unable to provide a macrophotograph of the specimen. However, SEM analysis was performed on the available specimen. The fracture feature revealed resembled the hackles typically observed in the model material system, AS4/3501-6 (Fig. 4.4-114).

Interlaminar Mode II Shear, 270°F/Wet. Visual examination revealed a fracture surface delaminated at various plies. Hackle formations were observed under the optical microscope (Fig. 4.4-115).

Figure 4.4-116 illustrates the SEM fractograph of the interlaminar Mode II shear specimen exposed to humidity and tested at 270°F. The fracture surface showed hackles throughout the specimen. Poor fiber/matrix adhesion was observed, which is typical for shear fractures.

Translaminar Tension, RT/Dry. Visual inspection revealed a region of numerous protruding fibers. The protruding fibers exhibited a white, powder-like texture and the fibers perpendicular to them were silvery.

The SEM analysis showed that the adhesion at the interface between the boron fibers and the epoxy matrix was poor at the time of the fracture. This was also evidenced by the fiber pullouts (Fig. 4.4-117).

Unlike those in glass and carbon fibers, the radial patterns on the boron fiber ends initiated at the tungsten core/boron interface (Fig. 4.4-118). This phenomenon may be due to the lower interfacial shear strength of the tungsten core/boron interface in comparison with the boron fiber/epoxy interface. The fracture features radiating from the center of the boron-tungsten fiber could not be used to determine the crack propagation direction. Cracks in glass and carbon fibers typically initiate at the outer surface and propagate from one fiber to another, and the average of the individual crack directions indicates the overall crack direction.

Translaminar Tension, 270°F/Wet. Visual examination revealed a fracture surface with numerous protruding fibers. Under the wide-field macroscope, it was evident that
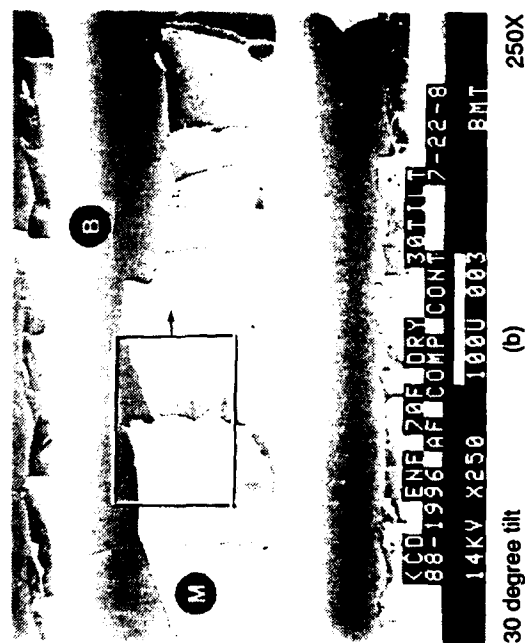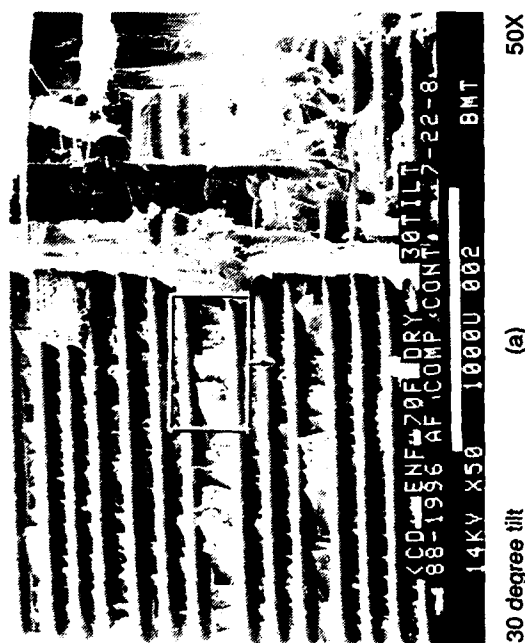
Legend:
B boron filament
M matrix fracture

Mechanically induced
crack direction
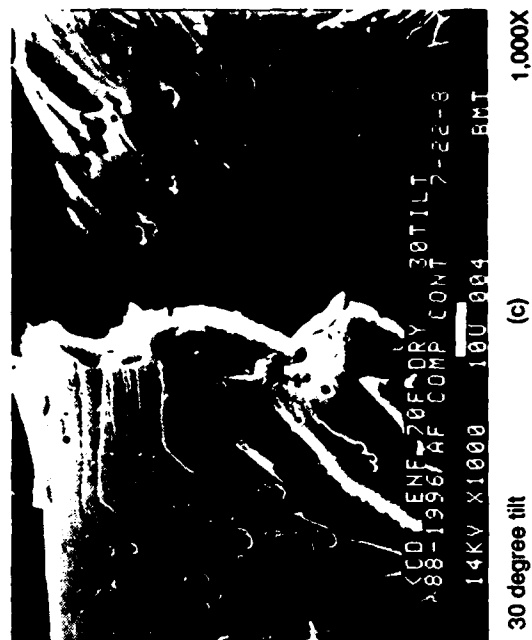
Figure 4.4-114. SEM Fractographs of Room Temperature/Dry, Interlaminar Mode II Shear, 0/90 Fracture in Boron/Epoxy

400X

100X

Mechanically induced
crack growth direction

FEP crack
starter region

End of
controlled
fracture
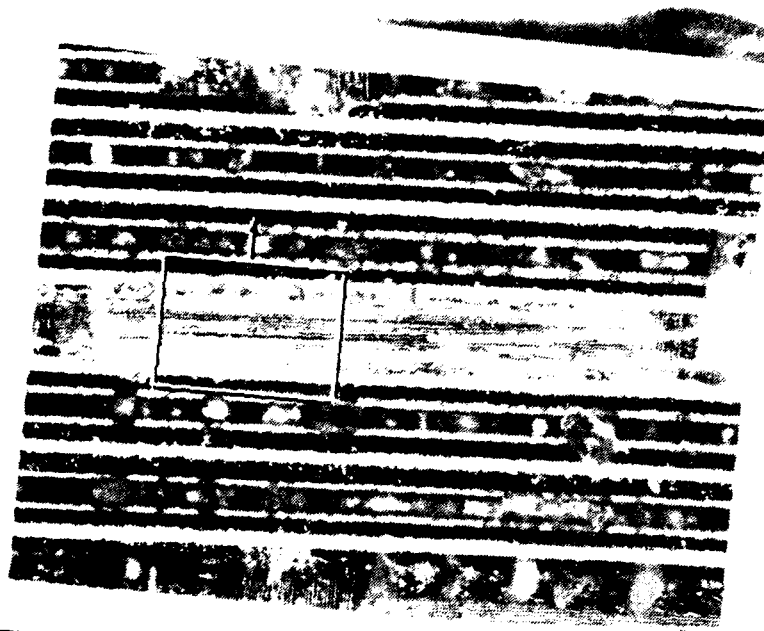
Figure 4.4-115. Optical Photomicrographs of 270 F/Wet, Interlaminar Mode II Shear, 0/90 Fracture in Boron/Epoxy

Mechanically induced crack direction

(b) 50X
45 degree tilt
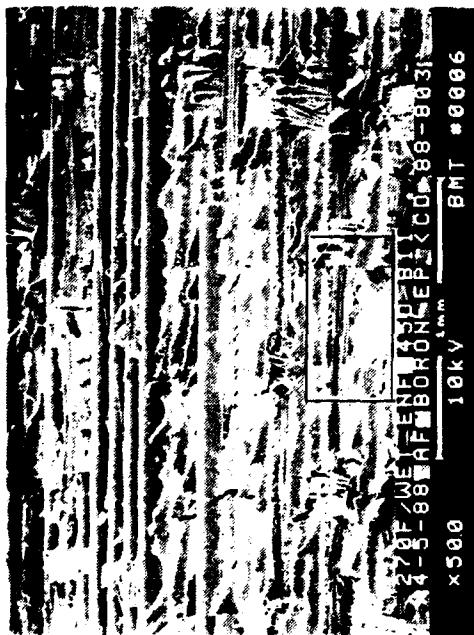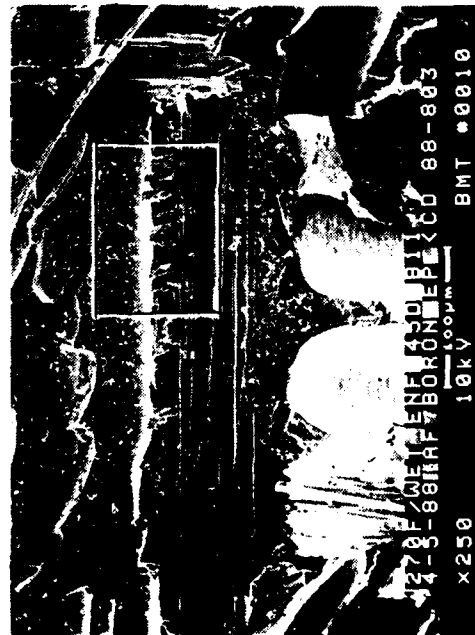
(b) 250X
45 degree tilt

(c) 1,000X
45 degree tilt

Figure 4.4-116. SEM Fractographs of 270 F/Wet, Interlaminar Mode II Shear Fracture in Boron/Epoxy
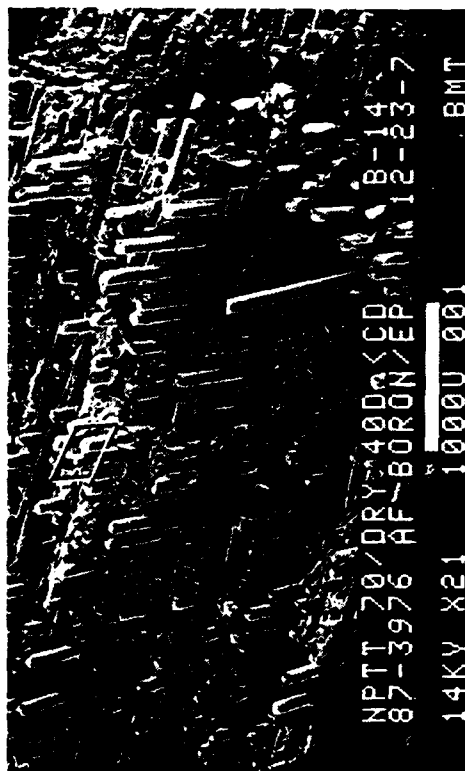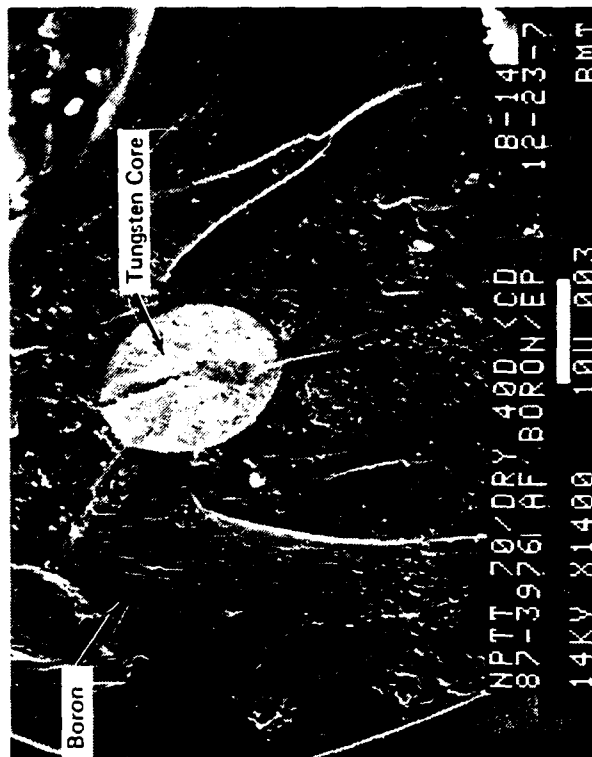
Figure 4.4-117. SEM Fractographs of Room Temperature/Dry, Translaminar Tension Fracture in Boron/Epoxy
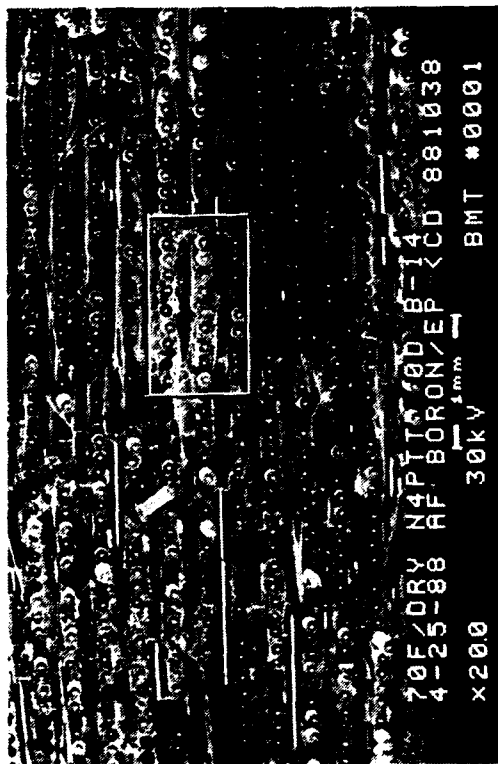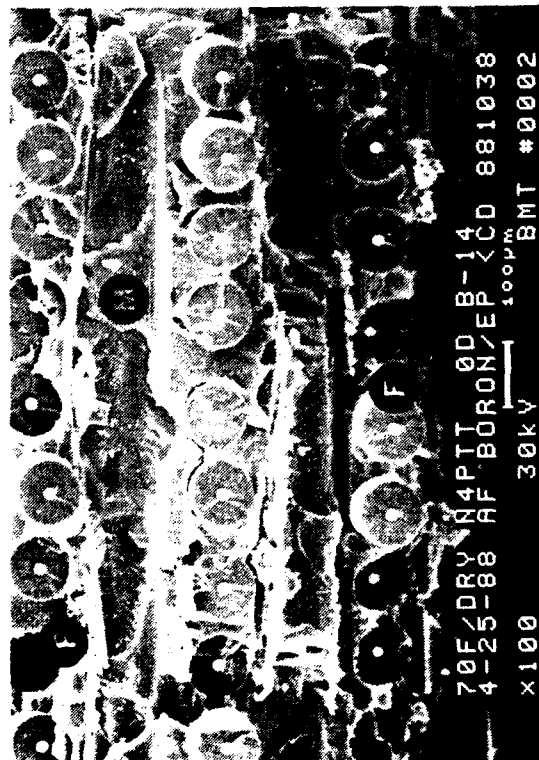
Legend:

P fiber pullout
F fiber end fracture
M matrix fracture

Mechanically induced
crack direction
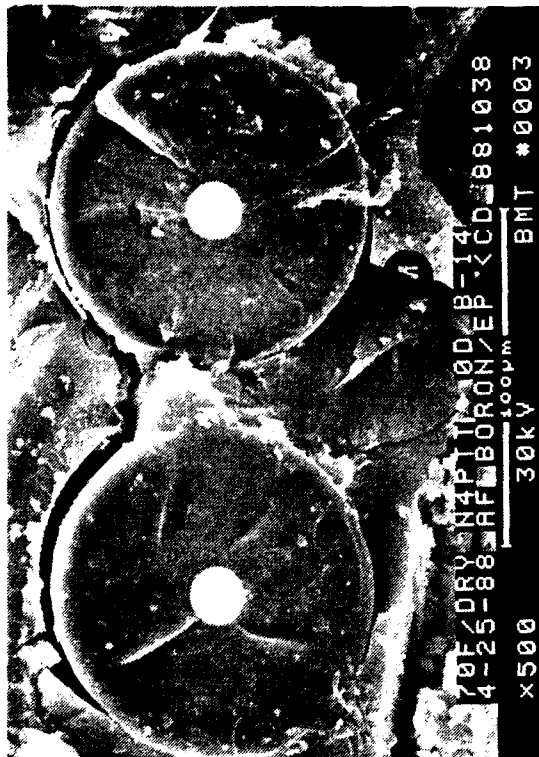
Figure 4.4-118. SEM Fractographs of Room Temperature/Dry, Translaminar Tension Fracture in Boron/Epoxy; Shown at 0 Degree Tilt

the fracture was fiber-dominated. The fracture surface exhibited many holes in the matrix, indicative of extensive fiber pullout (poor fiber/matrix adhesion). Additionally, the fibers pulled away from the matrix were much longer than those in the RT/dry specimen. This also indicating poor fiber/matrix adhesion (Fig. 4.4-119).

The resin around the boron filaments exhibited such features as rivermarks that could be used for crack mapping. The fracture features on the fiber ends appeared similar to the features observed on the translaminar tension RT/dry specimen. The radial pattern could not be used to determine the overall crack direction. The fiber surfaces were smooth and there were no traces of residual resin.

Further studies may need to be conducted to determine whether radial patterns on the boron fiber ends or the resin fracture features around the boron filament are usable for crack direction indication or crack mapping.

Translaminar Compression, RT/Dry. Visual observation revealed numerous protruded boron-tungsten filaments. SEM analysis shown in Figures 4.4-120 and 4.4-121 confirmed the visual result. Unlike the glass and carbon fibers, the boron-tungsten fibers exhibited similar fracture features in both tension and compression specimens. This may be due to the higher ductility of the boron-tungsten fibers in comparison with the glass and carbon fibers. This eliminates the microbuckling effects (from compression) typically exhibited in fibers with higher stiffness. The neutral axes observed on the glass and carbon fiber ends were not present on the boron-tungsten translaminar compression specimen tested under RT/dry condition.

Translaminar Compression, 270°F/Wet. Visual examination revealed a fracture surface with numerous protruding fibers, similar to the fracture surface of the tension specimen. The ends of the boron filaments exhibited radial patterns similar to those of the translaminar compression RT/dry specimen (Fig. 4.4-122). Boron fiber pullouts exhibited little residual resin on the fiber due to weak fiber/matrix adhesion; also, the boron fiber surface was not as smooth as is typical of carbon fiber (Fig. 4.4-123). This is due to the chemical deposition process of boron onto the tungsten core. The neutral axes typically observed on glass and carbon fiber ends, a result of microbuckling, were not present on the boron-tungsten translaminar compression specimen tested under 270°F/wet conditions.

Kevlar/Epoxy (49/F155). Fractures of various types were induced under RT/dry and hot/wet conditions.
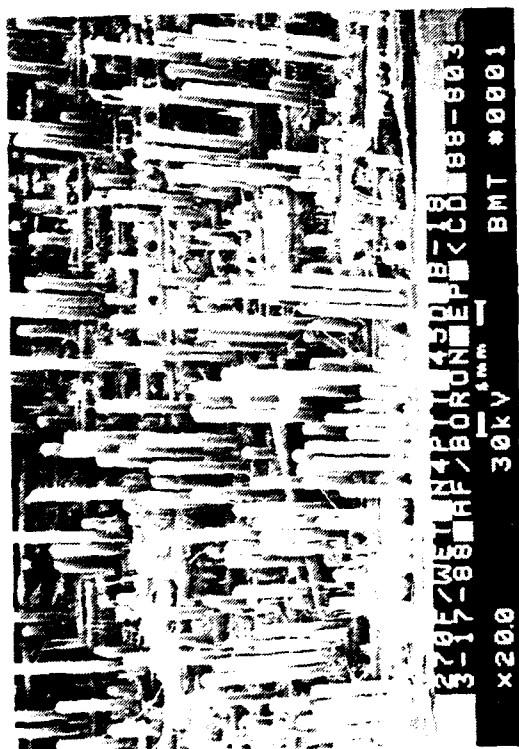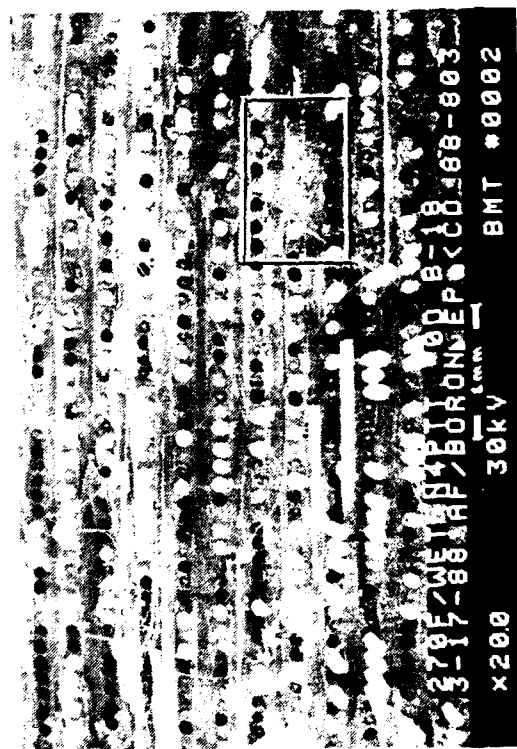
Mechanically induced crack direction

Interlaminar resin fracture (i.e. rivermarks)

(a) 45 degree tilt

(b) 0 degree tilt

(c) 0 degree tilt

Figure 4.4-119. SEM Fractographs of 270 F/Wet, Translaminar Tension Fracture in Boron/Epoxy; Shown at 45 and 0 Degree Tilts
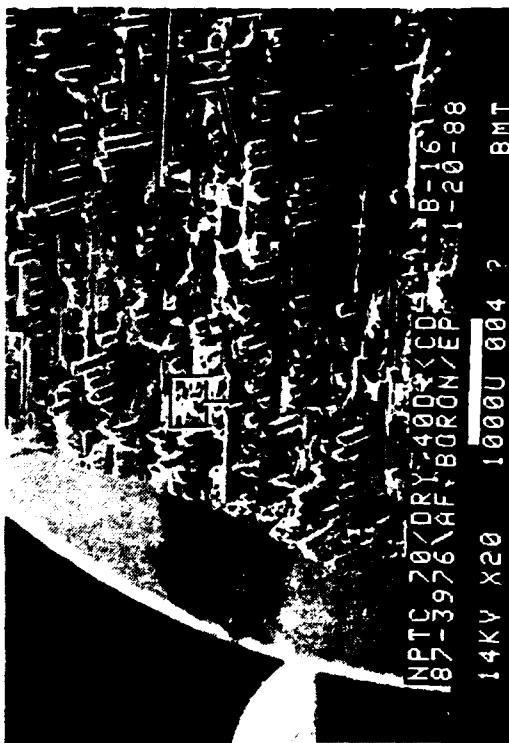
Mechanically induced crack direction

40 degree tilt   20X

40 degree tilt   400X

40 degree tilt   1,000X

Figure 4.4-120. SEM Fractographs of Room Temperature/Dry, Transiaminar Compression Fracture in Boron Epoxy. Shown at 40 Degree Tilt

Mechanically induced crack direction →
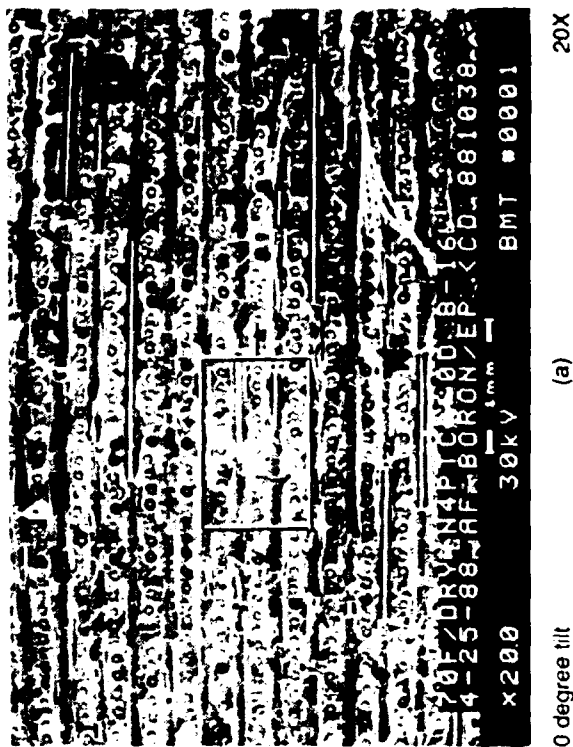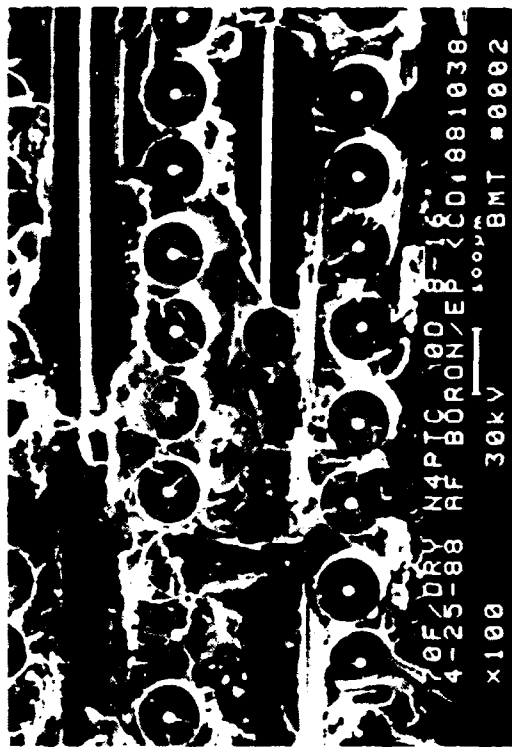
(a) 0 degree tilt   20X

(b) 0 degree tilt   100X

(c) 0 degree tilt   500X

Figure 4.4-121. SEM Fractographs of Room Temperature/Dry, Translaminar Compression Fracture in Boron/Epoxy: Shown at 0 Degree Tilt
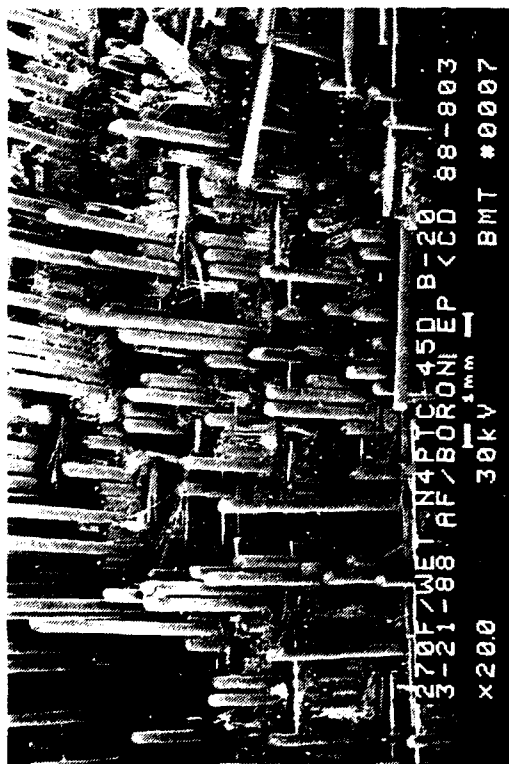
Mechanically induced crack direction

(a) 20X   45 degree tilt
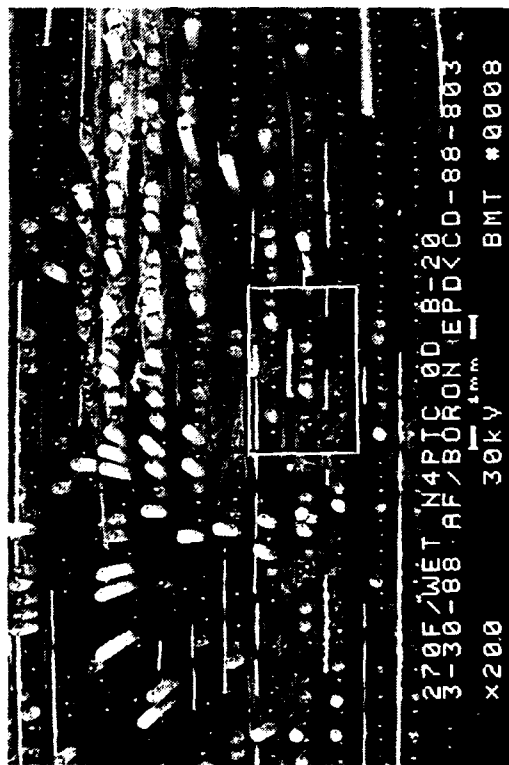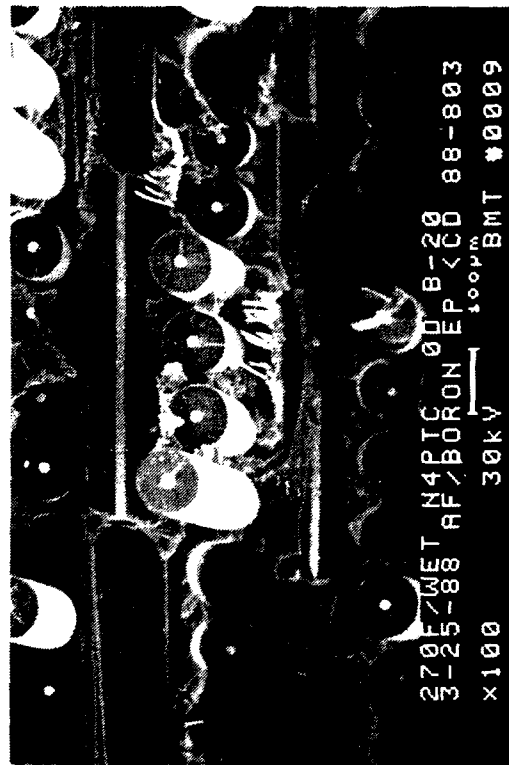
(b) 20X   0 degree tilt

(c) 100X   0 degree tilt

Figure 4.4-122. SEM Fractographs of 270 F/Wet, Translaminar Compression Fracture in Boron/Epoxy
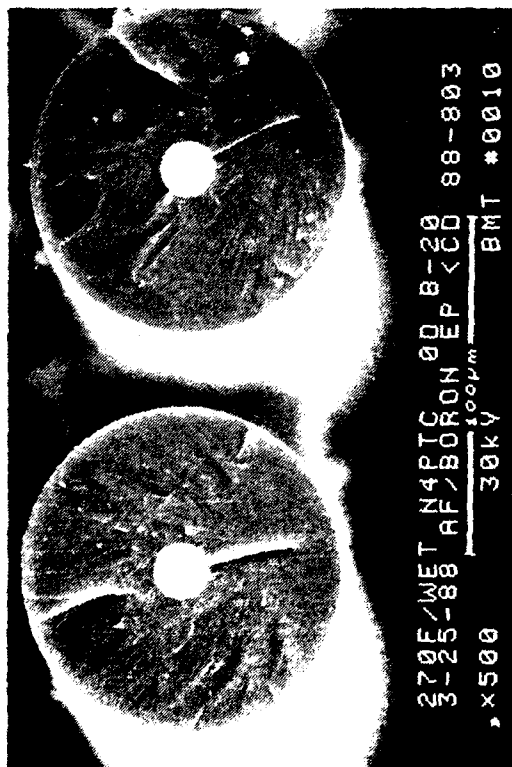
Mechanically induced crack direction
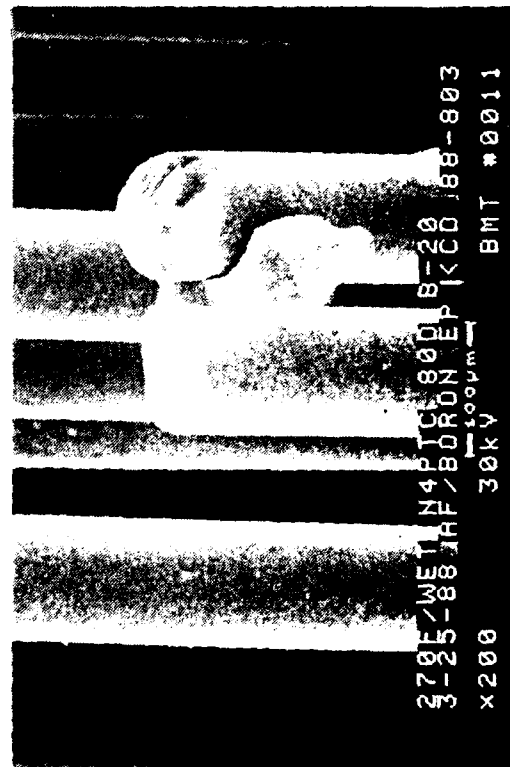
(a) 500X 0 degree tilt
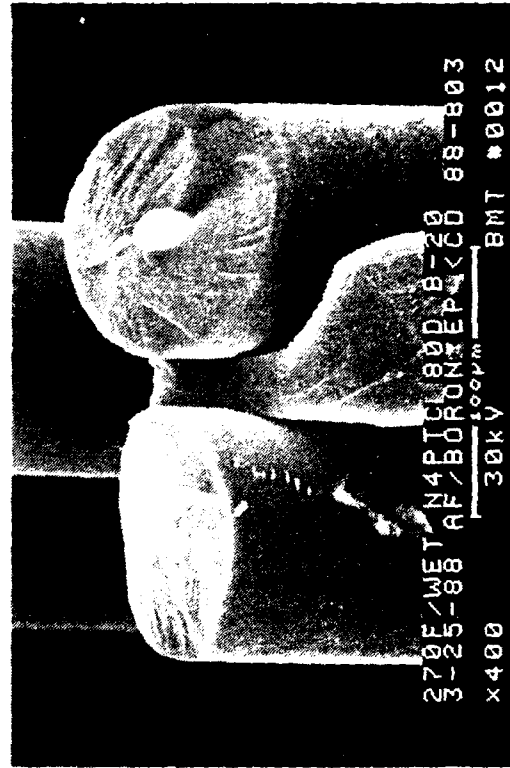
(b) 200X 80 degree tilt

(c) 400X 80 degree tilt

Figure 4.4-123. SEM Fractographs of 270 F/Wet, Translaminar Compression Fracture in Boron/Epoxy: High Magnification

Interlaminar Mode I Tension, RT/Dry. The RT/dry interlaminar fracture lacked rivermarks commonly observed in other epoxy-based interlaminar Mode I tension fractures (such as in glass or carbon-fiber reinforced specimens). There were no fracture features at the node or the center of the weave that could be used for determining the crack propagation direction (Fig. 4.4-124 and 4.4-125). The fiber/matrix adhesion was poor.

Interlaminar Mode I Tension, 200°F/Wet. Visual examination of the 200°F/wet interlaminar Mode I tension fracture revealed a smooth, shiny surface with patches of flakey resin on the fracture. The fractures of the RT/dry and 200°F/wet specimens appeared almost identical except for an apparent degradation in the patches of flakey resin on the 200°F/wet fracture. The fiber/matrix adhesion was poor as evidenced by the smooth fracture with fiber imprints. The difference between the RT/dry and the 200°F/wet specimens was the greater extent of fiber pullouts and fiber imprints in the 200°F/wet. This indicated weaker fiber/matrix adhesion than in the RT/dry specimen (Fig. 4.4-126).

Interlaminar Mode II Shear, RT/Dry. Visual observation revealed a surface with Kevlar fibers pulled away from the resin matrix. Optical examination did not provide much information due mainly to the translucence of the Kevlar fibers.

SEM analysis showed hackle formation and an adhesive-type fracture evidenced by the clean and smooth imprints of the fibers (Fig. 4.4-127).

Interlaminar Mode II Shear, 200°F/Wet. Visual examination of the interlaminar Mode II shear 200°F/wet fracture revealed a dull, rough surface similar to that of the RT/dry fracture. In addition, there were large tears in the fracture surface from what appears to have been a high energy fracture (Fig. 4.4-128). The energy of this fracture may have been due to the increase in toughness of the resin matrix due to the moisture exposure. The hackles were formed in a ductile fashion evidenced by the taffy-pull type fracture (commonly observed in metal fractures). This type of microscopic fracture behavior is due to an intrinsic characteristic of the epoxy matrix, which becomes more ductile when exposed to elevated temperature and humidity. The fiber/matrix adhesion was poor as evidenced by the smoothness of the resin fracture and the fiber imprints. A greater extent of fiber pullout (due to weak fiber/matrix adhesion) and more distinct hackles were observed in the 200°F/wet specimen than in the RT/dry specimen.
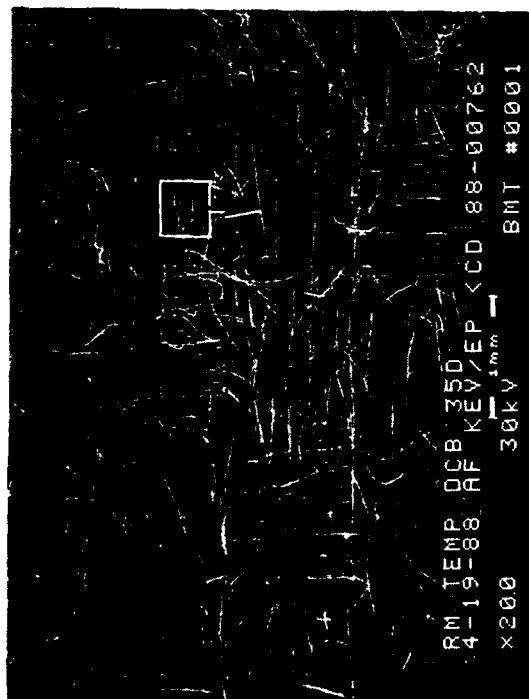
Legend:

L loose (stray) fibers
M matrix fracture
F fiber matrix fracture

Mechanically induced
crack direction
→

35 degree tilt

20X
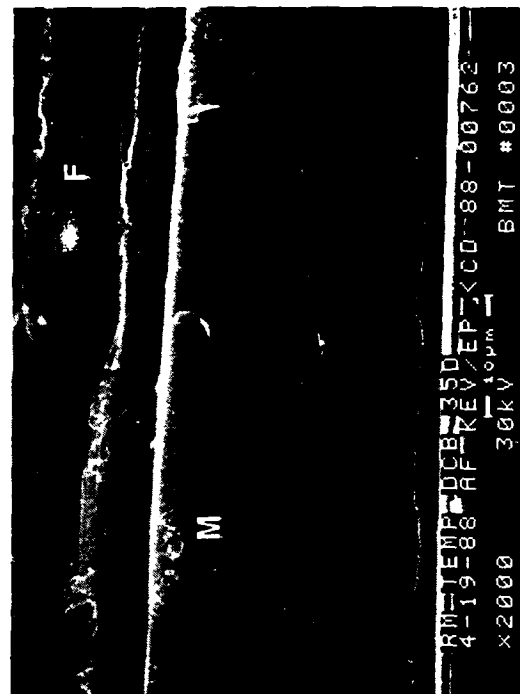
400X

2,000X

Figure 4.4-124. SEM Fractographs of Room Temperature, Interlaminar Mode I Tension Fracture in Kevlar/Epoxy (at the Center of the Weave)

Mechanically induced crack direction

(a) 20X

(b) 400X

(c) 2,000X

Figure 4.4-125. SEM Fractographs of Room Temperature, Interlaminar Mode I Tension Fracture in Kevlar/Epoxy (at the Node)
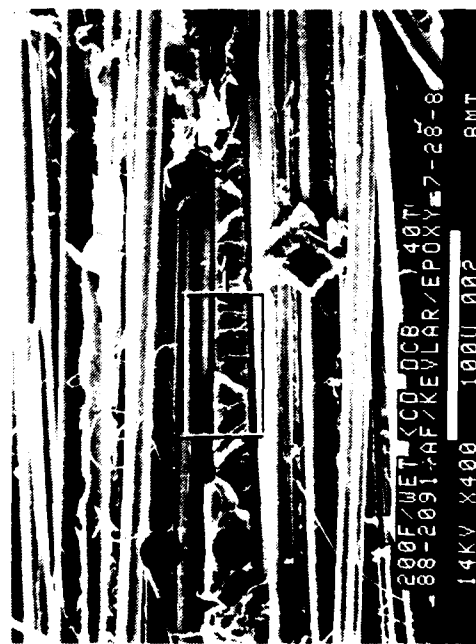
Legend:

F fiber matrix fracture
M matrix fracture

Mechanically induced
crack direction

(a) 20X

(b) 400X

(c) 2,000X

Figure 4.4-126. SEM Fractographs of 200 F/Wet, Interlaminar Mode I Tension Fracture in Kevlar/Epoxy
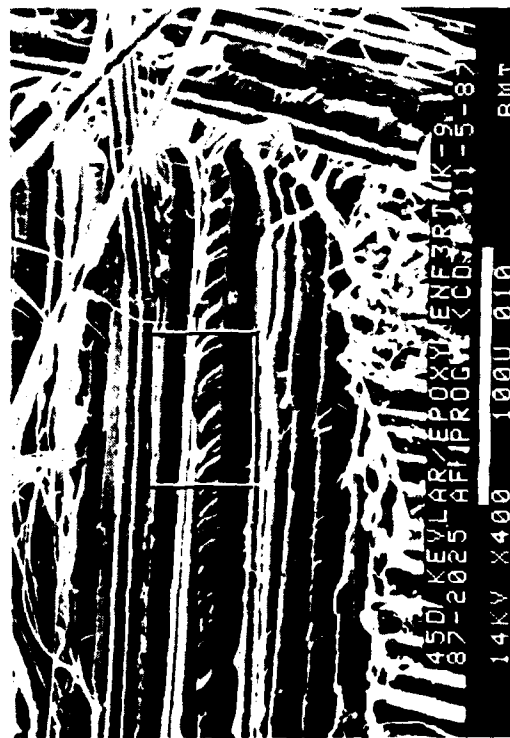
Legend:

F fiber matrix fracture
H hackles

Mechanically induced
crack direction
→

45 degree tilt   20X

45 degree tilt   400X

45 degree tilt   2,000X

Figure 4.4-127. SEM Fractographs of Room Temperature, Interlaminar Mode II Shear Fracture in Kevlar/Epoxy Fabric
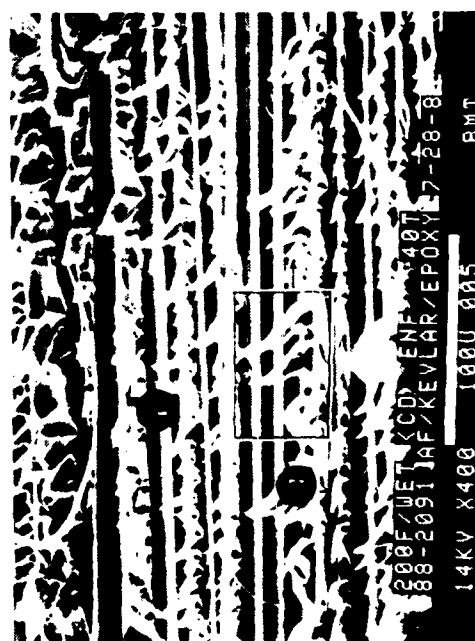
Legend:

F   fiber matrix fracture
H   hackle

Mechanically induced
crack direction →

(a)   20X

(b)   400X

(c)   2,000X

Figure 4.4-128. SEM Fractographs of 200 F/Wet, Interlaminar Mode II Shear Fracture in Kevlar/Epoxy

Translaminar Tension, RT/Dry. Visual and optical observation revealed a broom-like fracture surface indicating extensive fiber-dominated fracture. Under SEM, the fiber/matrix interface showed a very smooth surface and the fiber ends showed no sign of any crack direction (Fig. 4.4-129).

Translaminar Tension, 200°F/Wet. Figure 4.4-130 shows the SEM fractographs of a 200°F/wet translaminar tension fracture exhibiting a similar appearance to the RT/dry fracture, with no observable features, to differentiate environmental effects.

Both RT/dry and 200°F/wet specimens showed broom-like fibrillation of the Kevlar fibers. The Kevlar fibers failed differently than glass and carbon fibers. The radial pattern commonly observed in glass and carbon fibers, which provides information to determine the overall crack direction, was absent. The fiber/matrix interface showed a very smooth surface with poor adhesion in both cases.

Translaminar Compression, RT/Dry. Visual, optical, and SEM observations revealed a broom-like fracture surface with the protruding fibers twisted in all directions (Fig. 4.4-131).

Translaminar Compression, 200°F/Wet. Figure 4.4-132 shows the SEM fractograph of a translaminar Mode I compression, Kevlar/epoxy, 200°F/wet specimen. As in the translaminar Mode I tension specimen, the RT/dry and the 200°F/wet translaminar compression specimens exhibited similar fracture appearances and there was no distinguishable feature to differentiate the environmental effects. The debris on the fibers was mostly due to the wet cutting of the specimen.

Fiberglass/Epoxy (Hexcel E-glass/F155). RT/dry and hot/wet fractures of various types were examined visually and microscopically.

Interlaminar Mode I Tension, RT/Dry. Visual observation of the fracture revealed a smooth, glassy surface. Optical photomicrographs were not taken because of the transparency of the fiberglass/epoxy. Cleavage markings, (rivermarks) typically seen in Mode I tension fractures of carbon fiber reinforced epoxies were observed under the SEM (Fig. 4.4-133). These features were usually observed at the nodes where the weaves overlap one another. The fiber/matrix adhesion appeared to be poor at some locations. This is due to the low inherent interfacial shear strength at the fiberglass/epoxy interface.

Interlaminar Mode I Tension, 200°F/Wet. Visual inspection of the 200°F/wet fracture revealed a much rougher surface than was observed in the RT/dry specimen. The specimen exhibited more resistance to breakage than the RT/dry specimen, as
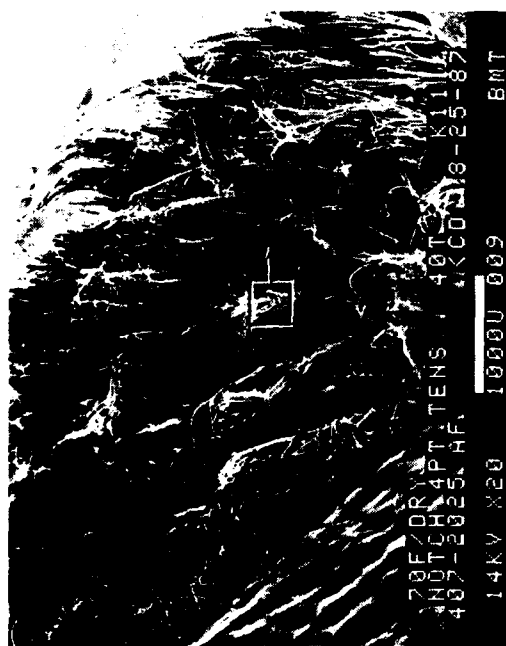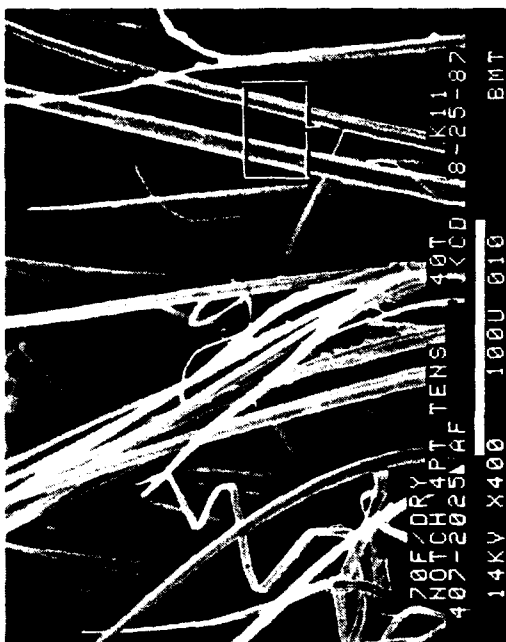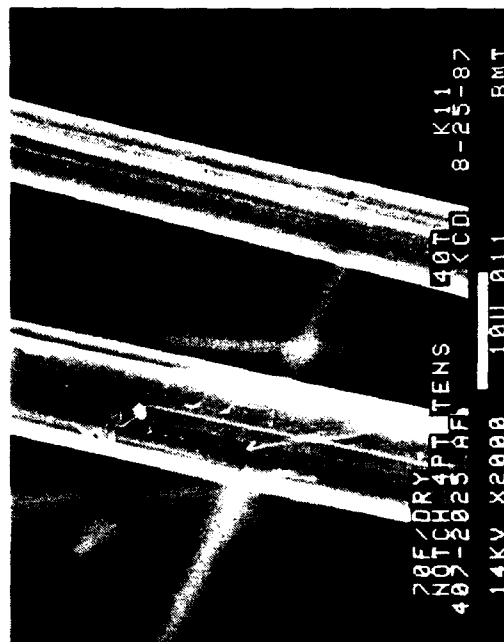
Figure 4.4-129. SEM Fractographs of 70 F/Dry, Translaminar Tension, 0/90 Fracture in Kevlar/Epoxy
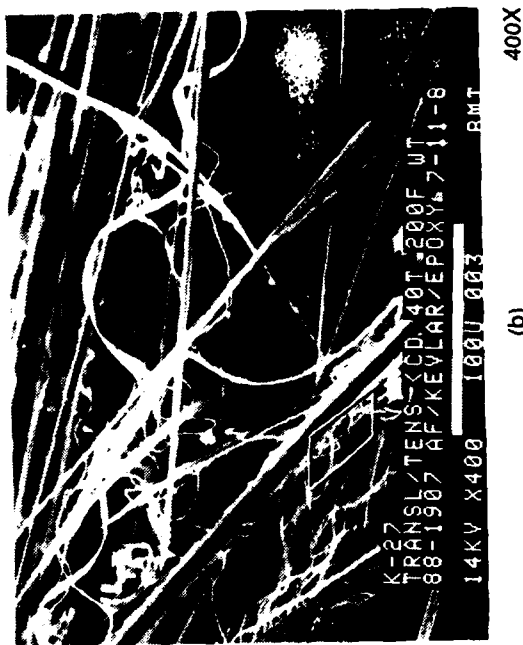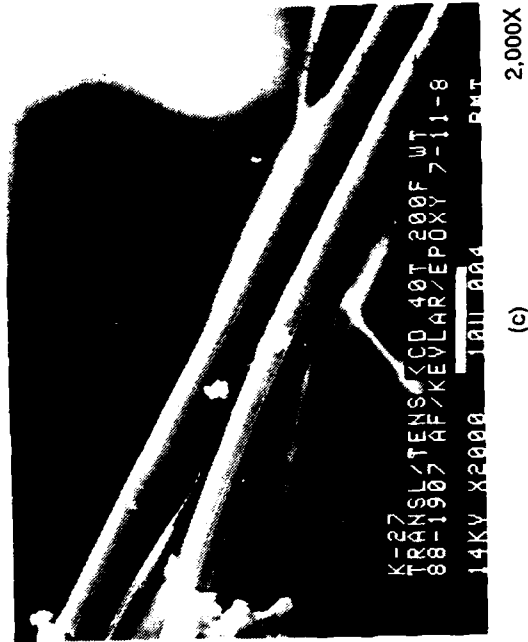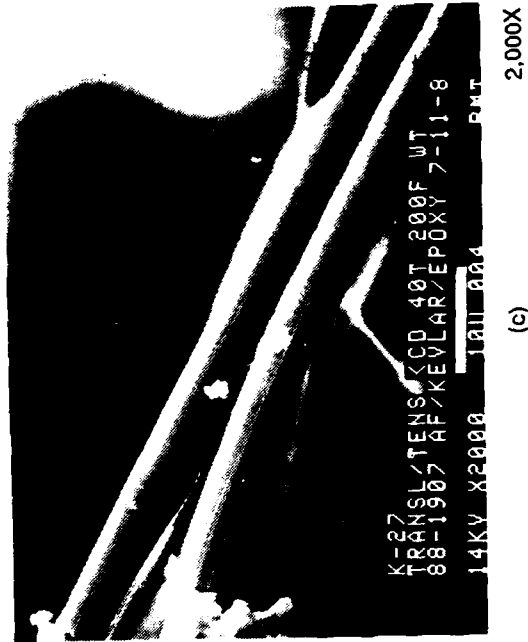
Figure 4.4-130. SEM Fractographs of 200 F/Wet, Translaminar Tension Fracture in Kevlar/Epoxy
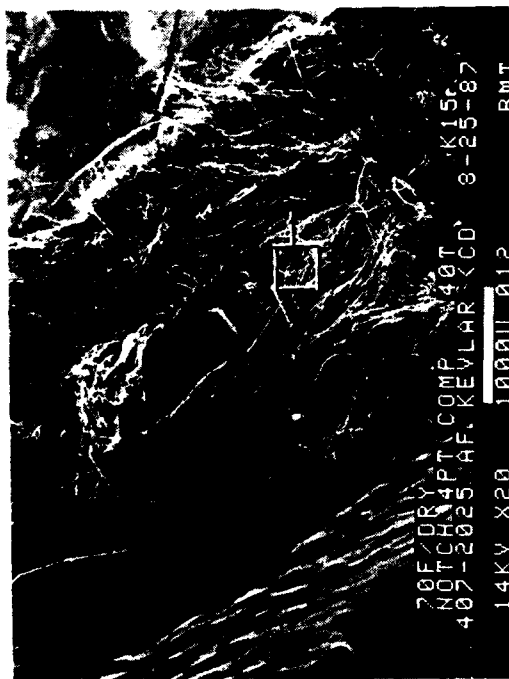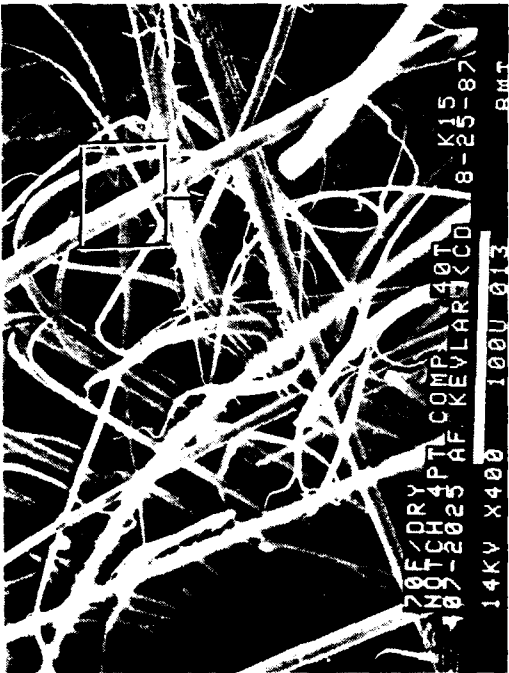
Figure 4.4-131. SEM Fractographs of 70 F/Dry, Translaminar Compression, 0/90 Fracture in Kevlar/Epoxy
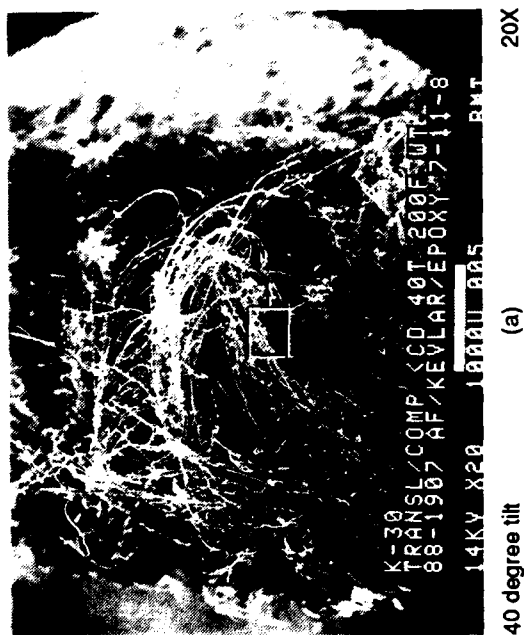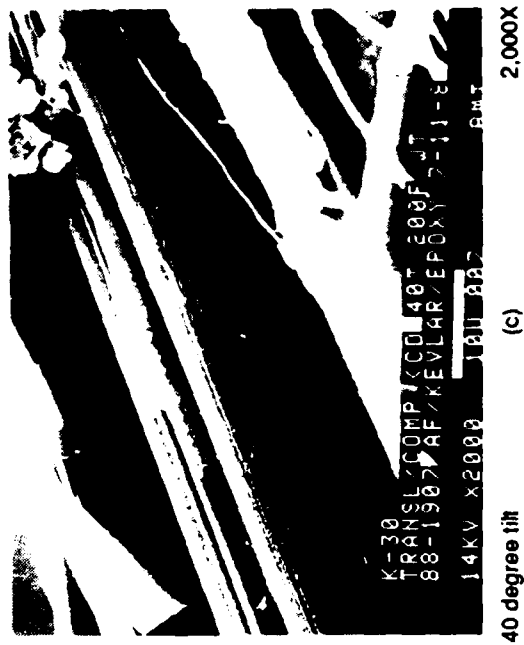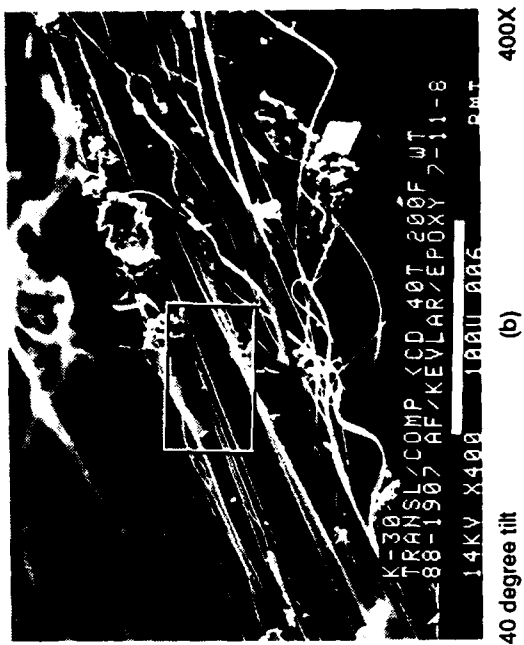
Figure 4.4-132. SEM Fractographs of 200 F/Wet, Translaminar Compression Fracture in Kevlar/Epoxy
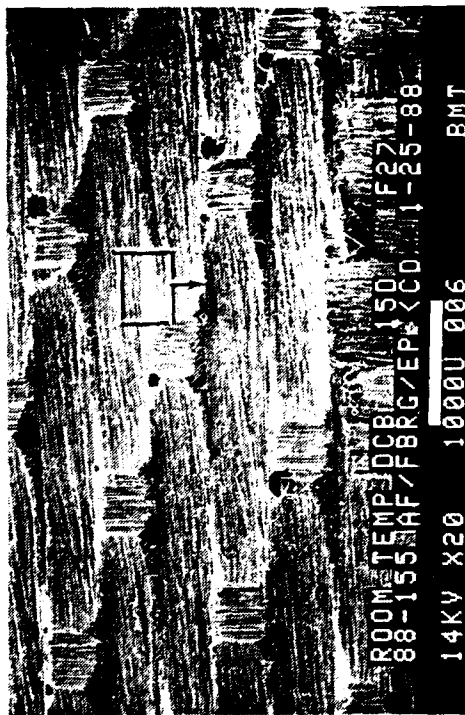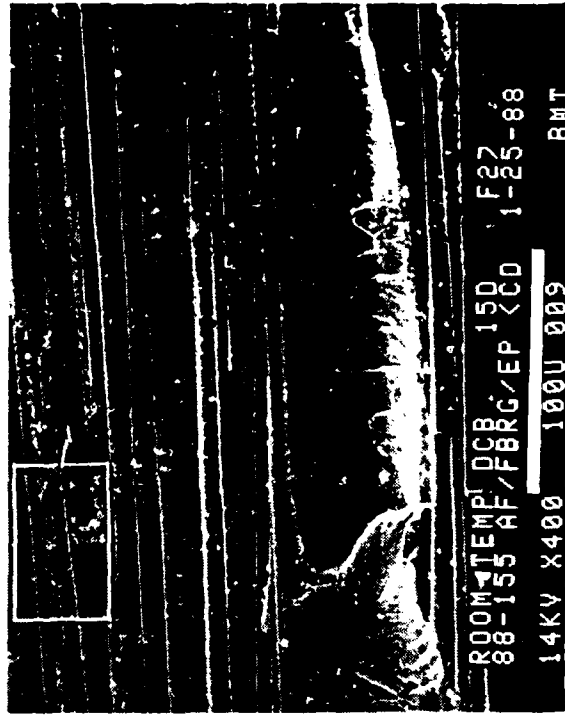
Legend:

F fiber matrix separation
R rivermark

Mechanically induced
crack direction

2,000X

15 degree tilt

20X

400X
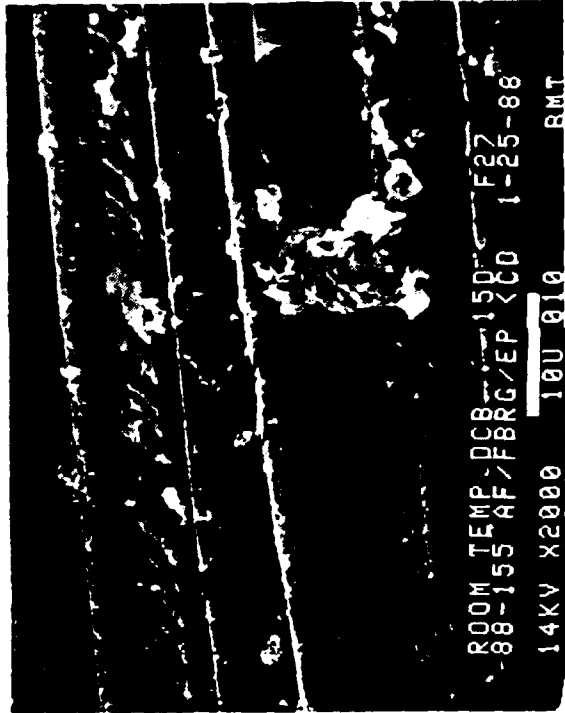
15 degree tilt

15 degree tilt

Figure 4.4-133. SEM Fractographs of Room Temperature, Interlaminar Mode I Tension Fracture in Fiberglass/Epoxy

evidenced by specimen end deflection and incomplete fracture into two halves. The resistance of the 200°F/wet specimen to fracture may be due to the increased toughness of the resin matrix due to moisture exposure.

Figure 4.4-134 shows the SEM fractographs of the interlaminar Mode I tension, 200°F/wet specimen. Fiber/matrix adhesion was poor as evidenced by the smoothness of the fiber surface. Unlike the RT/dry specimen, this specimen did not exhibit well-defined rivermarks indicating the crack direction. Instead, the surface showed taffy-pull hackles commonly seen in ductile resin matrices such as thermoplastics.

Interlaminar Mode II Shear, RT/Dry. Visual observations of the fracture revealed a rough, dull surface. There was evidence of surface ripples, running parallel to the direction of the crack growth, which could be used to identify shear mode fracture during macroscopic evaluation. This feature was not seen in any other material system evaluated in this program. The surface ripples were observed only under oblique lighting.

SEM analysis (Fig. 4.4-135) revealed a rough fracture surface consisting of large numbers of hackles, which appear similar to the platelets seen in Mode II shear fractures of carbon fiber reinforced epoxies. There was poor adhesion of the fiber/matrix interface at some locations, is due to the low inherent interfacial shear strength.

Under SEM, the fracture surface appeared very rough and hackles were observed throughout the specimen. Although the Mode I tension fracture showed a cohesive type fiber/matrix fracture in the Mode II shear fracture there was little resin debris on the fiber/matrix interface.

Interlaminar Mode II Shear, 200°F/Wet. Visual examination of the fracture revealed a rough, dull surface. The surface exhibited more of the white powder-like texture feature than the RT/dry specimen. The macroscopic ripples seen in the RT/dry specimen were also seen in these 200°F/wet specimen.

Figure 4.4-136 shows the SEM fractograph of the fracture surface which appeared rough and showed hackles as observed in the RT/dry specimen. These hackles were much larger, but fewer in number than those seen in the RT specimens.

Translaminar Tension, RT/Dry. Visual and optical observation revealed a rough topography with protruding fibers of different lengths and directions (Fig. 4.4-137). The surface of the fiber/matrix interface was smooth due to the fibers being pulled away from the matrix. There was evidence of fiber dominated fracture in the large percentage of fiber pullouts. Similar to the carbon fibers, the radial patterns were
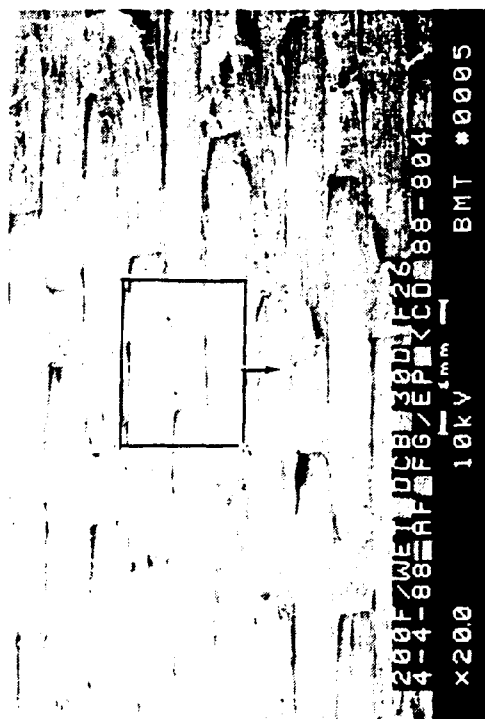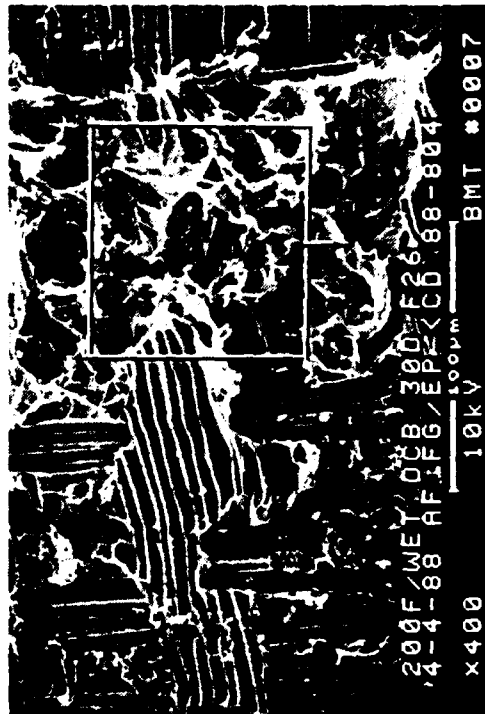
Figure 4.4-134. SEM Fractographs of 200!F Wet, Interlaminar Mode I Tension Fracture in Fiberglass/Epoxy

Mechanically induced crack direction

Legend:
F fiber/matrix seperation
H hackle

Mechanically induced
crack direction →

2,000X

15 degree tilt

20X

15 degree tilt

400X
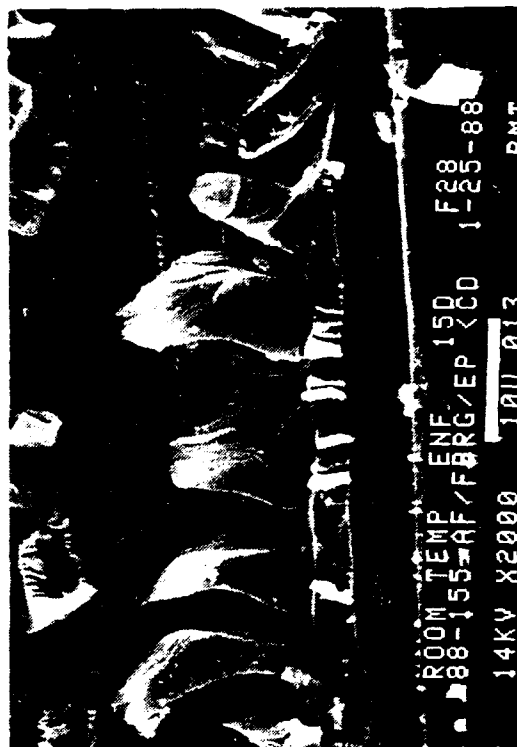
15 degree tilt

Figure 4.4-135. *SEM Fractographs of Room Temperature, Interlaminar Mode II Shear Fracture in Fiberglass/Epoxy*
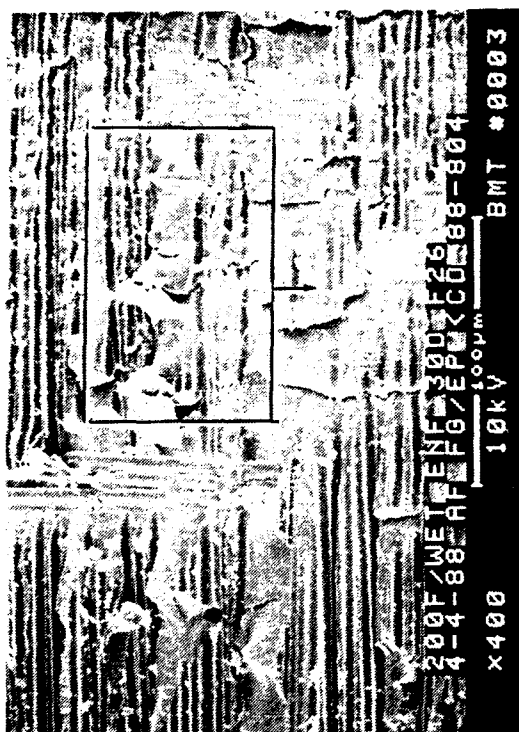
Figure 4.4-136. SEM Fractographs of 200 F/Wet, Interlaminar Mode II Shear Fracture in Fiberglass/Epoxy

Note: Higher magnifications of the boxed regions are shown in (c) and (d)

Mechanically induced crack direction
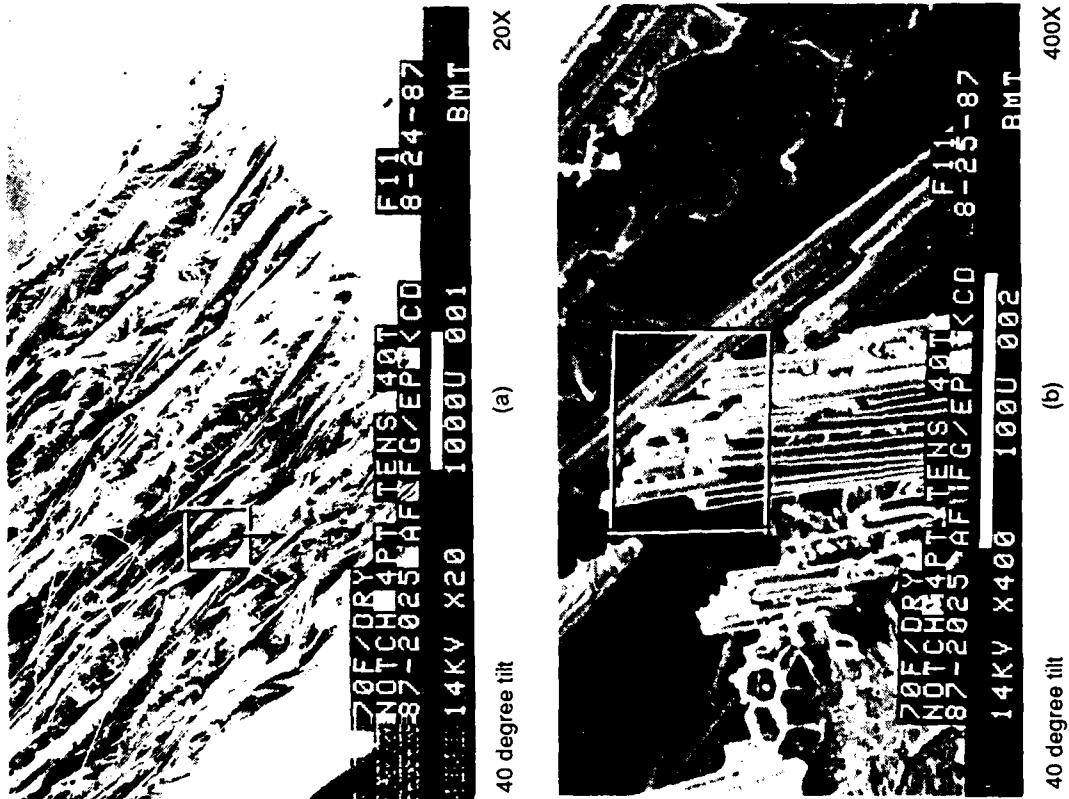
(a) 20X

40 degree tilt

(b) 400X

40 degree tilt

Figure 4.4-137. SEM Fractographs of 70 F/Dry, Translaminar Tension, 0/90 Fracture in Fiberglass/Epoxy

Mechanically induced
crack direction

(c)

40 degree tilt   2,000X

(d)

15 degree tilt   2,000X

Figure 4.4-137. SEM Fractographs of 70 F/Dry, Translaminar Tension, 0/90 Fracture in Fiberglass/Epoxy (Concluded)

observed on the glass fiber ends and can be used to determine crack growth direction.

Translaminar Tension, 200°F/Wet. The translaminar tension specimen buckled away from the notch at the reaction points. No fractography was performed on this specimen.

Translaminar Compression, RT/Dry. Visual and optical observations revealed a surface with uniform protruding fibers. The fiber/matrix interface showed good adhesion. Figures 4.4-138 and 4.4-139 show the SEM fractographs. A neutral axis line dividing the tension and compression regions on the fiber ends was observed.

Translaminar Compression, 200°F/Wet. Optical observation of the 200°F/wet specimen revealed a fracture surface like that typically seen in RT/dry translaminar compression specimens. The compression damage occurred in the region just outside of the notch. The typical fracture of a translaminar compression specimen exhibited a flat surface with "chop" makes on the fiber ends (Fig. 4.4-140). Compressively fractured fiber ends show two distinct regions separated by a neutral axis line. This line does not represent any kind of crack direction (Fig. 4.4-141).
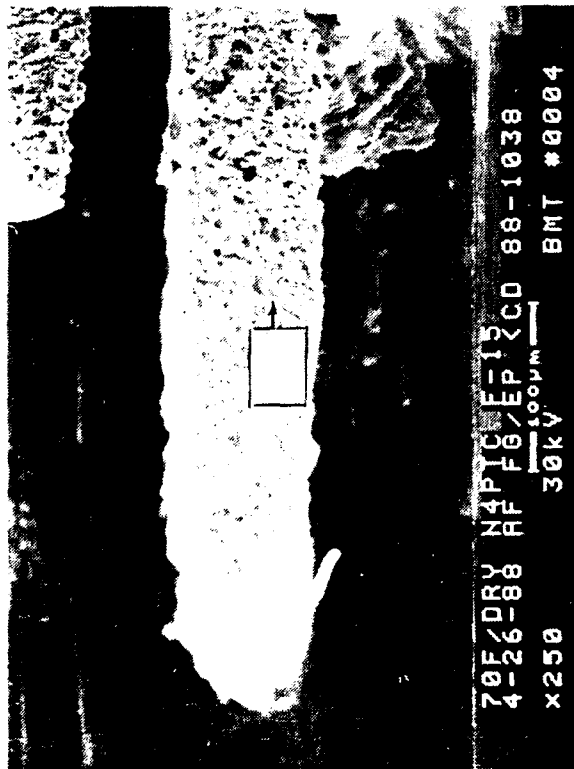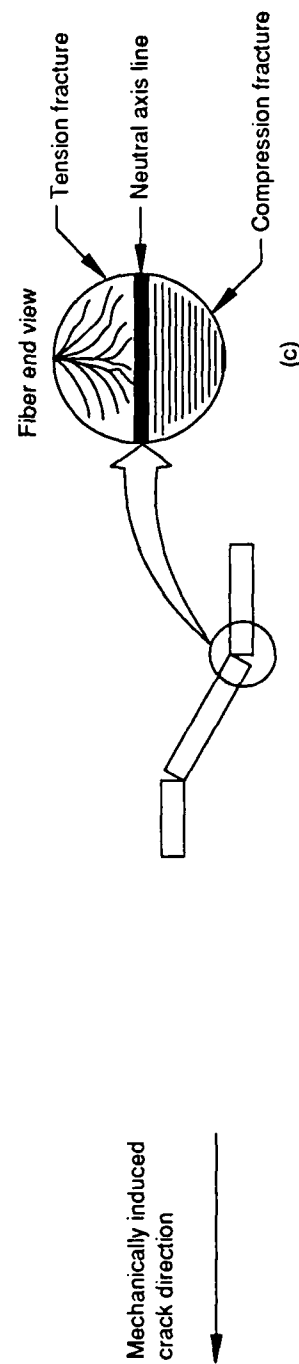
Figure 4.4-138. SEM Fractographs and Diagram of 70 F/Dry, Translaminar Compression Fracture in Fiberglass/Epoxy; Shown at 0 Degree Tilt
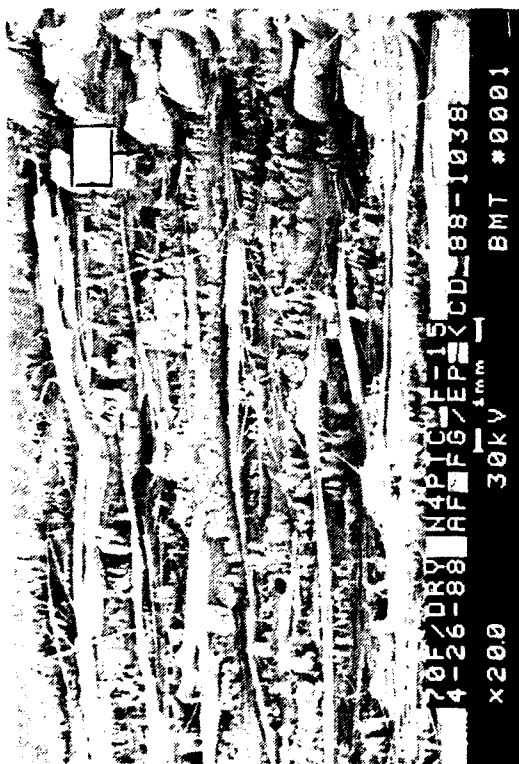
Mechanically induced
crack direction
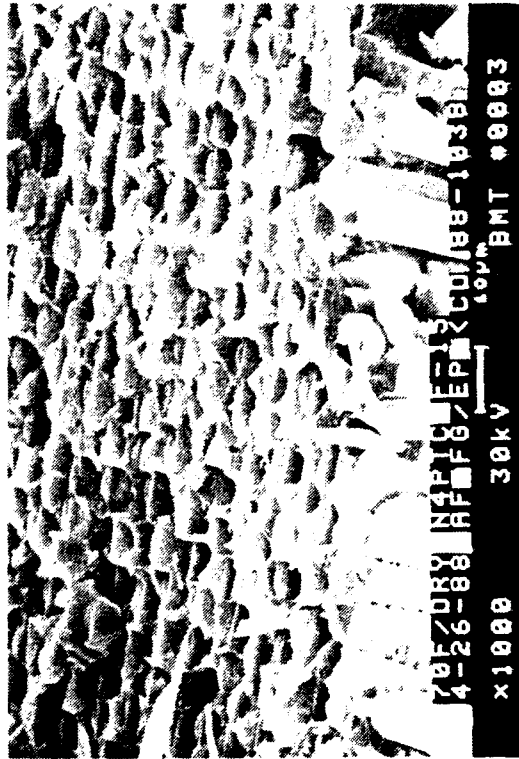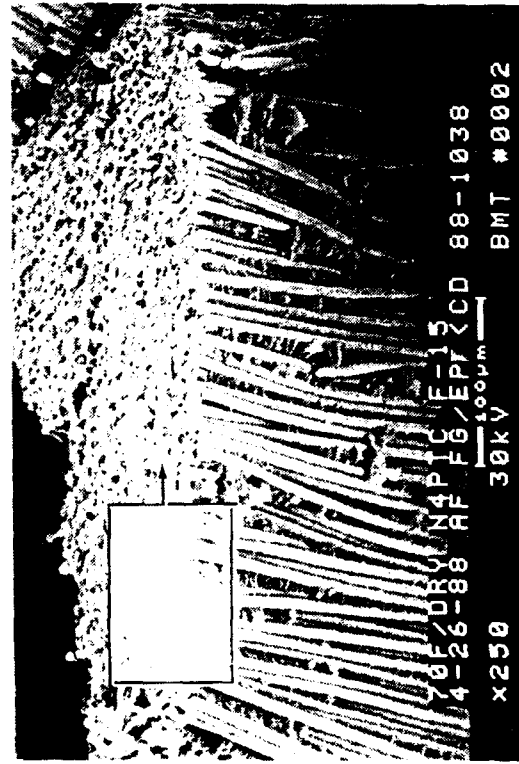
Figure 4.4-139. SEM Fractographs and 70 F/Dry, Translaminar Compression Fracture in Fiberglass/Epoxy; Shown at 45 Degree Tilt

Mechanically induced crack direction

Region representing the compression damage
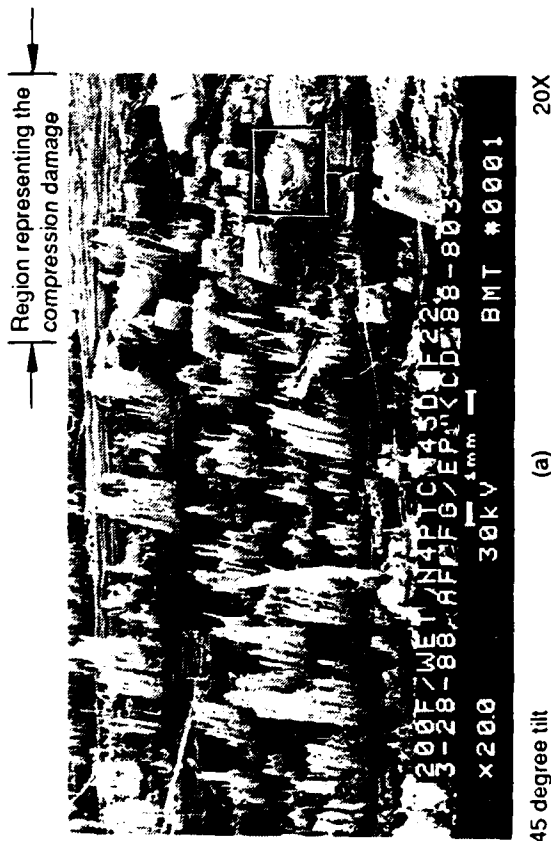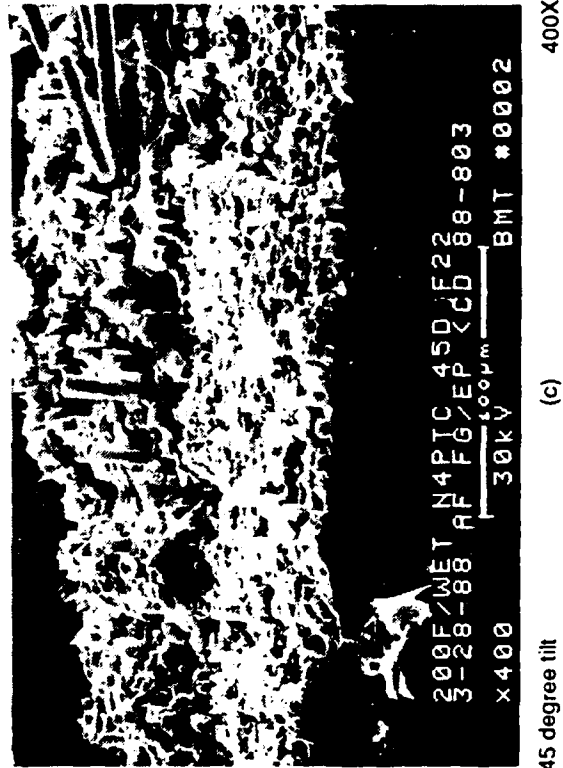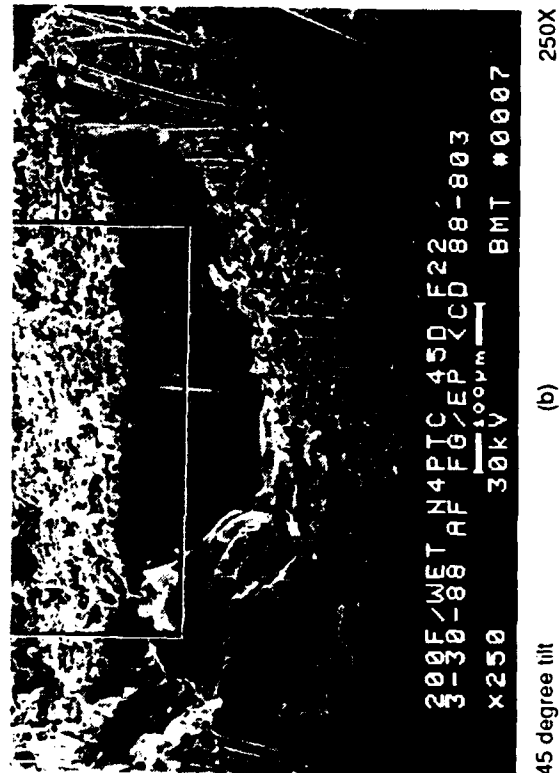
Figure 4.4-140. SEM Fractographs of 200 F/Wet, Translaminar Compression Fracture in Fiberglass/Epoxy; Shown at 45 Degree Tilt

200F/WET,N4PTC,0D,F22
3-28-88,AF,FG/EP,<CD>88-803
×2000   30kV   10µm   BMT #0006

(a)

0 degree tilt   400X   2,000X

200F/WET,N4PTC,45D,F22
3-30-88,AF,FG/EP,<CD>88-803
×400   30kV   100µm   BMT #0008

(a)

45 degree tilt

Fiber end view

Tension fracture

Neutral axis line

Compression fracture

Fiber microbuckling

Mechanically induced
crack direction
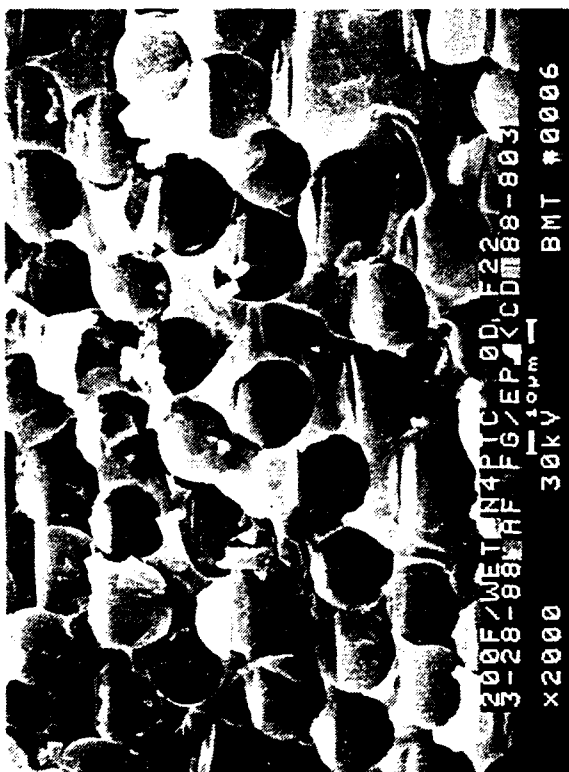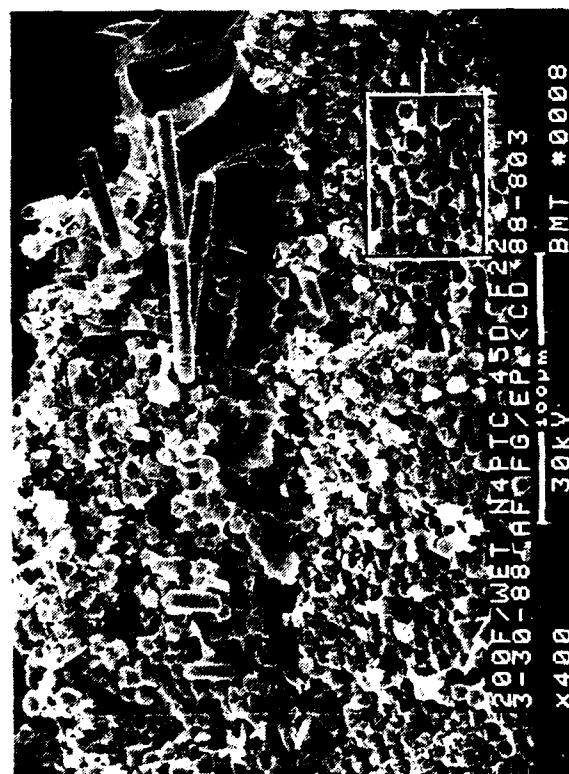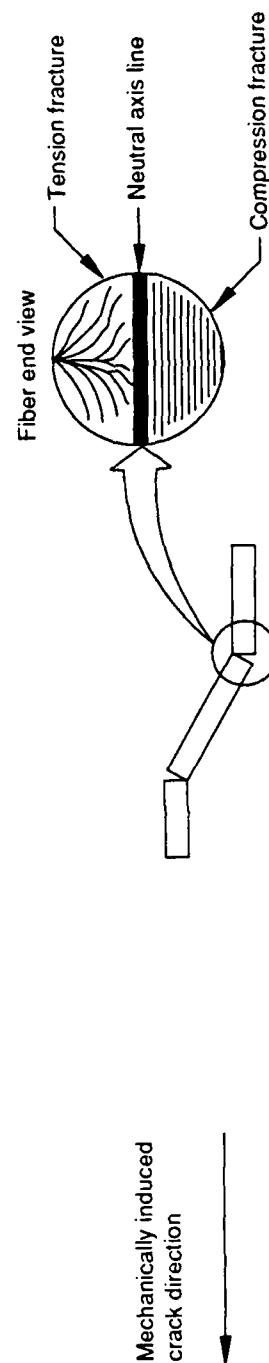
Figure 4.4-141. SEM Fractographs of 200 F/Wet, Translaminar Compression Fracture in Fiberglass/Epoxy; Higher Magnification

5.0 TASK 4: DEVELOPMENT OF DATA FORMAT

5.1 OBJECTIVE

The objective was to develop the Failure Analysis Collection and Tracking System (FACTS) Input Sheet. The FACTS input sheet ensured comprehensive data collection, and facilitated data storage for future computer tracking and analysis.

5.2 APPROACH

The approach was to produce comprehensive data collection formats so that pertinent physical data (such as background information, analytical methods used, and results) could be preserved, while keeping the format flexible. Multi-tiered data formats collect specific analytical data, supportive raw data, and detailed fracture analysis results. Each data sheet in the series contained the following information: background (part specific information); method used (analytical methods and instrument setting); results (presentation of (raw) data, observations, and conclusions); and keywords (words summarizing pertinent information for computer tracking and retrieval system). The Task 4 flow diagram is shown in Figure 5.2-1.

5.3 METHODS

Data collection formats were developed using input from the Air Force, Boeing, GE, current handbooks, and requirements for Government reporting methods. Six formats were provided to the Air Force Project Engineer (AFPE) for review. The six formats consisted of one overall Failure Analysis Collection and Tracking System (FACTS) input sheet, and five-tiered breakdown data input sheets specifically for macroscopic fractography, microscopic fractography, nondestructive evaluation (NDE), materials characterization, and stress analysis.

The FACTS input sheets were developed for use in creating a failure analysis report. Following AFPE approval of the proposed FACTS sheets, the formats were used for reporting of Task 6, Verification of Composites Failure Analysis Logic Network (FALN), to ensure data organization and completeness and to allow program information to be efficiently included in the handbook.

5.4 RESULTS

The approved FACTS sheets are shown in Appendix A.
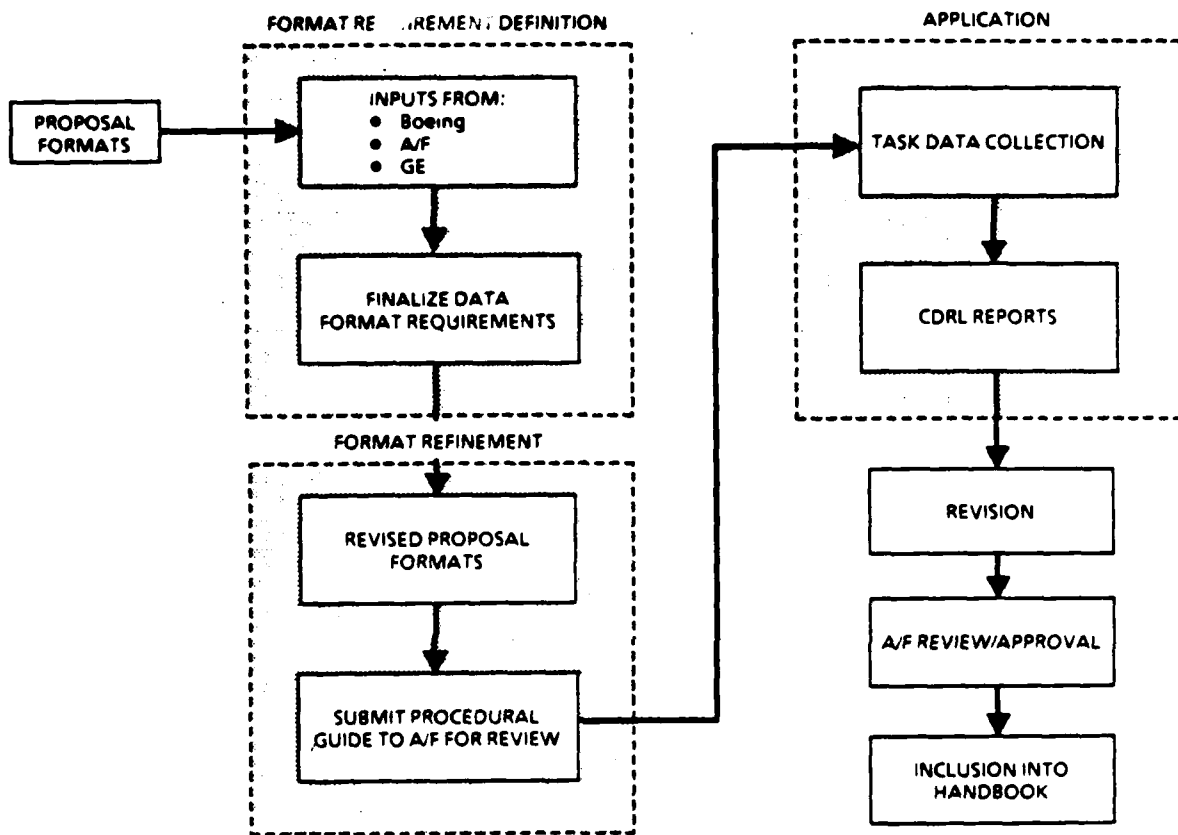
Figure 5.2-1. Task 4 Flow Diagram

6.0 TASK 5: DOCUMENTATION OF MATERIAL PROPERTIES

6.1 OBJECTIVE

The objective was to document material properties for reference during failure analysis. A failure analyst must have a broad array of supportive information available. A well-documented reference on material properties and variables affecting those properties is of significant value.

6.2 APPROACH

The approach was to provide a comprehensive yet cost-effective material properties database by:

a. Obtaining data from a broad resource base. This provided higher confidence in data accuracy through concurrence of sources.

b. Obtaining data from comprehensive documents such as handbooks. This reduced the cost of acquiring data through extensive searches of small documents.

c. Gathering constituent properties as well as composite properties. This allowed a larger, and more flexible material systems reference.

d. Obtaining information on how variables affect material properties. This will provide the failure analyst additional information for determining cause(s) of failure.

The Task 5 flow diagram is shown in Figure 6.2-1.

6.3 METHODS

Information on material properties was complied from applicable literature, based on current and anticipated use of aerospace composite materials. Source approvals were obtained for published data. Data identified were compared and divided into three categories: constituent properties, system properties, and variables affecting properties.

6.4 RESULTS

Figure 6.4-1 summarizes the figures and tables of all material properties collected under this task. The material properties are shown in Appendix B.
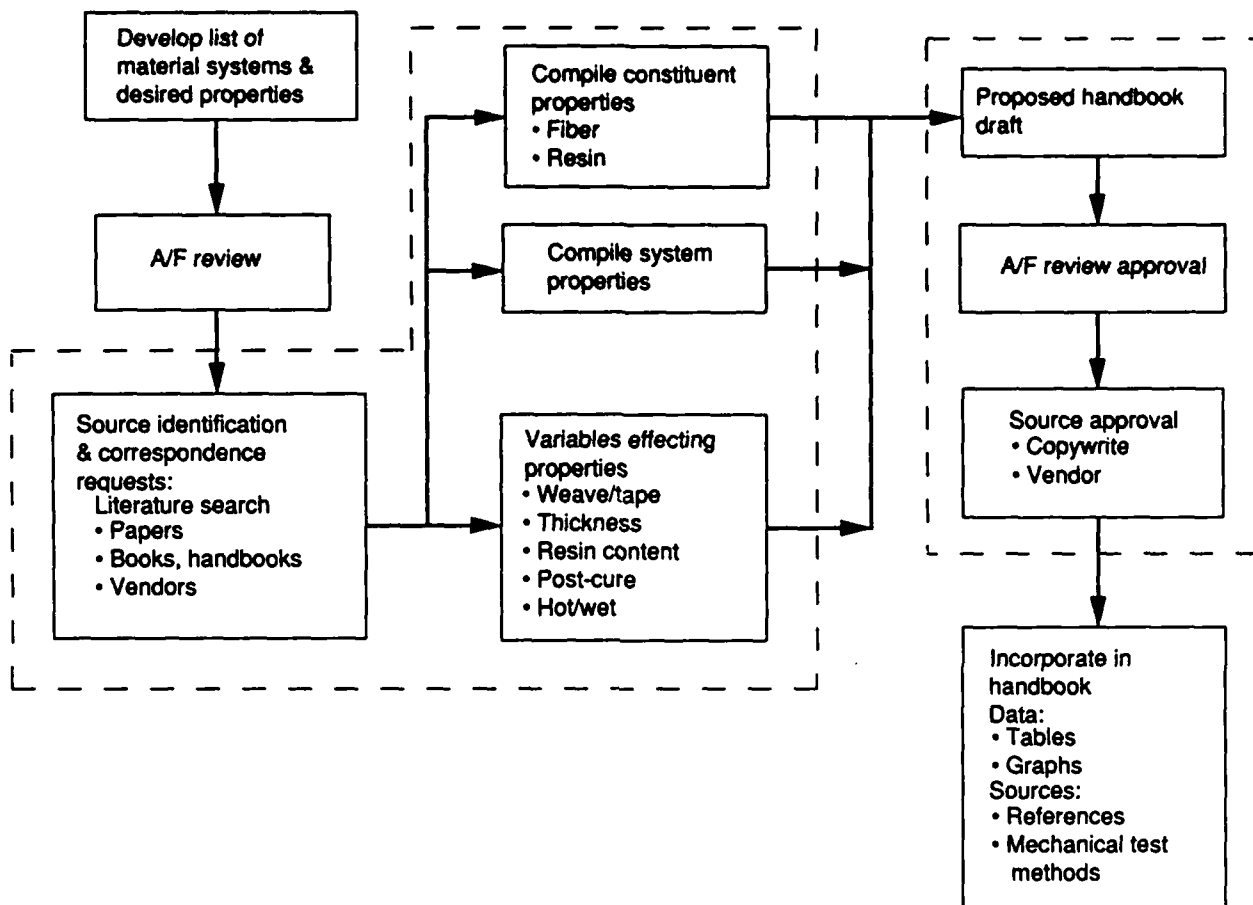
Figure 6.2-1. Task 5 Flow Diagram - Documentation of Mechanical Properties

Figure/table no.	Table/reference
Figure B-1	Mechanical Properties of Hercules Fiber/Data sheets provided by Hercules.
Figure B-2	Hercules Fiber Properties at Room Temperature/Data sheets provided by Hercules.
Figure B-3	Typical Epoxy Composite Properties at Room Temperature/Data sheets provided by Hercules.
Figure B-4	Properties of Typical Epoxy Composite at Room Temperature/Composite Design Encyclopedia University of Delaware, Vol 1 Mechanical Behavior, Carl Zweben and H. Thomas Hahn.
Figure B-5	0° Strength-to-Density Ratio of Typical Epoxy Composite/Composite Design Encyclopedia University of Delaware, Vol 1 Mechanical Behavior, Carl Zweben and H. Thomas Hahn.
Figure B-6	0° Tensile Properties of Typical Epoxy Composite/Composite Design Encyclopedia University of Delaware, Vol 1 Mechanical Behavior, Carl Zweben and H. Thomas Hahn.
Figure B-7	Physical Properties of Graphite Fabric Prepreg/Engineer's Guide to Composite Materials, John W. Weeton, American Society for Metals, 1987, p6-45.
Figure B-8	Graphical Representation of Tensile Properties of Graphite Fabric Prepreg/Engineer's Guide to Composite Materials, John W. Weeton, American Society for Metals, 1987, p6-45.
Figure B-9	Properties of Matrices/Engineer's Guide to Composite Materials, John W. Weeton, American Society for Metals, 1987, p6-45.
Figure B-10	Graphical Representation of Tensile Properties of Matrices/Engineer's Guide to Composite Materials, John W. Weeton, American Society for Metals, 1987, p6-45.
Figure B-11	Strength-to-Density Ratio of Matrices/Engineer's Guide to Composite Materials, John W. Weeton, American Society for Metals, 1987, p6-45.
Figure B-12	Neat Resin Properties at Room Temperature/Composite Design Encyclopedia, University of Delaware, Vol 1 Mechanical Behavior, Carl Zweben and H. Thomas Hahn.
Figure B-13	Graphical Representation of Neat Resin Properties at Room Temperature/Composite Design Encyclopedia, University of Delaware, Vol 1 Mechanical Behavior, Carl Zweben and H. Thomas Hahn.
Figure B-14	Deformation Stages of Fiber, Matrix and Composite/C. C. Chamis, "Simplified Composite Micromechanics Equations for Hygral, Thermal and Mechanical Properties" NASA TM 83320, 1983.
Figure B-15	Properties of Graphite (Carbon) Fibers/Composite Design Encyclopedia, University of Delaware, Vol 1 Mechanical Behavior, Carl Zweben and H. Thomas Hahn.
Figure B-16	Properties of Kevlar and Glass Fibers/Composite Design Encyclopedia, University of Delaware, Vol 1 Mechanical Behavior, Carl Zweben and H. Thomas Hahn.
Figure B-17	Tensile Strength of Neat Resins/Data Sheets Provided by Hercules.
Figure B-18	Graphical Representation of Tensile Strength of Neat Resins/Data Sheets Provided by Hercules.
Figure B-19	Young's Modulus of Neat Resins/Data Sheets Provided by Hercules.
Figure B-20	Graphical Representation of Young's Modulus of Neat Resins/Data Sheets Provided by Hercules.
Figure B-21	Physical Properties of Epoxy Preimpregnated Unidirectional Tapes/ Engineer's Guide to Composite Materials, John W. Weeton, American Society for Metal, 1987.
Figure B-22	Properties of Commercial Carbon Fibers/Engineer's Guide to Composite Materials, John W. Weeton, American Society for Metal, 1987.
Figure B-23	Graphical Representation of Tensile Properties of Commercial Carbon Fibers/Engineer's Guide to Composite Materials, John W. Weeton, American Society for Metal, 1987.
Figure B-24	Graphical Representation of Strength-to-Density Ratio of Commercial Carbon Fibers/Engineer's Guide to Composite Materials, John W. Weeton, American Society for Metal, 1987.
Figure B-25	Constituent Property Data of Fibers/Composite Design Encyclopedia, University of Delaware, Vol 1 Mechanical Behavior, Carl Zweben and H. Thomas Hahn 1982.

Figure 6.4-1. Material Properties Documentation Summary - Figures in Appendix B

7.0 TASK 6: VERIFICATION OF COMPOSITES
FAILURE ANALYSIS LOGIC NETWORK (FALN)

7.1 OBJECTIVE

The objectives were to (1) verify the FALN (developed under the previous program) by executing it during failure analysis investigation of semi-structural composite components submitted by the Air Force, (2) evaluate the Tasks 1 through 5 results developed under this contract to demonstrate their applicability and usefulness during failure investigation, and (3) incorporate the failure analysis results for the components into the handbook under the case history section.

7.2 APPROACH

Upon receipt of the failed composite structures from the Air Force, the investigation was initiated using the FALN and sub-FALN guidelines. First, visual examination was performed on the as-received component. Second, macroscopic fractography was performed to preliminarily determine the failure mode. Specimen cutting, handling, and cleaning guidelines developed under Task 1 were used to select areas of interest for further laboratory analyses. Third, NDE techniques were employed to identify the extent of damage. Fourth, various material verification techniques, such as thermal and physical analyses, were used to determine the component material characteristics. Material properties documentation, developed under Task 5, was used as supportive information. Fifth, references on microscopic fractography developed under Task 3 was used to determine the crack growth directions and mode of failure. Stress analysis, an optional sixth step under the FALN, was not required for this investigation. The Task 6 flow diagram is shown in Figure 7.2-1.

7.3 METHODS

Two failed semi-structural components were received and analyzed using the developed approaches and techniques. The results were incorporated into the Case History section of the handbook. The first component was a continuous fiber-reinforced composite; no historical background data was provided. The second component was a main landing gear strut, made of E-glass/epoxy material, from a Helio H-800 aircraft. Boeing conducted failure analysis of the first component and GE performed the analysis on the other.
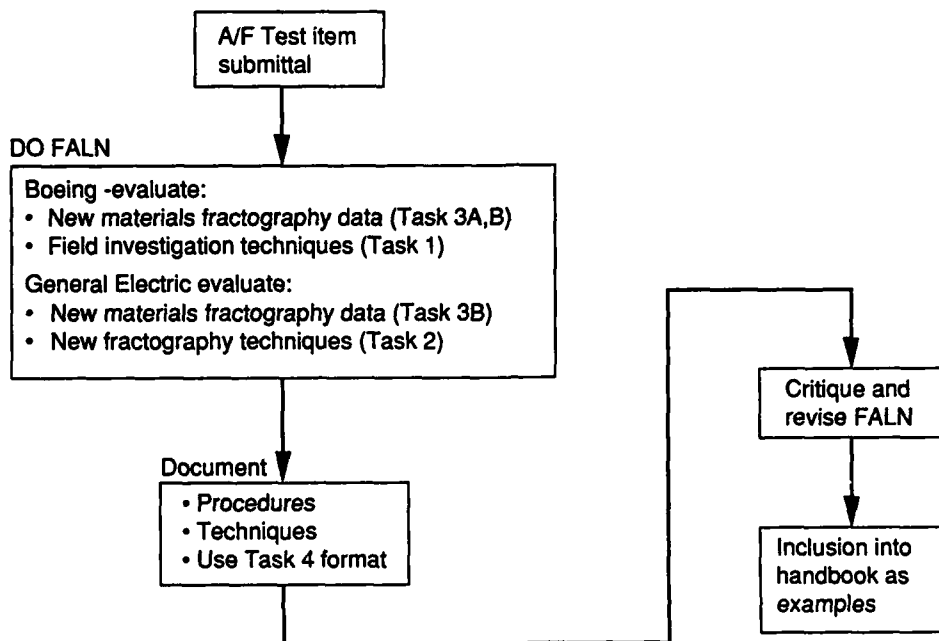
Figure 7.2-1. Task 6 Flow Diagram

FALN and sub-FALN guidelines were used to perform the investigation; visual examination, NDE, material characterization, macro- and microfractography were also used during the failure analysis. Stress analysis was an optional step on the FALN and was not required in either of these cases. Data collection format sheets for macroscopic fractography, NDE, material characterization, and microscopic fractography were used to ensure comprehensive data collection during failure investigation.

7.4 RESULTS

7.4.1 Failure analysis of the first component

Failure analysis of the first component was conducted by Boeing.

7.4.1.1 Background History

Figure 7.4-1 shows the fractured test panel in its as-received condition. The rectangular panel, with a dimension of 43 by 36 inches, appeared to have been fastened to one or more fixed structures during testing. Due to limited background information, the emphasis was placed on the visual examination. At the time of the part's receipt, it was speculated that the part had been fractured via impact loading. This speculation was made due to the appearance of the damage which was typical of that observed in impact loaded structures.

7.4.1.2 Factual Data

Visual Examination. As shown in Figure 7.4-2, the damage appeared to have been caused by an object penetrating through the panel from the interior surface (Fig. 7.4-2a), as evidenced by the brooming fibers on the exterior surface (Fig. 7.4-2b). These damage features are commonly observed in an impacted specimen.

In conjunction with stress analysis, visual examination was performed using fastener hole damage as evidence to determine the loading condition experienced by the panel during the test. The key evidence was the depth and elongation of the hole. In general, hole elongation indicates shear-type loading in which the head and the shank of the fastener tilt at an angle to the hole. Figure 7.4-3 illustrates the damage of a typical shear loaded fastener hole. The damage seen in the countersunk region of the fastener
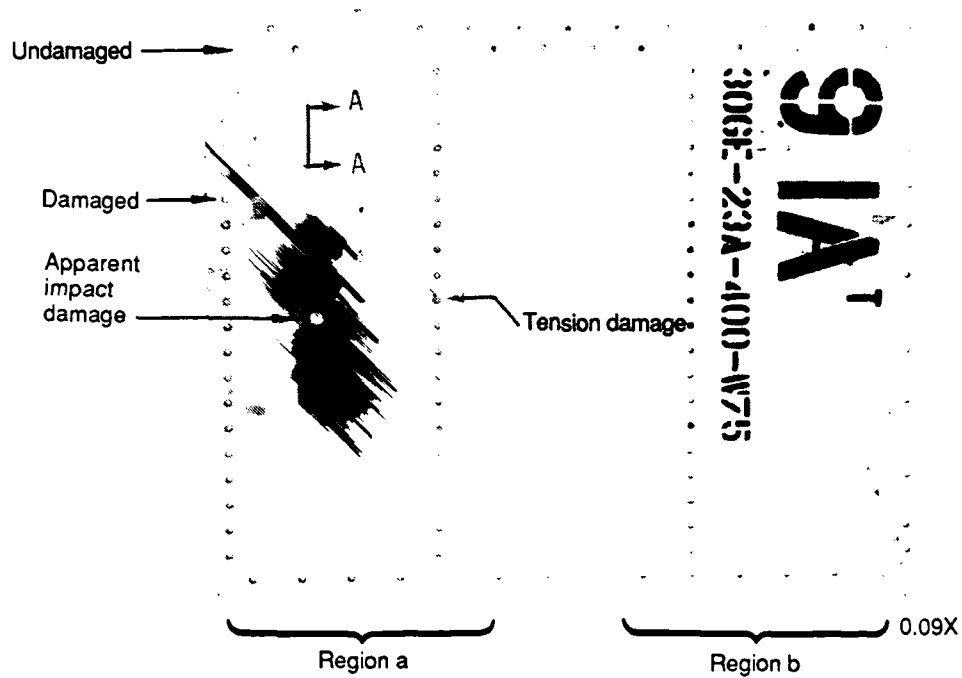
(a) Exterior (painted) surface
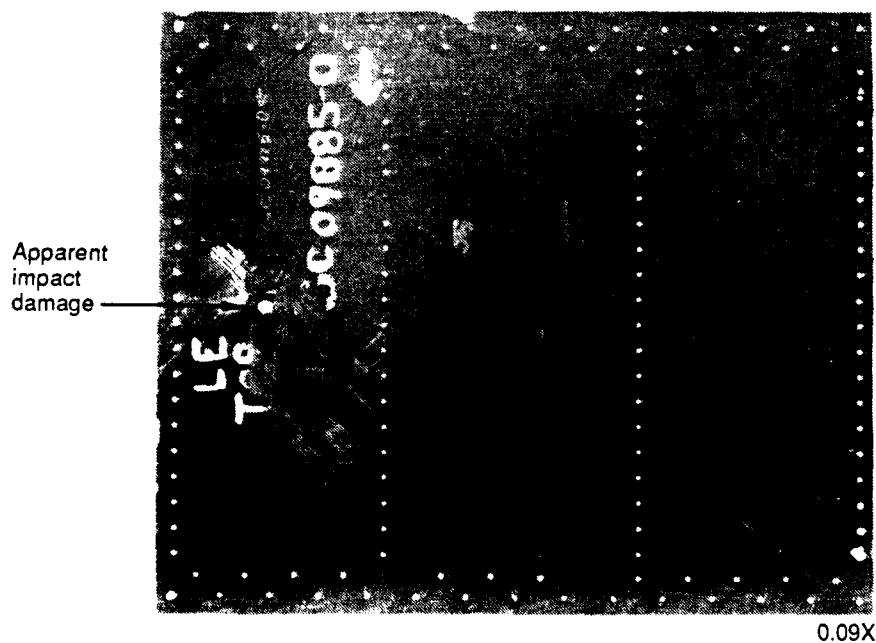
(b) Interior (unpainted) surface

Figure 7.4-1. Photomicrographs of the Component As Received

(b) Damage on the exterior surface

Exterior surface

Interior surface

Impact loading

(c) Clarification schematic

Brooming fiber

Note the depression at the impact site which indicates the direction of the penetration

Brooming fiber

(a) Damage on the interior surface

Figure 7.4-2. Apparent Impact Damage

Countersunk region

(a) Plan view

2.4X

Major fastener hole damage which indicated "rocking" of the fastener
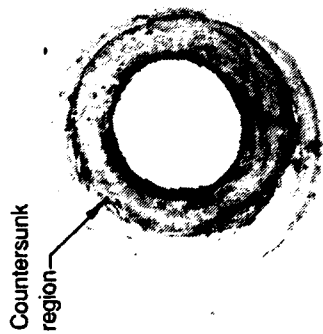
(b) Cross-sectional view

8X

Figure 7.4-3. Damage in Fastener Hole Loaded Under Shear

hole was created by the fastener head which dug into the laminate due to the test load. In contrast, tension loaded fastener holes did not show any sign of elongation, retaining their circular shape (Fig. 7.4-4). The fastener head dug beyond the countersunk region causing severe delamination near the inner edge of the hole. Figure 7.4-5 shows the mapping of the fastener hole damage. From the mapping, it was determined that Region A of the panel was loaded under tension and shear. However, Region B seemed to have been securely fastened to a fixed structure as evidenced by the lack of fastener hole damage in that portion of the panel.

The fastener hole damage also provided information to verify the proper use of the fasteners or the fastener holes for the particular load conditions applied. Two commonly used fasteners were placed into an undamaged fastener hole to determine which had been used (Fig. 7.4-6). The tensile fastener, which has a slightly larger head diameter than the (intermediate) shear fastener, fitted flush into the undamaged hole. However, when the fasteners were placed into one of the fastener holes damaged from tensile loading (Fig. 7.4-7) it was evident that the shear fastener was used. The tensile fastener head was too large for this particular fastener hole damage, but the shear fastener fitted almost perfectly into the damaged hole. The above macroscopic analysis suggests that the tensile fasteners were used for Region B and shear fasteners were used for Region A.

Non-Destructive Evaluation. To determine the extent of the damage, through-transmission ultrasonic inspection (C-scan) was performed. The dark-shaded regions in the vicinity of the fastener holes and at the apparent impact site indicate the damaged region. These regions are shaded due to higher attenuation from the anomalous regions. Most of the damage occurred on one half of the panel, Region A, as shown in Figure 7.4-8.

Materials Characterization. To characterize the material system, thermal/chemical analysis, electron microprobe analysis, and optical microscopy were performed.

A Fourier transform infrared (IR) spectrometer was used to determine the resin used to fabricate the component. Two samples from the panel were analyzed. Figure 7.4-9 shows the infrared (IR) spectra obtained from the test sample. The general resin type was determined to be a 350°F cure conventional epoxy system by the method of fingerprinting using the limited in-house database of IR spectrum. Figures 7.4-9b and c show the IR spectrum of Hercules 3501-6 and Hexcel F263 prepreg materials respectively; these spectra were used for fingerprinting those obtained from the sample.

(a) Plan view   2.4X

(b) Cross-sectional view   8X

Figure 7.4-4. Damage in the Fastener Hole Loaded Under Tension
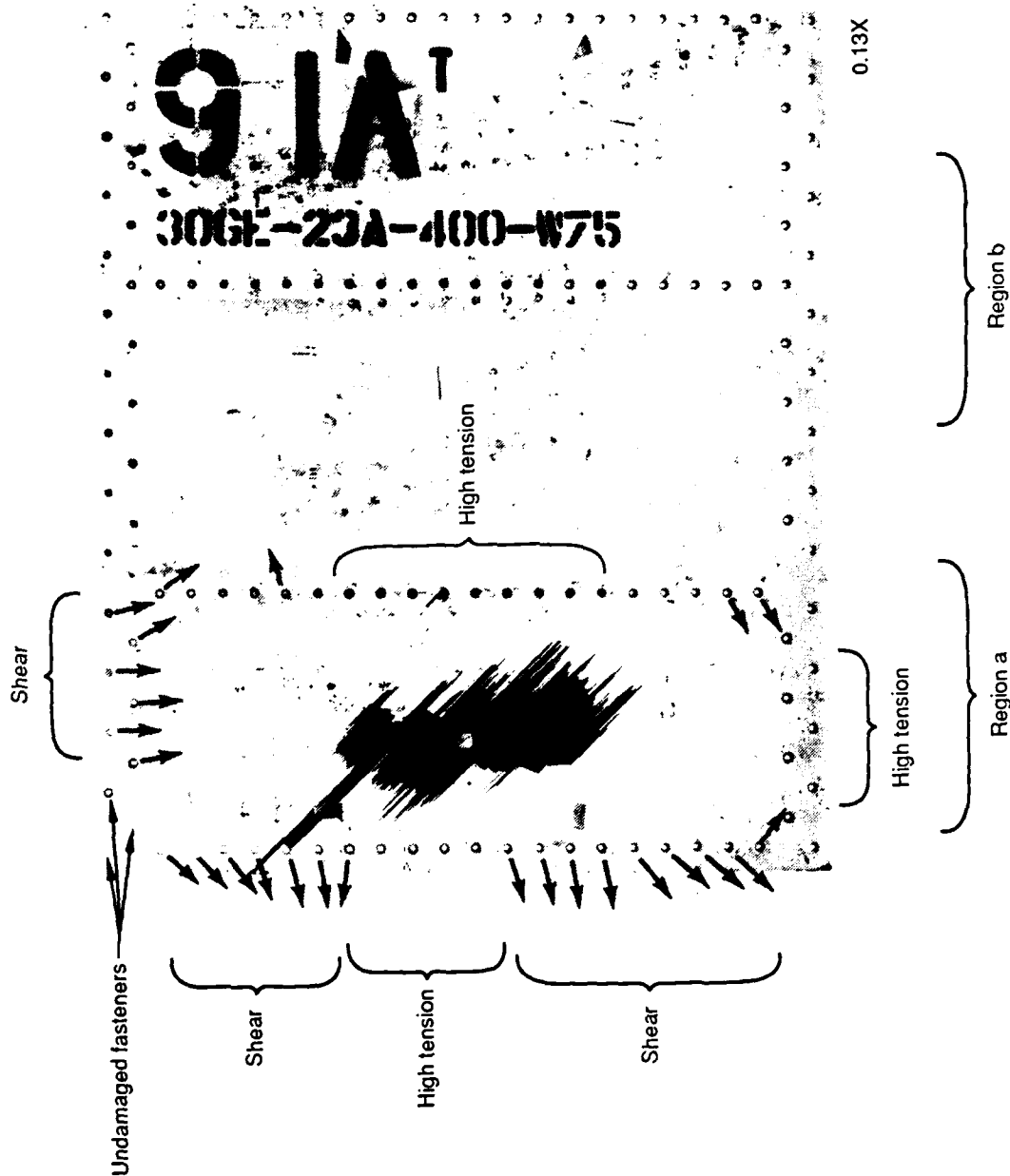
Figure 7.4-5. Mapping of the Fastener Hole Damage
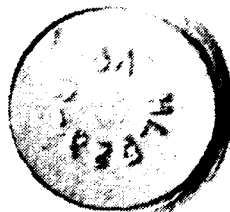
(a) Tensile fastener   2.7X   (b) Cross-sectional view   2.7X

Figure 7.4-6. Difference in Fastener Fit in the Undamaged Fastener Hole

0.9X

b. Shear (intermediate) fastener (fits snugly in fastener hole)

0.9X

a. Tensile fastener (fits loosely in fastener hole)

Figure 7.4-7. Macrophotographs Showing the Fit of the Fastener in the Damaged Holes
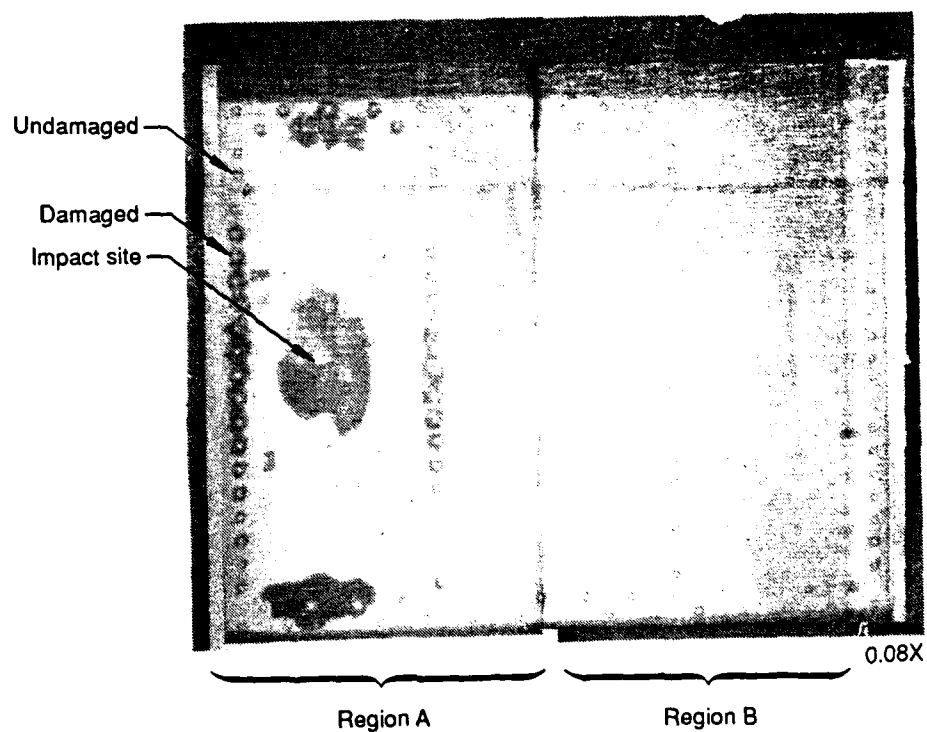
Figure 7.4-8. Through Transmission Ultrasonic (TTU) Scan of Component

(a) Sample No. 1

Wavenumber

(b) Hercules 3501-6

Wavenumber

(c) Hexcel F263

Wavenumber
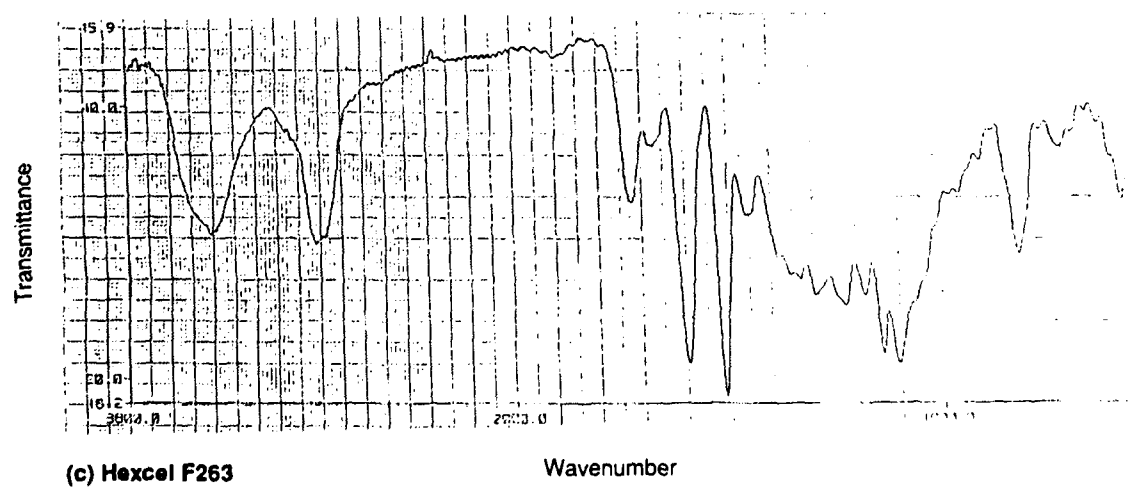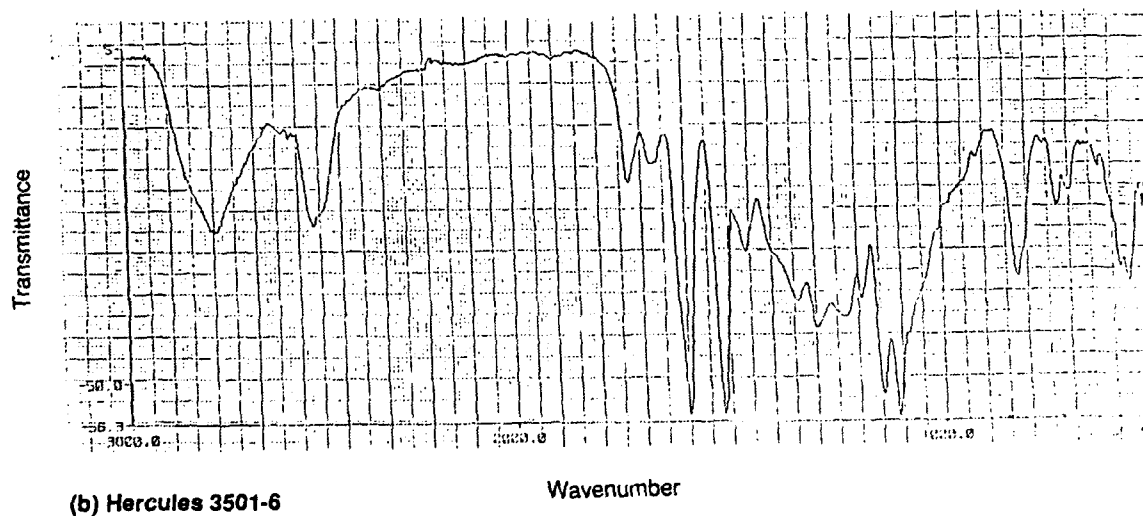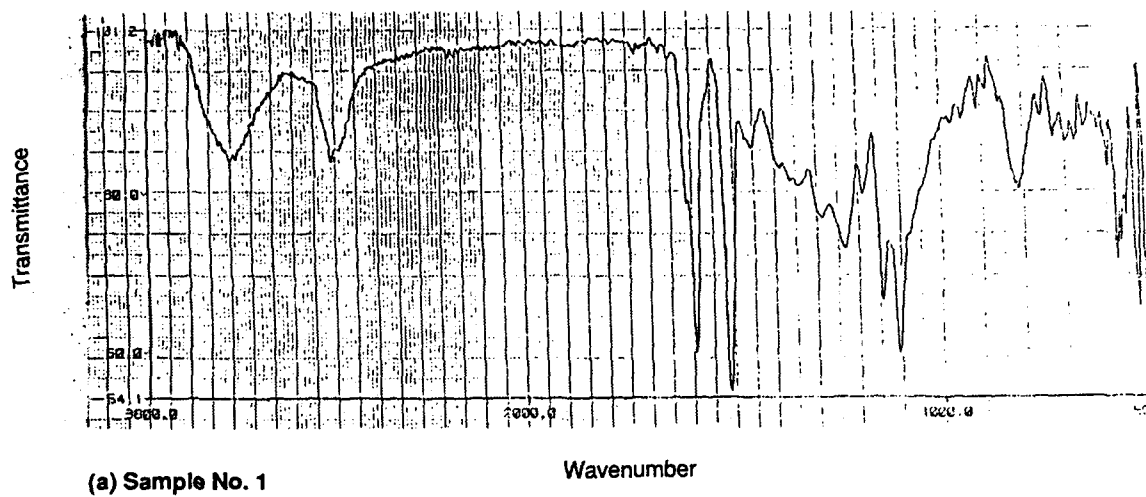
Figure 7.4-9. Infrared Spectroscopy Results

Differential scanning calorimetry (DSC) showed no exothermic peaks, indicating that the material was fully cured (Fig. 7.4-10). A decomposition at 378°C was also observed. Thermomechanical analysis (TMA) showed the average glass transition temperature (Tg) to be 210°C (410°F, Fig. 7.4-11). Thermogravimetric analysis (TGA) indicated the composite decomposed at approximately 357°C (675°F, Fig. 7.4-12).

Acid digestion was performed using nitric acid to determine the resin content. The average weight percent of resin content (three samples) was 29.3% as shown in Figure 7.4-13. Because of the lack of background information, it was impossible to tell whether the resin content was out of specification. However, from the fracture appearance it was determined that the resin content was not the primary cause of the fracture (since no major voids were observed near the fracture).

Figure 7.4-14 shows the wavelength dispersive X-ray (WDX) scan of the sample. The WDX scan indicated that the fiber used was carbon which is characterized by a K_α peak at 44.700A and 0.277 KeV. The WDX technique was used instead of EDX (energy dispersive X-ray) because WDX allows the detection of lighter elements such as carbon and oxygen.

Evaluation of an area away from the fracture showed that the quality of the laminate was good (with little porosity) and the ply stacking sequence was symmetrical (Fig. 7.4-15). Due to the severity of the fiber damage near the apparent impact site, it was impossible to perform an evaluation of the cross-section.

Fractography. Fractography of this component was largely macroscopic. The damaged region resembled an area typically observed in an impact loaded structure. The fracture exhibited complex mixed-mode features involving both tension and shear. Further microscopic analysis was not performed because the macrofractography of the fractured panel provided sufficient evidence to determine the crack direction, fracture mode, and origin.

Stress Analysis. Stress analysis was performed in conjunction with visual examination to determine the state of loading of the fractured panel.

7.4.1.3 Summary

The fastener hole damage indicated that Region A of the test panel was subjected to tensile and shear loading. Region B showed no sign of damage suggesting that it was fixed to some type of structure. The major damage on the panel appeared to have been
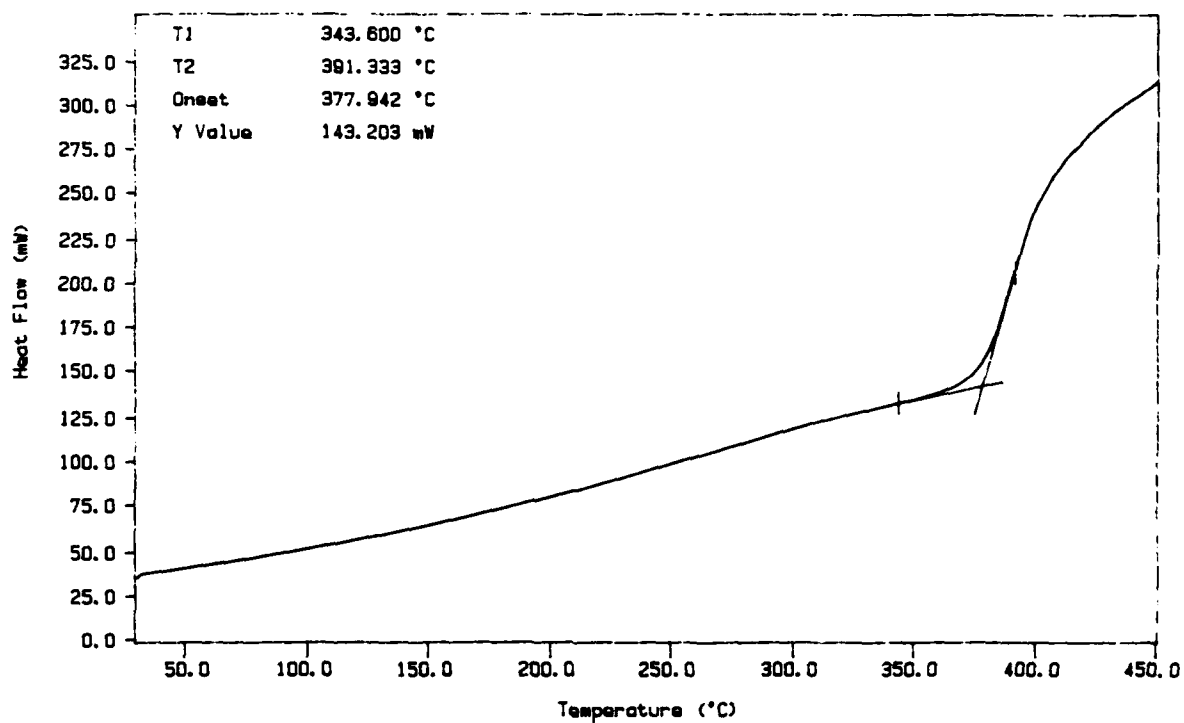
Figure 7.4-10. DSC Thermogram
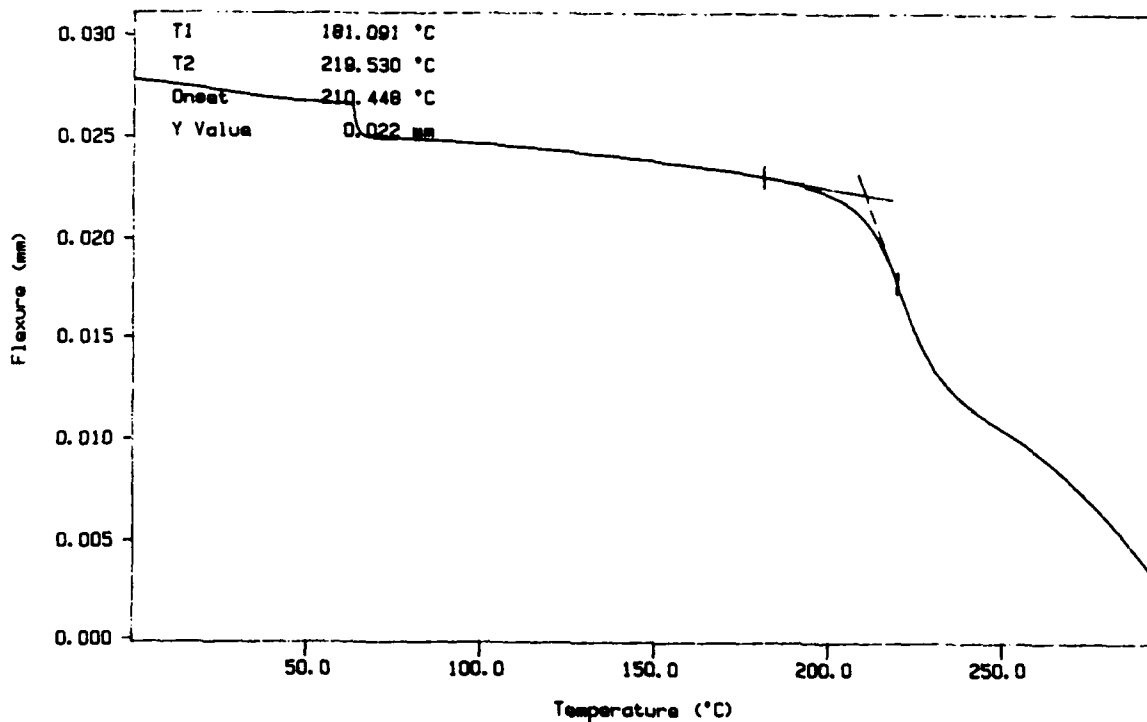
a. TMA of sample 1   Tg = 210.448°C
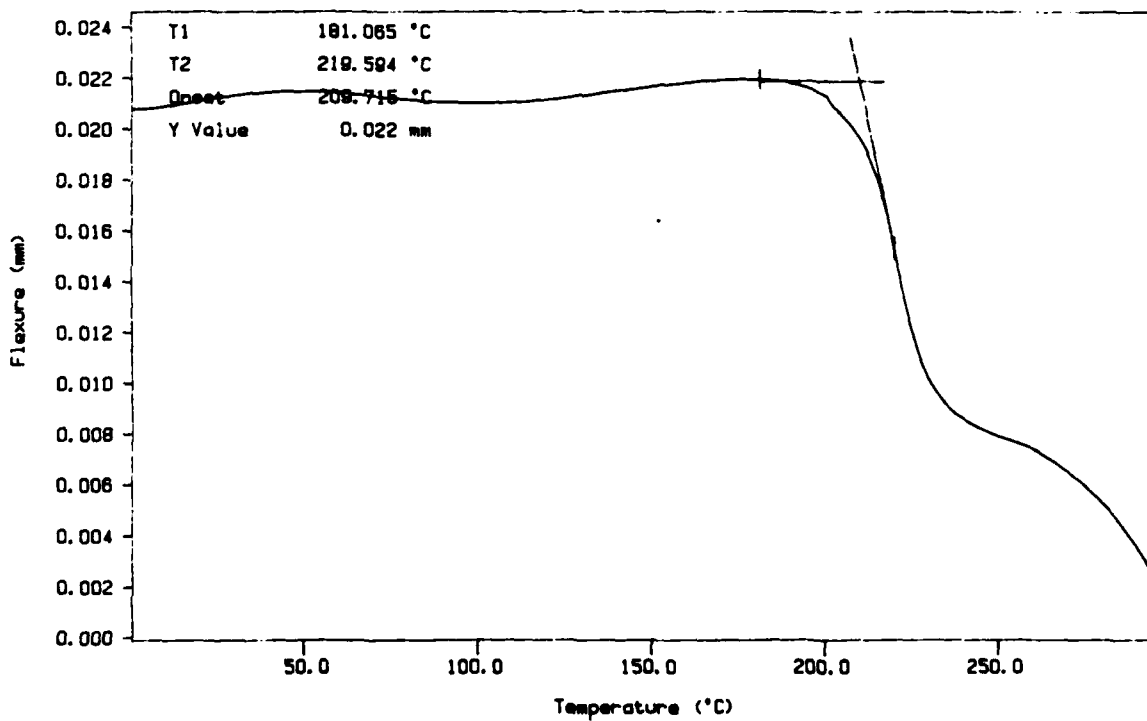
b. TMA of sample 2   Tg = 209.715°C

Figure 7.4-11. TMA Thermograms Showing an Average Glass Transition Temperature of 210 C

D180-31996-1

257
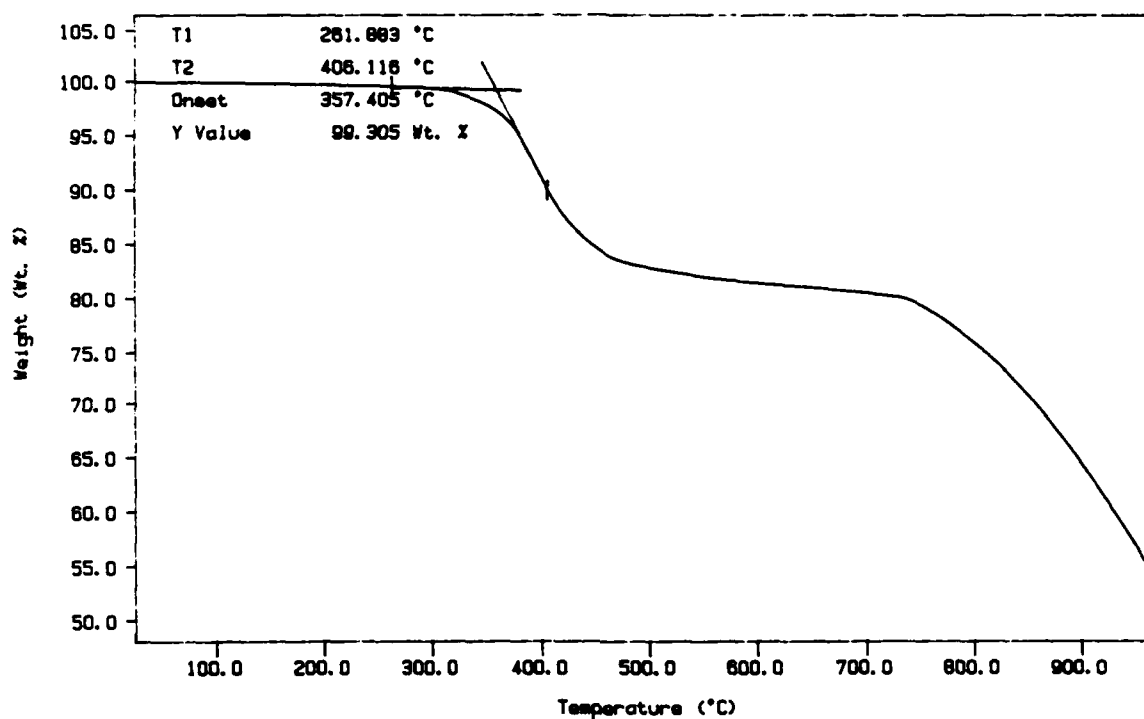
Figure 7.4-12. TGA Thermogram

Sample No.	Composite weight (grams)	Fiber weight (grams)	Resin content (% by weight)
A	1.6451	1.1691	28.9
B	1.3565	0.9571	29.4
C	1.7080	1.2028	29.6
Average:	1.5699	1.1097	29.3

Figure 7.4-13. Resin Content Determined by Acid Digestion
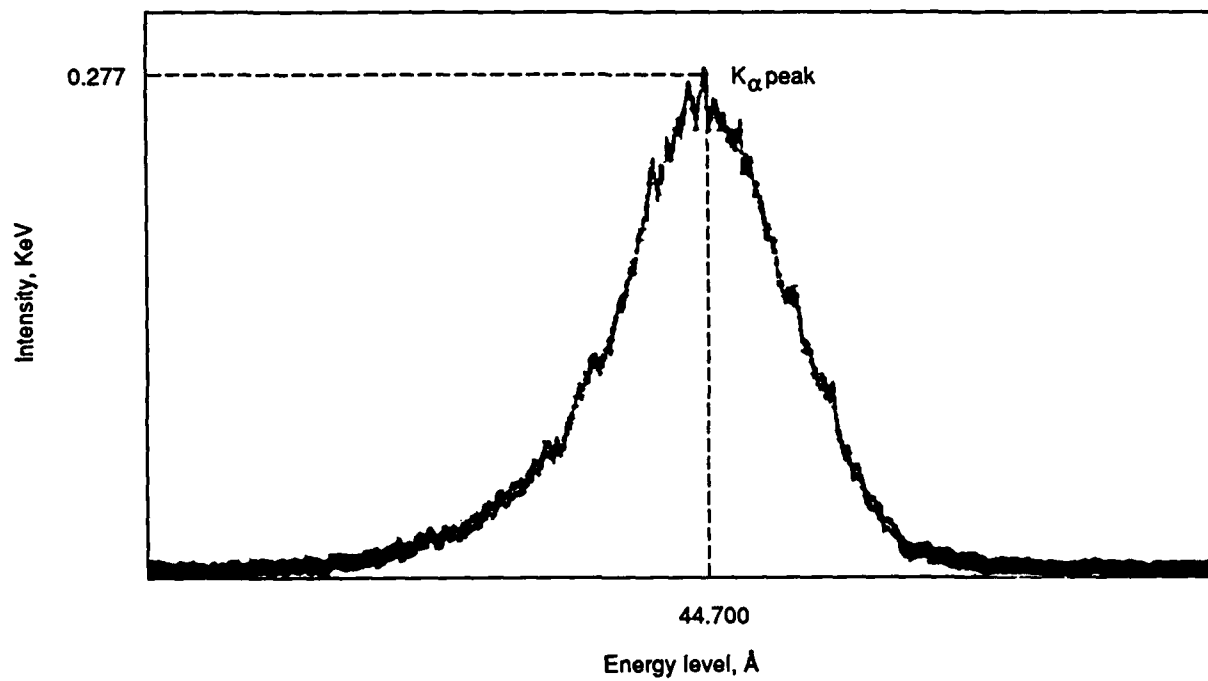
Figure 7.4-14. Wavelength Dispersive X-Ray (WDX) Scan of the Fiber

Ply stacking
sequence:

45
45
90
90
45
45
90
90
0
45
45
90
90
45
45
S

Total number
of plies is 30
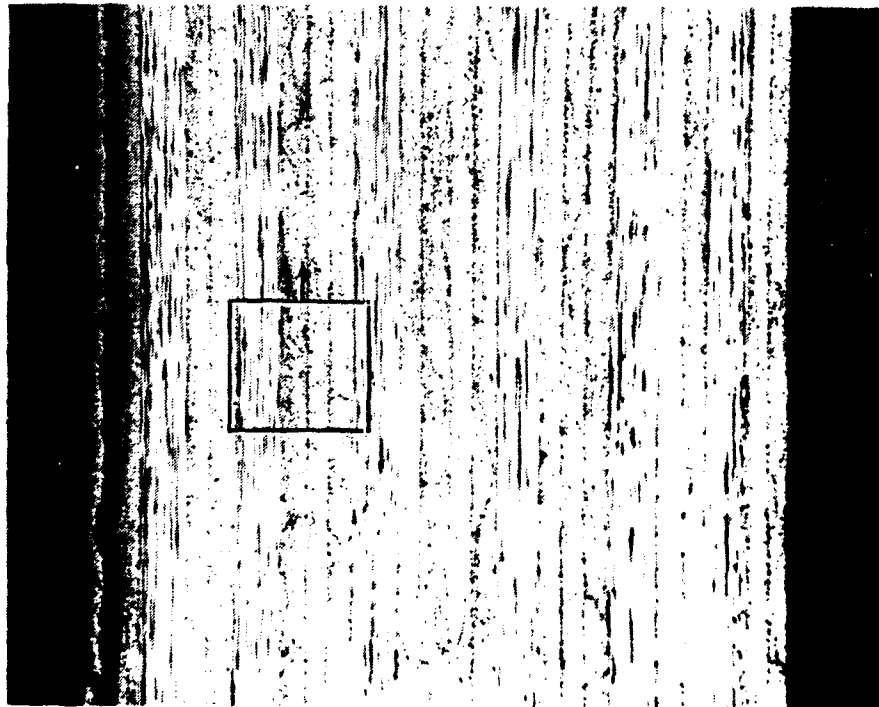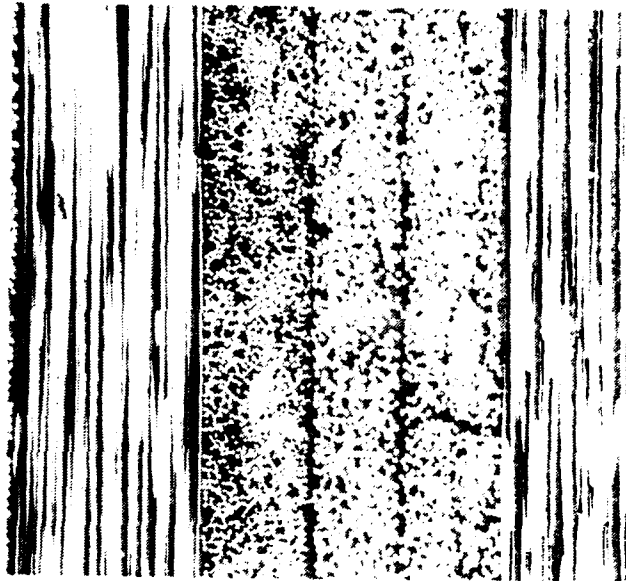
100X

25X

Figure 7.4-15. Cross-Sectional View of the Panel

caused by impact loading in which a projectile penetrated through the panel from the interior surface. Materials characterization revealed that the resin system used in fabricating this component was a 350°F cure conventional epoxy system reinforced with carbon fibers. This material system exhibited an average resin content of 29.3% by weight and was fully cured.

The cross-sectional evaluation away from the fracture revealed that the laminate quality and its symmetrical stacking response were good; little porosity was found. Further microscopic analysis was not performed because the macrofractography of the fractured panel provided sufficient evidence to determine the crack direction, fracture mode and origin.

7.4.1.4 Conclusions/Recommendations

The fastener hole damage observed in certain locations on the test panel indicated that some of fasteners were not designed for the particular application. The fasteners on the end of Region A experienced a substantial amount of shear loading compared to the rest of the panel. The recommendation would be to examine the hole damage and make appropriate changes in the fasteners (i.e., change to shear or tension) to accommodate the load conditions experienced during the initial testing. Due to the fact that the mechanical test was unknown, recommendation for design improvement is difficult.

Material anomalies such as contamination or poor processing were not related to the cause of the fracture. The cause of fracture appeared to be impact loading due to the penetration of a projectile.

It would be helpful for the investigator to be provided with additional background information and also other related parts such as the fasteners used during the test to verify in future analyses.

7.4.2 Failure Analysis of the Second Component

Failure analysis of the second component was conducted by GE.

7.4.2.1 Background History

The second component was a Helio H-800 main landing gear strut, which had fractured at the tapered end. The component received was an E-glass/epoxy composite

with a 0/90 layup. The strut is oriented approximately 40 degrees with respect to the wide end. The component is subjected to axial and shear stress, as well as a bending moment, induced by the weight of the aircraft. Visual examination revealed a translaminar fracture surface with evidence of tensile and compressive portions, indicating fracture due to a bending load. Three discontinuous delaminations, one located at the approximate mid-thickness of the small piece and two in the large piece, were observed in the strut.

7.4.2.2 Factual Data

Visual Examination. The fracture was located at the wide end of the strut at the point where the taper begins (see Fig. 7.4-16). This translaminar fracture revealed both tensile and compressive fracture characteristics, typical of fracture under a bending load (Fig. 7.4-17 and 7.4-18). Tensile fracture is indicated by multiplanar fracture with individual fibers or bundles observed, whereas compressive fracture is indicated by planar fracture. Translaminar fracture occurred at an angle such that it propagated through a bolthole on the lower surface and adjacent to the bolthole on the upper surface (see Fig. 7.4-16 and 7.4-19). The edge of the aircraft mounting plate is approximately located at the fracture location. The tensile and compressive portions of this fracture were consistent with the bending moment produced as installed in the aircraft (see Fig. 7.4-20). Three separate delaminations were observed in this strut. One delamination was observed in the small piece at approximately the mid-thickness of the strut, between the tensile and compressive portions of the fracture (neutral axis). Two delaminations were observed on the large (long) piece which divided the strut thickness approximately into thirds.

Non-Destructive Evaluation. Non-destructive evaluation was not performed on this component because the damage was considered to be readily apparent upon visual inspection.

Material Characterization. Nearly identical results were obtained from the glass transition temperature measurements by TMA and DSC (see Fig. 7.4-21). These values were 133°C (271°F) and 135°C (275°F), respectively. These are typical values for a 121°C (250°F) epoxy resin. Additional chemical evaluation should be performed to fully characterize the conformance of this material to specifications.
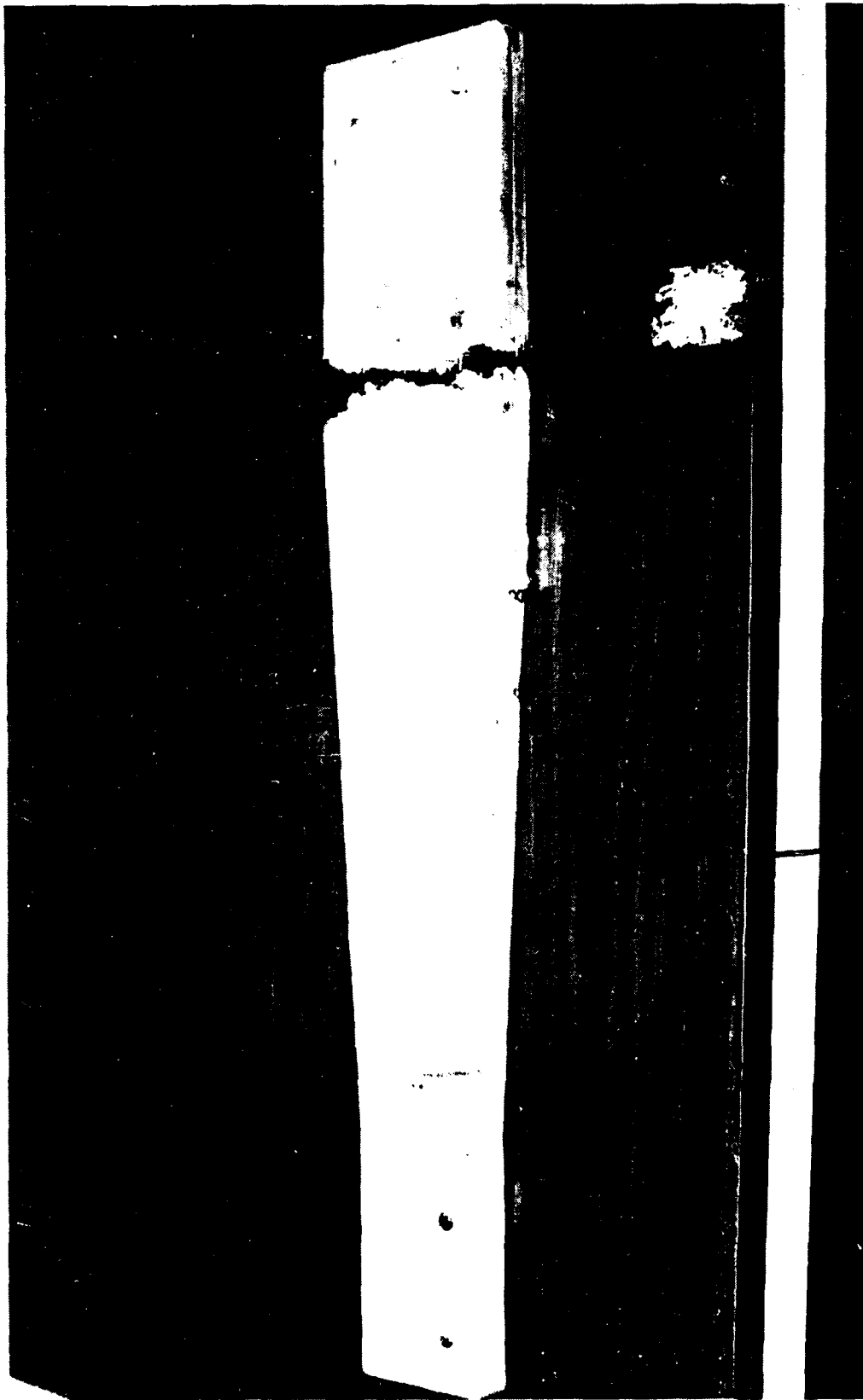
Upper surface

Approximately 1/4X

Figure 7.4-16. Macrophotograph of the Upper Surface of the Landing Strut as Recieved
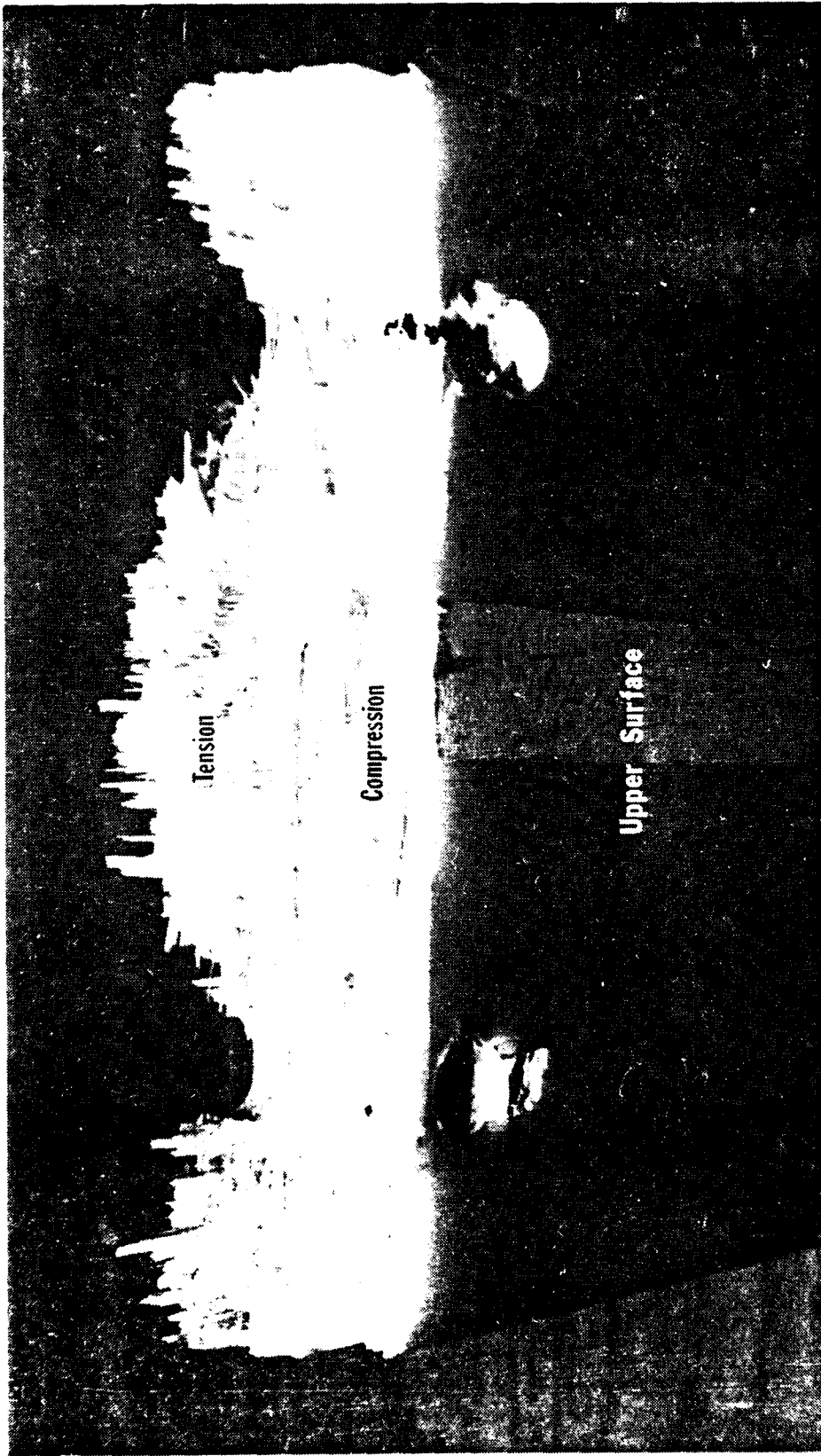
Fracture surface—small piece

1.3X

Figure 7.4-17. *Macrophotograph of the Translaminar Fracture Surface on the Small (Fixed Piece) of the Strut.* Tension fracture is multiplanar and shows individual fibers or bundles; compression fracture is planar.

Delamination

T

Upper surface

C

1X

Fracture surface—small piece

Delamination—upper half   0.6X   Delamination—upper half   0.6X
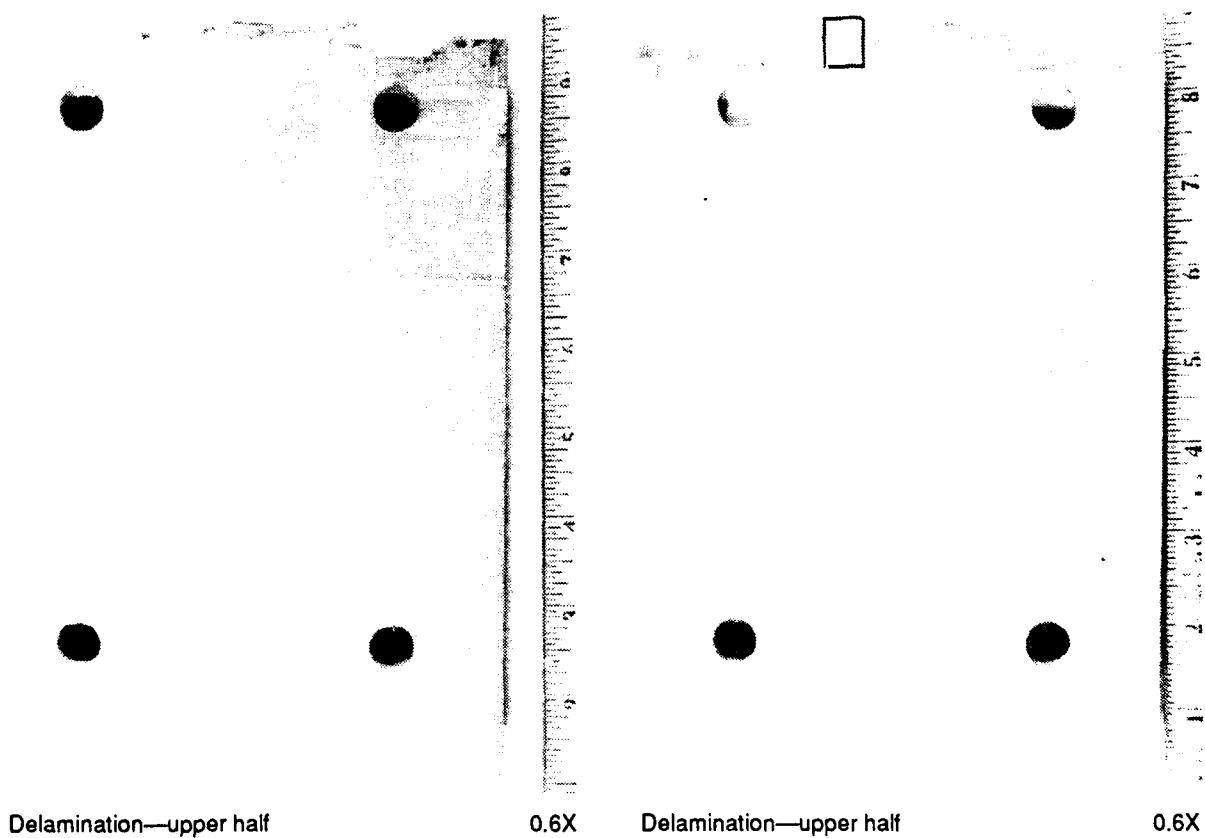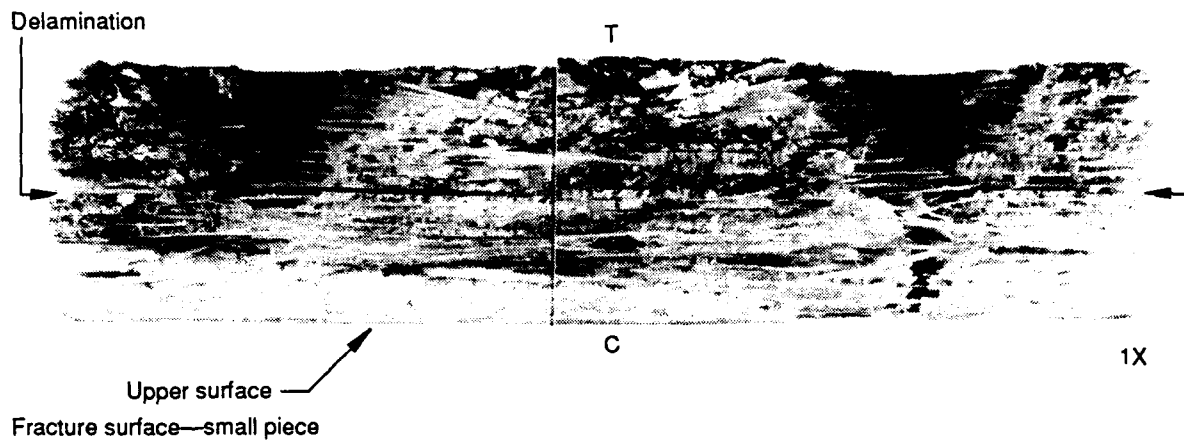
Figure 7.4-18. Macrophotographs of the Top of the Small Piece Fracture Surface Showing Delamination,
Upper Surface, Tension Fracture (T) and Compression Fracture (C). The lower
macrophotographs show the mating delamination surfaces after laboratory separation
of the delamination. The area shown by the small box is magnitied in figure 7.4-24.
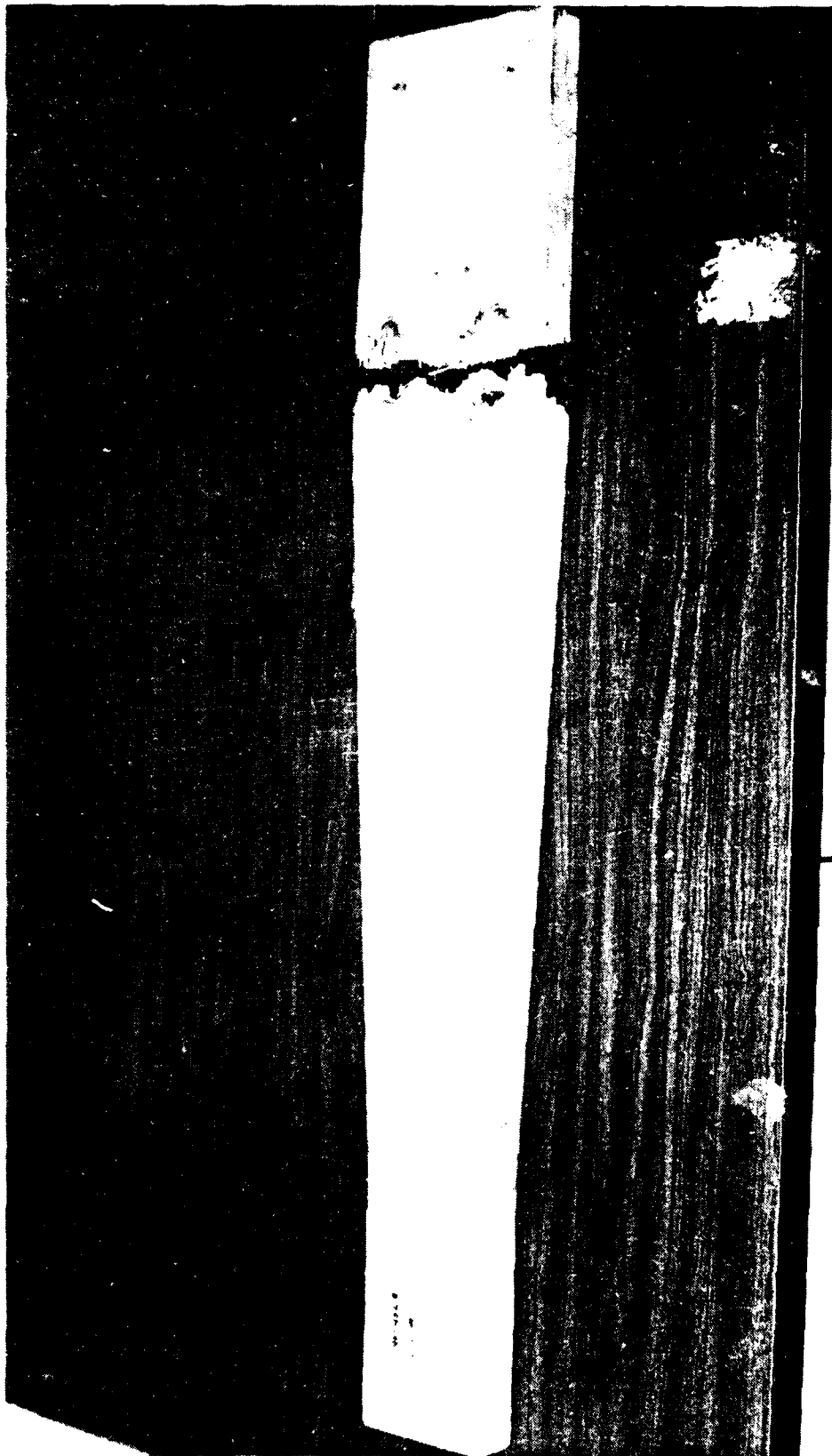
Lower surface

Approximately 1/4X

Figure 7.4-19. Macrophotograph of the Lower Surface of the Strut As Recieved. The translaminar fracture occured at the boltholes on this surfacc.

END
FILMED

DTIC
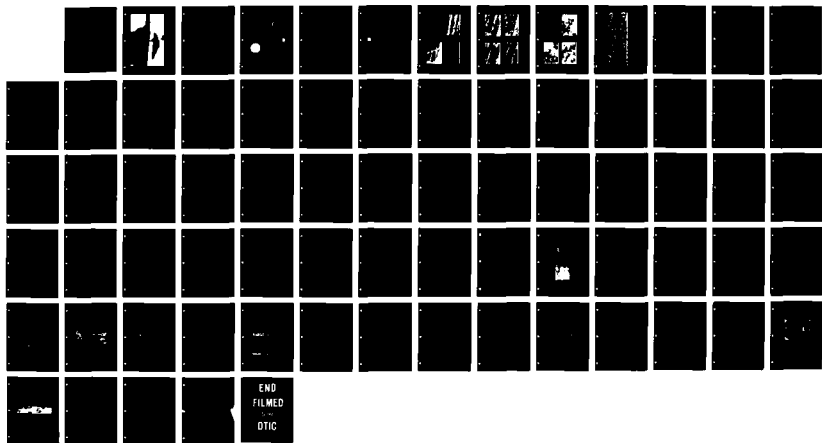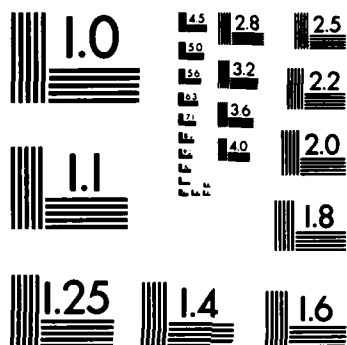
MICROCOPY RESOLUTION TEST CHART
NATIONAL BUREAU OF STANDARDS
STANDARD REFERENCE MATERIAL 1010a
(ANSI and ISO TEST CHART No. 2)
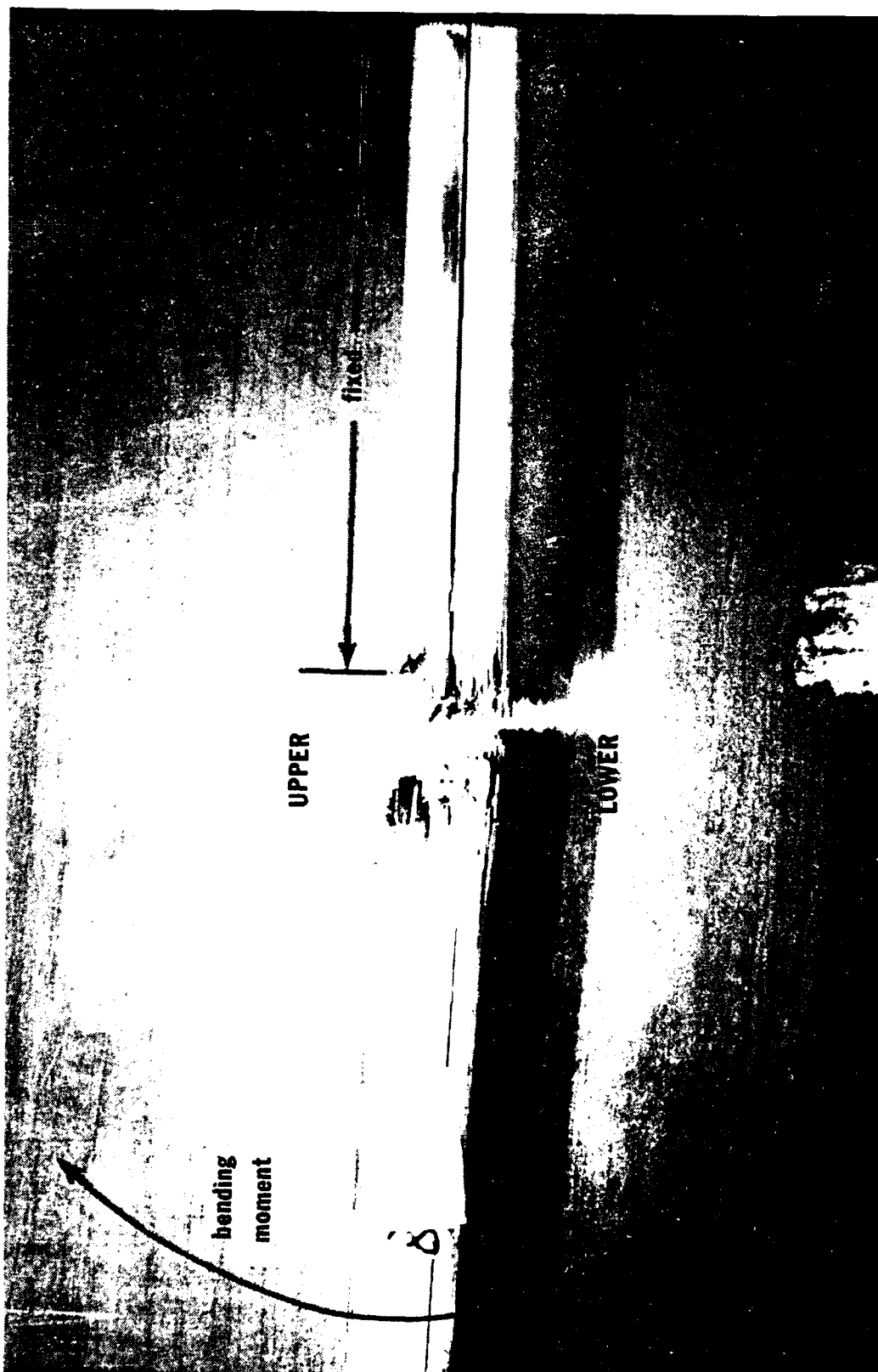
Side view—delaminations 0.6X

Figure 7.4-20. Macrophotographs of Side of Strut Showing Delaminations. Neither portion of this strut was completely separated by delaminations. The figure shows the apparent loading condition which led to failure. The bending moment was greatest at the edge of the fixed portion of the strut, the failure location. As anticipated from this loading condition, the upper surface failed in compression and the lower surface failed in tension.
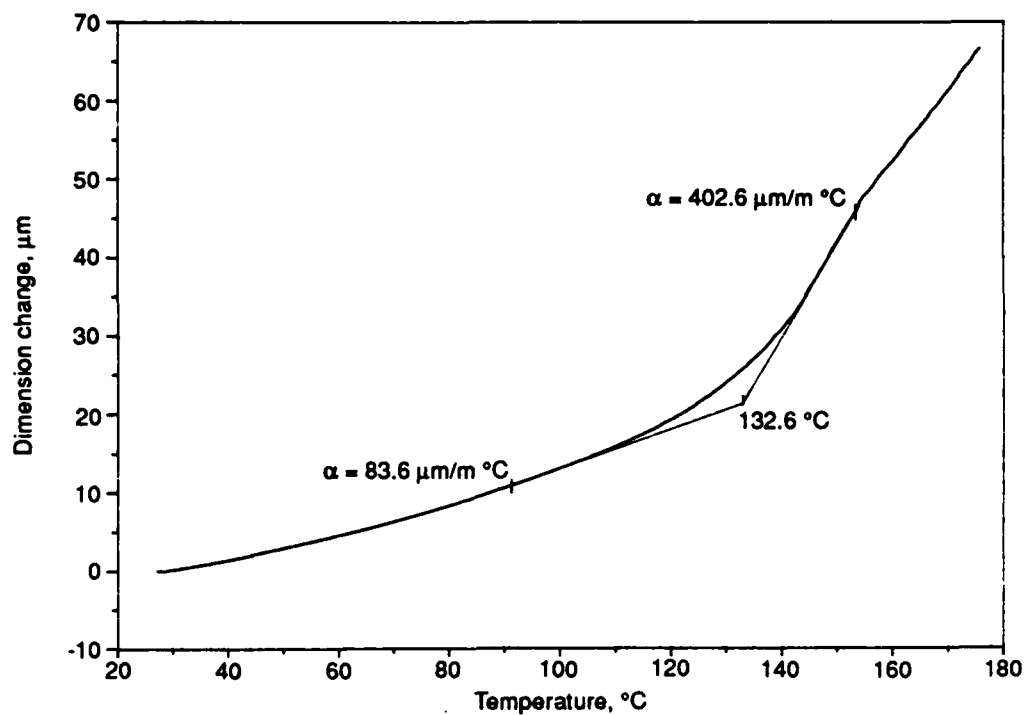
(a) TMA
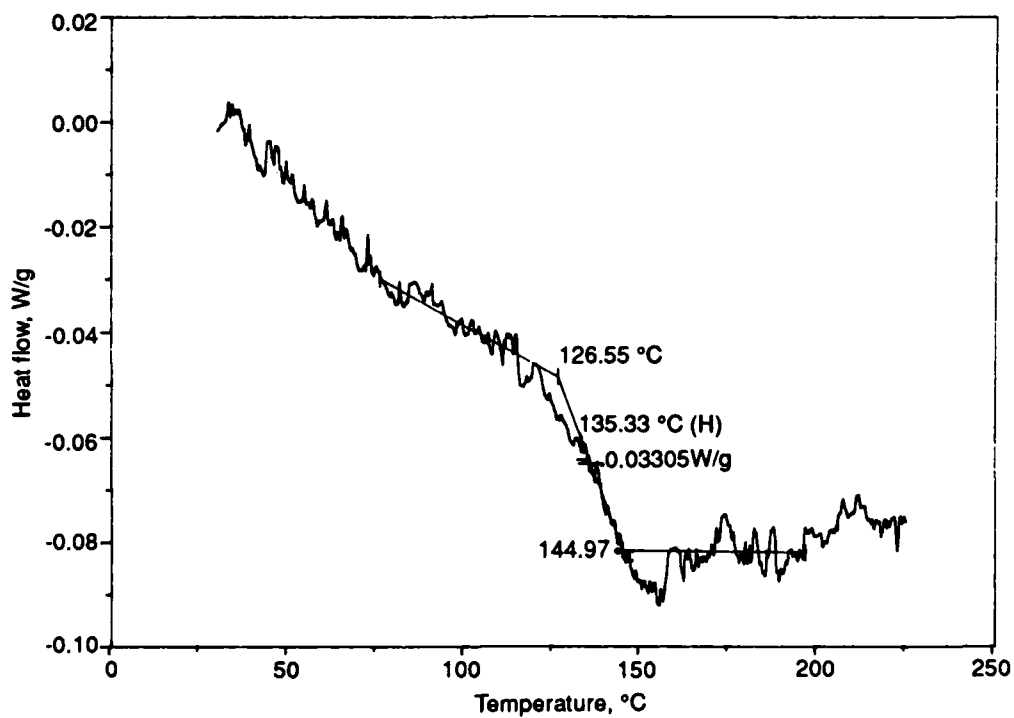
(b) DSC

Figure 7.4-21. TMA and DSC Thermograms of Strut

Lower surface   0.12X

Bolt hole—lower surface   3.1X
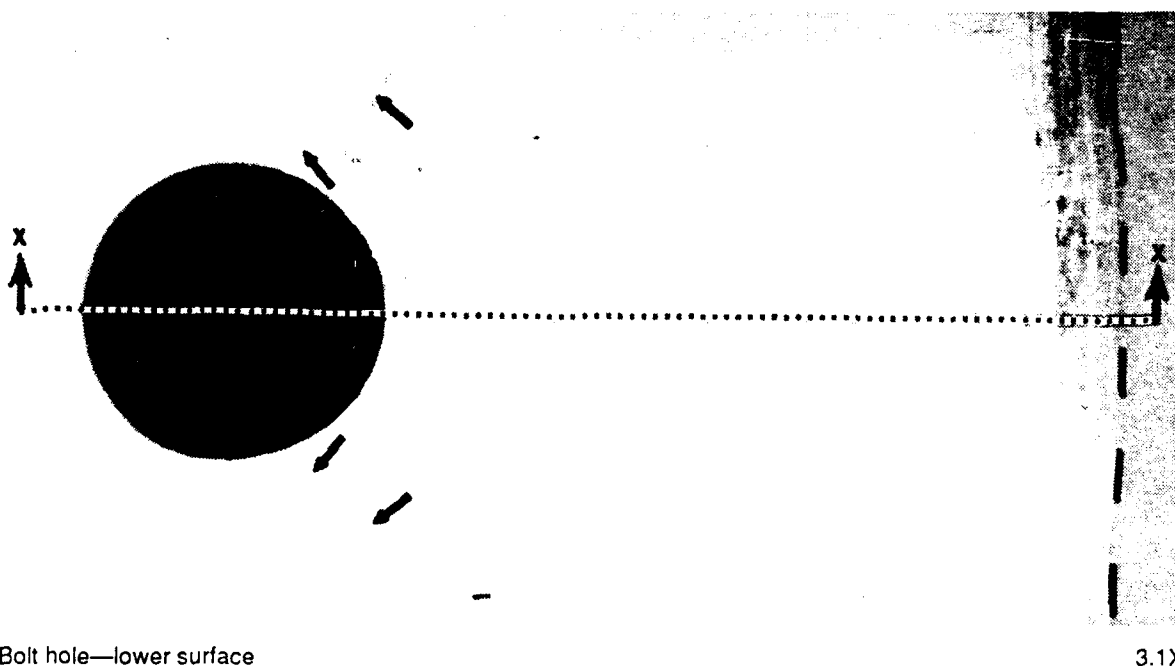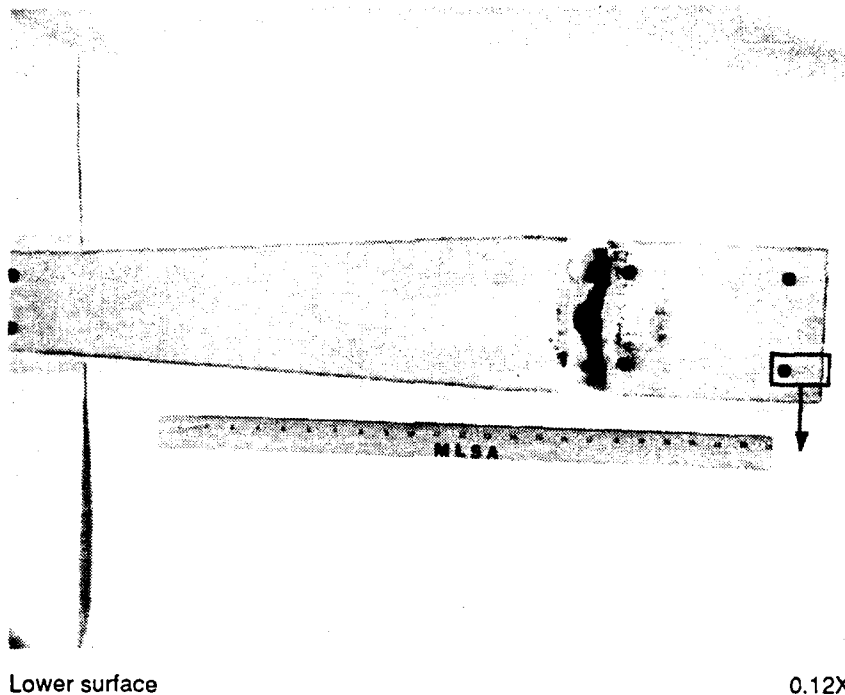
Figure 7.4-22. Macrophotographs of the Lower Surface of Strut. The figure shows the location and orientation of section x-x, magnified in figure 7.4-23. The local bulging at the end of the strut (emphasized by the segmented line) occurred as a result of restraint from the bolt. Cracks labeled by the small arrows were also generated by this loading condition.

A metallographic section was taken through a bulged area (see Figs. 7.4-22 and 7.4-23), found adjacent to a bolthole, which was apparently the result of constraint by the bolt. This section revealed microbuckling of fibers in a crack-like formation extending from the delamination toward the lower surface. Fiber and matrix details were difficult to discern from the prepared section, but the overall condition of the laminate appeared to be good.

Fractography. SEM examination was performed on the single delamination of the small piece and on the translaminar fracture on the small piece. Evidence of shear fracture (scallops and hackles) was observed on the laboratory-exposed surface of the single delamination in the small piece (see Figs. 7.4-24 and 7.4-25). The propagation direction was oriented axially along the length of the strut, but the exact direction could not be determined. Examination of the tensile half of the translaminar fracture revealed radial patterns on fiber end fractures (see Fig. 7.4-26). The resultant direction of crack propagation, determined by mapping the directions in which the lines radiate on the individual fiber fractures, was from the lower surface (tension) toward the delamination. Examination of the compressive half of the translaminar fracture revealed buckled fibers displaying chop marks (see Fig. 7.4-27), typical of compressive failures. Although SEM examination of the translaminar fracture was conducted around the bolthole region, the non-conducting surfaces encountered produced images which were not of sufficient quality to include in this report. SEM examination of the translaminar fracture was difficult to perform, due to the extreme depth of this fracture. This prevented adequate application of gold (even after multiple sputter applications) to get a uniformly covered surface. Therefore, charging of uncoated areas during SEM examination made the location of suitably informative, fiber fractures difficult to perform.

Stress Analysis. Preliminary stress analysis was performed in conjunction with visual examination to determine the state of loading of the strut.

7.4.1.3 Conclusion/Recommendation

All evidence observed during this investigation indicates failure of the strut due to a bending moment applied at the aircraft attachment plate (fracture location). The moment induced tensile and compressive fractures at the lower and upper surfaces, respectively, as well as the delaminations observed due to the acting shear plane. Since no material defects or anomalies were observed during this evaluation, the fracture apparently occurred due to overload, perhaps during hard landing. Due to the fact that
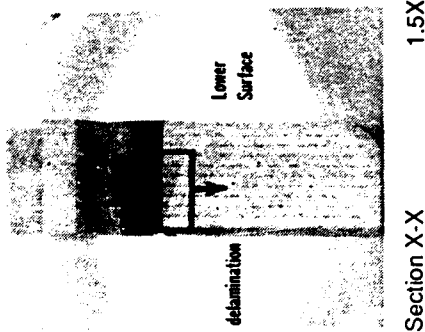
Section X-X   1.5X
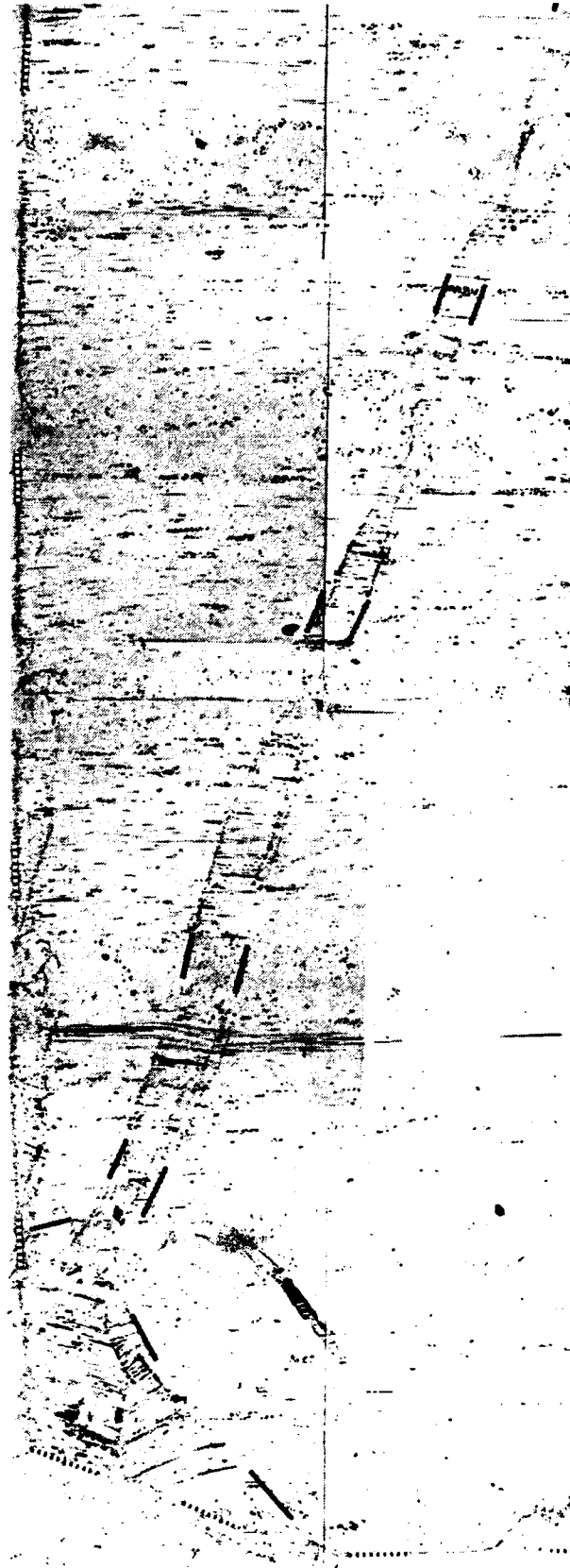
Section X-X   40X

Figure 7.4-23. *Macrophotograph (A) and Photomicrograph (B) of Section X-X Taken Through the Bolthole and End.* The segmented black lines outline a region of fiber microbuckling damage induced by the local restraint of the bolt on this side of the bolthole. The delamination and bolthole surfaces of this section are outlined by the segmented dashed lines.
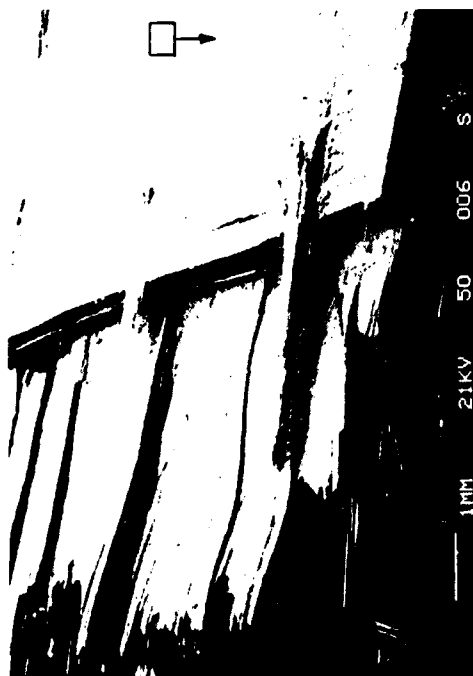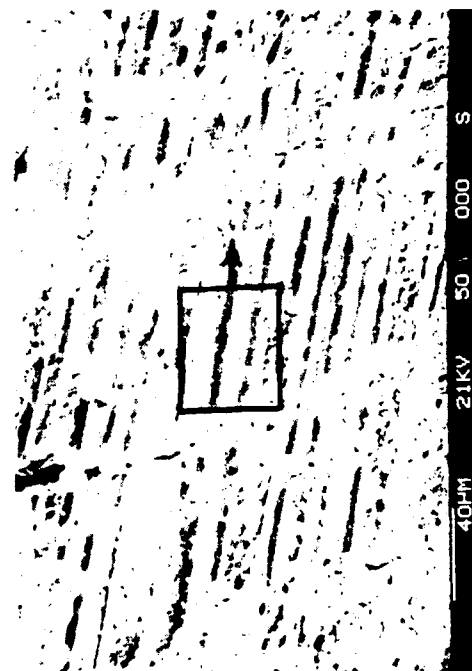
Figure 7.4-24. *SEM Fractographs of Delamination at the Translaminar Fracture Surface of the Small Piece. Scallops indicate shear fracture. The orientation of these scallops indicates progation of the delamination axially along the strut.*

Legend: S scallop

Figure 7.4-25. *SEM Fractographs of Delamination Adjacent to Translaminar Fracture.* Hackles indicate shear fracture and propagation of the delamination axially along the strut.

Delamination—50 degree tilt   400X

Delamination—50 degree tilt   400X

50 degree tilt   2,000X

50 degree tilt   2,000X

Legend: H hackle

Delamination
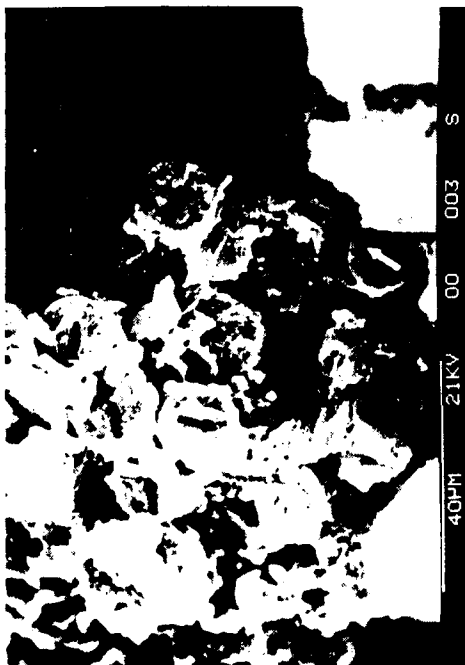
Lower surface

975X

Tensile fracture—0 degree tilt

950X

0 degree tilt

1000X

0 degree tilt

Figure 7.4-26. SEM Fractographs of the Tensile Half of the Translaminar Fracture Surface. Small arrows show crack propagation direction indicated by individual fiber end fractures. The overall crack propagation direction indicated by these fibers is toward the delamination from the lower (tensile) surface.

Compressive fracture—0 degree tilt   400X   0 degree tilt   1,400X

Legend:

C   compression
T   tension

Figure 7.4-27. SEM Fractographs of the Compressive Half of the Translaminar Fracture. These fractographs exhibit compressively loaded fiber fractures, as indicated by the presence of both tensile and compressive fracture morphology

tensile fiber radial patterns indicated propagation from the tensile surface toward the delaminations and since the observed delaminations are discontinuous, it is inferred that initiation of the translaminar fracture occurred prior to delamination.

More specific conclusions could be drawn concerning the loading of this component during fracture if some record of aircraft/component field service had been provided. Although this information was not provided, indication of some field service of this component was observed in the distortion at the boltholes.

ST6003/V277/355-9

APPENDIX A:

TASK 4 RESULTS — APPROVED DATA COLLECTION SHEETS

FAILURE ANALYSIS COLLECTION
AND TRACKING SYSTEM (FACTS)
DATA INPUT SHEET

OPERATOR: _____ DATE: _____

REPORT NUMBER: _____ DESIGN DRAWING PART NAME/NUMBER: _____

_____

_____

_____

PART LOCATION ON AIRCRAFT: ___ _____

MATERIAL/PROCESSING INFORMATION/SPECIFICATION: _____

_____

AIRPLANE INFORMATION: CUSTODIAN AFB: _____

MODEL: _____ FLIGHT HOURS: _____

NUMBER OF LANDINGS: _____

BACKGROUND/INFORMATION:

LOCATION OF DAMAGE: _____

ENVIRONMENTAL CONCERNS: _____

(OTHERS): _____

_____

_____

DATA: _____

_____

_____

_____

_____

_____

ANALYSES CONDUCTED: _____

_____

_____

_____

_____

RESULTS:_____

_____

_____

_____

_____

RECOMMENDATIONS: _____

_____

_____

_____

_____

KEYWORDS: _____ _____ _____

_____ _____ _____

OPERATOR: ————————————————————— DATE: ———————————————

PART NAME/NUMBER: ———————————————————————————————

MATERIALS & CONSTRUCTION: ——————————————————————————

——

——

LOCATION OF ANALYSIS: ————————————————————————————

REASON FOR ANALYSIS: ————————————————————————————

ANALYTICAL INSTRUMENT/SETTINGS: ——————————————————————

——

——

——

——

——

——

SUPPORTIVE DATA: ——————————————————————————————

——

——

——

——

——

——

RESULTS/INTERPRETATIONS:————————————————————————————

——

——

——

——

——

——

——

——

——

KEYWORDS: —————————————— ——————— ——————————

—————————————— ——————— ——————————

OPERATOR: _____ DATE: _____

PART NAME/NUMBER:_____

MATERIALS/SPECIFICATIONS:_____
_____

SPECIFICATION REQUIREMENTS:_____

CURE TEMP: _____

FIBER/RESIN DENSITIES: _____

VERIFICATION DATA:

- Tg DETERMINATION–

  INSTRUMENTATION: _____
  _____

  RESULTS: _____
  _____

- RESIN CHARACTERIZATION–

  INSTRUMENTATION: _____
  _____

  RESULTS: _____
  _____

- RESIN CONTENT–

  INSTRUMENTATION: _____
  _____

  RESULTS: _____
  _____

- SPECIALIZED ANALYSES METHODS USED (HPLC, GPC, DSC, SURF. ANALYSIS, ETC.): _____
  _____

RESULTS: _____
_____
_____
_____
_____
_____
_____

KEYWORDS: _____ _____ _____
          _____ _____ _____

- Diagram of specimen location

- Data/Graphs from analysis

COMMENTS: _____
_____
_____
_____
_____
_____
_____

OPERATOR: _____ DATE: _____

PART NAME/NUMBER: _____

MATERIAL: _____

VISUAL OBSERVATIONS: _____

_____

_____

_____

_____

_____

_____

_____

_____

_____

_____

_____

_____

_____

_____

_____

_____

_____

_____

_____

_____

_____

_____

_____

_____

_____

_____

_____

_____

_____

_____

KEYWORDS: _____ _____ _____

             _____ _____ _____

- Diagram or photo of part location on structure

- Photo of overall part

- Closeup of fracture origin or defect

MAG

MAGNIFICATION: _____

COMMENTS: _____

D180-31996-1

A-7

OPERATOR: _____ DATE: _____

PART NAME/NUMBER: _____

MATERIAL: _____

    RESIN/FIBER SYSTEM: _____

    LAYUP: _____

MICROSCOPIC OBSERVATIONS: _____

_____

_____

_____

_____

_____

_____

_____

_____

_____

_____

_____

_____

_____

_____

_____

_____

_____

_____

_____

_____

_____

_____

_____

_____

_____

_____

_____

_____

_____

_____

_____

_____

_____

_____

_____

KEYWORDS: _____ _____ _____

             _____ _____ _____

- Optical photomicrograph

- Low-Mag photomicrograph
  - SEM
  - TEM
  - STEM

- High-Mag photomicrograph
  - SEM
  - TEM
  - STEM

MAG

MAGNIFICATION: _____

COMMENTS: _____
_____
_____
_____
_____
_____
_____

STRESS ANALYSIS
DATA INPUT SHEET

OPERATOR: _____ DATE: _____

PART NA IE/NUMBER: _____

MATERIALS/SPECIFICATION/CONSTRUCTION: _____

_____

_____

ENVIRONMENTAL AND LOAD CONDITIONS (PRIOR TO AND DURING FRACTURE): _____

_____

_____

_____

INPUTS FROM FRACTOGRAPHY (ORIGIN, LOAD TYPES, DEFECTS): _____

_____

_____

_____

INITIAL STRUCTURAL REVIEW:

● GROSS STRAIN AT ORIGINS: _____

_____

● ALLOWABLES AT ORIGINS: _____

_____

● ANALYSIS METHODS: _____

_____

● RESULTS/COMMENTS: _____

_____

_____

_____

LAMINA LEVEL REVIEW:

● FAILURE CRITERIA USED: _____

_____

● ANALYSIS METHODS USED: _____

_____

● RESULTS: _____

_____

SUMMARY/INTERPRETATIONS: _____

_____

_____

_____

_____

KEYWORDS: _____ _____ _____

               _____ _____ _____

D180-31996-1

A-10

- Diagram of part loading

COMMENTS: _____
_____
_____
_____
_____
_____
_____

APPENDIX B:

TASK 5 RESULTS — MATERIAL PROPERTIES

Typical fiber properties	AS1	AS2	AS4	AS6	IM6	IM7
Tensile strength, ksi	451	401	551	601	636	684
MPa	3105	2760	3795	4140	4382	4713
Tensile modulus, msi	33	33	34	35	40	41
GPa	228	228	235	242	276	283
Ultimate elongation, %	1.32	1.20	1.53	1.65	1.50	1.60
Carbon content, %	92	94	94	94	94	--
Density, g/cm^3	1.80	1.80	1.80	1.83	1.73	1.78

Typical epoxy composite properties at RT	AS1	AS2	AS4	AS6	IM6	IM7
Tensile strength, ksi	280	290	342	373	395	424
MPa	1932	2001	2353	2567	2719	2922
Tensile modulus, msi	20	20	21	22	20	25
GPa	138	138	145	151	138	175
Flexural strength, ksi	250	240	260	272	250	237
MPa	1725	1656	1794	1877	1725	1635
Flexural modulus, msi	18	18	19	20	22	24
GPa	124	124	131	139	150	166
Short beam shear, ksi	19	18	18	19	18	19
MPa	131	124	124	129	124	129
Fiber volume, %	62	62	62	62	62	62

Figure B-1. Mechanical Properties of Hercules Fibers
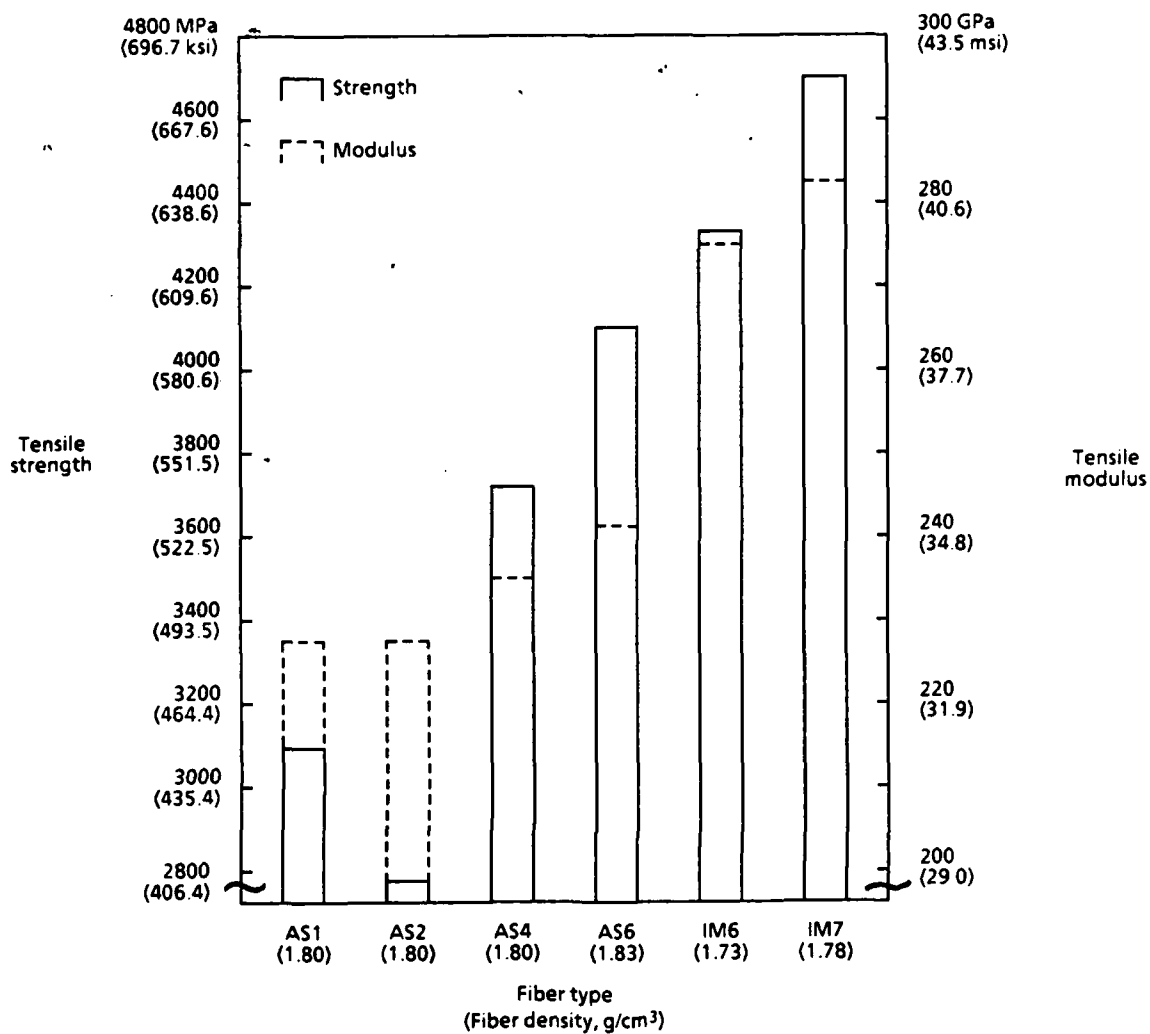
Figure B-2.   Hercules Fiber Properties at Room Temperature
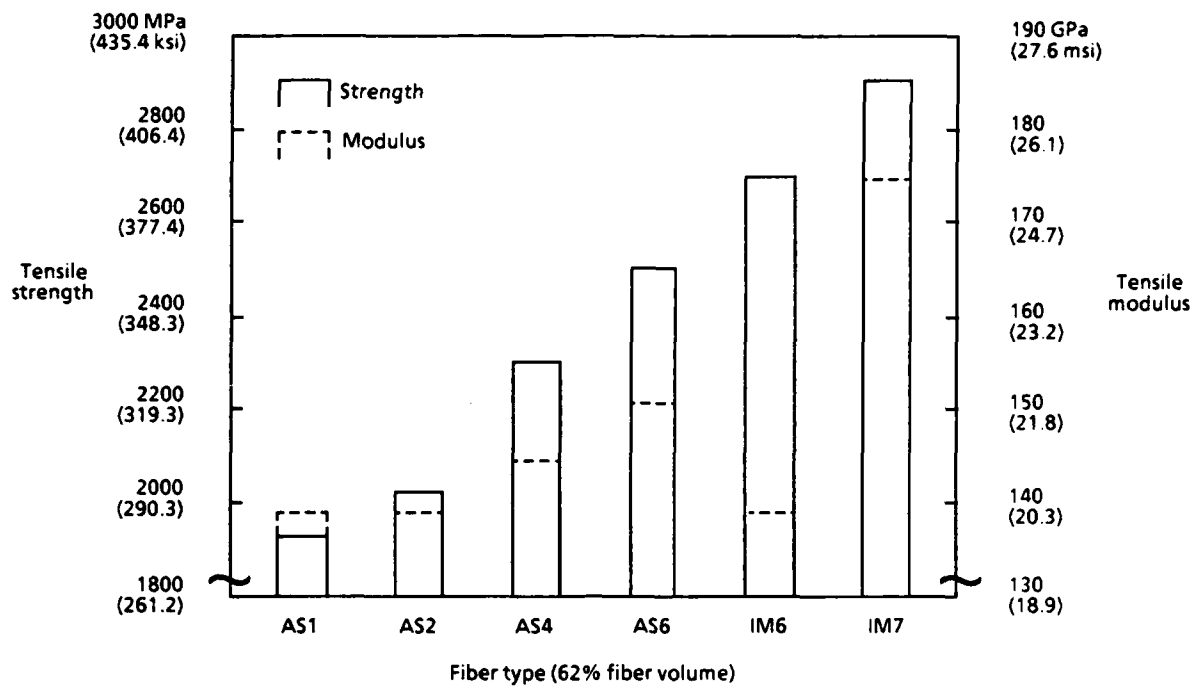
Figure B-3.   Typical Epoxy Composite Properties at Room Temperature

| Fiber type * | Tensile strength | | | | Young's modulus | | | | Poisson's ratio | Density | |
| | 0° | | 90° | | 0° | | 90° | | | | |
	MPa	ksi	MPa	ksi	GPa	msi	GPa	msi		g/cm³	lb/in³
E-Glass	1020	150	40	7	45	6.5	12	1.8	0.28	2.08	0.075
S-Glass	1620	230	40	7	55	8.0	16	2.3	0.28	2.02	0.073
Boron	1240	180	70	10	210	30.0	19	2.7	0.25	2.02	0.073
Kevlar 49	1240	180	280	40	76	11.0	5.5	0.8	0.34	1.39	0.050

* Fiber volume, V_f = 60%

Figure B-4.   Properties of Typical Epoxy Composites at Room Temperature
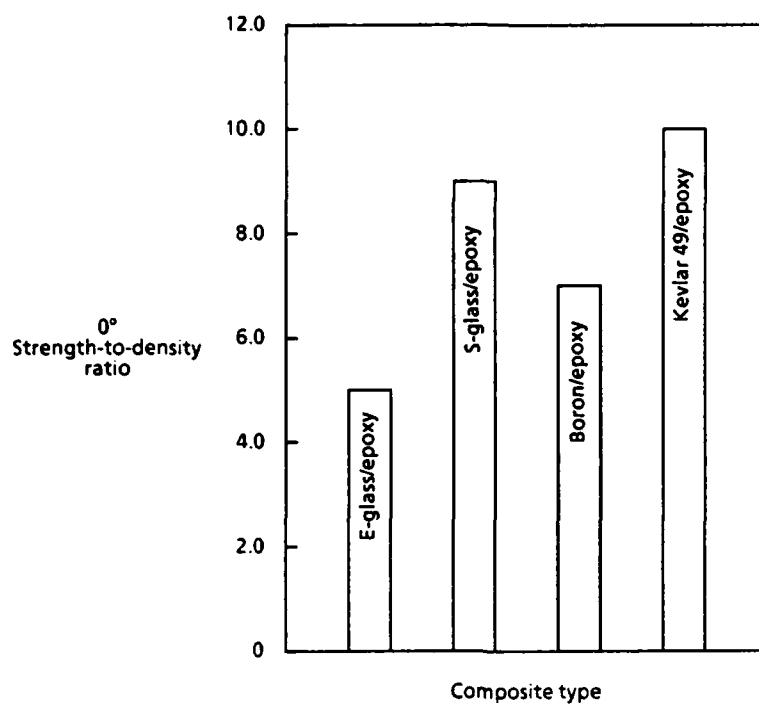
Figure B-5.   0° Strength-to-Density Ratio of Typical Epoxy Composites
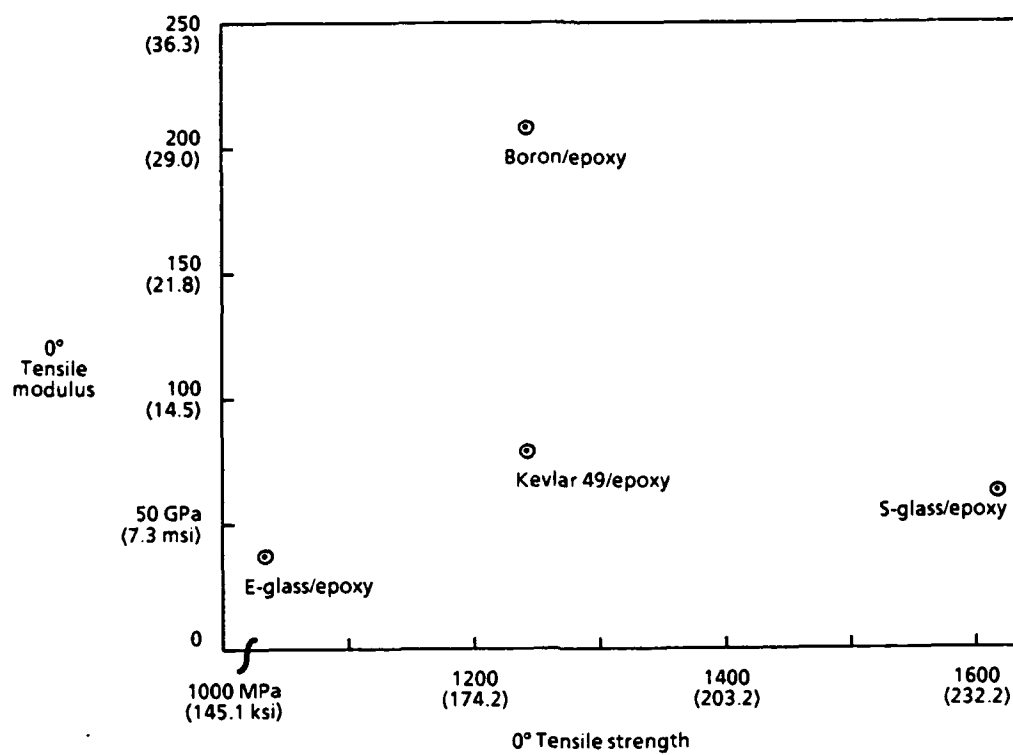
Figure B-6.   0° Tensile Properties of Typical Epoxy Composites

Type	Ultimate tensile strength		Tensile modulus		Poisson's ratio (V₁₂)	Ultimate compressive strength		Compressive modulus		Transverse shear strength		Shear modulus		Interlaminar shear strength		Specific gravity, g/cm³	Cured ply range	
	MPa	ksi	GPa	msi		MPa	ksi	GPa	msi	MPa	ksi	GPa	msi	MPa	ksi		µm	mils
Standard bidirectional graphite/epoxy	586	85	68.9	10.0	0.09	565	82	62.1	9.0	93.1	13.5	4.8	0.7	67.6	9.8	1.59	127-381	5-15
1.5%-strain bidirectional graphite/epoxy	690	100	68.9	10.0	0.09	586	85	62.1	9.0	93.1	13.5	4.8	0.7	66.2	9.6	1.60	178-381	7-15
High-modulus bidirectional graphite/epoxy	345	50	117.0	17.0	0.09	152	22	110.0	16.0	34.5	5.0	4.8	0.7	31.0	4.5	1.80	203-381	8-15
Ultrahigh-modulus bidirectional graphite/epoxy	345	50	152.0	22.0	0.09	152	22	152.0	22.0	34.5	5.0	4.8	0.7	34.5	5.0	1.80	152-330	6-13
Standard woven unidirectional graphite/epoxy	1310	190	129.0	18.7	0.25	1105	160	124.0	18.0	62.1	9.0	4.1	0.6	82.7	12.0	1.60	178-254	7-10
Standard bidirectional hybrid graphite/S-2 glass	483	70	51.7	7.5	0.09	565	82	48.3	7.0	34.5	5.0	4.1	0.6	65.5	9.5	1.80	254-381	10-15
Standard bidirectional hybrid graphite/Kevlar 49	448	65	51.0	7.4	0.09	276	40	41.4	6.0	-	-	-	-	34.5	5.0	1.55	254-381	10-15

Figure B-7.   Physical Properties of Graphite Fabric Prepreg (Data from Fiberite Corp)

Figure B-8.   Tensile Properties of Graphite Fabric Prepreg

(1) Standard bidirectional
     graphite/epoxy

(2) 1.5%-strain
     bidirectional
     graphite/epoxy

(3) High-modulus
     bidirectional
     graphite/epoxy
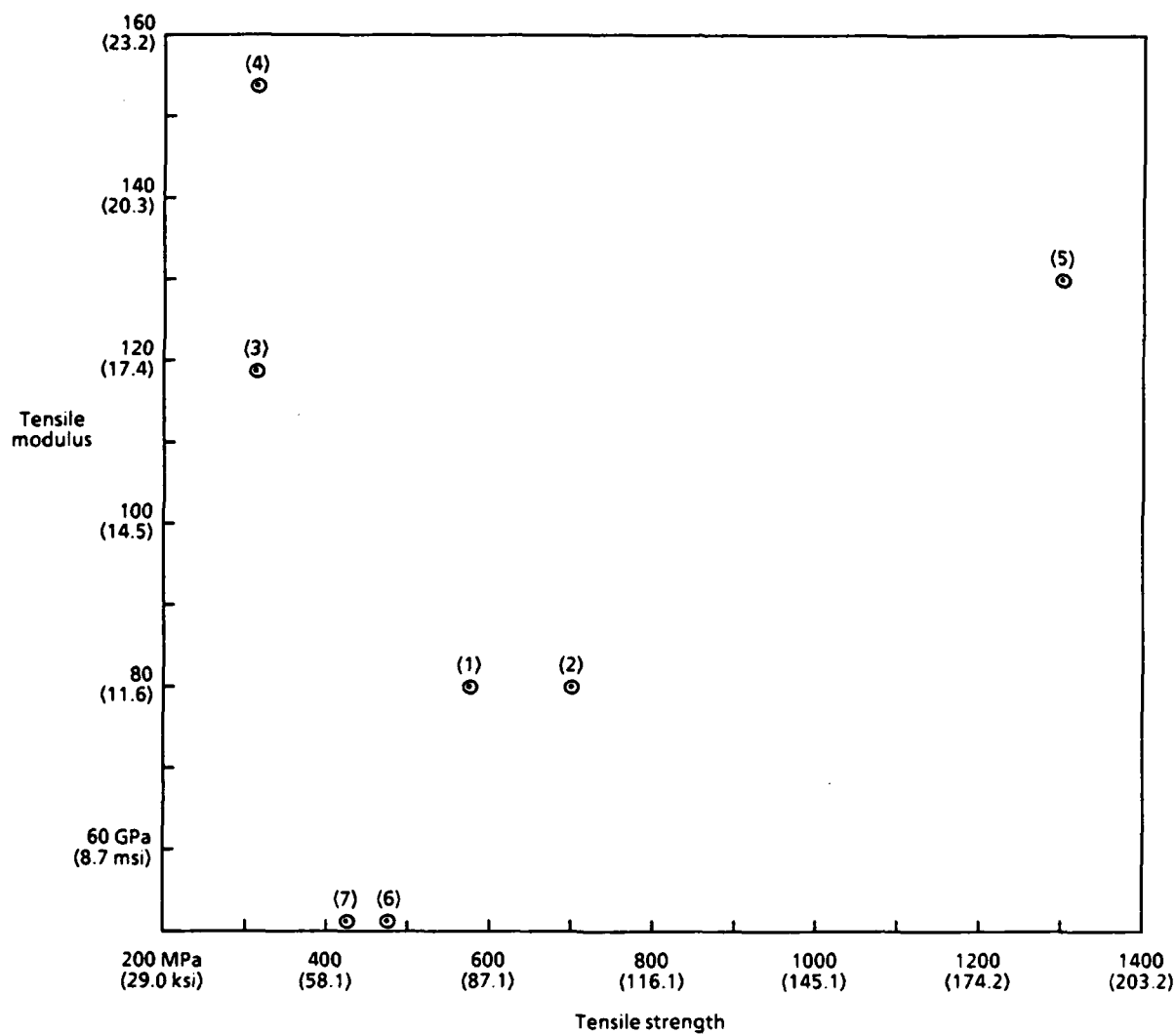
(4) Ultrahigh-modulus
     bidirectional
     graphite/epoxy

(5) Standard woven
     unidirectional
     graphite/epoxy

(6) Standard bidirectional
     hybrid graphite/S-2 glass

(7) Standard bidirectional
     hybrid graphite/
     Kevlar 49

Property	Units	LM	IMLS	IMHS	HM	Polyimide	PMR
Density	lb/in³ g/cm³	0.042 1.16	0.046 1.27	0.044 1.22	0.045 1.25	0.044 1.22	0.044 1.22
Modulus	msi GPa	0.32 2.20	0.50 3.45	0.50 3.45	0.75 5.17	0.50 3.45	0.47 3.24
Glass transition temperature (dry)	°C °F	177 350	216 420	216 420	216 420	371 700	371 700
Poisson's ratio	–	0.43	0.41	0.35	0.35	0.35	0.36
Thermal expansion coefficient	10^{-6} in./in.°F	57	57	36	40	20	28
Moisture expansion coefficient	in./in.m	0.33	0.33	0.33	0.33	0.33	0.33
Tensile strength	ksi MPa	8 55.1	7 48.2	15 103.4	20 137.8	15 103.4	8 55.1
Compression strength	ksi MPa	15 103.4	21 144.7	35 241.2	50 344.5	30 206.7	16 110.2
Shear strength	ksi MPa	8 55.1	7 48.23	13 89.57	15 103.4	13 89.57	8 55.1

Legend:
LM = Low modulus
IMLS = Intermediate modulus low strength
IMHS = Intermediate modulus high strength
HM = High modulus

Figure B-9. Properties of Matrices

Figure B-10.   Tensile Properties of Matrices
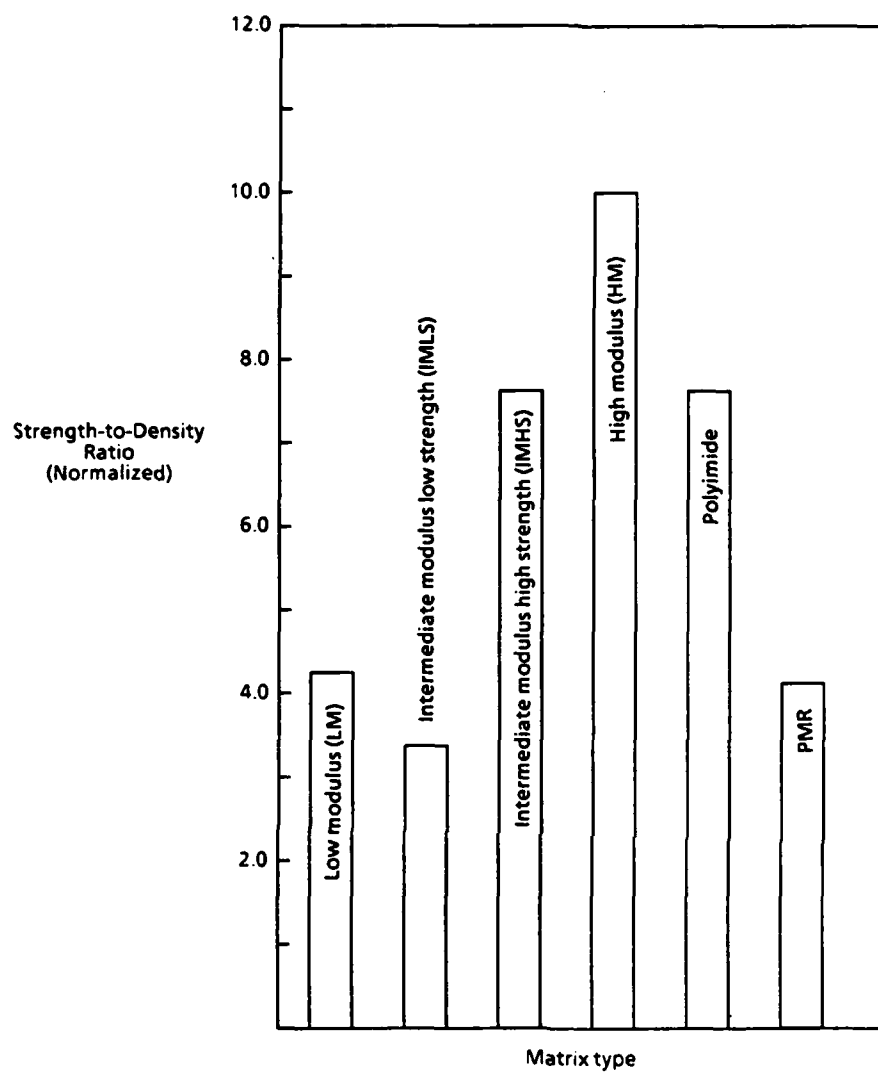
Figure B-11. Strength-to-Density Ratio of Matrices

Resin	Type	Specific gravity	Tensile modulus, GPa (msi)	Tensile strength, MPa (ksi)
Epoxy	Thermoset	1.1 - 1.4	2.1 - 5.5 (0.3 - 0.8)	40 - 85 (6 - 12)
Phenolic	Thermoset	1.2 - 1.4	2.7 - 4.1 (0.4 - 0.6)	35 - 60 (5 - 9)
Polyester	Thermoset	1.1 - 1.4	1.3 - 4.1 (0.2 - 0.6)	40 - 85 (6 - 12)
Acetal	Thermoplastic	1.4	3.5 (0.5)	70 (10)
Nylon	Thermoplastic	1.1	1.3 - 3.5 (0.2 - 0.5)	55 - 90 (8 - 13)
Polycarbonate	Thermoplastic	1.2	2.1 - 3.5 (0.3 - 0.5)	55 - 70 (8 - 10)
Polyethylene	Thermoplastic	0.9 - 1.0	0.7 - 1.4 (0.1 - 0.2)	20 - 35 (3 - 5)
Polyester	Thermoplastic	1.3 - 1.4	2.1 - 2.8 (0.3 - 0.4)	55 - 60 (8 - 9)

Figure B-12.   Table of Neat Resin Properties at Room Temperature
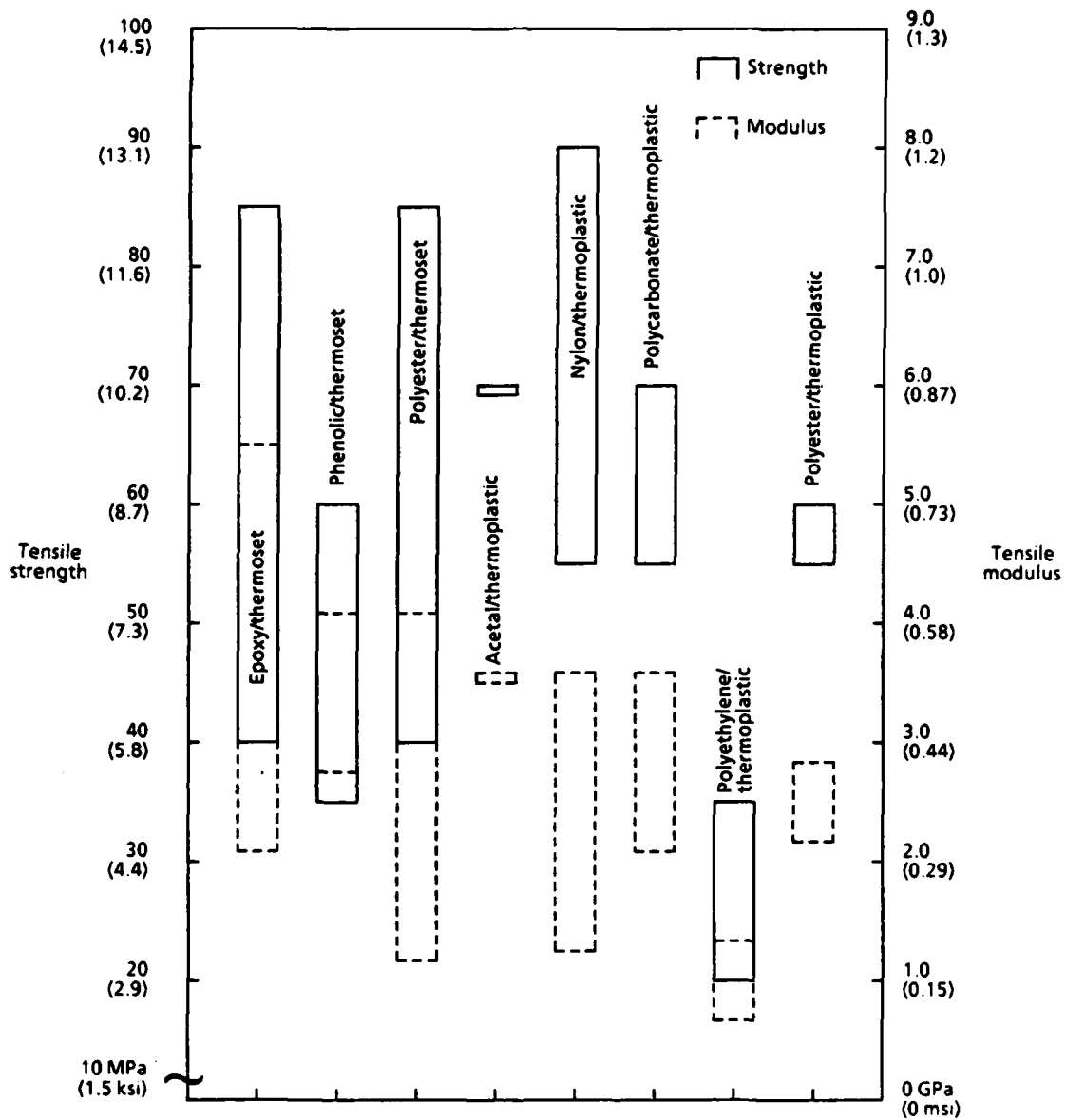
Figure B-13.   Neat Resin Properties at Room Temperature
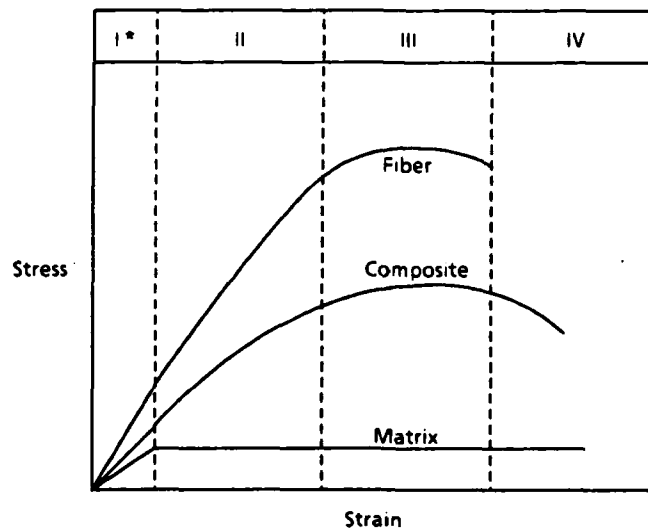
* Four stages of deformation of fibers, matrix, and
composite:

Stage I   – elastic deformation of both fibers
            and matrix.
Stage II – elastic deformation of fibers; plastic
            deformation of matrix.
Stage III – plastic deformation of both fibers
            and matrix.
Stage IV – failure of both fibers and matrix.

Figure B-14.   Deformation Stages of Fiber, Matrix, and Composite

	High strength	High modulus	Ultra-high modulus
Specific gravity, γ	1.8	1.9	2.0 - 2.1
Modulus, E, msi (GPa)	34 (230)	53 (370)	75 - 90 (520 - 620)
Tensile strength*, σ, ksi (MPa)	360 (2480)	260 (1790)	150 - 190 (1030 - 1310)
Tensile elongation, *%	1.1	0.5	0.2
Specific modulus, E/γ, msi (GPa)	19 (130)	20 (190)	38 - 45 (260 - 310)
Specific strength*, σ/γ, ksi (MPa)	200 (1380)	137 (940)	75 - 90 (520 - 620)
Longitudinal CTE, 10^{-6} in/in°F (10^{-6} m/m °C)	-0.2 (-0.4)	-0.3 (-0.5)	-0.6, est. (-1.1, est.)

* In a typical composite

Figure B-15. Properties of Graphite (Carbon) Fibers

Properties	E-glass	S-glass	Kevlar 29	Kevlar 49
Specific gravity, γ	2.60	2.5	1.44	1.44
Modulus, E, msi (GPa)	10.5 (72)	12.6 (87)	12** (83)	18 (124)
Tensile strength*, σ, ksi (MPa)	250 (1,720)	360 (2,530)	330 (2,270)	330 (2,270)
Tensile elongation*, %	2.4	2.9	2.8	1.8
Specific modulus, E/γ msi (GPa)	4.1 (28)	5.1 (35)	8.3 (57)	12.5 (86)
Specific strength*, σ/γ ksi (MPa)	96 (661)	145 (1,000)	230 (1,580)	230 (1,580)
Longitudinal, C.T.E., 10⁻⁶in/in °F (10⁻⁶m/m °C)	2.8 (5.0)	3.1 (5.6)		-1.1 (-2)

* In a typical composite

Figure B-16.   Properties of Kevlar and Glass Fibers

Neat Resin System	23°C (73.4°F)				82°C (179.6°F)				121°C (249.8°F)			
	Dry		Wet		Dry		Wet		Dry		Wet	
	MPa	ksi	MPa	ksi	MPa	ksi	MPa	ksi	MPa	ksi	MPa	ksi
Hercules 3502 - epoxy	41	6.0	36	5.2	42	6.1	25	3.6	54	7.8	15	2.2
Fibredux 914 - epoxy	28	4.0	48	7.0	32	4.6	32	4.6	19	2.8	8	1.2
Hercules 2220-1 - epoxy	43	6.3	68	9.9	73	10.6	46	6.7	60	8.7	23	3.4
Hercules 2220-3 - epoxy	46	6.7	67	9.7	70	10.2	44	6.4	62	9.0	21	3.0
Hexcel 1504 - epoxy	77	11.2	51	7.4	71	10.3	48	6.9	62	9.0	16	2.3
Narmco 5245C - Bismaleimide	74	10.7	47	6.8	62	9.0	57	8.2	76	11.0	28	4.0
American Cyanamid CYCOM 907 - multiphase epoxy, formerly BP907	86	12.5	59	8.4	67	9.7	2	0.3	1	0.1	–	–
Union Carbide 4901A - epoxy cured with MDA (Methylenedianaline)	109	15.8	79	11.5	57	8.2	3	0.4	10	1.4	–	–

Figure B-17. Table of Tensile Strength of Neat Resins
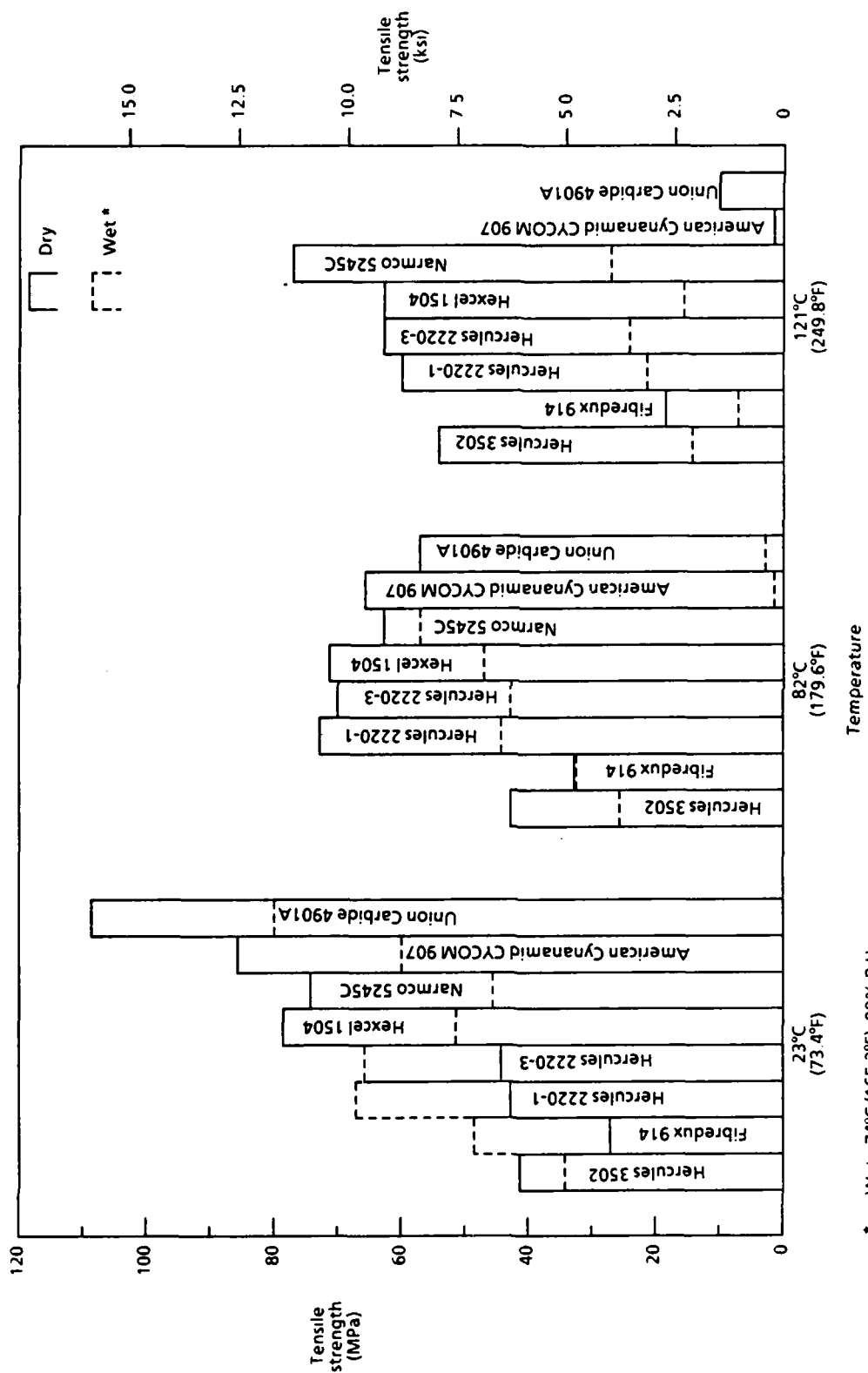
Figure B-18.   Tensile Strength of Neat Resins

Neat Resin System	23°C (73.4°F)				82°C (179.6°F)				121°C (249.8°F)			
	Dry		Wet		Dry		Wet		Dry		Wet	
	GPa	msi	GPa	msi	GPa	msi	GPa	msi	GPa	msi	GPa	msi
Hercules 3502 - epoxy	3.8	0.55	3.5	0.51	3.1	0.45	2.6	0.37	2.8	0.40	1.9	0.28
Fibredux 914 - epoxy	4.0	0.58	3.1	0.45	3.2	0.46	2.1	0.31	0.7	0.10	0.3	0.04
Hercules 2220-1 - epoxy	3.0	0.43	3.1	0.45	2.6	0.38	2.1	0.30	2.2	0.32	1.0	0.15
Hercules 2220-3 - epoxy	3.0	0.44	3.1	0.45	2.5	0.36	2.1	0.31	2.1	0.31	0.9	0.13
Hexcel 1504 - epoxy	3.9	0.57	3.5	0.51	3.3	0.48	2.8	0.40	2.7	0.39	0.9	0.13
Narmco 5245C - Bismaleimide	3.7	0.54	4.0	0.58	3.4	0.50	3.1	0.45	3.1	0.45	0.9	0.13
American Cyanamid CYCOM 907 - multiphase epoxy, formerly BP907	3.2	0.47	2.9	0.42	2.8	0.40	0.1	0.01	2.6	0.38	–	–
Union Carbide 4901A - epoxy, cured with MDA (methylenedianaline)	4.8	0.70	3.6	0.52	2.8	0.41	0.1	0.01	0.5	0.07	–	–

Figure B-19.   Table of Young's Modulus of Neat Resins

Figure B-20.   Young's Modulus of Neat Resins

D180-31996-1

B-21

Type	Ultimate tensile strength (MPa)	Ultimate tensile strength (ksi)	Tensile modulus (GPa)	Tensile modulus (msi)	Poisson's ratio (v_{12})	Ultimate compressive strength (MPa)	Ultimate compressive strength (ksi)	Compressive modulus (GPa)	Compressive modulus (msi)	Transverse shear strength (MPa)	Transverse shear strength (ksi)	Shear modulus (MPa)	Shear modulus (ksi)	Interlaminar shear strength (MPa)	Interlaminar shear strength (ksi)	Specific gravity, g/cm³	Cured ply range (μm)	Cured ply range (mils)
Standard graphite/epoxy	1515	220	131	19.0	0.3	1310	190	131	19.0	66	9.5	4.1	0.6	110	16.0	1.58	51-254	2-10
1.5%-strain graphite/epoxy	1895	275	134	19.4	0.3	1585	230	131	19.0	66	9.5	4.1	0.6	110	16.0	1.60	102-203	4-8
1.8%-strain graphite/epoxy	2585	375	138	20.0	0.3	1585	230	134	19.5	69	10.0	4.1	0.6	110	16.0	1.61	102-203	4-8
Intermediate-modulus graphite/epoxy	2760	400	165	24.0	0.3	1380	200	145	21.0	66	9.5	4.1	0.6	110	16.0	1.60	102-203	4-8
High-modulus graphite/epoxy	780	113	239	34.7	0.3	345	50	228	33.0	34	5.0	4.8	0.7	35	5.1	1.80	64-254	2.5-10
Ultrahigh-modulus graphite/epoxy	760	110	314	45.6	0.3	338	49	316	45.9	37	5.4	4.8	0.7	66	9.5	1.83	64-254	2.5-10
Pitch-100/epoxy	1035	150	421	61.0	0.3	255	37	310	45.0	34	5.0	4.8	0.7	31	4.5	1.83	64-127	2.5-5
Kevlar 49/epoxy	1365	198	46	6.7	0.3	207	30	41	6.0	59	8.5	2.1	0.3	52	7.5	1.45	127-254	5-10
E-glass/epoxy	1035	150	41	6.0	0.3	827	120	41	6.0	–	–	–	–	76	11.0	1.90	102-305	4-12
S-2 glass/epoxy	1690	245	52	7.6	0.3	827	120	60	8.7	–	–	–	–	76	11.0	2.02	102-305	4-12

Figure B-21. Physical Properties of Epoxy Preimpregnated Unidirectional Tapes

	Fiber diameter		Density		Tensile strength		Tensile modulus	
	μm	mils	g/cm³	lb/in³	MPa	ksi	GPa	msi
Magnamite AS1	8.00	0.315	1.80	0.065	3100	450	230	33
Magnamite AS4	8.00	0.315	1.80	0.065	3590	520	235	34
Magnamite AS6	–	–	1.82	0.066	4140	600	243	35
Magnamite IM6	–	–	1.74	0.063	4380	635	279	40
Celion GY-70	8.38	0.330	1.91-1.97	0.069-0.071	1520	220	485	70
Celion 3000	7.11	0.280	1.77	0.064	3790	550	231	34
Thornel T-300	6.93	0.273	1.77	0.064	3240	470	231	34

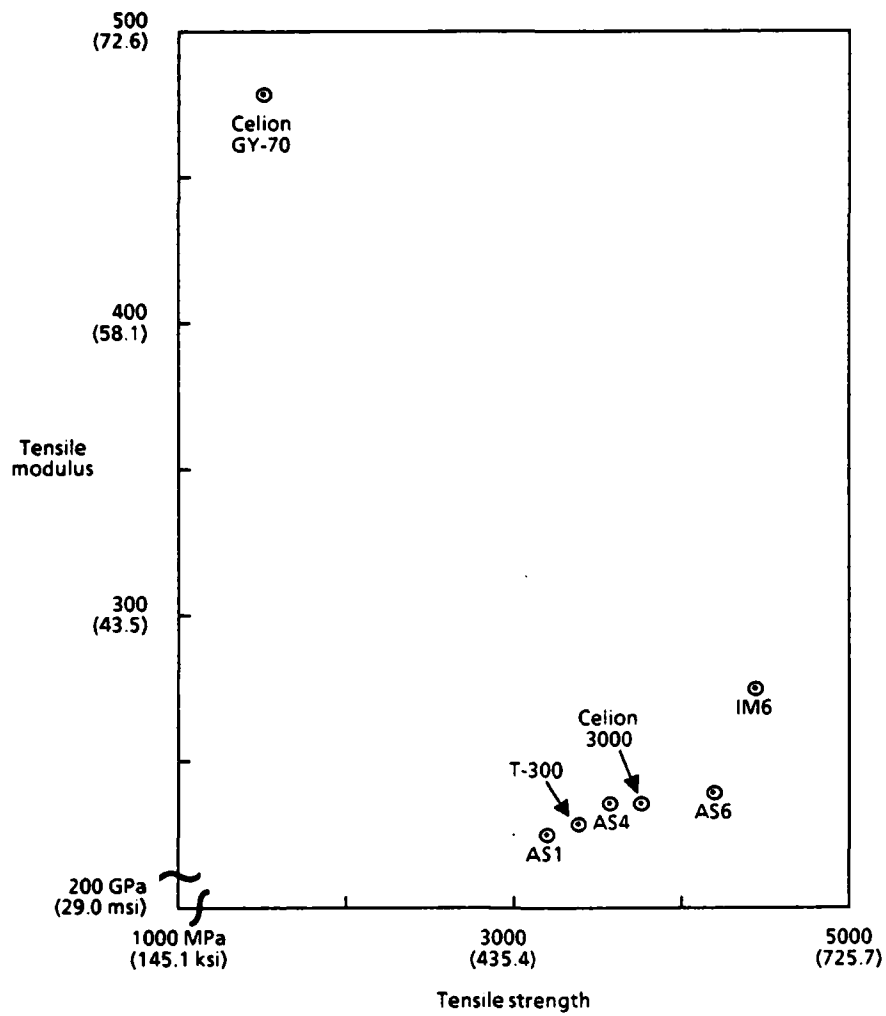*Figure B-22. Properties of Commercial Carbon Fibers*

Figure B-23.   Tensile Properties of Commercial Carbon Fibers
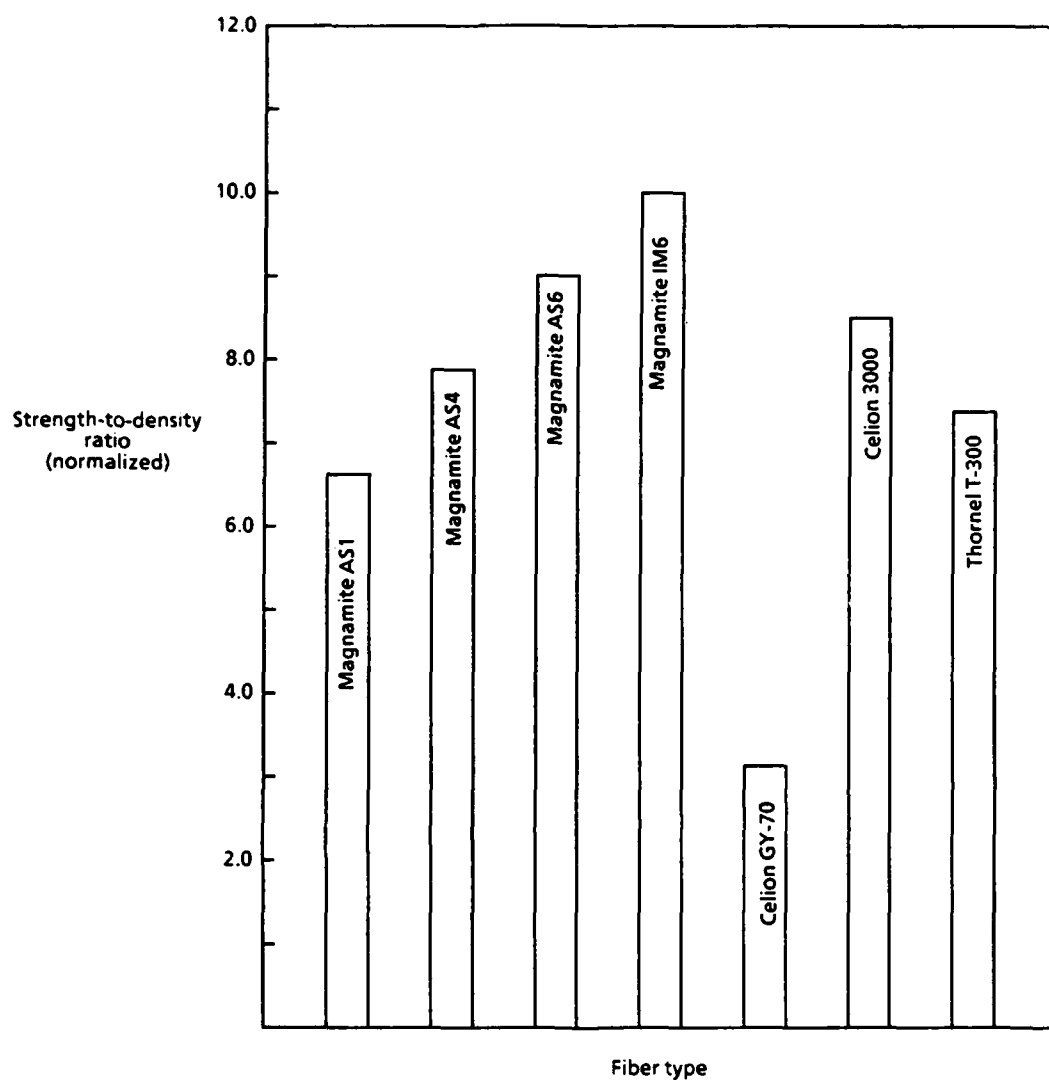
Figure B-24.   Strength-to-Density Ratio of Commercial Carbon Fibers

	Kevlar 29	Kevlar 49	E-glass	S-glass	High-strength carbon fiber	High-modulus carbon fiber	Ultra-high-modulus carbon fibers
Specific gravity	1.44	1.44	2.60	2.50	1.8	1.9	2.0-2.1
Modulus, msi (GPa)	12** (83)	18 (124)	10.5 (72)	12.6 (87)	34 (230)	53 (370)	75-90 (520-620)
Tensile strength, ksi (MPa)	330* (2270)	330* (2270)	250* (1720)	360* (2530)	360* (2480)	260* (1790)	150-190* (1030-1310)
Tensile elongation, %	2.8*	1.8*	2.4*	2.9*	1.1*	0.5*	0.2*
Specific modulus, msi (GPa)	8.3 (57)	12.5 (86)	4.1 (28)	5.1 (35)	19 (130)	28 (190)	3.8-45 (260-310)
Specific strength, ksi (MPa)	230* (1580)	230* (1580)	96* (661)	145* (1000)	200* (1380)	137* (940)	75-90* (520-620)
Longitudinal CTE, 10^{-6} in/in°F (10^{-6} m/m°C)	---	-1.1 (-2)	2.8 (5.0)	3.1 (5.6)	-0.2 (-0.4)	-0.3 (-0.5)	-0.6 (-1.1)

* In a typical composite.
** Modulus increases with stress. Initial value reported.

Figure B-25. Constituent Property Data of Fibers

APPENCIX C:

BOEING DATA FORMAT SHEETS

OPERATOR: C. T. Hua _____ DATE: October 1988 _____
REPORT NUMBER: _____ DESIGN DRAWING PART NAME/NUMBER: Air Force Panel _____

_____
_____
_____

PART LOCATION ON AIRCRAFT: Information not provided _____
MATERIAL/PROCESSING INFORMATION/SPECIFICATION: Information not provided _____

AIRPLANE INFORMATION: CUSTODIAN AFB: _____
                         MODEL: _____ FLIGHT HOURS: _____
                         NUMBER OF LANDINGS: _____

BACKGROUND/INFORMATION:
LOCATION OF DAMAGE: ___ Region A of the panel (see attached photo) _____
ENVIRONMENTAL CONCERNS: _____
(OTHERS): _____
_____
_____

DATA: _____
_____
_____
_____

ANALYSES CONDUCTED: ___ Macroscopic analysis included visual examination and macrophotograph.
Nondestructive examination included through transmission ultrasonics. Materials characterization included
thermomechanical analysis, infrared spectroscopy, acid digestion and wavelength dispersive X-ray. Microscopic
analysis included metallographic cross sectioning.

RESULTS: ___ The fastener hole damage indicated that Region A of the test panel was subject to tensile and shear
loading. The major damage appears to have been caused by impact loading in which a projectile penetrated
through the panel from the interior surface. Material characterization revealed the material system was 350°F
cure epoxy/carbon fiber, the resin content was 29.3% by weight, and the panel was fully cured. Cross-sectional
examination reveled a symmetrical and almost porosity-free laminate.

RECOMMENDATIONS: _____
_____
_____
_____
_____

KEYWORDS: Macroscopic analysis   Nondestructive examination _____
             Materials characterization   Microscopic analysis   _____

Exterior (painted) surface
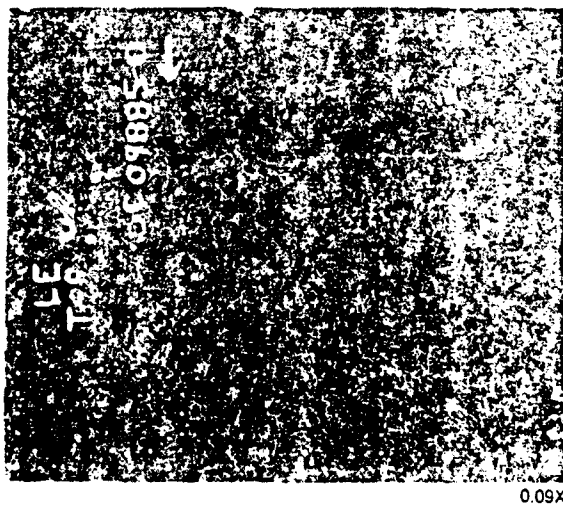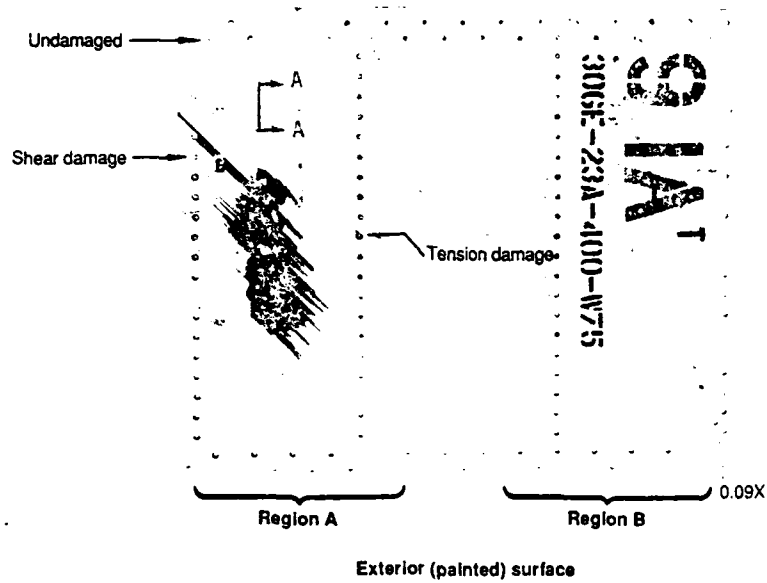
Interior (unpainted) surface

Photomacrograph of the Component as Received

OPERATOR: R. K. Krizanick   DATE: October 1988

PART NAME/NUMBER: Air Force panel

MATERIALS & CONSTRUCTION: Information not provided

LOCATION OF ANALYSIS: The entire panel.

REASON FOR ANALYSIS: To determine the damaged locations and the extent of damage
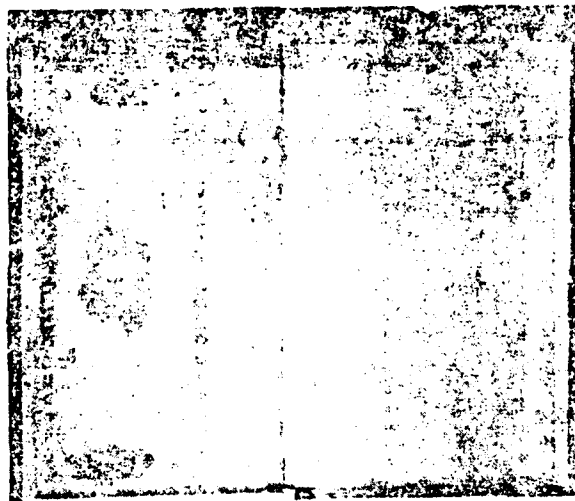
ANALYTICAL INSTRUMENT/SETTINGS: Through - transmission ultrasonics (TTU) at 5 MHz

SUPPORTIVE DATA: Attached C- Scan

RESULTS/INTERPRETATIONS: The major damage occurred at the center of one half of the panel. It appeared to be caused from impact loading with damaged fastener holes surrounding its perimeter.

KEYWORDS: NDE   TTU
          Delamination

0.08X

C-Scan of Component

OPERATOR: __Robert T. Parker__   DATE: __October 1988__

PART NAME/NUMBER: __Air Force Panel__

MATERIAL: __Information not provided__

VISUAL OBSERVATIONS: _Fastener hole damage was visually examined to determine the state of loading experienced by the panel during the test. The key evidence was the elongation of the hole and depth of the hole damage. The loading direction of the fastener is usually parallel to the major axis of the elongated hole. In general, the hole elongation indicates shear type loading where the head and the shank of the fastener tilts in an angle with respect to the hole. From mapping the fastener hold damage, it was determined that side A of the panel was loaded under tension. However, side B seemed to have been securely fastened to a fixed structure which was evidenced by the lack of fastener hole damage in that portion of the panel. The major delamination was caused by some type of object penetrating through the panel from the inner surface (the side without the paint finish). The evidence that suggested that the penetration occurred from the inside was the "brooming" fibers on the outer surface; commonly observed in an impact specimen. Two types of fasteners were placed into an undamaged fastener hole to verify whether the appropriate fasteners were used. The tensile fastener, which has a slightly larger head diameter than the shear fastener, fitted flush into the hole. However, upon placing each fastener into one of the fastener holes damaged from tensile loading, it was evident that the shear fastener was used. A tensile fastener fitted into a damaged hole did not match the hole damage. This suggests that the wrong fastener was used for the particular fastener hole._
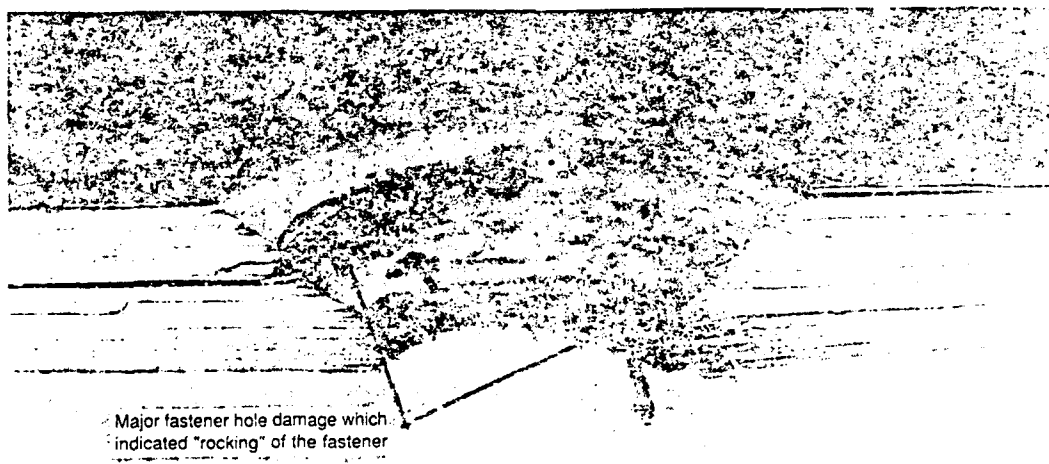
KEYWORDS: Fastener hole damage   Tensile loading

                 Hole elongation   Shear loading

Countersunk region

Plan view   2.4x

Major fastener hole damage which
indicated "rocking" of the fastener

Cross-sectional view   8x

Damage in the Fastener Hole Loaded Under Shear

Plan view   2.4X

Cross-sectional view   8X

Damage in the Fastener Hole Loaded Under Tension

Brooming fibers
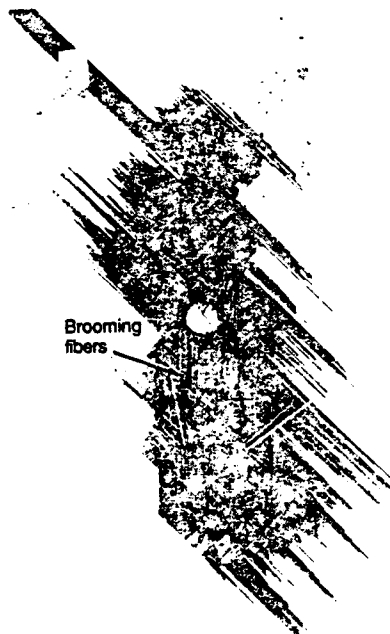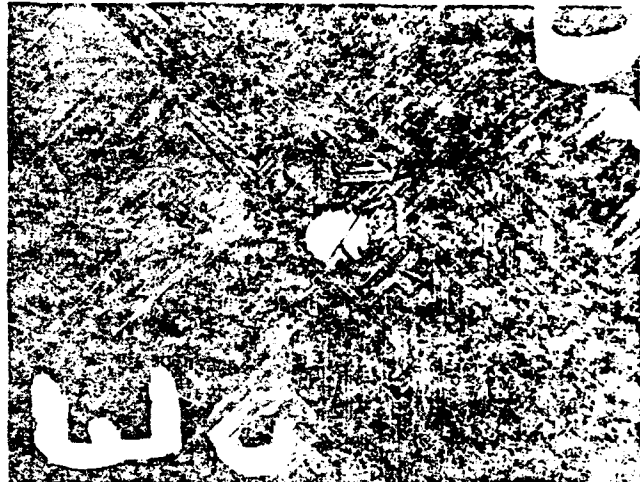
Damage on the exterior surface   0.23X   Damage on the interior surface   0.5X

Impact Damage
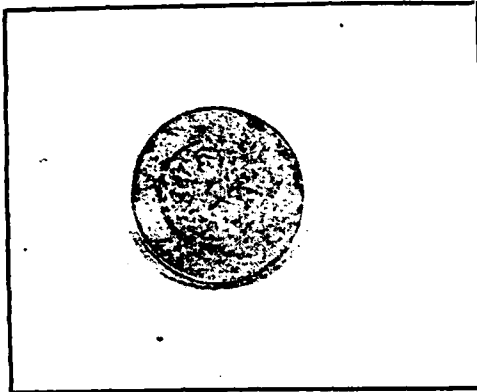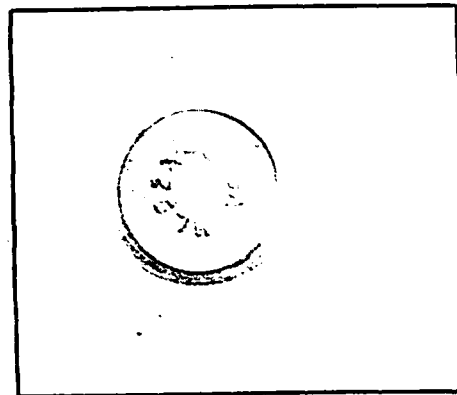
Tensile fastener   2.7X   Shear fastener   2.7X

Difference in Fastener Fit in the Undamaged Fastener Hole

OPERATOR: M. M. Yamashita   DATE: October 1988

PART NAME/NUMBER: Air Force Panel

MATERIAL: Continuous fiber reinforced composites

    RESIN/FIBER SYSTEM: Information not provided

    LAYUP: Information not provided

MICROSCOPIC OBSERVATIONS: Crack mapping of the delamination was not performed because the cause of the damage was determined by macroscopic analysis.

The layup sequence and ply count of the cross-section was performed by using optical microscopy. Although the specification requirement was unavailable, the symmetry of the ply stacking and sequence was determined. The laminated quality was good; no porosity.

KEYWORDS: Ply count   Laminate quality

                    Optical microscopy   Porosity

Ply stacking
sequence:

$$\begin{bmatrix} 45 \\ 45 \\ 90 \\ 90 \\ 45 \\ 45 \\ 90 \\ 90 \\ 0 \\ 45 \\ 45 \\ 90 \\ 90 \\ 45 \\ 45 \end{bmatrix}_S$$

Total number
of plies is 30
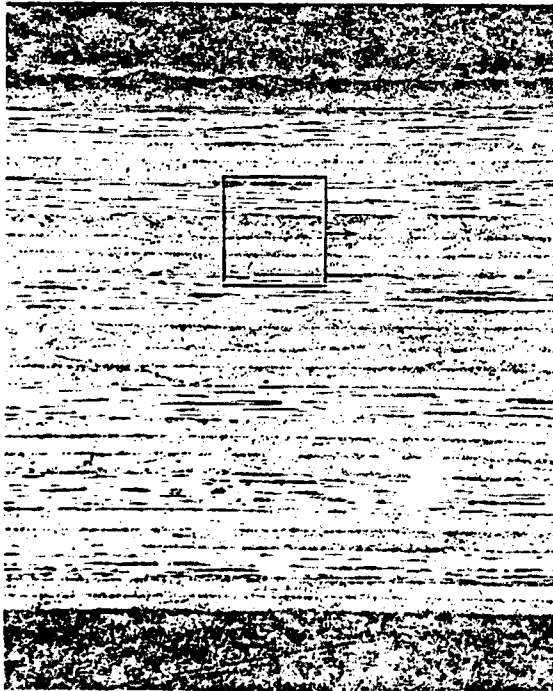
25X
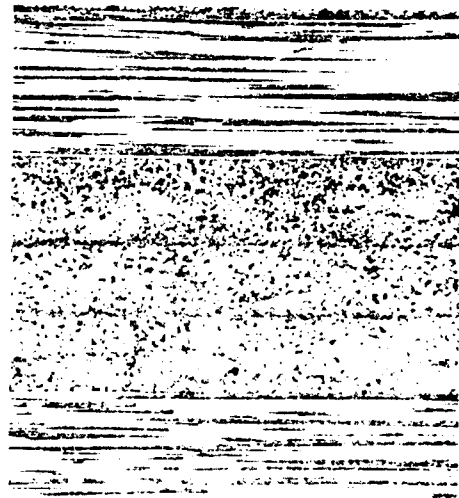
100X

Cross-Sectional View of the Panel

OPERATOR: <u>J. C. Chen</u>   DATE: <u>October 1988</u>

PART NAME/NUMBER: <u>Air Force Panel</u>

MATERIALS/SPECIFICATIONS: <u>Continuous fiber reinforced composites</u>

SPECIFICATION REQUIREMENTS: <u>None</u>

CURE TEMP: <u>Information not provided</u>

FIBER/RESIN DENSITIES: <u>Information not provided</u>

VERIFICATION DATA:

- Tg DETERMINATION—
  INSTRUMENTATION: <u>Thermomechanical analysis (TMA) - flexure method</u>

  RESULTS: <u>210.448°C, 209.715°C (average 210°F)</u>

- RESIN CHARACTERIZATION—
  INSTRUMENTATION: <u>Infrared (IR) spectroscopy</u>

  RESULTS: <u>The spectra obtained from the unknown resembled the spectra of either Hercules 3501-6 or Hexcel F-263 (epoxies) by "fingerprinting".</u>

- RESIN CONTENT—
  INSTRUMENTATION: <u>Acid digestion with nitric acid</u>

  RESULTS: <u>28.9, 29.4, 29.6% by weight (average 29.3%)</u>

- SPECIALIZED ANALYSES METHODS USED (HPLC, GPC, DSC, SURF. ANALYSIS, ETC.): <u>Wavelength dispersive X-ray (WDX) spectroscopy verified that the fiber was carbon.</u>

RESULTS: <u>The resin system used in fabricating this component was either Hercules 3501-6 or Hexcel F-263 with a glass transition temperature (Tg) of 410°F and a resin content of 29.3% by weight. The fiber was identified as a carbon fiber.</u>

KEYWORDS: <u>Thermomechanical analysis</u>   <u>Infrared (IR) spectroscopy</u>   <u>Acid digestion</u>

                         <u>Wavelength dispersive X-ray (WDX)</u>
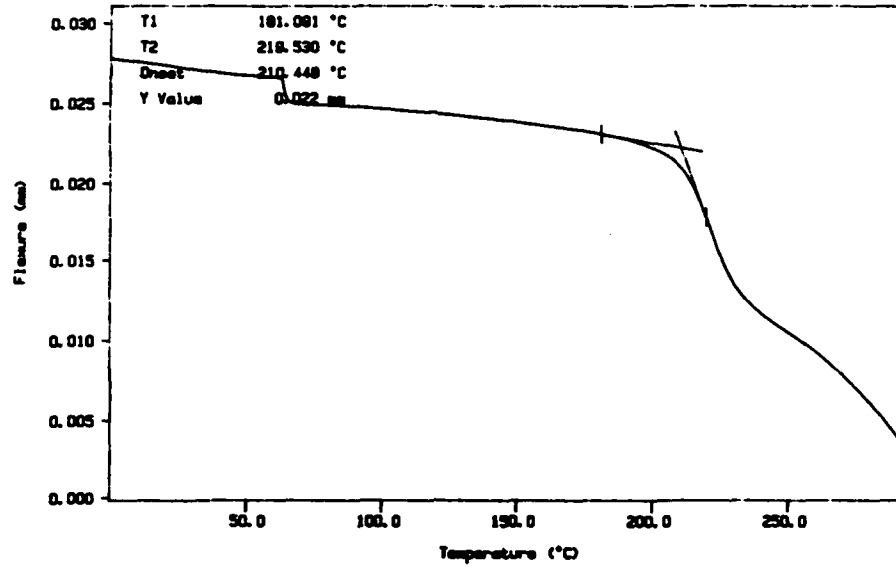
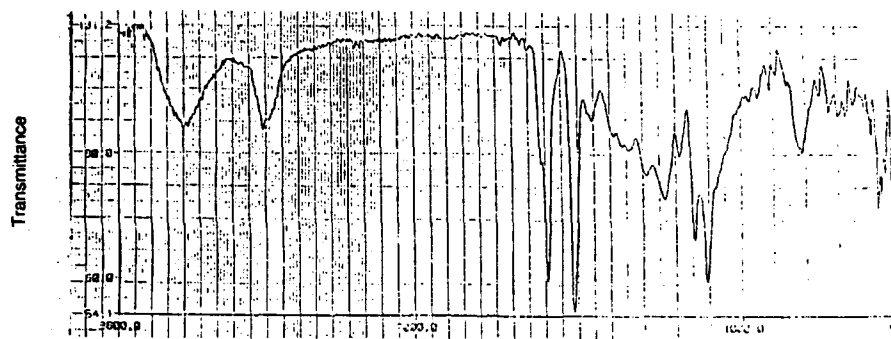TMA of sample 1   Tg = 210.448°C
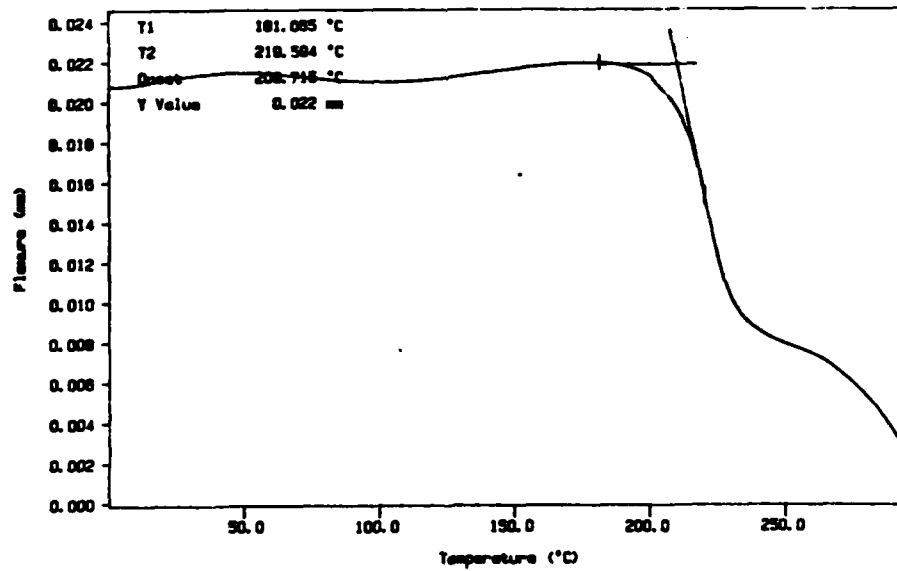
TMA of sample 2   Tg = 209.715°C

TMA Thermograms Showing an Average Glass Transition Temperature of 210°C

Sample No. 1   Wavenumber
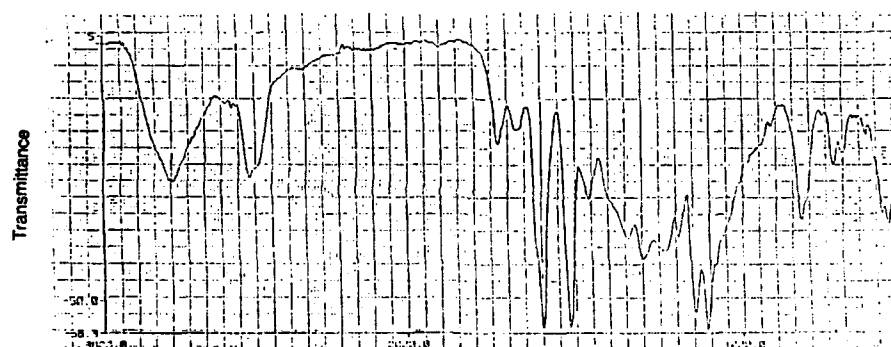
Hercules 3501-6   Wavenumber
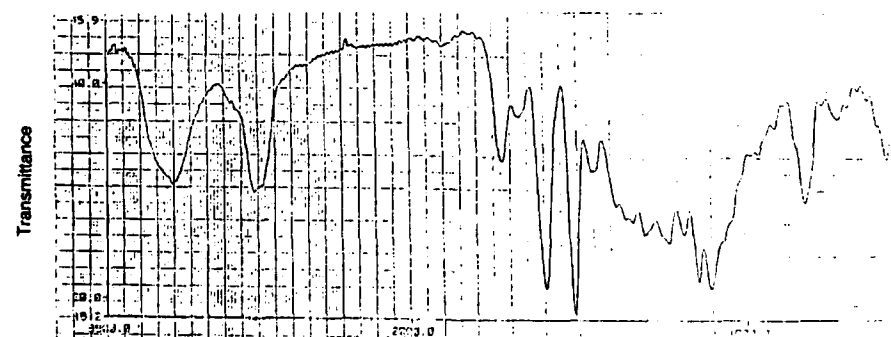
Hexel F263   Wavenumber

Infrared Spectroscopy Results

Sample No.	Composite weight (grams)	Fiber weight (grams)	Resin content (% by weight)
A	1.6451	1.1691	28.9
B	1.3565	0.9571	29.4
C	1.7080	1.2028	29.6
Average:	1.5699	1.1097	29.3

Resin Content Determined by Acid Digestion
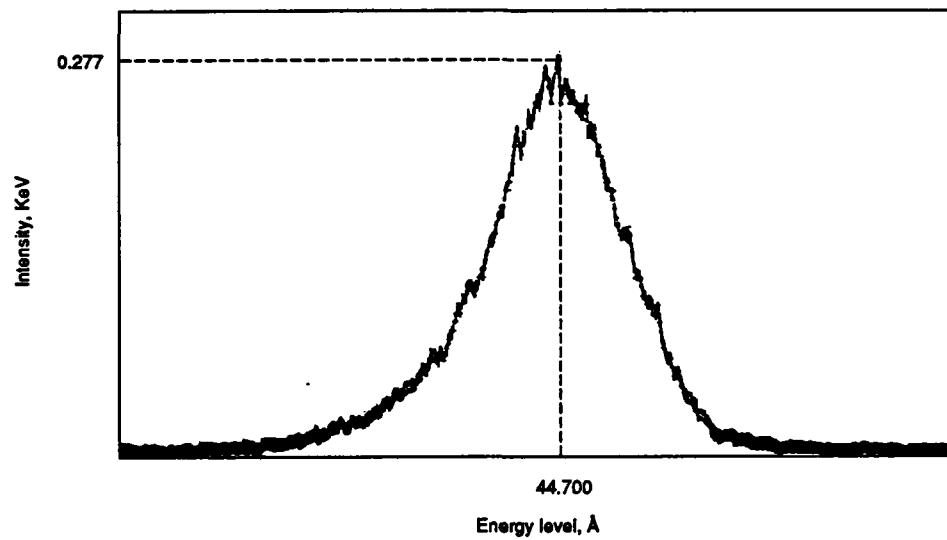
Wavelength Dispersive X-ray (WDX) Scan for Carbon K_α

APPENDIX D:

GE DATA FORMAT SHEETS

OPERATOR: G. White/GE   DATE: October 14, 1989
REPORT NUMBER: _____ DESIGN DRAWING PART NAME/NUMBER: _____

PART LOCATION ON AIRCRAFT: Main Landing Gear Strut
MATERIAL/PROCESSING INFORMATION/SPECIFICATION: E-Glass/Epoxy Composite

AIRPLANE INFORMATION: CUSTODIAN AFB: _____
                        MODEL: _____   FLIGHT HOURS: _____
                        NUMBER OF LANDINGS: _____

BACKGROUND/INFORMATION:
LOCATION OF DAMAGE: Wide End of Strut at Taper
ENVIRONMENTAL CONCERNS: Exposure to Moisture
(OTHERS): _____

DATA: _____

ANALYSES CONDUCTED: Visual Examination, SEM Examination, Metallographic Sectioning, Glass Transition
Temperature Measurement

RESULTS: Translaminar fracture and delamination occurred as a result of a bending load applied at the fracture
location. Material condiiton was good.

RECOMMENDATIONS: _____

KEYWORDS: _____

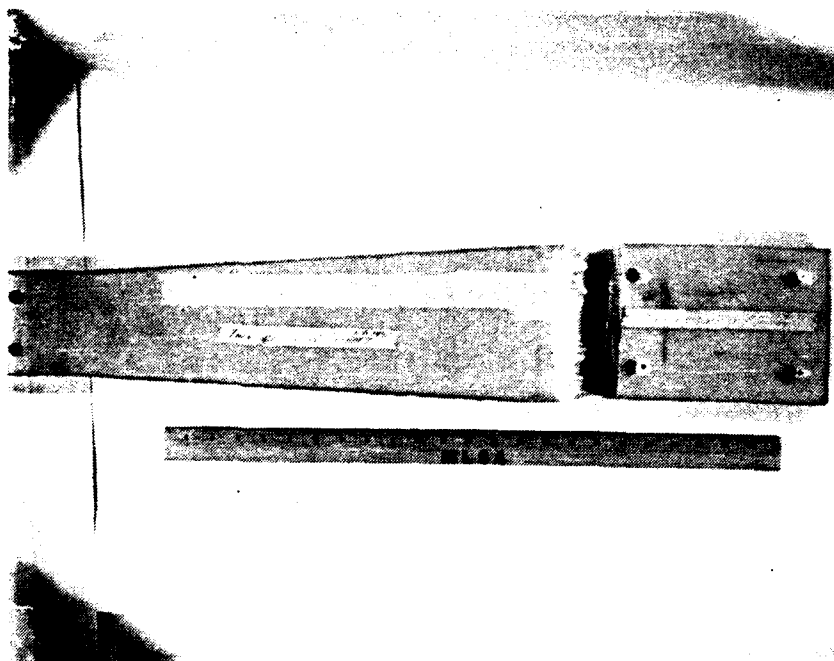OPERATOR: __G. White/GE__ DATE: __October 14, 1988__

PART NAME/NUMBER: __Helio H-800 Main Landing Gear Strut__

MATERIAL: __E-Glass/Epoxy Composite__

VISUAL OBSERVATIONS: __The fracture was located at the wide end of the strut at the point where the taper begins.__ __This translaminar fracture revealed both tensile and compressive fracture characteristics, typical of fracture under a__ __bending load. The tensile and compressive portions of this fracture were consistent with aircraft orientation. A dis-__ __continuous delamination was observed on both the large (long) and small pieces of this fracture. The delamination__ __was located at approximately the mid-thickness of the strut, between the tensile and compressive portions of the__ __fracture.__

KEYWORDS: __Translaminar__ __Delamination__ _____

MAGNIFICATION: 0.12X

COMMENTS: Photomacrograph of the strut upper surface in the as-received condition.

MAGNIFICATION: 1X

COMMENTS: Photomacrograph of the translaminar fracture surface (small end) with the tensile portion in the lower half of the photo.

OPERATOR: G. White/GE   DATE: October 14, 1988

PART NAME/NUMBER: Helio H-800 Main Landing Gear Strut

MATERIAL: Composite

    RESIN/FIBER SYSTEM: E-Glass/Epoxy

    LAYUP: 0°, 90° Plies

MICROSCOPIC OBSERVATIONS: Evidence of shear fracture (scallops and hackles) were observed on the delamination surface. The propagation direction was oriented axially along the length of the strut, but the exact direction could not be determined. Examination of the tensile half of the translaminar fracture revealed radial patterns on fiber end fractures which indicated propagation from the lower surface (tension) toward the delamination. Examination of the compressive half to the translaminar fracture revealed buckled fibers and individual fibers displaying both tensile and compressive fracture features, typical of compressive failures.

KEYWORDS: Scallops   Hackles   Delamination

                Translaminar

OPERATOR: G. White/GE   DATE: October 14, 1988

PART NAME/NUMBER: Helio H-800 Main Landing Gear Strut

MATERIALS/SPECIFICATIONS: E-Glass/Epoxy Composite

SPECIFICATION REQUIREMENTS: _____

CURE TEMP: _____

FIBER/RESIN DENSITIES: _____

VERIFICATION DATA:

- Tg DETERMINATION–
  INSTRUMENTATION: ___TMA, DSC_____

  RESULTS: 133°C, 135°C _____

- RESIN CHARACTERIZATION–
  INSTRUMENTATION: _____

  RESULTS: _____

- RESIN CONTENT–
  INSTRUMENTATION: _____

  RESULTS: _____

- SPECIALIZED ANALYSES METHODS USED (HPLC, GPC, DSC, SURF. ANALYSIS, ETC.): _____
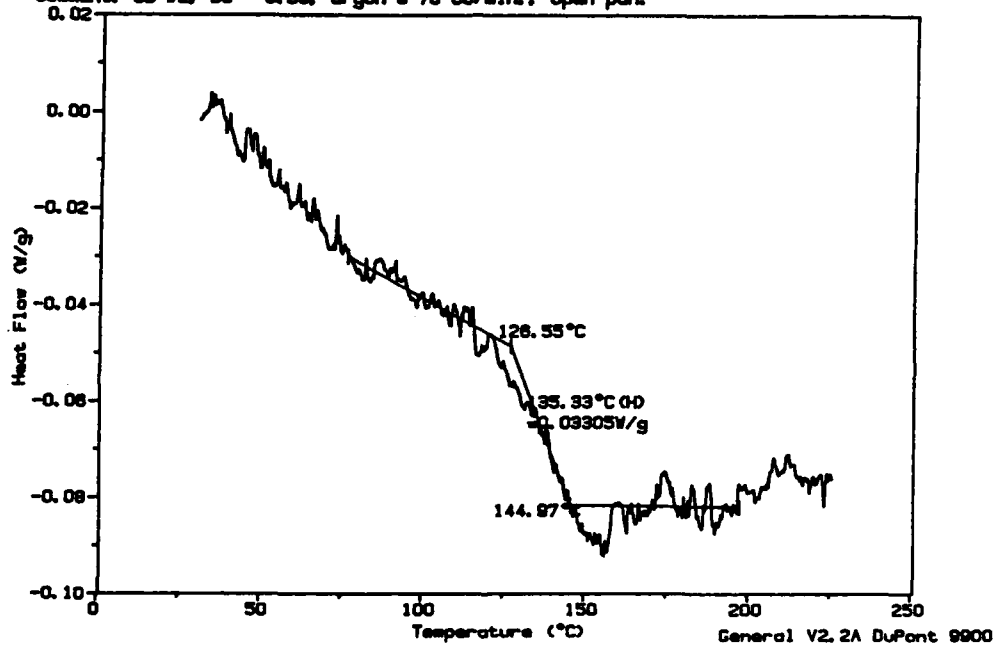
RESULTS: _____

KEYWORDS: _____

Sample: Glass fiber/Epoxy Laminate DSC File: E:810050SC.02
Size: 19.4300 mg Operator: SLC
Method: 20°C/min. DSC Run Date: 07/21/88 15:49
Comment: CB #2, BS = 5.09, argon @ 70 cc/min., open pan.

COMMENTS: Glass transition temperature was measured as 135°C by DSC.

D180-31996-1

D-8